

Electronic Structure and Reactivity of Transition Metal Complexes Incorporating Pro-Radical Bis- Phenoxide Ligands

by

Ryan Michael Clarke

B.Sc. (Hons), Mount Allison University, 2012

Thesis Submitted in Partial Fulfillment of the
Requirements for the Degree of
Doctor of Philosophy

in the
Department of Chemistry
Faculty of Science

© Ryan Michael Clarke
SIMON FRASER UNIVERSITY
Spring 2018

Copyright in this work rests with the author. Please ensure that any reproduction or re-use is done in accordance with the relevant national copyright legislation.

Approval

Name: Ryan Michael Clarke
Degree: Doctor of Philosophy (Chemistry)
Title: *Electronic Structure and Reactivity of Transition Metal Complexes Incorporating Pro-Radical Bis-Phenoxide Ligands*
Chair: Dr. Michael H. Eikerling
Professor

Examining Committee:

Dr. Tim Storr
Senior Supervisor
Associate Professor

Dr. Daniel B. Leznoff
Supervisor
Professor

Dr. Vance E. Williams
Supervisor
Associate Professor

Dr. Loren Kaake
Internal Examiner
Assistant Professor

Dr. Andrew S. Borovik
External Examiner
Professor
Department of Chemistry
University of California, Irvine

Date Defended/Approved: April 5, 2018

Abstract

Transition metal complexes with pro-radical ligands have received considerable research attention due to their interesting electronic structures, photophysical properties, and applications in catalysis. The relative ordering of metal and ligand frontier orbitals in a complex incorporating pro-radical ligands dictates whether oxidation/reduction occurs at the metal centre or at the ligand. Many metalloenzymes couple redox events at multiple metal centres or between metals and pro-radical ligands to facilitate multielectron chemistry. Owing to the simplicity of the active sites, many structural and functional models have been studied. One class of pro-radical ligand that has been investigated extensively are bis-imine bis-phenoxide ligands (i.e. salen) due to their highly modular syntheses. In this thesis, projects related to the synthesis, electronic structure, and reactivity of mono and bimetallic complexes incorporating the salen framework are explored.

Chapter 2 presents a systematic investigation of the effects of geometry on the electronic structure of four bis-oxidized bimetallic Ni salen species. The tunability of their intense intervalence charge transfer (IVCT) transitions in the near infrared (NIR) by nearly 400 nm due to exciton coupling in the excited states is described. For the first time, this study demonstrates the applicability of exciton coupling to ligand radical systems absorbing in the NIR region. Chapter 3 investigates the ground-state electronic structure of a bis-oxidized Co dimer. Enhanced metal participation to the singly occupied molecular orbitals results in both high spin Co(III) and Co(II)-L* character in the ground state, and no observable band splitting in the NIR due to exciton coupling. Finally, Chapter 4 describes a series of oxidized nitridomanganese(V) salen complexes with different *para* ring substituents (R = CF₃, tBu, and NMe₂), demonstrating that nitride activation is dictated by remote ligand electronics. Upon one-electron oxidation, electron deficient ligands afford a Mn(VI) species and nitride activation, whereas an electron-rich ligand results in ligand based oxidation and resistance to N coupling of the nitrides. This study highlights the alternative reactivity pathways that pro-radical ligands impose on metal complexes and represents a key step in the use of NH₃ as a hydrogen storage medium. The results presented herein provide a starting point for further efforts in reactivity with the salen platform.

Keywords: pro-radical ligands; electronic structure; bioinorganic chemistry; intervalence charge transfer; salen; ligand design

To my parents, who were my first teachers

Acknowledgements

Many individuals have made contributions to this thesis both academically and personally. The contributions of my parents, Michael and Julie, cannot be overstated, and to them I extend my deepest gratitude. You have provided me with all the tools and unwavering support necessary to succeed, for which there are no words or the space required to write them. You are my first and longest tenured teachers, and I continue to learn from you every day. To the rest of my family who have provided a nurturing (and oftentimes wildly entertaining) environment in which to grow, thank you. Finally, I'd like to extend a deep appreciation to my grandparents Robert and Elizabeth Walton. Although my grandfather surely holds the world record for asking 'when are you going to graduate?', your contributions to this thesis are innumerable. Hopefully now I can finally start working towards my tab...

To my senior supervisor Prof. Tim Storr, thank you for allowing me to freely explore my interests while working in your research group, and always facilitating my advancement as a scientist by sending me to conferences, publishing my work, or sending me off to France. Thank you for the many formative discussions concerning both science and life in general, your mentorship will be greatly missed.

I was fortunate in 2016 to be able to spend some time in France working with long-time Storr group collaborator Prof. Fabrice Thomas on a few different projects – some of which is included in Chapter 2. Everyone in the lab who made my short stay in France memorable deserves recognition here. Fabrice Thomas, Nicolas Leconte, Olivier Jarjayes, Vianney Reginer, and Jules Moutet – thank you all for being so welcoming!

To all the support staff at SFU, you have my thanks. Specifically, I want to thank Dr. Andrew Lewis for his help with the VT NMR experiments outlined in Chapter 3, and Paul Mulyk for running all the elemental analyses in this thesis, as well as helping me with all the GC-MS experiments outlined in Chapter 4. I gave Paul very little notice when I needed the GC carrier gas switched to helium, and if I drove him crazy he didn't show it. I owe you a case of beer or two...

To my committee members, Prof. Daniel Leznoff and Prof. Vance Williams, thank you for taking the time to serve on my committee and for your helpful suggestions during committee meetings over the years.

I had the great privilege of working with many talented lab mates during my time as a graduate student, and I thank you all for the discussions we've had both scientific and otherwise. Special recognition to Khrystyna Herasymchuk who worked with me on the redox-active ligand projects and took on a lot of the administrative duties of the group – I look forward to our continued friendship. Also thanks to Luiza Gomes for obtaining a lot of the MALDI-MS data found within. To new student Diego Martelino, keep working hard and you will be successful, and even if it makes things a little bit harder, stand up for yourself when you need to.

Along with talented lab mates, I had the pleasure of working with a number of visiting students and undergraduates (Adrian Woenckhaus, Tiffany Jeen, Serena Rigo, Makrum Guterres, and Christophe Mayer) over the years. Tiffany and Serena provided contributions to the work described in Chapter 2, and I hope that you learned as much from me as I did from you! Thanks for all your hard work.

I leave graduate school with two lifelong friends in John Thompson and Michael Cooper-Jones. You guys showed me the way early, and taught me what it meant to be a graduate student (in very different ways...). And even though I didn't get invited to John's wedding, and I usually only eat one lunch, you guys are some of the closest friends I have ever had.

Many other friends have made my time here more enjoyable, usually over beers and board games. Eric Bowes, Jessica Allanach, Tom Kostelnik, Curtis Gibbs, Aaron Chester, Ania Sergeenko, and David Weber – you have all provided momentary relief from the stresses of graduate school, so thank you! Also, Eric and I probably logged more hours playing Halo these last few years (~2,500 Warthog kills, and counting!) than is healthy...

Finally, Jessica Miller. Although my parents got me here, its inarguable that you got me through it. If nothing else, this will all be worth it because of you. You are my support system, and my very best friend. I hope that I have made you proud. I promise that one day we'll go back to Italy, and you can go for the gelato world record!

Thanks everyone!

Ryan

Table of Contents

Approval.....	ii
Abstract.....	iii
Dedication.....	v
Acknowledgements.....	vi
Table of Contents.....	viii
List of Tables.....	xi
List of Figures.....	xii
List of Schemes.....	xviii
List of Acronyms.....	xix
Chapter 1. Introduction.....	1
1.1. Pro-Radical Ligands.....	1
1.1.1. Pro-Radical Ligands in Nature.....	2
1.1.2. Synthetic Models Incorporating Pro-Radical Ligands.....	4
1.2. Salen as a Pro-Radical Ligand.....	8
1.2.1. Effect of Metal Ion.....	13
1.2.2. Effect of Peripheral Substituents.....	15
1.2.3. Effect of Solvent and Temperature.....	16
1.3. Multimetallic Cooperativity.....	17
1.4. Multimetallic Salen Complexes.....	20
1.4.1. Catalysis.....	21
1.4.2. Magnetics and Small Molecule/Ion Sensing.....	24
1.5. Thesis Synopsis.....	26
Chapter 2. Exploiting Exciton Coupling of Ligand Radical Intervalence Charge Transfer Transitions to Tune NIR Absorption.....	29
2.1. Introduction.....	29
2.2. Results.....	32
2.2.1. Synthesis.....	32
2.2.2. Solid-State Characterization.....	34
2.2.3. Electrochemistry.....	38
2.2.4. Electron Paramagnetic Resonance Spectroscopy.....	41
2.2.5. Electronic Absorption Spectroscopy.....	46
2.2.6. Theoretical Calculations.....	49
2.3. Discussion and Summary.....	53
2.4. Experimental.....	53
2.4.1. Materials.....	53
2.4.2. X-ray Structure Determination.....	54
2.4.2.1. X-ray Structure Determination of 2.....	54
2.4.2.2. X-ray Structure Determination of 4 and 5.....	55
2.4.3. Oxidation Protocol.....	55
2.4.4. Theoretical Calculations.....	55

2.4.5. Synthesis.....	56
Chapter 3. Electronic Structure Description of a Doubly Oxidized Bimetallic Cobalt Complex with a Proradical Ligand	61
3.1. Introduction.....	61
3.2. Results	65
3.2.1. Synthesis and Solution-State Characterization	65
3.2.2. Solid-State Characterization of CoL^1 and Co_2L^2	66
3.2.3. Electrochemistry	68
3.2.4. Synthesis and Characterization of Oxidized Complexes	70
3.2.5. Electronic Absorption Spectroscopy	71
3.2.6. Electron Paramagnetic Resonance Spectroscopy	74
3.2.7. Solid-State Magnetism.....	75
3.2.8. Theoretical Analysis.....	79
3.2.8.1. Neutral CoL^1 and Co_2L^2	79
3.2.8.2. $[\text{CoL}^1\text{-H}_2\text{O}]^+$ and $[\text{Co}_2\text{L}^2\text{-2H}_2\text{O}]^{2+}$	81
3.2.9. Double Oxidation of CoL^1	87
3.3. Discussion and Summary	90
3.4. Experimental	92
3.4.1. Materials.....	92
3.4.2. Instrumentation.....	92
3.4.3. X-ray Structure Determination	93
3.4.3.1. CoL^1	93
3.4.3.2. $[\text{CoL}^1\text{-H}_2\text{O}]^+$	94
3.4.3.3. Co_2L^2	94
3.4.4. Solid-State Magnetism.....	95
3.4.5. Theoretical Calculations	95
3.4.6. Synthesis.....	95
Chapter 4. Tuning Electronic Structure to Control Manganese Nitride Activation ..	99
4.1. Introduction.....	99
4.2. Results	102
4.2.1. Synthesis.....	102
4.2.2. Solid-State Characterization	103
4.2.3. Electrochemistry	106
4.2.4. Electronic Absorption Spectroscopy	110
4.2.5. Electron Paramagnetic Resonance Spectroscopy	113
4.2.6. Decay Kinetics.....	116
4.2.7. Theoretical Calculations	121
4.3. Discussion and Summary	122
4.4. Experimental	123
4.4.1. Materials.....	123
4.4.2. Instrumentation.....	124
4.4.3. X-ray Structure Determination	124

4.4.4.	Oxidation Protocol	125
4.4.5.	Kinetics Measurements	125
4.4.6.	Isotopic Detection by GC-MS.....	125
4.4.7.	Theoretical Calculations	126
4.4.8.	Synthesis.....	126
Chapter 5.	Ongoing and Future Directions.....	132
5.1.	Thesis Summary.....	132
5.2.	Chapter 2 and Chapter 3	132
5.2.1.	Reactivity of Bimetallic Salen Constructs	132
5.2.1.1.	C-H Fluorination	133
5.2.1.2.	Oxidative Transformations.....	135
5.2.2.	Aggregation of $[5^{**}]^{2+}$	136
5.3.	Chapter 4	137
5.3.1.	Mechanism for N-N Coupling.....	137
5.3.2.	N-Atom Transfer	138
5.3.3.	C-H Bond Activation	139
5.3.3.1.	Photolysis of $[Mn^V(Sal^{NMe_2})N]^{*+}$	140
5.3.3.2.	Protonolysis of $[Mn^V(Sal^{NMe_2})N]^{*+}$	143
5.3.4.	Oxidation of Ammonia to H_2 and N_2	145
5.4.	Experimental	146
5.4.1.	Protocol for C-H Fluorination of 4-Ethylbiphenyl	146
5.4.2.	Synthesis.....	146
5.4.3.	Photolysis of $[Mn(Sal^{NMe_2})N]^{*+}$	151
References.....		152
Appendix A.	Supplementary Information for Chapter 2.....	178
Appendix B.	Supplementary Information for Chapter 3	187
Appendix C	Supplementary Information for Chapter 4	189

List of Tables

Table 1.1.	Optical properties of IVCT bands in mixed-valence compounds.....	11
Table 1.2.	Experimental and theoretical techniques commonly used in studying oxidized metal-salen complexes.....	12
Table 2.1.	Selected crystallographic data for 2 , 4 , and 5	37
Table 2.2.	Experimental and calculated (in parentheses) ^a coordination sphere metrical parameters for the complexes [Å].	37
Table 2.3.	Redox potentials for 1-5 vs. $F_c^+/F_c^{a,b}$, and the comproportionation constant (K_c).....	40
Table 2.4.	EPR simulation parameters for [1^{•+}] and [2-5^{•+}]²⁺	42
Table 2.5.	Spectroscopic properties of the Ni complexes in CH ₂ Cl ₂ solution. ^a	49
Table 2.6.	TD-DFT predicted energies and oscillator strengths for the broken symmetry ($S = 0$) solution for the doubly oxidized dimers. ^{a,b,c}	50
Table 3.1.	Selected crystallographic data for CoL¹ , Co₂L² , and [CoL¹-H₂O]⁺	68
Table 3.2.	Redox potentials for CoL¹ and Co₂L² versus $F_c^+/F_c^{a,b}$	69
Table 3.3.	Spectroscopic properties of the Co complexes in CH ₂ Cl ₂ solution.	72
Table 3.4.	Experimental ^a and calculated (in parentheses) ^b coordination sphere metrical parameters for the neutral complexes (in Å).	80
Table 3.5.	DFT-calculated energy differences of possible spin states for [CoL¹-H₂O]⁺	82
Table 3.6.	Experimental and calculated ^a coordination sphere metrical parameters for [CoL¹-H₂O]⁺ (in Å).....	83
Table 4.1.	Selected crystallographic data for Mn(Sal^{CF3})N , Mn(Sal^{NMe2})N , and [Mn(Sal^{tBu})] [SbF₆]	106
Table 4.2.	Redox potentials for Mn(Sal^{tBu})N , Mn(Sal^{CF3})N , and Mn(Sal^{NMe2})N versus $F_c^+/F_c^{a,b}$	107
Table 4.3.	EPR simulation parameters for [Mn(Sal^R)N]^{+a}	114
Table 4.4.	Headspace gas analysis results for the room temperature oxidation of Mn(Sal^{tBu})^{14/15}N 10 minutes after addition of AgSbF ₆	118
Table 4.5.	Headspace gas analysis results for the room temperature oxidation of Mn(Sal^{CF3})^{14/15}N 10 minutes after addition of AgSbF ₆	119
Table 4.6.	Headspace gas analysis results for the room temperature oxidation of Mn(Sal^{NMe2})^{14/15}N 10 minutes after addition of AgSbF ₆	120
Table 4.7.	Headspace gas analysis results for the room temperature oxidation of Mn(Sal^{NMe2})^{14/15}N 24 hours after addition of AgSbF ₆	120
Table 5.1.	Redox potentials for Mn(Sal^{tBu})N (+ 1 and 2 eq. [H(Et ₂ O) ₂][BF ₄]) versus $F_c^+/F_c^{a,b}$	144

List of Figures

Figure 1.1.	Possible oxidation or reduction processes for metal complexes with pro-radical ligands. Red electrons represent electrons gained or lost in the reduction/oxidation event.	1
Figure 1.2.	Possible electronic structures of O ₂ transport proteins proposed by Pauling and Weiss that give an $S_{\text{Total}} = 0$, illustrating the redox ambiguity of dioxygen, and the resulting effect on the oxidation state of the central Fe.	2
Figure 1.3.	(A) Galactose oxidase rendered using PyMol, ²⁷ (B) Mechanism of aerobic oxidation of primary alcohols to aldehydes by galactose oxidase.	3
Figure 1.4.	(A) Cytochrome P450 rendered using PyMol, ²⁷ (B) Mechanism of action of cytochrome P450.	4
Figure 1.5.	(A) Three charge states for dithiolene ligands; (B) Early examples of Ni complexes with dithiolene ligands in different charge states.	5
Figure 1.6.	Three potential charge states for <i>o</i> -amidophenolate ligands. R ₁ is typically an aryl group.	5
Figure 1.7.	Possible charge states for the bis(imino)pyridines (PDI) used extensively by Chirik and co-workers.	7
Figure 1.8.	Biomimetic Cu(II) models studied by Stack and co-workers for the oxidation of alcohols to aldehydes. ^{62, 67}	8
Figure 1.9.	Synthetic strategies for symmetric and asymmetric salen ligands.	9
Figure 1.10.	Potential energy curves for electron transfer in ligand-bridged bimetallic complexes (or metal-bridged bis-phenoxide complexes) with negligible (Class I), weak (Class II), and strong (Class III) electronic coupling. E_{Th} represents the energy required for thermal electron transfer in a Class II system. The red arrows represent IVCT transitions.	11
Figure 1.11.	UV-vis-NIR spectra of (A) Mn(Sal ^{tBu}) and (B) Ni(Sal ^{tBu}) in neutral (black) and oxidized (red) forms, highlighting the change in IVCT bands observed for different metal ions. ^{120, 124}	14
Figure 1.12.	Spin density plots of Ni(Sal ^R) where R = CF ₃ (left), tBu (middle), and NMe ₂ (right). The DFT calculated contribution of Ni to the SOMO, as well as the experimentally observed g_{ave} values are shown. ^{114, 126}	15
Figure 1.13.	(A) Effect of exogenous ligands (coordinating solvents/anions) on the locus of oxidation in Ni(salen) complexes. (B) Temperature dependent valence tautomerism observed in oxidized Cu(Sal) complexes.	17
Figure 1.14.	Representative active sites for multimetallic metalloenzymes.	18
Figure 1.15.	Selected bimetallic cobalt complexes studied by Collman and co-workers, ¹⁵³ Nocera and co-workers, ¹⁶⁰ and Love and co-workers ¹⁶⁵ for the reduction of dioxygen.	19
Figure 1.16.	(A) Two potential coupling strategies towards multimetallic ligands. (B) Strategy developed by Kleij and co-workers for the synthesis of asymmetric salen ligands by templation of metal ions. Controlled synthesis of heterometallic complexes is possible through the stepwise addition of different metal ions (M ₁ and M ₂). ¹⁷⁰⁻¹⁷¹	21

Figure 1.17.	(A) Metal complexes of ‘triple salen’ (talen) ligands developed by Glaser and co-workers for magnetics applications. (B) Molecular structure of Cu(talen ^{tBu2}) highlighting the bowl-like structure when tBu is employed in the <i>ortho</i> position. (C) Molecular structure of [((talen ^{tBu2})Mn(III) ₃) ₂ (Cr(III)(CN) ₆) ₃] ³⁺ . Peripheral tBu groups, Mn axially bound ligands, and hydrogen atoms omitted for clarity. Rendered using PyMol. ²⁷	25
Figure 1.18.	A Pt(Sal) bimetallic complex capable of a selective colorimetric and luminescent response to Pb(II) cations reported by Chan and co-workers. ²¹¹⁻²¹³	26
Figure 1.19.	Binucleating ligands employed by Thomas and co-workers, ²¹⁸⁻²¹⁹ and Storr and co-workers. ²¹⁴⁻²¹⁶	27
Figure 2.1.	Exciton coupling of the excited states leads to band shifting and splitting relative to the analogous monomeric transition depending on the molecular geometry. Solid and dashed lines represent allowed and forbidden transitions, respectively. Small black arrows represent transition moment dipoles.	30
Figure 2.2.	Monometallic and bimetallic salen complexes studied. 1 and 3 – previous work, ²¹⁶ 2 , 4 , and 5 – this work.	32
Figure 2.3.	POV-Ray representation of 2	35
Figure 2.4.	POV-Ray representation of 4	36
Figure 2.5.	POV-Ray representation of 5	36
Figure 2.6.	Cyclic voltammograms of 1-5 (top to bottom).	39
Figure 2.7.	Differential pulse voltammetry (DPV) scans of 2 (black line), 4 (blue line), and 5 (red line).	40
Figure 2.8.	X-band EPR spectra (black) of [1] ^{•+} and [2-4] ^{•2+} recorded in frozen CH ₂ Cl ₂ at 0.33 mM. Red lines represent simulations of the experimental data. Inset: weak half-field $\Delta M_s = 2$ transition for [2] ^{•2+}	42
Figure 2.9.	X-band EPR spectrum of [2] ^{•+} recorded in frozen CH ₂ Cl ₂ at 1.2 mM.	44
Figure 2.10.	Top: Room temperature X-band EPR spectrum of [5] ^{•2+} (black) recorded in CH ₂ Cl ₂ at 0.35 mM (simulation in red). Inset: Saturation curve of the signal at $g_{iso} = 2.014$ with increasing concentration suggesting aggregation above 0.5 mM. Bottom: X-band EPR spectrum of [5] ^{•2+} oxidized at 77 K.	45
Figure 2.11.	NIR region in the absorption spectra of [1] ^{•+} and [2-5] ^{•2+} . (A) Black line: [1] ^{•+} , red line: [3] ^{•2+} ; (B) [2] ^{•2+} ; (C) [4] ^{•2+} ; (D) [5] ^{•2+} . The dashed black line represents λ_{max} for [1] ^{•+} . Coloured dashed lines represent λ_{max} for the respective bis-ligand radical complex.	47
Figure 2.12.	Full oxidation titration data for (A) 2 (black) to [2] ^{•2+} (blue), 0.33 mM; (B) 4 (black) to [4] ^{•2+} (blue), 0.33 mM; (C) 5 (black) to [5] ^{•2+} (blue), 298 K, 0.08 mM; (D) 5 to [5] ^{•2+} , 195 K, 0.33 mM. Red lines represent the addition of one equivalent of oxidant.	48
Figure 2.13.	Spin density plots for [1] ^{•+} and the broken symmetry ($S = 0$) solution for [2-5] ^{•2+} . See the experimental section for calculation details.	50
Figure 2.14.	Kohn-Sham molecular orbitals for the broken symmetry ($S = 0$) of [2] ^{•2+} associated with the calculated NIR transitions at 4,995 and 3,590 cm ⁻¹ . The	

	predicted low energy bands are symmetric and antisymmetric linear combinations of the α HOMO \rightarrow α LUMO (black arrow), and β HOMO \rightarrow β LUMO (red arrow) local transitions on the individual salen radicals.....	51
Figure 2.15.	Kohn-Sham molecular orbitals for the broken symmetry ($S = 0$) solution of $[4^{\bullet}]^{2+}$ associated with the calculated NIR transitions at 5,570 and 4,935 cm^{-1} (black and red arrows; α/β HOMO \rightarrow α/β LUMO). Predicted transitions are a result of symmetric and asymmetric linear combinations of the orbitals shown.	52
Figure 2.16.	Kohn-Sham molecular orbitals for the broken symmetry ($S = 0$) solution of $[5^{\bullet}]^{2+}$ associated with the calculated NIR transitions at 5,495 and 4,390 cm^{-1} (black and red arrows; α/β HOMO \rightarrow α/β LUMO). Predicted transitions are a result of symmetric and asymmetric linear combinations of the orbitals shown.	52
Figure 3.1.	Possible electronic structures for $\text{Co}(\text{C}_6\text{H}_4(\text{NH})_2)_2$	61
Figure 3.2.	Selected examples of Co(II) and Co(III) complexes with pro-radical ligands.	62
Figure 3.3.	Select examples of bimetallic Co(Sal) complexes investigated by Coates and co-workers, ¹⁷⁹ Kleij and co-workers, ³⁴⁹ and Hong and co-workers ¹⁷⁴ for epoxide polymerizations, ARO of epoxides, and nitro-aldol reactions, respectively.	64
Figure 3.4.	Monometallic and bimetallic salen complexes studied.....	65
Figure 3.5.	POV-Ray representation of CoL^1	66
Figure 3.6.	POV-Ray representation of Co_2L^2	67
Figure 3.7.	Cyclic voltammograms of CoL^1 (black line) and Co_2L^2 (grey line) in CH_2Cl_2 at 233 K.	69
Figure 3.8.	POV-Ray representation of $[\text{CoL}^1\text{-H}_2\text{O}][\text{SbF}_6]$	71
Figure 3.9.	(A) vis-NIR spectra of CoL^1 (black line) and $[\text{CoL}^1\text{-H}_2\text{O}]^+$ (red line). (B) vis-NIR spectra of Co_2L^2 (black line) and $[\text{Co}_2\text{L}^2\text{-2H}_2\text{O}]^{2+}$ (red line). DFT transitions are shown as vertical green lines (<i>vide infra</i>).....	73
Figure 3.10.	Temperature dependant Vis-NIR spectra of: (A) $[\text{CoL}^1\text{-H}_2\text{O}]^+$ and (B) $[\text{Co}_2\text{L}^2\text{-2H}_2\text{O}]^{2+}$ at 298 K (black lines) and 195 K (red lines).	73
Figure 3.11.	X-band EPR spectra of 0.3 mM solutions of: (A) CoL^1 (black line) and $[\text{CoL}^1\text{-H}_2\text{O}]^+$ (red line) and (B) Co_2L^2 (black line) and $[\text{Co}_2\text{L}^2\text{-2H}_2\text{O}]^{2+}$ (red line).....	75
Figure 3.12.	$\chi_M T$ vs T data for Co_2L^2 (black) and $[\text{Co}_2\text{L}^2\text{-2H}_2\text{O}][2\text{SbF}_6]$ (red) at 10,000 Oe between 1.8 and 300 K.....	76
Figure 3.13.	Field dependence of the magnetization for Co_2L^2 at 1.8, 3, 5, and 8 K between 0 and 7 T.	76
Figure 3.14.	$\chi_M T$ versus T data for $[\text{CoL}^1\text{-H}_2\text{O}]^+$ at 10,000 Oe between 1.8 and 300 K (o).	77
Figure 3.15.	Field dependence of the magnetization for $[\text{CoL}^1\text{-H}_2\text{O}]^+$ at 1.8, 3, 5 and 8 K between 0 and 7 T.	78
Figure 3.16.	Field dependence of the magnetization for $[\text{Co}_2\text{L}^2\text{-2H}_2\text{O}]^{2+}$ at 1.8, 3, 5, and 8 K between 0 and 7 T.	79
Figure 3.17.	DFT-predicted SOMOs for CoL^1 and Co_2L^2	81

Figure 3.18.	(left) Predicted spin-density plot for the BS solution of Co₂L² . (right) Predicted spin-density plot for the triplet solution of Co₂L² . The two electronic structure solutions are isoenergetic ($\Delta E = 0.005 \text{ kcal mol}^{-1}$). ...	81
Figure 3.19.	(left) Predicted spin-density plot for the triplet solution. (right) Predicted spin-density plot for the BS anti-ferromagnetically coupled ligand radical solution, $\uparrow\text{Co}^{2+}\text{-}\downarrow\text{L}^{\cdot}$	82
Figure 3.20.	Kohn-Sham molecular orbitals for the triplet solution of [CoL¹-H₂O]⁺ associated with the calculated NIR transition at $10,050 \text{ cm}^{-1}$ ($\beta\text{HOMO} \rightarrow \beta\text{LUMO}$).	84
Figure 3.21.	(left) Predicted spin-density plot for the quintet (bis-triplet) spin state. (right) Predicted spin-density plot for the bis-BS singlet solution.....	85
Figure 3.22.	Kohn-Sham molecular orbitals for the quintet solution of [Co₂L²-2H₂O]²⁺ associated with the calculated NIR transitions at $10\,403 \text{ cm}^{-1}$ ($\beta\text{HOMO} \rightarrow \beta\text{LUMO}$; black line) and $10\,757 \text{ cm}^{-1}$ ($\beta\text{HOMO} \rightarrow \beta\text{LUMO}+1$; red line)...	86
Figure 3.23.	Cyclic voltammograms of: (left) [CoL¹-H₂O]⁺ and (right) [Co₂L²-2H₂O]²⁺ at 298 K (black) and 233 (grey).....	87
Figure 3.24.	Oxidation titration of [CoL¹-H₂O]⁺ (red) to the doubly oxidized species (blue) with the chemical oxidant $[\text{N}(\text{C}_6\text{H}_3\text{Br}_2)_3][\text{SbF}_6]$	88
Figure 3.25.	X-band EPR spectrum of doubly oxidized CoL¹ (blue) in frozen CH_2Cl_2 with $g = 2.00$ (blue). Simulation (grey).	89
Figure 3.26.	Spin-density plot of the dication [CoL¹-2H₂O]²⁺ , 98% spin-density localized to the salen ligand.	89
Figure 4.1.	Select examples of coupling of terminal nitrido ligands to yield N_2 or $\mu\text{-N}_2$ bridged dimeric species.....	102
Figure 4.2.	POV-Ray representation of Mn(Sal^{CF₃})N	104
Figure 4.3.	POV-Ray representation of Mn(Sal^{NMe₂})N	105
Figure 4.4.	POV-Ray representation of [Mn(Sal^{tBu})]⁺[SbF₆]	105
Figure 4.5.	Cyclic voltammograms of Mn(Sal^R)N . R = CF ₃ (green); R = tBu (black); and R = NMe ₂ (blue). The first oxidation potential is tunable by ca. 490 mV. Inset: Hammett plot of the redox potentials of Mn(Sal^R)N vs σ_{para} of the <i>para</i> ring substituent.....	107
Figure 4.6.	Scan rate dependence of Mn(Sal^R)N . (A) R = tBu; (B) R = CF ₃ ; (C) R = NMe ₂	108
Figure 4.7.	CV curve of Mn(Sal^{NMe₂})N (black) overlaid with a differential pulse voltammetry (DPV) scan (red) which better resolves the two closely spaced oxidation events.	110
Figure 4.8.	UV-vis-NiR spectrum of Mn(Sal^{tBu})N (black), and [Mn^{VI}(Sal^{tBu})N]⁺ (red) at 0.2 mM in CH_2Cl_2 at 195 K.	111
Figure 4.9.	UV-vis-NiR spectrum of Mn(Sal^{CF₃})N (black), and [Mn^{VI}(Sal^{CF₃})N]⁺ (red) at 0.2 mM in CH_2Cl_2 at 195 K.	112
Figure 4.10.	UV-vis-NiR spectrum of Mn(Sal^{NMe₂})N (black), and [Mn^V(Sal^{NMe₂})N]⁺ (red) at 0.2 mM in CH_2Cl_2 at 195 K.	113
Figure 4.11.	X-band EPR spectra of [Mn(Sal^R)N]⁺ recorded in frozen CH_2Cl_2 at 0.4 mM. (top) R = tBu; (middle) R = CF ₃ ; (bottom) R = NMe ₂ . Grey lines represent simulations of the experimental data.	114

Figure 4.12.	X-band EPR spectrum of $[\text{Mn}(\text{Sal}^{\text{NMe}_2})\text{N}]^{*+}$ (0.4 mM) recorded in toluene at room temperature (blue line). The gray line represents simulation of the experimental spectrum.	115
Figure 4.13.	Second order kinetic decay plots for $[\text{Mn}(\text{Sal}^{\text{R}})\text{N}]^+$ (R = tBu and CF ₃ , 195 K; R = NMe ₂ , 298 K).	117
Figure 4.14.	Representative GC-MS results (vial 1, run 2 – Table 4.4) for the headspace examination of the $[\text{Mn}^{\text{VI}}(\text{Sal}^{\text{tBu}})^{14/15}\text{N}]^+$ decay. (A) headspace of a blank sample. (B) headspace of a sample of $\text{Mn}(\text{Sal}^{\text{tBu}})^{14/15}\text{N}$ 10 minutes after addition of 1 equivalent of AgSbF ₆ at 298 K.	118
Figure 4.15.	Representative GC-MS results (vial 1, run 2 – Table 4.5) for the headspace examination of the $[\text{Mn}^{\text{VI}}(\text{Sal}^{\text{CF}_3})^{14/15}\text{N}]^+$ decay. (A) headspace of a blank sample. (B) headspace of a sample of $\text{Mn}(\text{Sal}^{\text{CF}_3})^{14/15}\text{N}$ 10 minutes after addition of 1 equivalent of AgSbF ₆ at 298 K.	119
Figure 4.16.	Representative GC-MS results for the headspace examination of $[\text{Mn}^{\text{V}}(\text{Sal}^{\text{NMe}_2})^{14/15}\text{N}]^+$. (A) headspace of a blank sample. (B) headspace of a sample of $\text{Mn}(\text{Sal}^{\text{NMe}_2})^{14/15}\text{N}$ 10 minutes after addition of oxidant. (C) headspace of the sample in (B) 24 hours after the addition of oxidant..	120
Figure 4.17.	DFT predicted SOMOs for $[\text{Mn}(\text{Sal}^{\text{R}})\text{N}]^+$. (A) R = tBu; (B) R = CF ₃ ; (C) R = NMe ₂ . Both R = tBu and CF ₃ SOMOs are predicted to be of d _{xy} character, while the R = NMe ₂ SOMO is ligand-based, and localized to one side of the bis-phenoxide salen ligand. See the experimental section for calculation details.	121
Figure 4.18.	Spin density plots for the three oxidized complexes. (A) $[\text{Mn}^{\text{VI}}(\text{Sal}^{\text{tBu}})\text{N}]^+$; (B) $[\text{Mn}^{\text{VI}}(\text{Sal}^{\text{CF}_3})\text{N}]^+$; (C) $[\text{Mn}^{\text{V}}(\text{Sal}^{\text{NMe}_2})\text{N}]^+$. See the experimental section for calculation details.....	122
Figure 5.1.	Mono and bimetallic Mn complexes prepared for use as fluorination catalysts.....	134
Figure 5.2.	Potential oxidative transformations to be targeted by multimetallic complexes employing mild oxidants (O ₂ /H ₂ O ₂).....	135
Figure 5.3.	(left) 1 mM solutions of $[\text{5}^{\bullet+}]^{2+}$ in CH ₂ Cl ₂ and toluene; (right) dilution of a CH ₂ Cl ₂ solution (1 mM) of $[\text{5}^{\bullet+}]^{2+}$ into toluene (0.2 mM final concentration) causes disaggregation of $[\text{5}^{\bullet+}]^{2+}$. The black spectrum is recorded at time 0, grey lines are recorded every 2.5 minutes until the red spectrum is reached (~25 minutes). Isobestic points at 5,000, 18,500, 24,500, and 26,500 cm ⁻¹ indicate clean conversion from one species to another.	136
Figure 5.4.	(A) Orbital interactions involved in a radical coupling pathway. (B) Orbital interactions involved in a donor/acceptor coupling pathway. Adapted from reference 121.....	138
Figure 5.5.	Exploratory reactions with phosphines (left) and Gomberg's dimer (right) to investigate the feasibility of one and two-electron reactivity pathways..	139
Figure 5.6.	Intermolecular C-H bond activation with a Ru nitride supported by the salen framework reported by Lau and co-workers. ⁴⁰⁵	140
Figure 5.7.	UV-vis-NIR spectra of $\text{Mn}(\text{Sal}^{\text{NMe}_2})\text{N}$ (black), $[\text{Mn}^{\text{V}}(\text{Sal}^{\text{NMe}_2})\text{N}]^{*+}$ (red), and after irradiation for ~5 minutes with a long wavelength UV lamp (λ _{ex} = 365 nm). Inset: photographs of $[\text{Mn}^{\text{V}}(\text{Sal}^{\text{NMe}_2})\text{N}]^{*+}$ before and after irradiation.	141

Figure 5.8.	Spin density plots for $[\text{Mn}(\text{Sal}^{\text{NHMe}_2}(\text{NMe}_2)\text{N})]^{2+}$ and $[\text{Mn}(\text{Sal}^{\text{NHMe}_2})\text{N}]^{3+}$. See the Experimental Section in Chapter 4 for calculation details.	143
Figure 5.9.	Cyclic voltammograms of $\text{Mn}(\text{Sal}^{\text{NMe}_2})\text{N}$ in the presence of 1 and 2 equivalents of $[\text{H}(\text{Et}_2\text{O})_2][\text{BF}_4]$	144
Figure 5.10.	Scan rate dependence of $\text{Mn}(\text{Sal}^{\text{NMe}_2})\text{N}$ with two equivalents of $[\text{H}(\text{Et}_2\text{O})_2][\text{BF}_4]$ (left) and without (right).	145

List of Schemes

Scheme 1.1.	'Oxidative addition' and 'reductive elimination' reactions at Zr(IV) reported by Heyduk and co-workers. ⁴⁵⁻⁴⁶	6
Scheme 1.2.	A $[2\pi + 2\pi]$ ring-closing catalytic reaction at Fe(II) reported by Chirik and co-workers. E = alkyl, Si-R, N-R; Ar = iPr. ⁵⁶	7
Scheme 1.3.	Proposed catalytic cycle for the oxidation of methane by N-bridged high-valent diiron-oxo species supported by porphyrin platforms reported by Sorokin and co-workers.....	20
Scheme 1.4.	Bimetallic salen complexes linked by varying tether lengths for the catalytic asymmetric ring opening of epoxides ¹⁷² and the conjugate cyanation of α,β -unsaturated imides. ¹⁷³	22
Scheme 1.5.	Bimetallic Ni catalysts developed by Shibasaki and co-workers for Mannich-type reactions ¹⁸² and the synthesis of 3-aminooxindoles. ¹⁷⁵	23
Scheme 1.6.	Co-polymerization of amino olefins with ethylene catalyzed by a bimetallic Ni Schiff-base complex reported by Agapie and co-workers. ¹⁸⁶⁻¹⁸⁷	24
Scheme 2.1.	Synthesis of 2	33
Scheme 2.2.	Synthesis of 4	33
Scheme 2.3.	Synthesis of 5	34
Scheme 3.1.	Redox-active ligand-mediated oxidative addition and reductive elimination reactions at Co(III) investigated by Soper and co-workers.....	63
Scheme 4.1.	Select examples of nitrene transfer reactions from nitridomanganese(V) complexes. (A) nitridomanganese(V) porphyrins for the aziridination of cyclooctene; (B-C) nitridomanganese(V) salens for nitrene transfer to alkenes and silyl enol ethers.	100
Scheme 4.2.	Oxidation of Mn(V) nitride complexes to afford high-valent metal or ligand radical electronic structures; subsequent homocoupling affords N ₂ in the case of the Mn(VI) complexes.	101
Scheme 4.3.	Synthesis of Mn(Sal^{CF3})N	103
Scheme 4.4.	Synthesis of Mn(Sal^{NMe2})N	103
Scheme 5.1.	Proposed catalytic cycle for the manganese porphyrin/salen-catalyzed C-H fluorination reactions reported by Groves and co-workers. ⁴⁵⁶⁻⁴⁵⁹ The ellipsoid represents the porphyrin/salen ligand. Ethylbenzene is used as an example substrate.....	133
Scheme 5.2.	Proposed photoelectrochemical catalytic cycle for the activation of C-H bonds with Mn(Sal^R)N . The ellipsoid represents the salen ligand.....	142
Scheme 5.3.	Spontaneous hydrogen evolution from a low-valent Mo-NH ₃ complex reported by Chirik and co-workers. ⁵⁰⁸	146

List of Acronyms

Å	Ångström, 10^{-10} meters
A	Hyperfine coupling constant
ARO	Asymmetric Ring Opening (of epoxides)
Ap	Amidophenolate
BDE	Bond Dissociation Energy
B.P.	Boiling Point
BS	Broken Symmetry (DFT)
Ca.	Circa
cm^{-1}	Wavenumbers
CT	Charge Transfer
CV	Cyclic Voltammetry
d	Doublet (NMR)
DCM	Dichloromethane
dd	Doublet of doublets (NMR)
DDQ	2,3-dichloro-5,6-dicyano-1,4-benzoquinone
DFT	Density Functional Theory
DLS	Dynamic Light Scattering
DME	Dimethoxyethane
DMF	Dimethylformamide
DMSO	Dimethyl sulfoxide
DPV	Differential Pulse Voltammetry
$\Delta v_{1/2}$	Peak width at half height
ϵ	Dielectric constant
ϵ	Extinction coefficient (UV-vis)
E_{pa}	Anodic peak potential
E_{pc}	Cathodic peak potential
EA	Elemental Analysis
EPR	Electron Paramagnetic Resonance
ESI	Electrospray Ionization
eV	Electron Volts
f	Oscillator strength (DFT)
F	Faraday's constant

Fc	Ferrocene
Fc ⁺	Ferrocenium
g_{ave}	Average g value
g_e	Free electron g value (2.0023)
g_{iso}	Isotropic g value
GC	Gas Chromatography
GC-MS	Gas Chromatography-Mass Spectrometry
GHz	Gigahertz
GOase	Galactose Oxidase
GO _{ox}	Oxidized form of galactose oxidase
GO _{red}	Reduced form of galactose oxidase
HAT	Hydrogen Atom Transfer
HAA	Hydrogen Atom Abstraction
HOMO	Highest Occupied Molecular Orbital
HKR	Hydrolytic Kinetic Resolution (of epoxides)
I	Nuclear spin
Iq	Iminoquinone
Isq	Iminosemiquinone
IVCT	Intervalence Charge Transfer
K	Kelvin
K_c	Comproportionation constant
kHz	Kilohertz
kcal	Kilocalorie
λ_{max}	Wavelength of maximum absorption
LLCT	Ligand-to-ligand charge transfer
LMCT	Ligand-to-metal charge transfer
μA	Microampere
μ_{eff}	Effective magnetic moment
μL	Microliters
μm	Micrometre
<i>m</i> -CPBA	Meta-chloroperoxybenzoic acid
MLCT	Metal-to-ligand charge transfer
mol	Mole
mg	Milligrams

mL	Milliliters
mm	Millimeters
mmol	Millimoles
MO	Molecular Orbital
MS	Mass Spectrometry
mT	Milliteslas
mV	Millivolts
mW	Milliwatts
NIR	Near-Infrared
nm	Nanometers
NMR	Nuclear Magnetic Resonance
OAc	Acetate
Oe	Oersted
PCM	Polarized Continuum Model
PDI	Bis(imino)pyridine
PMMA	Poly(methyl methacrylate)
ppm	Chemical shift
pyz	Pyrazine
rR	Resonance Raman
R	Ideal gas constant
S	Spin
Salen (Sal)	<i>Bis</i> -(Schiff base) <i>bis</i> -(phenol)
SD	Spin Density
SMM	Single molecule magnet
SOMO	Singly Occupied Molecular Orbital
σ_{para}	Hammett parameter (<i>para</i> substituent)
T	Temperature
$t_{1/2}$	Half-life
TBAP	Tetra- <i>n</i> -butyl ammonium perchlorate
TD-DFT	Time-Dependent Density Functional Theory
TEM	Transmission Electron Microscopy
THF	Tetrahydrofuran
UV-vis	Ultraviolet-visible spectroscopy
V	Volts (Electrochemistry)

VT Variable Temperature
ZFS Zero-Field Splitting

Chapter 1. Introduction

Adapted from: Clarke, R.M.; Herasymchuk, K.; and Storr, T. *Coord. Chem. Rev.*, **2017**, 352, 67-82.

RMC wrote the introduction as well as sections on manganese, cobalt, and nickel. KH contributed sections on copper, as well as 'other metals' and salen derivative ligands.

and

Clarke, R.M.; and Storr, T. *Dalton. Trans.*, **2014**, 43, 9380-9391.

1.1. Pro-Radical Ligands

The vast majority of traditional ligands used in inorganic chemistry (ammonia, triphenylphosphine, halides) are termed 'innocent' – the energy required to oxidize or reduce them is significantly higher than that needed to oxidize or reduce the metal centre.¹ Conversely, ligands with energetically accessible levels susceptible to oxidation or reduction are termed 'redox-active' or 'non-innocent'.² Ligands were first recognized as suspect in 1966 by Jørgensen and he coined the terms 'innocent' and 'non-innocent' for ligands depending on whether the oxidation state of the central metal ion could be easily assigned.³ The relative ordering of the metal and ligand frontier molecular orbitals in a transition metal complex ($M^{n+}L$) incorporating redox-active ligands dictates whether oxidation/reduction occurs at the metal or the ligand (Figure 1.1).

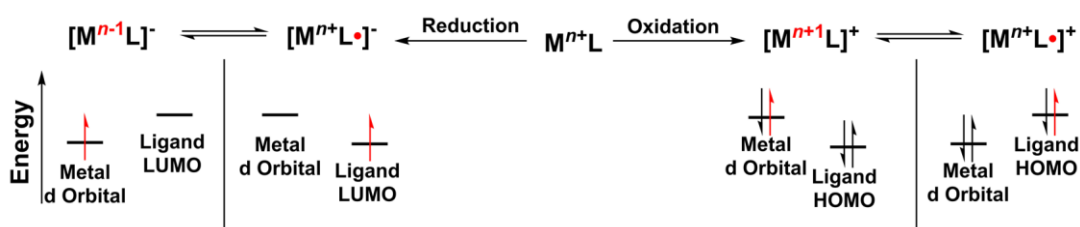


Figure 1.1. Possible oxidation or reduction processes for metal complexes with pro-radical ligands. Red electrons represent electrons gained or lost in the reduction/oxidation event.

Simple examples of non-innocent ligands include dioxygen (O_2), which can undergo two one-electron reductions to form superoxide ($O_2^{\bullet-}$) and peroxide (O_2^{2-}) anions;⁴

and nitric oxide which can exist in cationic (NO^+ , linear binding), neutral (NO^\cdot , bent binding), and anionic (NO^- , bent binding) forms.⁵ As an example of the redox ambiguity of dioxygen and the associated difficulty in assigning oxidation states when non-innocent ligands are involved, the oxygen transport protein oxymyoglobin/oxyhemoglobin is illustrated in Figure 1.2. Two electronic structures are possible to explain the observed diamagnetic ground state. The first, put forth by Pauling, has the central Fe ion in the +2 oxidation state, with a neutral O_2 ligand bound in the apical position.⁶ Weiss proposed the second electronic structure in which the central Fe ion is in the +3 oxidation state, with an antiferromagnetically coupled superoxide ligand in the apical position.⁷ Only through extensive spectroscopic characterization coupled with theoretical investigations can the electronic structure be accurately defined, and debate over the nature of Fe- O_2 binding in proteins persists, with the electronic structure being highly sensitive to factors such as the axial ligand and surrounding protein environment.⁸⁻¹²

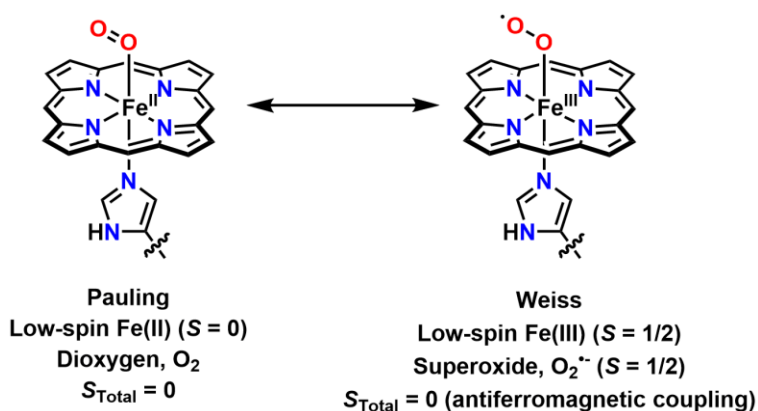


Figure 1.2. Possible electronic structures of O_2 transport proteins proposed by Pauling and Weiss that give an $S_{\text{Total}} = 0$, illustrating the redox ambiguity of dioxygen, and the resulting effect on the oxidation state of the central Fe.

Oftentimes, the terms ‘redox-active’ and ‘non-innocent’ are used interchangeably in the literature when describing ligands with ambiguous charge states.¹³ In this thesis, the term ‘pro-radical’ ligand is used, as all of the metal complexes prepared within incorporate closed-shell dianionic ligands which are subsequently oxidized.

1.1.1. Pro-Radical Ligands in Nature

The study of transition metal complexes with pro-radical ligands is an area of considerable research interest due to their relevance in biological systems, as well as the ability of these ligands to confer noble-metal reactivity to base metals.^{1, 13-17} Pro-radical

ligands are essential in the active sites of many metalloenzymes as the coupling of redox events at both metal and ligand allows for efficient multielectron chemistry;¹⁸ examples include photosystem II,¹⁹⁻²⁰ cytochrome *c* oxidase²¹ and P450,²² glyoxal oxidase,²³ and galactose oxidase.²⁴

Galactose oxidase (GOase) is a copper containing fungal metalloenzyme that catalyzes the oxidation of primary alcohols to aldehydes with the concomitant reduction of O₂ to H₂O₂.²⁵⁻²⁶ The active site coordination sphere is composed of two equatorial histidine residues (His₄₉₆ and His₅₈₁), a post-translationally modified tyrosine residue (Tyr₂₇₂) cross-linked with a cysteine residue (Cys₂₂₈), and an axial tyrosine residue (Tyr₄₉₅). Figure 1.3 depicts the mechanistic steps involved in this transformation.²⁵ The catalytically active form, GO_{ox}, incorporates a Cu(II) metal centre and a tyrosyl ligand radical, with each undergoing one-electron reduction during substrate oxidation.²⁴

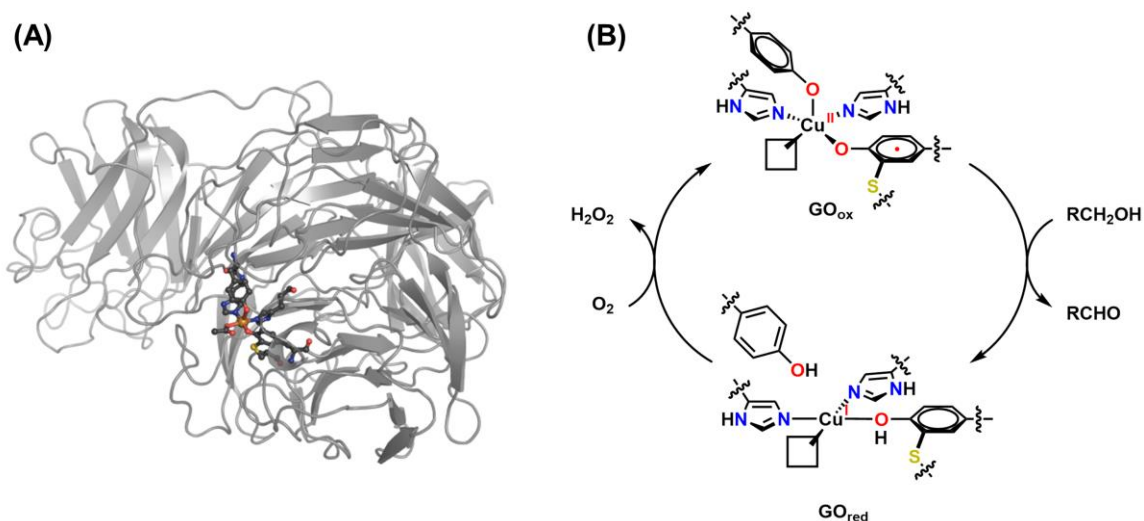


Figure 1.3. (A) Galactose oxidase rendered using PyMol,²⁷ (B) Mechanism of aerobic oxidation of primary alcohols to aldehydes by galactose oxidase.

The cytochrome P450 family of monooxygenase enzymes are found in all branches of life and are responsible for the hydroxylation of unactivated C-H bonds.²⁸ Despite sharing less than 20% sequence identity across the P450 gene superfamily (>10,000 identified P450 genes),²⁹ all P450s share a common overall fold and topology.³⁰ The active-site contains a heme group anchored to the protein via a cysteine residue, in contrast to the histidine residues employed by O₂ transport proteins.³¹ The cysteine residue is proposed to play a role in stabilizing the high-valent Fe-oxo core, as well as tuning the pK_a of the Fe-oxo species, both critical aspects to the observed reactivity.³²

Dioxygen uptake is mediated by an Fe(II) centre which through the addition of an electron and two protons to the Fe-O₂ adduct produces H₂O and the active oxidant, 'Compound I'.³³ Compound I is highly reactive, and is able to abstract a hydrogen atom (with bond dissociation energies (BDEs) as high as 100 kcal mol⁻¹)¹² from the substrate, forming an Fe(IV)-hydroxo intermediate, which undergoes rapid oxygen-rebound with the substrate radical to afford the hydroxylated product.^{32, 34-35} Reduction to Fe(II) regenerates the O₂ binding species (Figure 1.4).

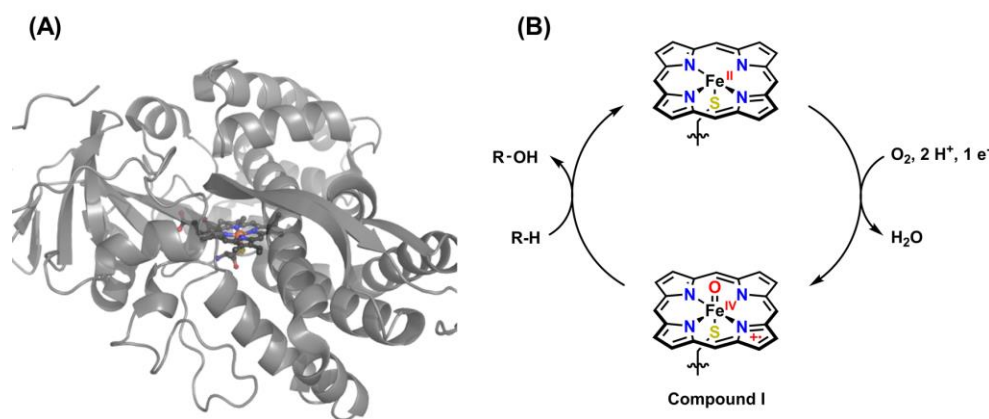


Figure 1.4. (A) Cytochrome P450 rendered using PyMol,²⁷ (B) Mechanism of action of cytochrome P450.

1.1.2. Synthetic Models Incorporating Pro-Radical Ligands

The electronic structures of metal complexes containing pro-radical ligands was thoroughly investigated long before the identification of their involvement in biological systems. As early as the 1960's, groups at the University of Munich,³⁶ The University of Columbia,³⁷⁻³⁸ and Harvard University³⁹ were investigating the electronic structures of metal complexes with dithiolene⁴⁰ ligands (Figure 1.5). In an initial report by Schrauzer and Mayweg, a neutral Ni complex with dithiolene ligands was reported following reaction of NiS₂ with diphenylacetylene.³⁶ The complex was assigned a square planar Ni(II) geometry on the basis of magnetic measurements, as well as its behavior in solution with coordinating solvents. This oxidation state assignment necessitated that each ligand be one-electron reduced, rather than neutral ligands with a formally Ni(0) centre. Following this initial report, Gray and co-workers reported Ni(II) complexes with dithiolene ligands in the -2 and -1 charge state, depending on the dithiolene backbone substituent.³⁷⁻³⁸ Recognizing the 2-electron difference between the diphenyl-dithiolene complexes

reported by Schrauzer and Mayweg, and the cyano-dithiolene complexes reported by Gray, Davison and co-workers developed a series of CF_3 substituted dithiolene complexes that could undergo sequential one-electron redox transformations (Figure 1.5).³⁹ Since these initial investigations, there have been a number of reports detailing the electronic structure and reactivity of dithiolene complexes using both experimental and theoretical methods.⁴¹⁻⁴³

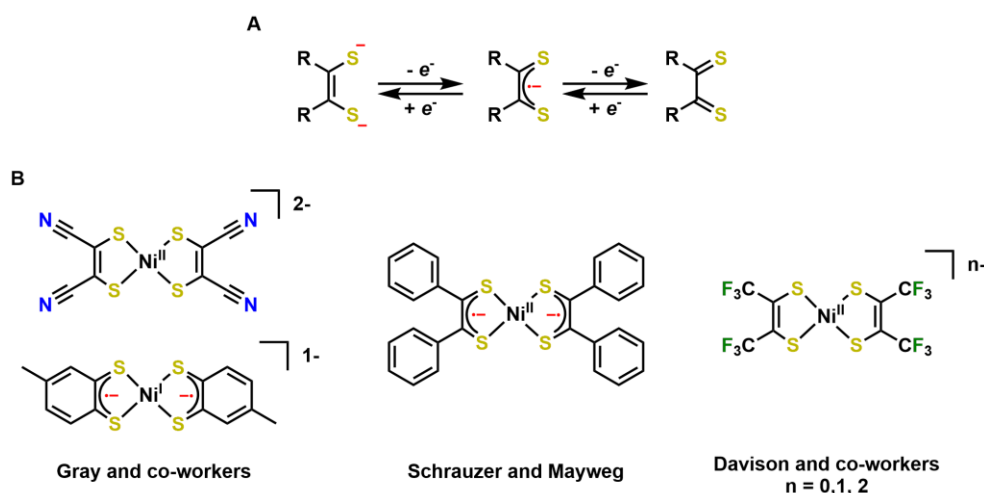


Figure 1.5. (A) Three charge states for dithiolene ligands; (B) Early examples of Ni complexes with dithiolene ligands in different charge states.

Although the dithiolenes were amongst the first studied pro-radical ligands, a number of classes have emerged and been thoroughly studied for both electronic structure and reactivity reasons. Like dithiolene ligands, *o*-amidophenolate (ap) ligands have the potential to exist in three different charge states (Figure 1.6).⁴⁴

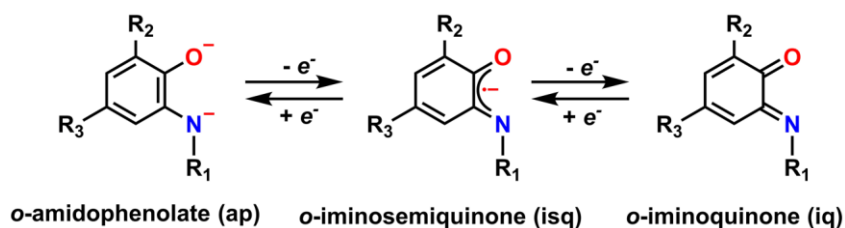
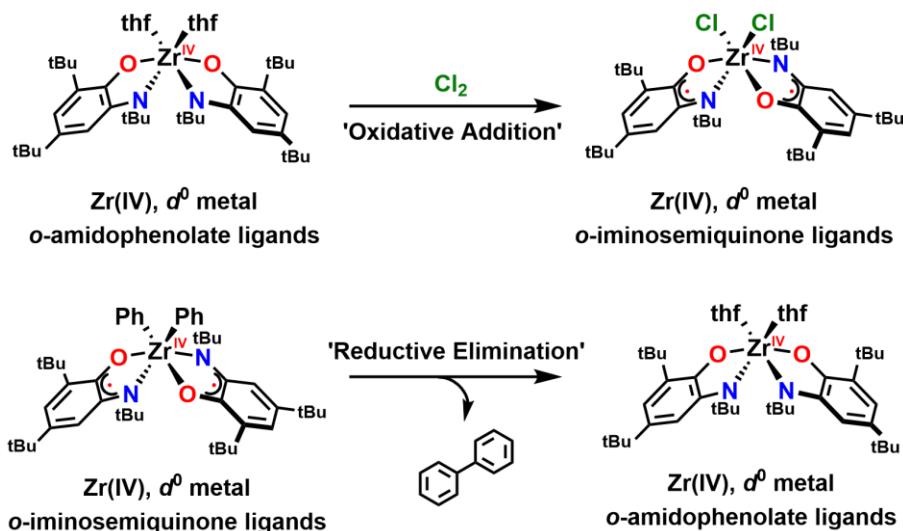


Figure 1.6. Three potential charge states for *o*-amidophenolate ligands. R_1 is typically an aryl group.

Elegant work by Heyduk and co-workers demonstrated ‘oxidative addition’ and ‘reductive elimination’ reactions at Zr(IV) supported by *o*-amidophenolate ligands.⁴⁵⁻⁴⁶ Exposure of $\text{Zr}(\text{ap})_2(\text{thf})_2$ to chlorine gas results in chlorine addition at the Zr centre via one-electron oxidation of each ap ligand (Zr(IV) has no *d* electrons to contribute towards

the oxidative addition of Cl_2) (Scheme 1.1 – top).⁴⁵ Temperature-dependent magnetic measurements suggest that the unpaired electrons in $\text{Zr}(\text{isq})_2\text{Cl}_2$ (isq = *o*-iminosemiquinone) are spin-paired to afford a singlet ground state. $\text{Zr}(\text{isq})_2\text{Cl}_2$ can also be prepared via complexation of ZrCl_4 with 2 equivalents of preoxidized ligand $\text{Li}(\text{isq})$ which has identical spectroscopic properties to the complex prepared via exposure to Cl_2 . The X-ray metrical parameters of the oxidized complex can also be used to assign radical character to the ligands, with contraction of the C-O and C-N bonds suggesting an increase in double bond character upon oxidation.⁴⁷ Elongation of the Zr-O and Zr-N bonds is also observed, as the monoanionic isq ligands are weaker donors in comparison to their ap counterparts. Finally, the C-C bond lengths in the aromatic rings adopt an alternating pattern which is suggestive of quinoidal structures in the oxidized species. In a subsequent paper,⁴⁶ a ‘reductive elimination’ reaction to form biphenyl from $\text{Zr}(\text{isq})_2\text{Ph}_2$ was reported. The electrons from the reductive elimination reduce the isq ligands back to ap moieties (Scheme 1.1 – bottom).

Scheme 1.1. ‘Oxidative addition’ and ‘reductive elimination’ reactions at Zr(IV) reported by Heyduk and co-workers.⁴⁵⁻⁴⁶



Bis(imino)pyridine (PDI) ligands originally developed by Brookhart and Gibson for the polymerization of ethylene⁴⁸⁻⁴⁹ have been used extensively by Chirik and co-workers for a number of electronic structure⁵⁰⁻⁵¹ and reactivity studies (Figure 1.7).⁵²⁻⁵⁸ These complexes find utility in the hydrogenation and hydrosilation of olefins,⁵² the cyclization of enynes and diynes⁵⁷, and the $[2\pi + 2\pi]$ cycloaddition of α,ω -dienes.⁵⁶

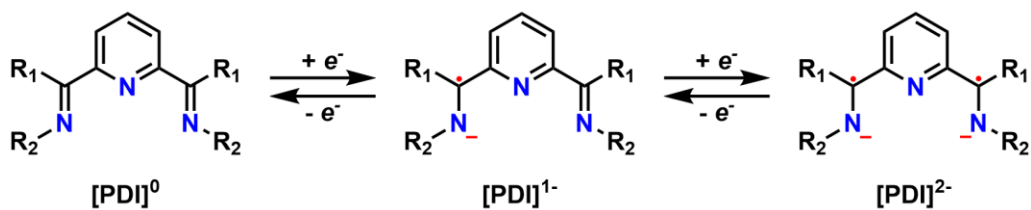
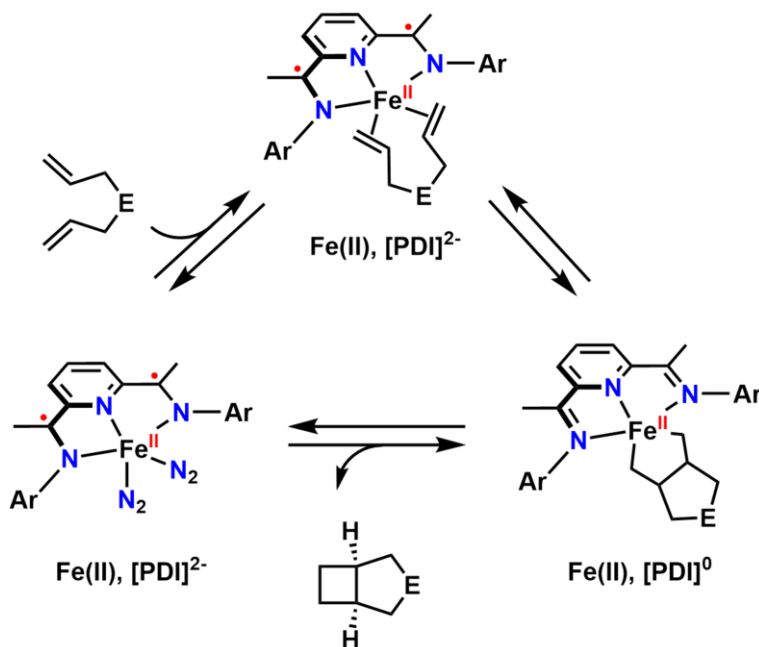


Figure 1.7. Possible charge states for the bis(imino)pyridines (PDI) used extensively by Chirik and co-workers.

Scheme 1.2 depicts the catalytic cycle for the $[2\pi + 2\pi]$ cycloaddition of α,ω -dienes catalyzed by $(^R\text{PDI})\text{Fe}(\text{N}_2)_2$; which was previously established via experimental and theoretical techniques to be an Fe(II) complex with a doubly reduced $[\text{PDI}]^{2-}$ ligand.⁵⁵ Cyclization is afforded with electron equivalents from the $[\text{PDI}]^{2-}$ ligand, which is re-reduced to $[\text{PDI}]^{2-}$ upon reductive elimination of the product. Spectroscopic (Mössbauer) and crystallographic studies on model complexes support a pathway in which the Fe(II) oxidation state is maintained throughout the catalytic cycle.

Scheme 1.2. A $[2\pi + 2\pi]$ ring-closing catalytic reaction at Fe(II) reported by Chirik and co-workers. E = alkyl, Si-R, N-R; Ar = *i*Pr.⁵⁶



Owing to the simplicity of the active sites in GOase, P450, and other metalloenzymes, many structural and functional small molecule models of these enzymes have been studied.⁵⁹⁻⁶⁶ In particular, Stack and co-workers developed some of the first structural and functional models of GOase capable of the catalytic transformation of benzylic and allylic alcohols to aldehydes with >1,000 turnovers under mild conditions

(Figure 1.8).^{62, 67} Like galactose oxidase, these models are demonstrated via Cu K-edge X-ray absorption spectroscopy (XAS) to contain Cu(II) in both the neutral and one-electron oxidized forms of the complexes.

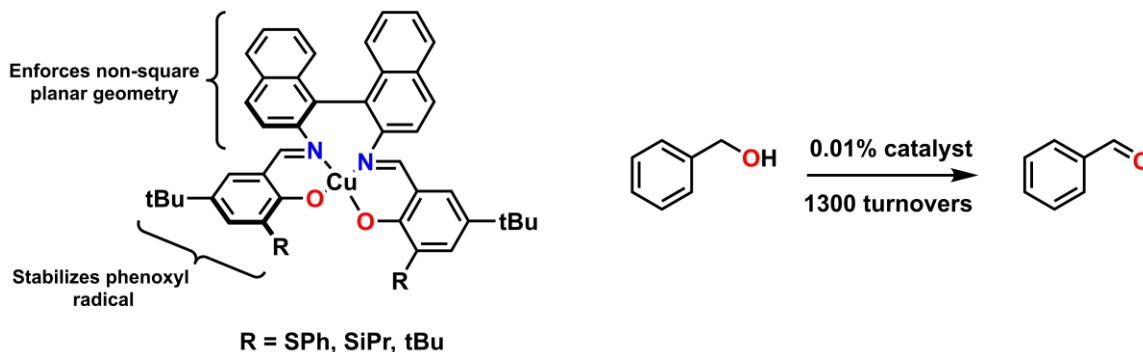


Figure 1.8. Biomimetic Cu(II) models studied by Stack and co-workers for the oxidation of alcohols to aldehydes.^{62, 67}

Biomimetic Fe-oxo model complexes of the cytochrome P450 family and other oxygenase enzymes supported by porphyrin and other ligand platforms are abundant in the literature.⁶⁸⁻⁷² Early models developed by Groves and co-workers incorporate a porphyrinyl radical cation analogous to the electronic structure of Compound I, characterized by large downfield shifts of the porphyrin mesityl protons in the ¹H NMR spectrum, UV-vis spectral features, and Mössbauer parameters (0.05 mm s⁻¹, ΔE_Q = 1.49 mm s⁻¹) indicative of Fe(IV).⁷³ Despite the success in mimicking the observed electronic structure and reactivity, the catalytic activity of this and subsequent Fe-oxo porphyrin model complexes was hampered by porphyrin decomposition reactions and μ-oxo dimer formation. Improved catalytic activities were achieved through incorporation of alkyl, halogen, or other substituents to the *meso* or β-pyrrole positions of the porphyrin ring.⁷⁴

1.2. Salen as a Pro-Radical Ligand

The electronic structure of one-electron oxidized metal complexes of phenolate containing ligands such as salen (salen is a common abbreviation for N₂O₂ bis-Schiff-base bis-phenoxide ligands) have been extensively studied due to their modular syntheses allowing for facile tuning of both steric and electronic properties, versatility in catalysis, and structural similarity (N and O donor moieties) to biological coordination spheres.⁷⁵⁻⁸⁰ Furthermore, salen ligands are known to coordinate to a wide variety of transition and main group elements in a number of oxidation states.⁸¹ Traditionally, the term salen refers

to ligands specifically prepared via condensation of ethylene diamine with two equivalents of salicylaldehyde, but has come to include ligands with varying phenyl ring substituents and diamine backbones.⁸² The imine functionalities can be reduced to afford the corresponding tetrahydrosalen analogues,⁸³⁻⁸⁶ while half-reduced salen ligands can be prepared via reduction of only one imine function.⁸⁰ The development of synthetic methodologies for asymmetric salens (ligands with different substitution patterns on each of the phenol moieties) allows for the preparation of a diverse library of ligands (Figure 1.9).⁸⁷

Symmetric Salen Ligands:



Asymmetric Salen Ligands:

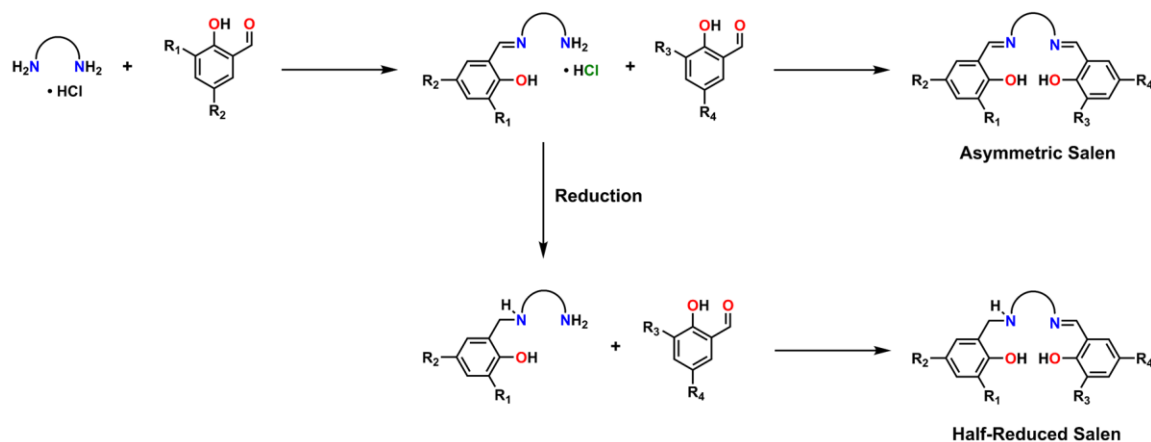


Figure 1.9. Synthetic strategies for symmetric and asymmetric salen ligands.

Metal-salen complexes can exhibit redox activity at either the ligand or the metal centre upon one-electron oxidation, depending on the transition metal, the peripheral ligand substituents, the solvent, or the temperature. Without the use of *ortho*- and *para*-phenolate protecting groups to prevent radical coupling, oxidized metal-salen complexes can be prone to rapid polymerization, restricting the study of oxidized species.⁸⁸⁻⁹² While not the focus of this thesis, it is also possible to reduce salen ligands with strong reducing agents (Li, Na, K) with the reduction locus (metal or ligand) dependant on the reductant employed.⁹³

Metal-salen ligand radical complexes are amongst a class of compounds known as mixed-valence compounds, which traditionally consist of two metal ions in different formal oxidation states bridged by an organic linker ($M^{n+}-L-M^{n+1}$).⁹⁴⁻⁹⁵ The archetypical example of a mixed-valence compound of this type is the Creutz-Taube ion, a diruthenium complex bridged by a pyrazine ligand with the formula $[(\text{NH}_3)_5\text{Ru}(\mu\text{-pyz})(\text{Ru}(\text{NH}_3)_5)]^{5+}$.⁹⁶ The mixed-valency is inverted in the case of metal-salen ligand-radical complexes, in which two redox-active phenolates are bridged by a transition metal centre ($L-M^{n+}-L\cdot$).⁹⁷⁻⁹⁸ Robin and Day established a classification system for the characterization of mixed-valence compounds depending on the degree of electronic communication between the valencies,⁹⁹ and Hush provided a theoretical model to describe the intervalence charge transfer (IVCT).¹⁰⁰ Class I mixed-valence compounds are those that are unable to undergo intramolecular electron transfer from one valence site to another due to the distance between the valence site, or limited coupling through the spacer group. Class II mixed-valence compounds are those in which the valences can interconvert under thermal or photochemical activation; while Class III mixed-valence compounds are coupled so strongly that delocalization occurs and the formal charge on each valence is averaged (Figure 1.10). The Creutz-Taube ion is an example of a Class III mixed-valence compound in which the Ru centres are best described as $\text{Ru}^{2.5+}-L-\text{Ru}^{2.5+}$.^{95, 101} Class II and III systems exhibit IVCT bands in the NIR region of their absorption spectra, and thus information pertaining to the degree of delocalization in these systems can be easily extracted.¹⁰²⁻¹⁰³ Class II mixed-valence species are characterized by broad, relatively weak and solvent dependent IVCT bands, whereas compounds belonging to Class III are characterized by sharp, intense and solvent independent IVCT bands (Table 1.1). It is important to note that while Class III complexes are said to display IVCT transitions, the transitions do not involve net transfer of charge from one valence to the other, but instead the IVCT transition occurs within the molecular orbital manifold of the system. As a consequence of the sensitivity of the IVCT bands to localization/delocalization, and the significant theory developed to account for these bands, UV-vis-NIR spectroscopy is routinely employed in the study of one-electron oxidized metal-salen complexes to deduce the degree of localization/delocalization of the resultant electron hole.^{95, 104-106}

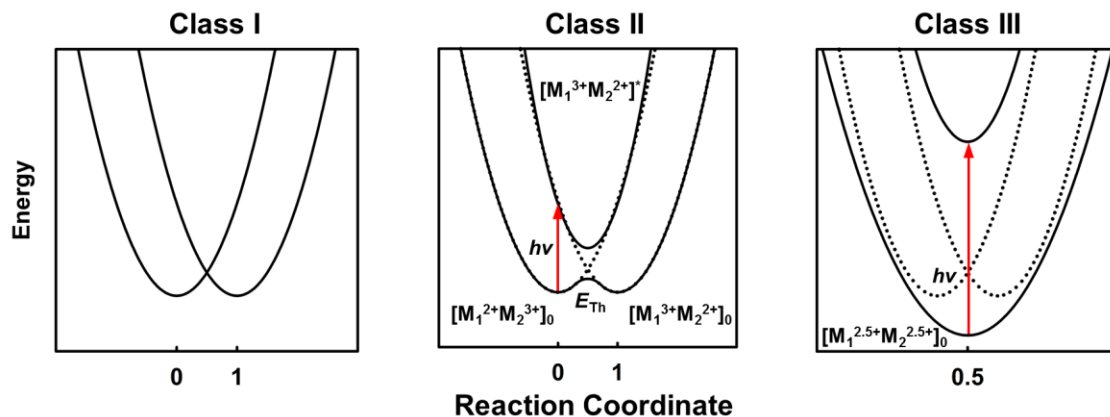


Figure 1.10. Potential energy curves for electron transfer in ligand-bridged bimetallic complexes (or metal-bridged bis-phenoxide complexes) with negligible (Class I), weak (Class II), and strong (Class III) electronic coupling. E_{Th} represents the energy required for thermal electron transfer in a Class II system. The red arrows represent IVCT transitions.

Table 1.1. Optical properties of IVCT bands in mixed-valence compounds.

	$\Delta\nu_{1/2}$	ϵ_{max}
Class I	No coupling	
Class II	$\geq 2,000 \text{ cm}^{-1}$	$\leq 5,000 \text{ M}^{-1} \text{ cm}^{-1}$ (solvent dependent)
Class III	$\leq 2,000 \text{ cm}^{-1}$	$\geq 5,000 \text{ M}^{-1} \text{ cm}^{-1}$ (solvent independent)

$\Delta\nu_{1/2}$ = full width at half-maximum of the IVCT transitions.

While UV-vis-NIR spectroscopy is an invaluable tool for determining the extent to which the electron hole is delocalized, other experimental and theoretical techniques are routinely employed (Table 1.2). Electrochemical analysis is often the first technique investigated as it provides the oxidation potential of the system under study. This allows for the careful selection of an appropriate chemical oxidant¹⁰⁷ or the potential for electrolysis. Information on delocalization can also be determined from electrochemical measurements, as two uncoupled phenolate rings (Class I) will undergo oxidation at approximately the same potential (effectively doubling the observed current);¹⁰⁸ any electronic interaction between the two rings however (Class II or III) will manifest as a larger separation of oxidation events for each phenolate ring.¹⁰⁹⁻¹¹¹ Electrochemical data can be misleading however, due to the significant dependence of redox potentials on solvent, as well as the electrolyte.¹⁰⁵

Table 1.2. Experimental and theoretical techniques commonly used in studying oxidized metal-salen complexes.

Technique	Readout
UV-vis-NIR spectroscopy	Energy, shape, and intensity of NIR bands provide insight into the electronic structure and degree of radical delocalization
Electrochemistry	Accessibility and reversibility of redox processes, stability of oxidized forms, coupling between redox-active moieties
Electron paramagnetic resonance (EPR)	Locus of oxidation. Interaction of unpaired electron with spin-active nuclei. Ligand-based oxidation results in g values close to the free electron value ($g_e = 2.002319$), with any deviation associated with metal character in the SOMO
Resonance Raman (rR)	Vibrational modes associated with the phenoxyl and phenolate ligand redox states. Radical localization results in the appearance of both phenoxyl and phenolate bands
X-ray crystallography	Ligand and coordination sphere bond length changes that can be assigned to localization/delocalization of the ligand radical, or metal-based oxidation
X-ray absorption spectroscopy (XAS)	Metal oxidation state and nearest neighbor distances in the solid-state or frozen solution
Magnetic susceptibility	Solid-state and solution (^1H Evans' method) ¹¹²⁻¹¹³ measurements to assign ground-state electronic structure
Theoretical calculations	Prediction of electronic ground state, visualization of SOMO, spin density, and donor/acceptor orbitals associated with NIR bands

Metal or ligand-based oxidation can be distinguished in many cases by electron paramagnetic resonance (EPR) spectroscopy. Ligand-based radicals will exhibit g values close to the free electron value ($g_e = 2.002319$). Furthermore, the observed g value is sensitive to metal ion contribution to the singly occupied molecular orbital (SOMO).¹¹⁴⁻¹¹⁵ In some cases, hyperfine coupling to spin-active nuclei is resolvable, for example 3 or 5 line patterns in the g_{zz} component of octahedral pyridine adducts of Ni(III)-salen complexes arising from hyperfine coupling to one or two axially bound N_{pyr} atoms ($I_N = 1$). Resonance Raman (rR) spectroscopy is a useful tool for assigning an oxidized salen complex as Class II or III. Class II complexes exhibit vibrational modes resonant with both phenoxyl $\pi \rightarrow \pi^*$ and phenolate $\rightarrow \text{Ni(II)}$ ligand-to-metal charge transfer (LMCT) transitions, whereas only modes resonant with phenoxyl $\pi \rightarrow \pi^*$ transitions are observed for a fully delocalized Class III system.¹¹⁶⁻¹¹⁹ In cases where X-ray quality crystals of oxidized products are obtained, solid-state metrical parameters can provide insight into the locus of oxidation and degree of delocalization. For example, a symmetric distribution of metrical parameters suggests either a fully delocalized electronic structure or metal-based oxidation, whereas an asymmetric distribution, with one side of the salen ligand exhibiting a quinoidal

distribution of bond lengths, and the other aromatic, is suggestive of a localized electronic structure in the solid-state.¹²⁰ X-ray absorption spectroscopy (XAS) can be used to probe the metal oxidation state, as well as nearest neighbor distances in the solid-state or frozen solution. For example, in Cu-salen complexes, the Cu K-edge 1s → 3d transition is a sensitive indicator of Cu oxidation state¹²¹ and a shift to higher energy can be attributed to an increase in metal oxidation state. Additionally, nearest neighbor distances can be obtained, but extracting bond length changes upon oxidation can be complicated for salens due to an inability to discriminate between N and O atoms in the backscattering data. Finally, theoretical calculations (such as density functional theory – DFT) are very useful in further understanding the electronic ground state, visualization of the SOMO and spin density, as well as the predicted donor and acceptor orbitals associated with the IVCT transition (via time-dependent density functional theory – TD-DFT). There is a tendency for DFT calculations to favor more symmetrically delocalized structures,^{114, 122} and thus one must be cautious in interpreting DFT results and consider benchmarking against experimental data.

Factors such as the central metal ion, the peripheral substituents on the ligand, and the solvent and temperature all affect the locus of oxidation, as well as the degree of localization and subsequent IVCT bands observed in oxidized metal-salen complexes. Each of these will be briefly discussed in the following sections.

1.2.1. Effect of Metal Ion

The use of different central metal ions has profound effects on the degree of localization and observed IVCT bands in oxidized metal-salen complexes. Figure 1.11 depicts the UV-vis-NIR spectra for neutral and oxidized Ni and Mn salen complexes of the same ligand. As evidenced by the intense IVCT band at 4,700 cm⁻¹ ($\epsilon = 21,500 \text{ M}^{-1} \text{ cm}^{-1}$), [Ni^{II}(Sal^{tBu})]^{•+} is a fully delocalized Class III mixed-valence species, while the analogous [Mn^{III}(Sal^{tBu})]^{•+} represents a Class II mixed-valence species on the basis of its weaker and broader IVCT band at 6,760 cm⁻¹ ($\epsilon \sim 1,000 \text{ M}^{-1} \text{ cm}^{-1}$). The extent of delocalization in oxidized metal-salen complexes depends on two factors, 1) the number of metal d electrons, and 2) the energy of metal d orbitals relative to those of the salen ligand.¹²³

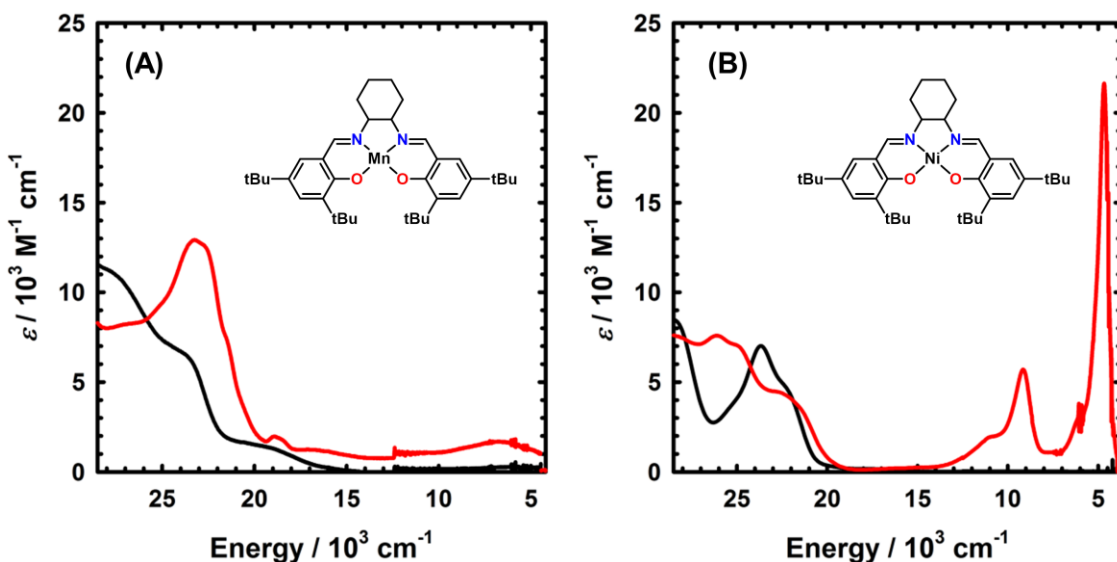


Figure 1.11. UV-vis-NIR spectra of (A) Mn(Sal^{tBu}) and (B) Ni(Sal^{tBu}) in neutral (black) and oxidized (red) forms, highlighting the change in IVCT bands observed for different metal ions.^{120, 124}

Oxidation of a salen ligand to a phenoxyl radical causes the π MO (HOMO) of the phenolate to become the SOMO of the complex. Charge transfer (CT) occurs from the metal-based d_{π} orbital into the SOMO, and increased CT (due to the population of the d_{π} orbital) into the SOMO results in less geometric distortion between the unoxidized phenolate and phenoxyl radical which increases the delocalization of the ground-state electronic structure. In the Ni(II) d^8 complex, the d_{π} orbital is doubly occupied and thus induces more CT to the SOMO. In the high-spin Mn(III) d^4 complex in which the metal d_{π} orbital is singly occupied, CT is possible in both directions (to the metal from the ligand and to the ligand from the metal) which enhances the geometric differences between phenolate and phenoxyl radical, causing more localized electronic structures.

The primary mechanism for communication between the two phenolate rings in oxidized metal-salen complexes is through the metal centre, analogous to the mediation of electronic coupling by the linker group in organic bridged multimetallic complexes such as the Creutz-Taube ion. Metal d orbitals with appropriate symmetry that are of relatively equal energy to the SOMO can better facilitate coupling between the two pro-radical phenolate rings. High-valent metals generally form localized ligand radicals due to contracted, low energy metal d orbitals which may also be involved in bonding to axial ligands (such as nitrido or oxo – see Chapter 4).^{115, 125}

1.2.2. Effect of Peripheral Substituents

The degree of delocalization of the unpaired electron in oxidized metal-salen complexes has been demonstrated to be sensitive to the overall electronics of the ligand as dictated by the substituent in the *para* position of the phenolate ring.^{114, 125-128} As an example, Figure 1.12 highlights the electronic structure differences in a series of oxidized Ni(Sal^R) complexes where R = CF₃ (electron withdrawing), tBu (weakly electron donating), and NMe₂ (strongly electron donating). The EPR spectra of the three complexes reflect a decreased spin-density at the Ni(II) centre as the electron donating ability of the *para* substituent increases. The g_{ave} values for complexes in which the SOMO has a non-negligible contribution from the central metal ion are greater than that for the free electron, and move closer to the free electron g value as the metal character of the SOMO decreases ($g_{ave} = 2.067$ for R = CF₃ > 2.023 for R = tBu > 2.004 for R = NMe₂).^{114, 120, 126} Theoretical calculations reproduce this experimental result, with decreased metal contribution to the spin density of the Ni complexes as the electron donating ability of the substituent increases (SD_{Ni} = 34% for R = CF₃ > 16% for R = tBu > 2% for R = NMe₂). Furthermore, the R = NMe₂ complex forms a localized ligand radical based on UV-vis-NIR, EPR, and DFT experiments. Taken together, these data suggest that participation of the NMe₂ group in the localization of the electron hole provides a stabilization pathway other than delocalization through the central Ni ion.¹¹⁴

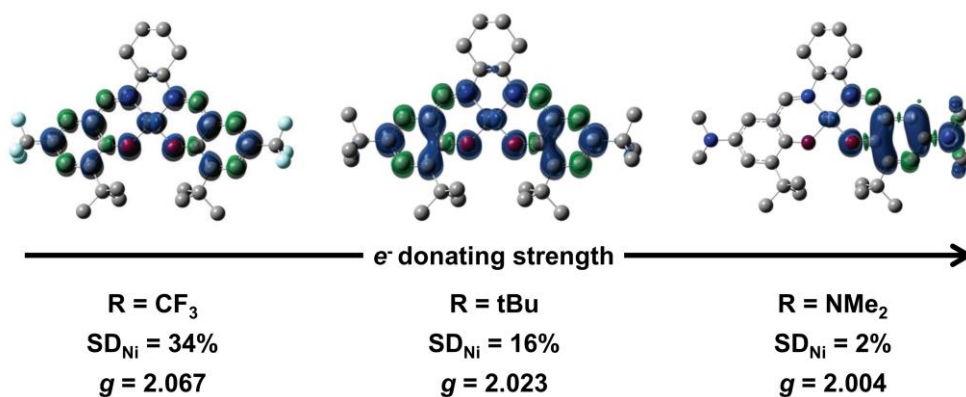


Figure 1.12. Spin density plots of Ni(Sal^R) where R = CF₃ (left), tBu (middle), and NMe₂ (right). The DFT calculated contribution of Ni to the SOMO, as well as the experimentally observed g_{ave} values are shown.^{114, 126}

1.2.3. Effect of Solvent and Temperature

Early investigations into the electronic structure of electrochemically oxidized Ni(Sal) complexes were performed in coordinating solvents such as DMF/DMSO and in all cases Ni(III) EPR signals were observed (Ni(III) EPR signals are characterized by g_{ave} values >2.15).^{92, 129-130} Isolation of a Ni(II)-salen radical was first achieved in 1996 by Peng and co-workers, who postulated that initial formation of a Ni(III) species, followed by intramolecular electron transfer resulted in the observed stable Ni(II) radical.¹³¹ A few reports followed which focused on an apparent temperature dependent valence tautomerism between Ni(II)-salen radical and Ni(III)-phenolate electronic structures.^{117, 132-133} In 2007, two reports described the temperature independence of the Ni(II)-salen radical electronic structure, and attributed the previously observed temperature dependent valence tautomerism to differences in oxidation protocol (the use of coordinating vs. non-coordinating counterions), as well as the axial binding of water (or other impurities) at the solvent freezing point.^{120, 134} It was thus concluded that in the absence of axial donors, oxidation of Ni(II)-salen complexes results in a phenoxyl radical electronic structure. Addition of exogenous ligands (commonly pyridine) shifts the oxidation locus from the ligand to the metal, which can be experimentally observed in the EPR spectrum. The EPR spectrum of genuine square-planar Ni(II)-phenoxyl radical electronic structures have g_{ave} values close to that of the free electron, whereas octahedral Ni(III) species exhibit g_{ave} values >2.15 (Figure 1.13A). Furthermore, depending on the axial donor, hyperfine coupling in the g_{zz} component of the EPR spectrum for octahedral Ni(III) complexes is characteristic of exogenous ligands coordinating to the Ni centre, with the hyperfine coupling constant (A_{zz}) reflective of the strength of interaction.

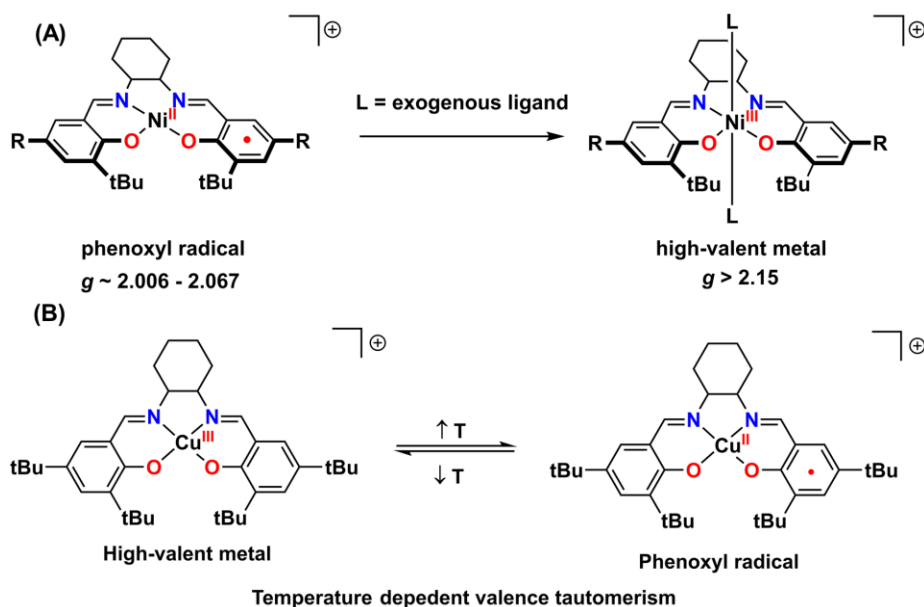


Figure 1.13. (A) Effect of exogenous ligands (coordinating solvents/anions) on the locus of oxidation in Ni(salen) complexes. (B) Temperature dependent valence tautomerism observed in oxidized Cu(Sal) complexes.

Thorough characterization of $[\text{Cu}(\text{Sal}^{\text{tBu}})]^+$ demonstrated that the complex exists as two essentially isoenergetic valence tautomers at 298 K, a triplet ferromagnetically coupled Cu(II)-phenoxyl radical species ($S = 1$) and a diamagnetic Cu(III) species (d^8 , $S = 0$).¹²¹ At low temperature (and in the solid-state) the Cu(III) electronic structure is stabilized as demonstrated by XAS, X-ray photoelectron spectroscopy (XPS), X-ray crystallography, rR and magnetic measurements. Variable temperature UV-vis-NIR, and solution susceptibility measurements confirmed the presence of both valence tautomers in a *ca.* 1:1 ratio at 298 K. Shifting to a Cu(III) species at low temperature is similar to the temperature dependent valence tautomerism observed in a number of metal-dioxolene complexes.¹³⁵⁻¹³⁹ Taken together, the above examples highlight the sensitivity of the electronic structures of metal-salen complexes to the coordination environment, and the temperature.

1.3. Multimetallic Cooperativity

The reversibility of imine formation can be harnessed to synthesize larger structures such as ring systems and macromolecules, and there is now increased interest in the study of multimetallic salen complexes for applications in catalysis, magnetics, and sensing.¹⁴⁰⁻¹⁴² Like pro-radical ligands, metalloenzymes are one area of inspiration, as

many multimetallic active sites have expanded redox reservoirs in order to drive multi-electron pathways for small molecule activation.¹⁴³ Examples include the hydrogenases (NiFe, FeFe),¹⁴⁴⁻¹⁴⁷ nitrogenases (FeMo, FeV, Fe-only)¹⁴⁸⁻¹⁵⁰ and particulate (Cu cluster)¹⁵¹ and soluble (FeFe) methane monooxygenase (Figure 1.14).¹⁵²

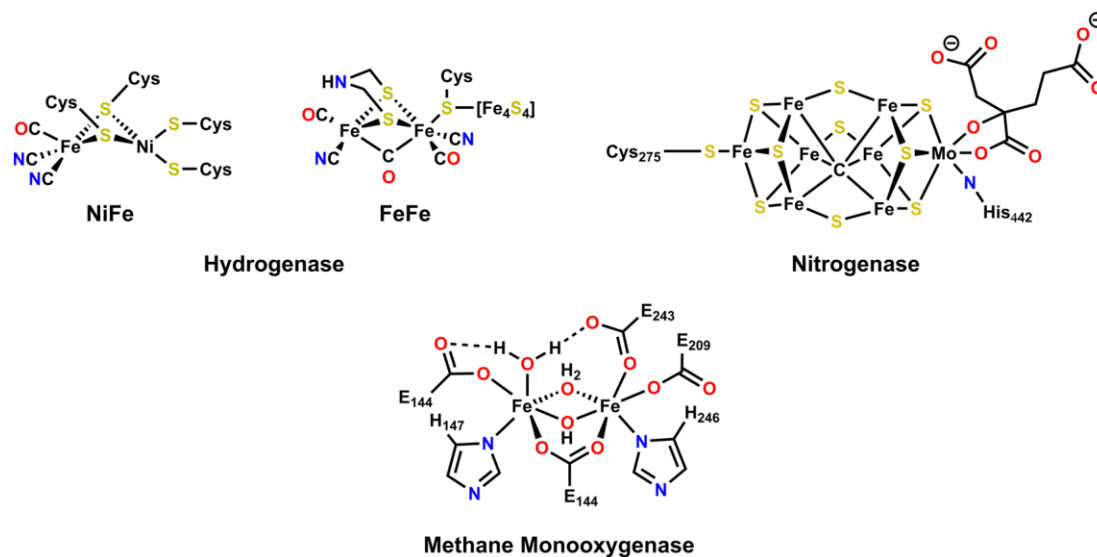


Figure 1.14. Representative active sites for multimetallic metalloenzymes.

Numerous small molecule models have been synthesized as a means to better understand the functionality of multimetallic active sites to promote chemistry along multielectron pathways.¹⁵³⁻¹⁵⁷ Bimetallic systems offer advantages over their mononuclear counterparts via enhanced substrate binding, increase in the rate of electron transfer from complex to bound substrate, the inhibition of problematic side reactions, and the stabilization of reactive intermediates inside the binding pocket.¹⁵⁸ Specific substrates can be targeted by tailoring of the binding pocket through the use of rigid or flexible spacers.¹⁵⁸ For example, Collman,^{153, 159} and more recently, Nocera¹⁶⁰⁻¹⁶² have developed metallodiporphyrin complexes for O₂ activation reactions, and Love has since made use of calixpyrroles for similar chemistry (Figure 1.15).¹⁶³⁻¹⁶⁵

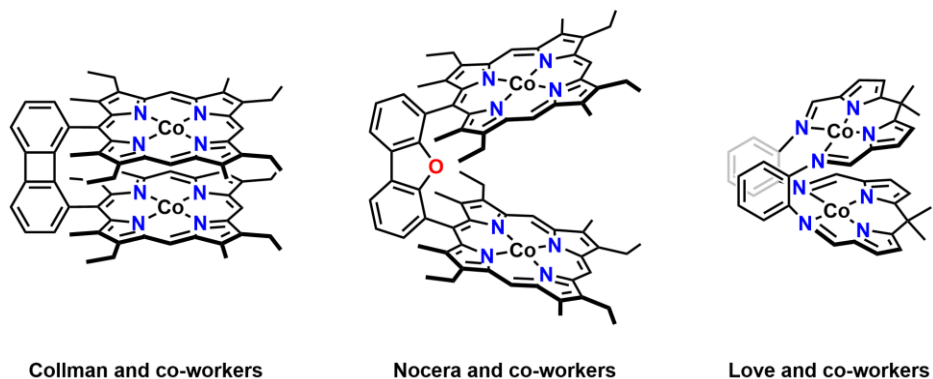
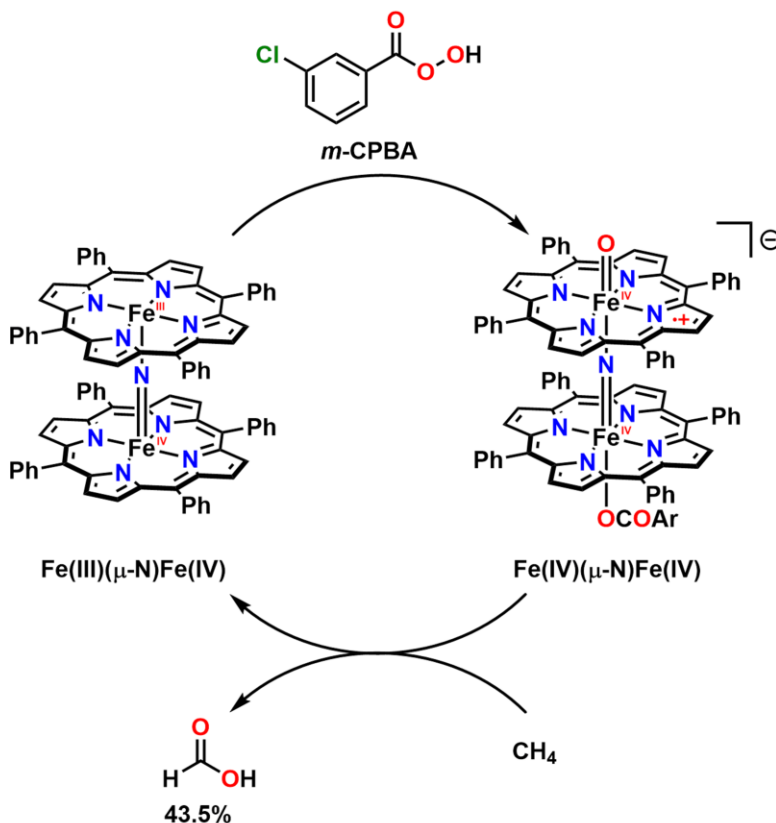


Figure 1.15. Selected bimetallic cobalt complexes studied by Collman and co-workers,¹⁵³ Nocera and co-workers,¹⁶⁰ and Love and co-workers¹⁶⁵ for the reduction of dioxygen.

Of particular relevance to this thesis, Sorokin and co-workers recently reported an *N*-bridged diiron species supported by porphyrin (or phthalocyanine) ligands capable of oxidizing methane (Scheme 1.3).^{64, 166-167} Upon oxidation with *meta*-chloroperoxybenzoic acid (*m*-CPBA), a high-valent Fe(IV)-oxo is formed, which when supported on silica results in 43.5% yield of formic acid based on the oxidant. On the basis of EPR and Mössbauer data, the *N*-bridged diiron(IV)-oxo core is strongly antiferromagnetically coupled to give an $S_{\text{Fe-Fe}} = 0$ species and a porphyrinyl radical cation. Furthermore, the *N*-bridged diiron(IV)-oxo is more active in C-H activation reactions than its mononuclear counterpart, as well as some of the most active heme and non-heme models reported by Groves^{73, 168} and Nam,¹⁶⁹ respectively.

Scheme 1.3. Proposed catalytic cycle for the oxidation of methane by *N*-bridged high-valent diiron-oxo species supported by porphyrin platforms reported by Sorokin and co-workers.



1.4. Multimetallic Salen Complexes

Salen ligands in particular find great utility due to their excellent replication of biological coordination environments, ease of synthesis, and ability to form stable complexes with a wide variety of metal ions. Multinucleating salen ligands typically have more involved syntheses in comparison to their mononuclear counterparts as a result of their multiple metal binding sites joined through rigid or flexible spacers. The design of multinuclear salen ligands relies heavily on the nature of the spacer group, which dictates both the distance and orientation of the metal centres in the resulting multimetallic complex (Figure 1.16A). One technique recently developed by Kleij and co-workers involves the templating of ligand precursors with metal ions (Figure 1.16B).¹⁷⁰⁻¹⁷¹ The utility of this technique is twofold as it allows for both the non-symmetric synthesis of bimetallic salen ligands, as well as the ability to selectively generate heterobimetallic complexes, which

show promise in the field of multifunctional materials and could have great applicability in cascade or tandem catalytic processes.

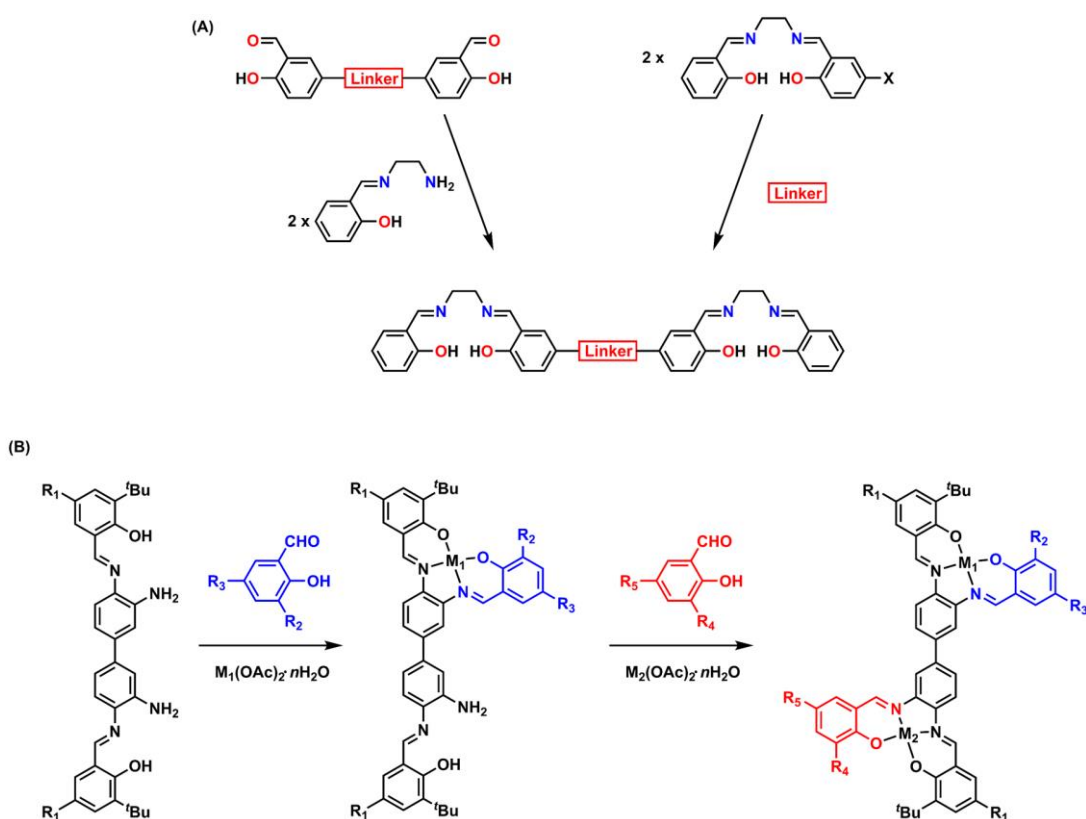


Figure 1.16. (A) Two potential coupling strategies towards multimetallic ligands. (B) Strategy developed by Kleij and co-workers for the synthesis of asymmetric salen ligands by templating of metal ions. Controlled synthesis of heterometallic complexes is possible through the stepwise addition of different metal ions (M_1 and M_2).¹⁷⁰⁻¹⁷¹

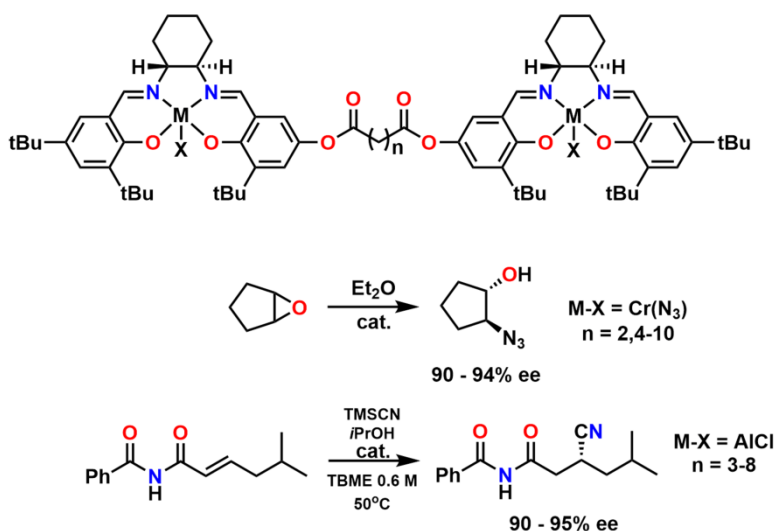
1.4.1. Catalysis

In the active sites of many metalloenzymes, two or more metal centres are capable of simultaneously activating both electrophilic and nucleophilic reactive partners. Interestingly, numerous reactivity studies involving metal-salen complexes have demonstrated second-order kinetic dependence with respect to the metallosalen catalyst.¹⁴² As a result, multiple catalytic sites have been incorporated into the same molecule as a means to enhance reactivity, and oftentimes cooperativity was observed as well as enhanced rates and selectivities.¹⁷²⁻¹⁷⁶ This methodology has been applied to, for example, the hydrolytic kinetic resolution (HKR) of epoxides,¹⁷⁷ asymmetric ring opening (ARO) of epoxides,¹⁷² cycloaddition reactions between enolates and electrophiles,¹⁷⁸

cyanation of α,β -unsaturated imides,¹⁷³ nitro-aldol reactions,¹⁷⁴ and polymerizations.¹⁷⁹ Outlined below are a few examples that highlight the cooperative nature of this chemistry.

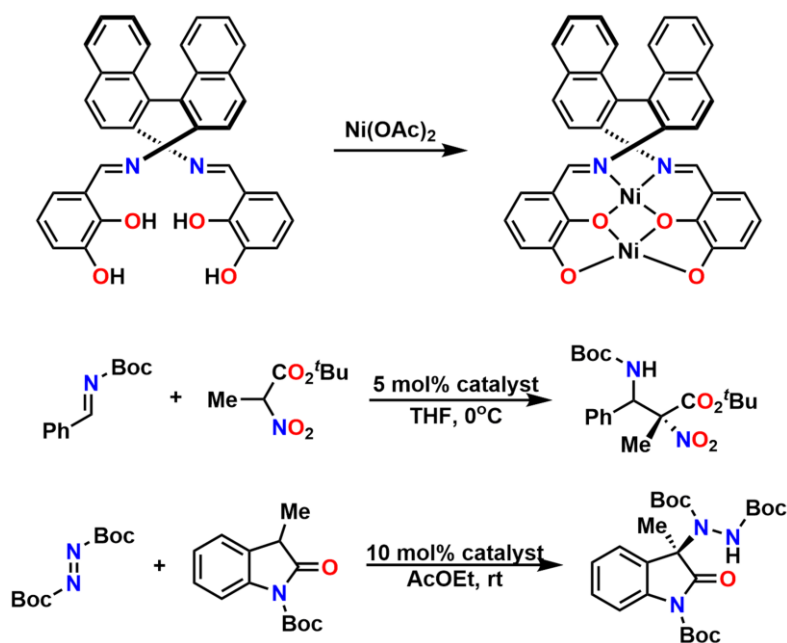
Initial studies by Jacobsen and co-workers investigated the ARO of epoxides with nucleophilic azide using bimetallic Cr(salen) catalysts linked by varying tethers (Scheme 1.4).¹⁷² Varying tether lengths were investigated as a means to increase conformational flexibility in the transition state. Significant dependence on tether length was observed, with a C5 linker affording the highest intramolecular rate constant, while shorter linkers resulted in significantly lower intramolecular rate constants due to the difficulty in obtaining the optimal transition state geometry as a result of restricted flexibility. Longer tethers (>5) also significantly decrease the magnitude of the intramolecular rate constant as a result of the high entropic cost associated with optimal transition state formation. Importantly, the catalysis is possible with catalyst concentrations an order of magnitude below the lower limit of reactivity for monomeric analogues, while still affording comparable enantiopurity of ring opened products. More recent work in the Jacobsen group has investigated the conjugate cyanation of α,β -unsaturated imides with bimetallic Al salen complexes as a means to incorporate chirality into bifunctional building blocks.¹⁷³ The catalysts display remarkable activity and increased substrate scope in comparison to their monomeric Al counterparts.¹⁸⁰

Scheme 1.4. Bimetallic salen complexes linked by varying tether lengths for the catalytic asymmetric ring opening of epoxides¹⁷² and the conjugate cyanation of α,β -unsaturated imides.¹⁷³



Complexes in which two metal centres are bound to the same salen moiety have also been explored for catalytic applications. Examples from Shibasaki and co-workers reported a homobimetallic Ni complex derived from 1,1'-binaphthyl-2,2'-diamine, as well as a heterobimetallic Cu/Sm complex for the catalysis of Mannich-type reactions with nitroacetates, malonates, β -keto esters, and β -keto phosphonates.¹⁸¹⁻¹⁸² The bimetallic Ni catalyst affords product with excellent enantio- and diastereoselectivity. Mononuclear complexes with the same backbone resulted in ee values of less than 5%, a remarkable result illustrating the advantages of bimetallic cooperativity. Recent work has focused on the synthesis of 3-aminooxindoles, which are a common structural motif in natural products and biologically active compounds, using bimetallic catalysts of Mn, Co, Ni, Cu, Zn, and Pd.¹⁷⁵

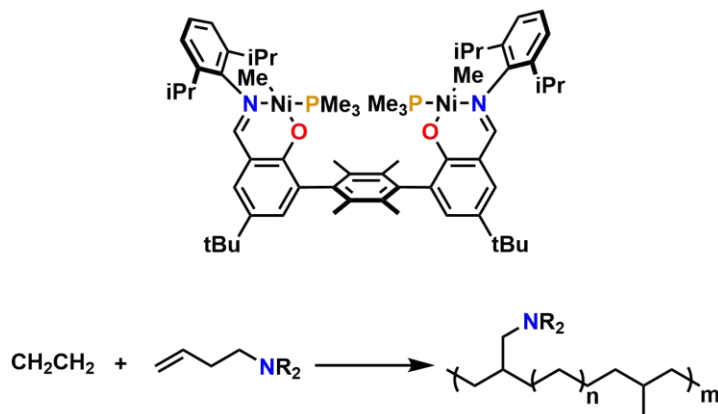
Scheme 1.5. Bimetallic Ni catalysts developed by Shibasaki and co-workers for Mannich-type reactions¹⁸² and the synthesis of 3-aminooxindoles.¹⁷⁵



Although not strictly salen constructs, Agapie and co-workers have reported bimetallic Schiff-base catalysts incorporating phenol moieties for polymerization reactions.¹⁸³⁻¹⁸⁷ In one example, copolymerization of amino olefins with ethylene is possible. Binding of an amino olefin to one metal centre creates steric bulk at the second metal centre, preventing the binding of a second amino olefin. Polymerization occurs at the second metal centre due to the lower steric profile of the ethylene monomer over the

amino olefin. In this regard, the amino olefin is incorporated into the polymer, rather than shutting down catalysis as is generally the case with Lewis basic substrates.

Scheme 1.6. Co-polymerization of amino olefins with ethylene catalyzed by a bimetallic Ni Schiff-base complex reported by Agapie and co-workers.¹⁸⁶⁻¹⁸⁷



1.4.2. Magnetics and Small Molecule/Ion Sensing

Magnetic interactions between paramagnetic metal centres and in certain cases pro-radical ligands, in multimetallic salen complexes have provided important information on spin interaction mechanisms. The degree of magnetic interaction in multimetallic complexes (whether ferromagnetic or antiferromagnetic) is dependent on a number of factors including the relative orientation of the relevant magnetic orbitals and the distance between the paramagnetic centres. The relative ease and modularity of synthesis make the salen framework an ideal medium for studying spin interaction mechanisms.

Single molecule magnets have attracted widespread attention since the discovery of spontaneous magnetization below a critical temperature.¹⁸⁸⁻¹⁸⁹ Employing appropriate ligand scaffolds can enforce ferromagnetic interactions between metal centres.¹⁹⁰ Early work reported by Glaser and co-workers employed phloroglucinol as a linker between paramagnetic metal-salen units¹⁹¹⁻¹⁹³ (*m*-phenylene linkers are well established to enforce ferromagnetic coupling, and have been used extensively to generate high spin organic radicals).¹⁹⁴ Highly modular ‘triple salen’ ($\text{H}_6\text{talen}^{\text{R}}$) ligands were developed to promote ferromagnetic coupling between three metal salen units (Figure 1.17A). These ligands combine the phloroglucinol bridging unit for ferromagnetic coupling with the salen functionality as a means to (a) utilize a modular ligand set, (b) implement a well-established, stabilizing coordination environment for first row transition metals, and (c)

introduce magnetic anisotropy, which along with high spin ground states is an important factor for the design of single-molecule magnets. The ‘triple salen’ ligand has been used to produce complexes with a variety of transition metals, including V(IV)=O,¹⁹⁵ Mn(III),¹⁹⁶ Fe(III),¹⁹⁷ Ni(II),¹⁹⁸ and Cu(II).^{192, 199} Installation of tBu at the *ortho* position of the phenolate ring (R₂) results in a systematic folding of the three salen units to produce a bowl-like structure (Figure 1.17B).

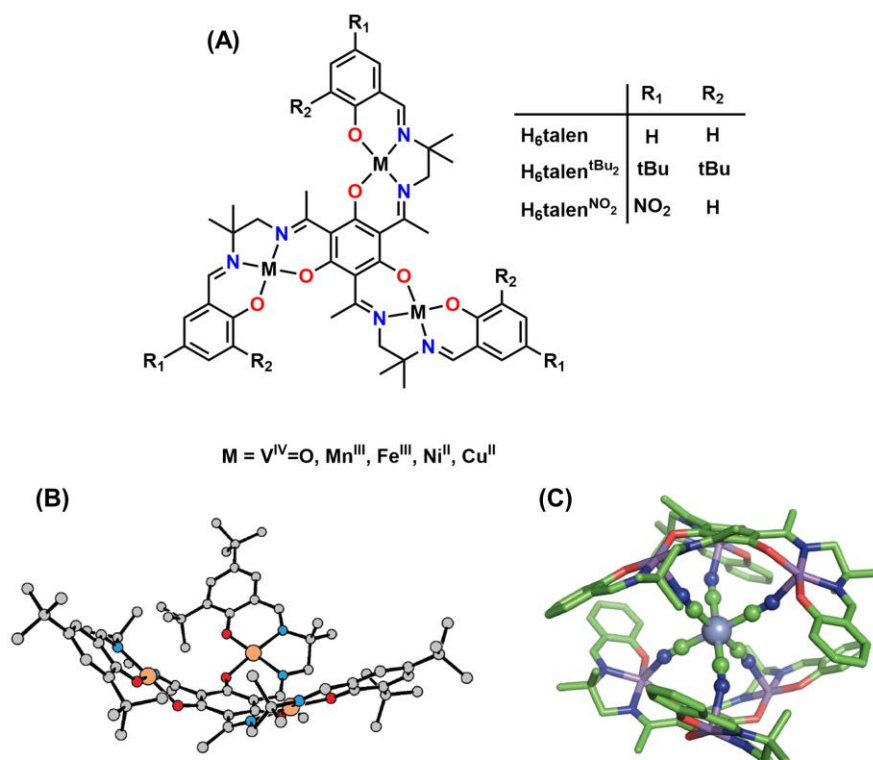


Figure 1.17. (A) Metal complexes of ‘triple salen’ (talen) ligands developed by Glaser and co-workers for magnetics applications. (B) Molecular structure of Cu(talen^{tBu₂}) highlighting the bowl-like structure when tBu is employed in the *ortho* position. (C) Molecular structure of [((talen^{tBu₂})Mn(III)₃)₂(Cr(III)(CN)₆)]³⁺. Peripheral tBu groups, Mn axially bound ligands, and hydrogen atoms omitted for clarity. Rendered using PyMol.²⁷

The bowl-like structure adopted when tBu is installed in the *ortho* position allows for controlled orientation of the three metal centres for binding to facially oriented atoms of a hexacyanometallate (Figure 1.17C). Glaser and co-workers have reacted the triple salen trinuclear complexes with hexacyanometallates in order to prepare heptanuclear complexes of the general formula [((talen^{tBu₂})(M¹(III)₃)₂(M²(III)(CN)₆)]³⁺, where M¹ = Mn(III),

and $M^2 = \text{Cr(III)},^{200} \text{Fe(III)},^{201-203}$ and $\text{Co(III)}.$ ²⁰⁴ When $M^2 = \text{Cr}$, strong Mn-Cr antiferromagnetic interactions force a parallel alignment of the terminal Mn(III) spins (high spin, d^4 , $S = 2$) leading to an extremely large high-spin ground state ($S_{\text{total}} = 21/2$). Coupled with the significant single ion anisotropy of the Mn(III) triple salen subunits, this results in $[\text{Mn(III)}_6\text{Cr(III)}]^{3+}$ exhibiting single molecule magnet (SMM) behaviour.

The use of multimetallic salen assemblies as small-molecule and ion sensors has been well documented in the literature, showing considerable promise for practical applications.^{141, 205-210} Multimetallic salen frameworks have been demonstrated to act as metallohosts forming adduct complexes with further structural ordering upon substrate binding. For example, Chan and co-workers have developed a series of bimetallic salen systems separated by a rigid pillar for metal sensing applications (Figure 1.18).²¹¹⁻²¹³ Backbone components such as xanthene and dibenzofuran were used to alter the binding pocket dimensions in which the oxygen atoms are oriented for guest binding. The photophysical properties of the complexes were studied in the presence of selected cations, and impressively a selective colorimetric and luminescent response in the presence of Pb(II) was reported. Experimental studies and theoretical calculations support cation occupation of the O(salphen)-binding cavity in these systems which alters the offset π -stacked constricts in the structure.

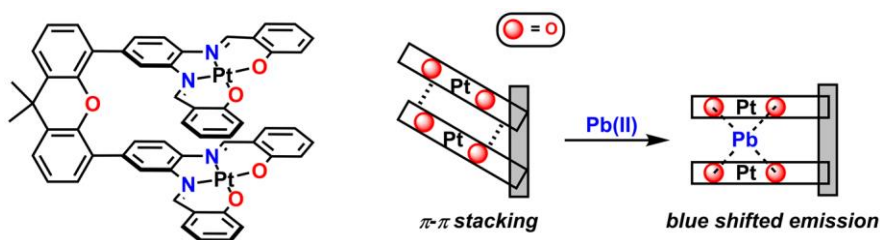


Figure 1.18. A Pt(Sal) bimetallic complex capable of a selective colorimetric and luminescent response to Pb(II) cations reported by Chan and co-workers.²¹¹⁻²¹³

1.5. Thesis Synopsis

In combining the ideas discussed so far, our group, and others, have investigated the electronic structures of oxidized monometallic and multimetallic salen complexes.²¹⁴⁻²¹⁹ The ambiguity often associated with pro-radical ligands is enhanced in the case of multimetallic complexes of pro-radical ligands as a result of multiple paramagnetic metal centres and magnetic coupling between metal spins. Despite extensive investigations into

catalytic properties of multimetallic salen systems, the study of electronic structures that may play a role during catalytic turnover are less prevalent. Figure 1.19 depicts some binucleating ligands employed by Thomas and co-workers,²¹⁸⁻²¹⁹ as well as Storr and co-workers²¹⁴⁻²¹⁶ for the electronic structure elucidation in multimetallic salen complexes.

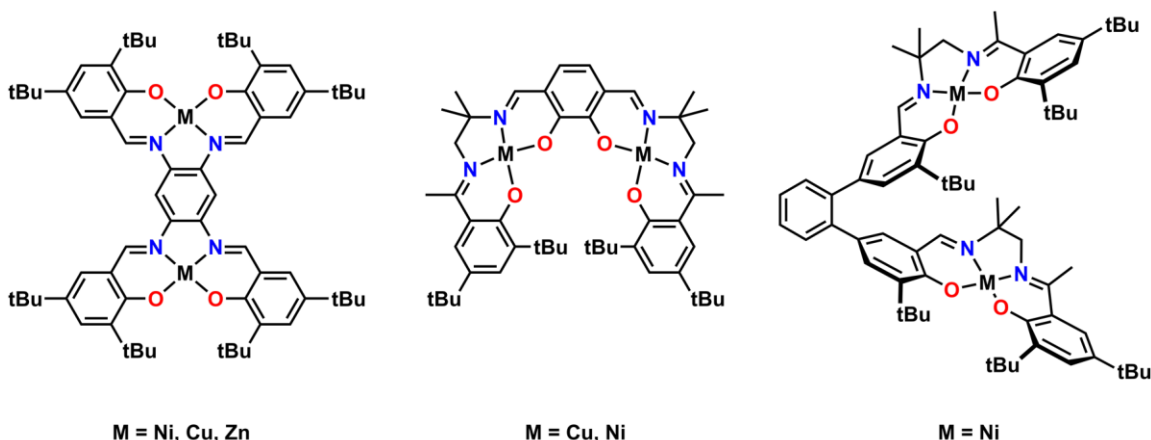


Figure 1.19. Binucleating ligands employed by Thomas and co-workers,²¹⁸⁻²¹⁹ and Storr and co-workers.²¹⁴⁻²¹⁶

As a means to investigate the effects of varying linkers and intermetallic distances on the electronic structure of oxidized metal salens, one particular study investigated a Ni salen dimer complex in which the salen units were connected via a 1,2-phenylene linker (Figure 1.19 – Right).²¹⁶ Double oxidation affords a bis-ligand radical system in which the ligand radicals are confined to each of the Ni(Sal) units, with VT-EPR experiments showing no evidence for electronic coupling between the two ligand radicals (a weak antiferromagnetic interaction $J = -17 \text{ cm}^{-1}$ is predicted by theoretical calculations). The oxidized monomeric analogue of the 1,2-phenylene bridged dimer was characterized as a fully delocalized Class III system based on the shape and intensity of its NIR features. Interestingly, instead of a NIR band of twice the intensity for the doubly oxidized dimer (as expected for non-interacting salen units), exciton coupling (*vide infra*) causes the NIR band to split into two bands equally spaced about the monomer transition. In Chapter 2, the distance and orientation between ligand radicals is systematically varied in a series of new bimetallic Ni(Sal) complexes in order to confirm exciton coupling as the mechanism of band splitting observed in the previous 1,2-phenylene linked dimer. New binucleating ligands tethered via a 1,3-phenylene linker, 1,4-phenylene linker and a xanthene linker are prepared providing a mechanism to tune the energy of the intense ligand radical NIR absorption in these systems.

The analogous Co complex of the 1,2-phenylene linked dimer is prepared and discussed with its monometallic Co counterpart in Chapter 3, with the aim of investigating the effects of the central metal ion on the overall electronic structure of bis-oxidized bimetallic salen complexes. Significant metal contribution to the SOMOs results in a less delocalized electronic structure in comparison to the Ni analogues, resulting in much broader NIR features which lack observable splitting due to exciton coupling.

In Chapter 4, efforts to prepare *N*-bridged Mn salen complexes analogous to those reported by Sorokin and co-workers resulted in the preparation of a series of nitridomanganese(V) salen complexes with different *para* substituents (R = tBu, CF₃, NMe₂). One-electron oxidation of these complexes uncovered interesting nitride activation chemistry that was further investigated. These studies demonstrated that nitride activation is dictated by remote ligand electronics. For R = tBu and CF₃, oxidation affords a Mn(VI) species and nitride activation, with dinitrogen homocoupling accelerated by the more electron-withdrawing CF₃ substituent. Employing an electron-donating substituent (R = NMe₂) results in a localized (Class II) ligand radical species that is resistant to N coupling of the nitrides and is stable in solution at both 195 and 298 K.

Finally, Chapter 5 discusses ongoing and future directions of the projects outlined in Chapters 2-4. Preliminary results on bimetallic catalysis, photo- and acid activation of electron-rich oxidized nitridomanganese complexes, as well as N-atom transfer chemistry are described. This thesis provides significant new information on how electronic structure dictates photophysical properties and reactivity in monometallic and bimetallic complexes employing the salen ligand framework.

Chapter 2. Exploiting Exciton Coupling of Ligand Radical Intervalence Charge Transfer Transitions to Tune NIR Absorption

Adapted from: Clarke, R.M.¹; Jeen, T.¹; Rigo, S.¹; Thompson, J.R.¹; Kaake, L.G.¹; Thomas, F.²; and Storr, T.¹ *Chem. Sci.*, **2018**, 9, 1610-1620.

¹Department of Chemistry, Simon Fraser University, Burnaby, British Columbia, Canada.

²Département de Chimie Moléculaire – Chimie Inorganique Redox (CIRE) – UMR CNRS 5250, Université Joseph Fourier, B.P. 53, 38041 Grenoble Cedex 9, France

RMC performed the synthesis with assistance from TJ and SR. RMC carried out the chemical oxidation, electrochemistry (with assistance from TJ), UV-vis-NIR, EPR experiments and theoretical calculations. RMC and JRT performed the crystallography. FT collected the EPR data, and simulated the Q-band frequency data.

2.1. Introduction

The photophysical properties of molecular aggregates continue to receive widespread attention due to their potential incorporation into display and wearable technologies,²²⁰⁻²²¹ and photovoltaic devices.²²² While the vast majority of molecular aggregates absorb in the visible region, there is significant interest in molecules that absorb in the near-infrared (NIR) due to the novel optical and electronic applications in this energy range.²²³ NIR absorbing materials include conjugated organic molecules and aggregates,²²⁴⁻²²⁶ polymers,²²⁷ transition metal complexes,²²⁸⁻²³³ and inorganic materials such as quantum dots²³⁴ and perovskites.²³⁵ Interestingly, mixed valence species can exhibit low energy intervalence charge transfer (IVCT) bands in the NIR, providing an additional class of low energy absorbing materials.²³⁶⁻²³⁷

The relationship between molecular packing and photophysical properties was eloquently described by Kasha, who showed that the alignment of transition dipoles and resulting coulombic interaction induces spectral shifts via exciton coupling when compared to uncoupled molecules (Figure 2.1).²³⁸⁻²⁴⁰ For transition moment dipoles aligned in a head-to-tail fashion (Figure 2.1A, J-aggregates), an in phase alignment of transition

moment dipoles corresponds to a red-shifted band of double intensity relative to a monomeric analogue; while a blue-shifted band of double intensity is the result of in phase transition moment dipoles aligned in a cofacial manner (Figure 2.1B, H-aggregates). Chromophores with transition moment dipoles oriented in an oblique arrangement will result in both red and blue-shifted bands as both orientations have net in phase alignment (Figure 2.1C). Exciton coupling is common in the absorption spectra of aggregated dye molecules, and has also been well studied in *meso*-linked porphyrin arrays,²⁴¹⁻²⁴³ and the π - π^* transitions of dipyrinato²⁴⁴⁻²⁵⁵ and azadipyrannato²⁵⁶⁻²⁵⁷ complexes. While the above description is sufficient in many cases, materials in alternate geometries and/or exhibiting short-range interactions (i.e. orbital overlap) have provided additional mechanisms to tune exciton coupling in molecular aggregates.²⁵⁸

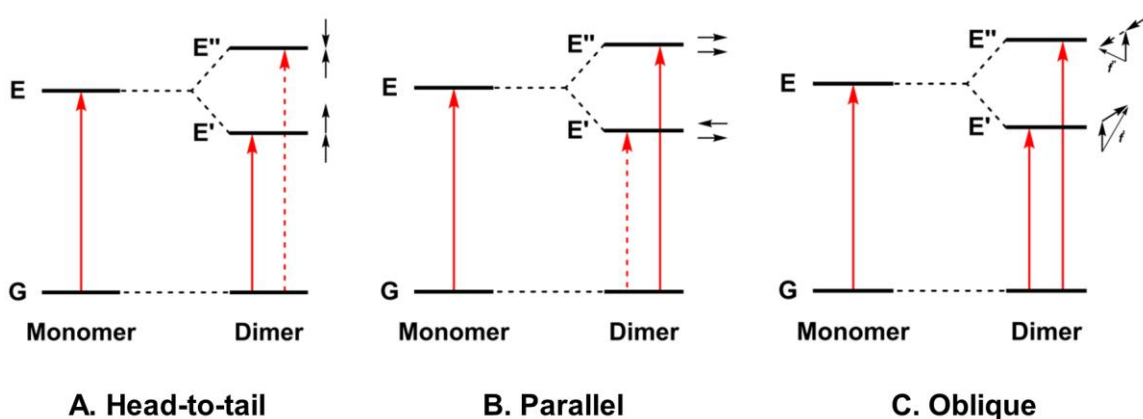


Figure 2.1. Exciton coupling of the excited states leads to band shifting and splitting relative to the analogous monomeric transition depending on the molecular geometry. Solid and dashed lines represent allowed and forbidden transitions, respectively. Small black arrows represent transition moment dipoles.

IVCT bands in the NIR provide a sensitive probe of electron transfer, and Robin and Day provided a classification system for localized (Class I, where the valences cannot interconvert, and Class II where interconversion can occur under thermal or photochemical activation) and delocalized (Class III) mixed-valence species,⁹⁹ with Hush providing a theoretical model for intervalence charge transfer in these species.¹⁰⁰

Our group, and others, have investigated the relationship between electronic structure and NIR band energy and intensity in transition metal complexes employing pro-radical ligands.^{114, 120, 123-124, 126, 216-217, 259-261} Alteration of ligand electronics,^{114, 261} ligand chromophore orientation,^{216, 262-264} metal ion^{124, 265} and oxidation state¹²³ are all important

factors controlling the energy and intensity of the resulting NIR band in these systems. As a practical example, stable Ni(II) dithiolene ligand radical complexes,^{1, 14, 43, 266-267} which exhibit intense NIR absorptions, have been applied as low energy absorbers to limit the transmittance of NIR radiation from plasma displays,²⁶⁸ and incorporated into materials for electronic applications.²⁶⁹⁻²⁷⁴ One prevalent class of pro-radical ligand that has been investigated extensively are bis-imine bis-phenoxide complexes (i.e. salen) due to their facile and highly modular synthesis which allows for tuning of both the steric and electronic properties.^{80, 275-276} As an example, one-electron oxidation of the Ni salen complex **1** (Figure 2.2) forms the ligand radical **[1]^{•+}**, which exhibits a sharp, intense IVCT band in the NIR ($\lambda_{\text{max}} = 4,500 \text{ cm}^{-1}$, $\epsilon = 27,700 \text{ M}^{-1} \text{ cm}^{-1}$, $\Delta\nu_{1/2} = 650 \text{ cm}^{-1}$), indicative of a Class III fully delocalized ligand radical in the Robin-Day classification system.²¹⁶ The ligand radical **[1]^{•+}** is stable for weeks in CH_2Cl_2 solution and in a PMMA film, and does not show any concentration-dependent aggregation effects in solution. In this chapter, further considerations of the applicability of oxidized Ni salen systems, and tunability of the intense NIR absorption for NIR absorbing materials is undertaken. A series of salen dimers **2-5** (Figure 2.2) is investigated to probe salen radical excited state electronic coupling.

In related work, our group has investigated the synthesis and oxidation of multimetallic salen complexes for potential catalytic applications.²¹⁶⁻²¹⁷ While pursuing this work, our group synthesized **3** (Figure 2.2) and investigated the doubly oxidized form **[3^{••}]²⁺**. The NIR region of the absorption spectrum for **[3^{••}]²⁺** exhibited two intense NIR bands, equally spaced at higher and lower energies in comparison to the monomer **[1]^{•+}**. While the possibility that the observed splitting was due to different conformers of **[3^{••}]²⁺** could not be discounted, experimental and theoretical analysis suggested that the NIR band splitting could be accounted for by exciton coupling. Related work in this area has demonstrated the interesting intermolecular interactions and resulting photophysical properties of salen systems.^{211-213, 277-283}

In this chapter, a full experimental and theoretical study of exciton coupling in a series of bimetallic bis-ligand radical complexes, where the distance and orientation of the NIR chromophores are varied systematically is provided (Figure 2.2). The resulting analysis supports exciton coupling of the intense NIR bands, providing a mechanism to tune the energy of the intense ligand radical NIR absorption in these systems.

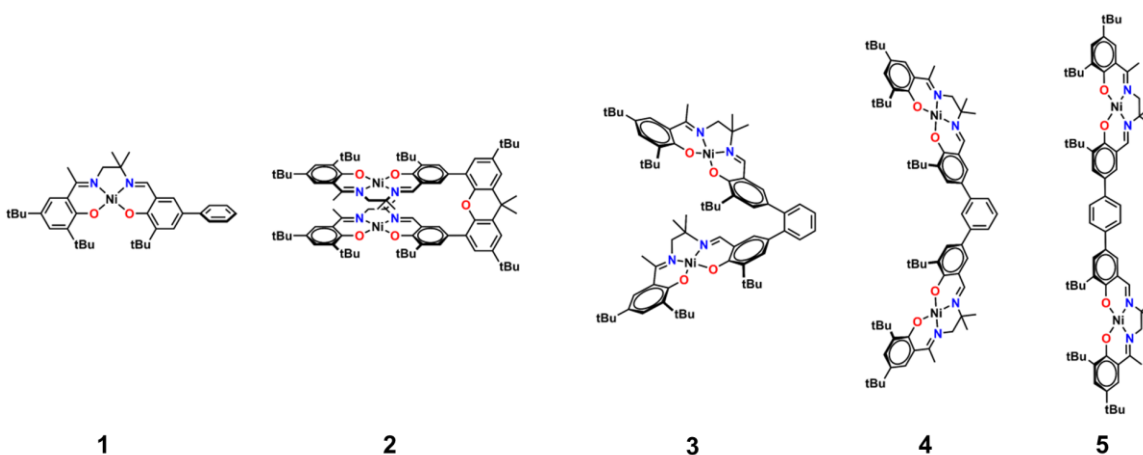


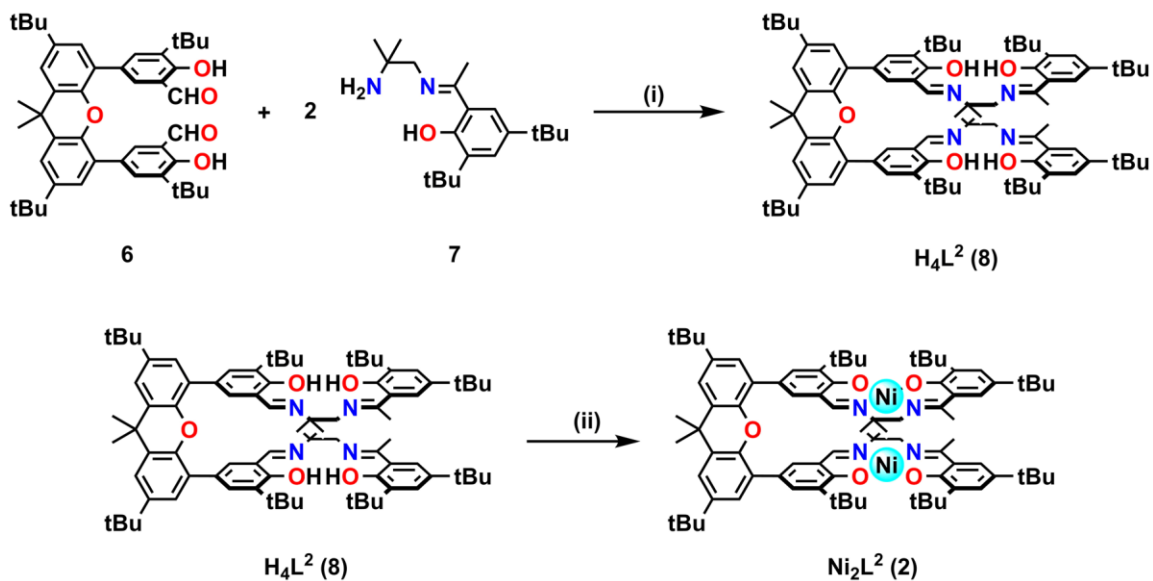
Figure 2.2. Monometallic and bimetallic salen complexes studied. **1** and **3** – previous work;²¹⁶ **2**, **4**, and **5** – this work.

2.2. Results

2.2.1. Synthesis

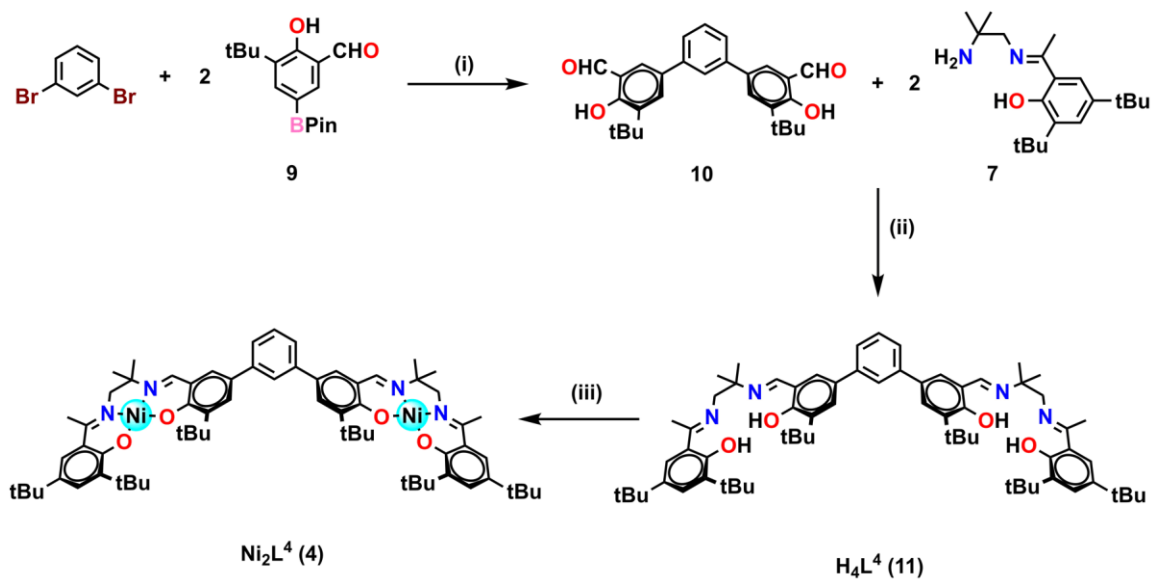
The synthetic strategies to form ligands (H_4L^2 , H_4L^4 , and H_4L^5) and complexes are presented in Scheme 2.1-2.3. All three ligands are synthesized via Suzuki coupling of the corresponding linking unit and a salicylaldehyde boronate ester, followed by condensation with 2 equivalents of a ‘half-salen’ unit (compound **7**). Complexes **3**, **4**, and **5** alternate substitution patterns around the central phenylene linker (*ortho*, *meta*, and *para*, respectively), while the xanthene spacer is employed in **2**. This spacer has been used by Nocera to cofacially align porphyrin rings for dioxygen activation reactions,¹⁶¹ Chan for the alignment of Pt(Sal) complexes,²¹¹⁻²¹² and Wasielewski for the alignment of organic chromophores.²⁸⁴⁻²⁸⁵

Scheme 2.1. Synthesis of **2**.



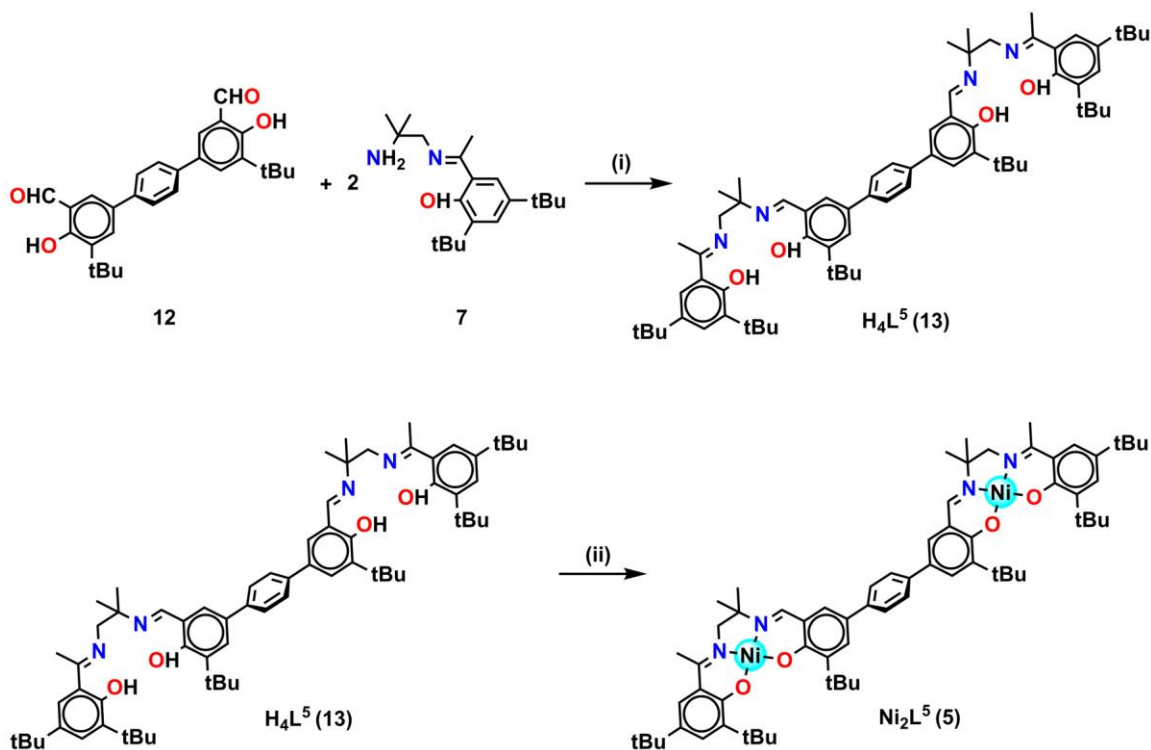
Reaction Conditions: (i) CH_2ClCH_2Cl , 52%; (ii) 3 equivalents $Ni(OAc)_2 \cdot 4H_2O$, DMF, 82%.

Scheme 2.2. Synthesis of **4**.



Reaction Conditions: (i) 5% $Pd(PPh_3)_4$, K_2CO_3 , 5:1 DME/ H_2O , 53%; (ii) THF, 75%; (iii) 3 equivalents $Ni(OAc)_2 \cdot 4H_2O$, DMF, 91%.

Scheme 2.3. Synthesis of 5.



Reaction Conditions: (i) THF, 87%; (ii) 3 equivalents Ni(OAc)₂·4H₂O, DMF, 88%.

2.2.2. Solid-State Characterization

The solid-state structures of new bimetallic Ni(Sal) complexes are presented in Figure 2.3-2.5. The Ni N₂O₂ coordination sphere in all complexes is slightly distorted from a square planar geometry likely due to the sterically demanding tBu substituents in the *ortho* positions of the phenols. DFT calculations on **2**, **4**, and **5** well reproduce the coordination sphere bond lengths of the three complexes, with the coordination sphere metrical parameters replicated to within ± 0.02 Å of the experimental values (Table 2.2). Furthermore, the calculations also accurately reproduce the slight asymmetry in the coordination spheres due to the asymmetric salen ligands. The individual Ni(Sal) moieties are oriented in a *trans* conformation relative to one another in the solid-state in **2**, with the sterically demanding tBu substituents facing away from each other. This is in contrast to the previously reported *cis* orientation for **3** in the solid-state, however in solution both conformers were observed by VT ¹H NMR with a DFT computed rotational barrier of ca. 6 kcal mol⁻¹.²¹⁶ DFT calculations on **2** predict the *trans* conformation to be ca. 2.7 kcal mol⁻¹ lower in energy in comparison to the *cis* conformation (*vide infra*). Additionally, the close spatial proximity between the salen moieties enforced by the xanthene spacer (Ni--Ni

distance of 3.98 Å) prohibits rotation of the salen units, and thus **2** is locked in a *trans* conformation at room temperature. The recrystallized *trans* form of **2** was used in all subsequent experiments. The angle between the salen planes in **2** is only 8.2°, highlighting the essentially cofacial arrangement of the salen units in this derivative (*vide infra*).

Similarly to **2**, **4** adopts a *trans* conformation of the salen units in the solid-state, although DFT calculations predict both *cis* and *trans* conformers to be essentially isoenergetic (difference of ca. 0.11 kcal mol⁻¹). The observed solid-state *trans* conformation is likely a result of solid-state packing effects and there is expected to be a relatively small rotational barrier of the salen units in solution.

Finally, the solid-state structure of **5** adopts a *cis* conformation of the salen units, in similar fashion to **3**. DFT calculations predict both *cis* and *trans* conformers to be essentially isoenergetic (difference of ca. 0.09 kcal mol⁻¹). Overall, the X-ray results show the expected configuration of the salen units in **2**, **4**, and **5** as mediated by the linker, and steric interactions responsible for the restricted rotation of the salen units observed for **2**.

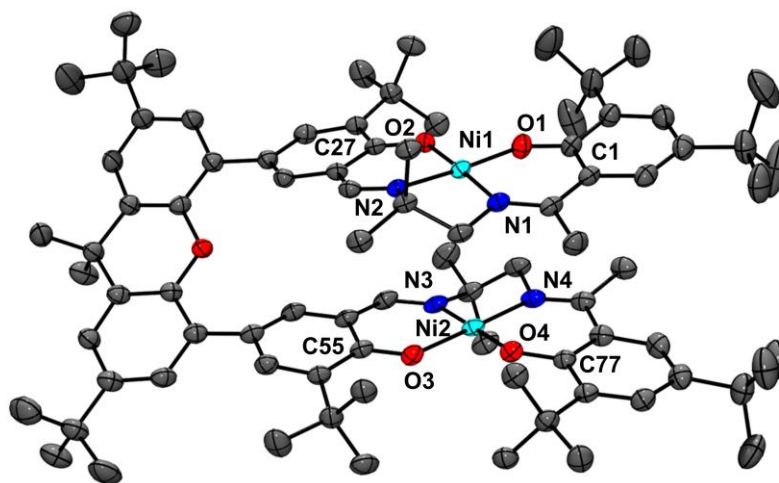


Figure 2.3. POV-Ray representation of **2**.

Thermal ellipsoids shown at 50% probability level. Hydrogen atoms and solvent omitted for clarity. Ni, cyan; C, gray; O, red; N, blue. Selected interatomic distances [Å] and angles [deg]: Ni(1)-O(1): 1.827(2), Ni(1)-O(2): 1.870(2), Ni(1)-N(1): 1.861(2), Ni(1)-N(2): 1.842(2), O(1)-C(1): 1.310(3), O(2)-C(27): 1.307(2), Ni(2)-O(3): 1.855(2), Ni(2)-O(4): 1.836(2), Ni(2)-N(3): 1.842(2), Ni(2)-N(4): 1.861(2), O(3)-C(55): 1.309(3), O(4)-C(77): 1.313(3); Angles: O(1)-Ni(1)-O(2): 85.6(2), O(1)-Ni(1)-N(1): 94.0(1), O(1)-Ni(1)-N(2): 176.3(5), O(2)-Ni(1)-N(1): 175.2(2), O(2)-Ni(1)-N(2): 94.1(1), N(1)-Ni(1)-N(2): 86.7(6), O(3)-Ni(2)-N(3): 93.6(8), O(3)-Ni(2)-O(4): 85.9(6), O(3)-Ni(2)-N(4): 178.4(5), O(4)-Ni(2)-N(3): 179.4(5), O(4)-Ni(2)-N(4): 93.5(8), N(3)-Ni(2)-N(4): 87.1(1).

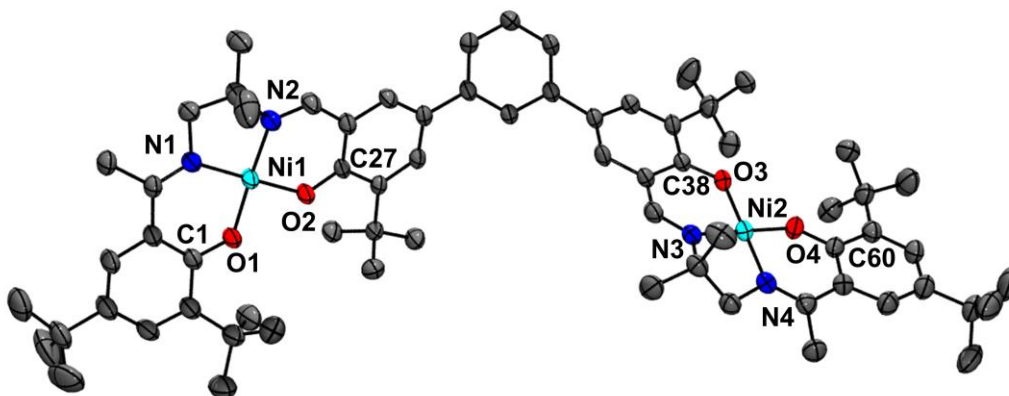


Figure 2.4. POV-Ray representation of **4**.

Thermal ellipsoids shown at 50% probability level. Hydrogen atoms and solvent omitted for clarity. Ni, cyan; C, gray; O, red; N, blue. Selected interatomic distances [Å] and angles [deg]: Ni(1)-O(1): 1.832(2), Ni(1)-O(2): 1.854(2), Ni(1)-N(1): 1.859(2), Ni(1)-N(2): 1.845(3), O(1)-C(1): 1.311(4), O(2)-C(27): 1.306(4), Ni(2)-O(3): 1.859(2), Ni(2)-O(4): 1.833(2), Ni(2)-N(3): 1.851(3), Ni(2)-N(4): 1.855(3), O(3)-C(38): 1.305(3), O(4)-C(60): 1.311(4); Angles: O(1)-Ni(1)-N(1): 93.1(1), O(1)-Ni(1)-O(2): 86.3(1), O(1)-Ni(1)-N(2): 177.9(1), N(1)-Ni(1)-N(2): 87.4(1), N(1)-Ni(1)-O(2): 179.0(1), O(2)-Ni(1)-N(2): 93.1(1), O(3)-Ni(2)-N(3): 93.6(1), O(3)-Ni(2)-O(4): 85.7(1), O(3)-Ni(2)-N(4): 174.0(1), N(3)-Ni(2)-N(4): 87.3(1), N(3)-Ni(2)-O(4): 175.5(1), O(4)-Ni(2)-N(4): 93.8(1).

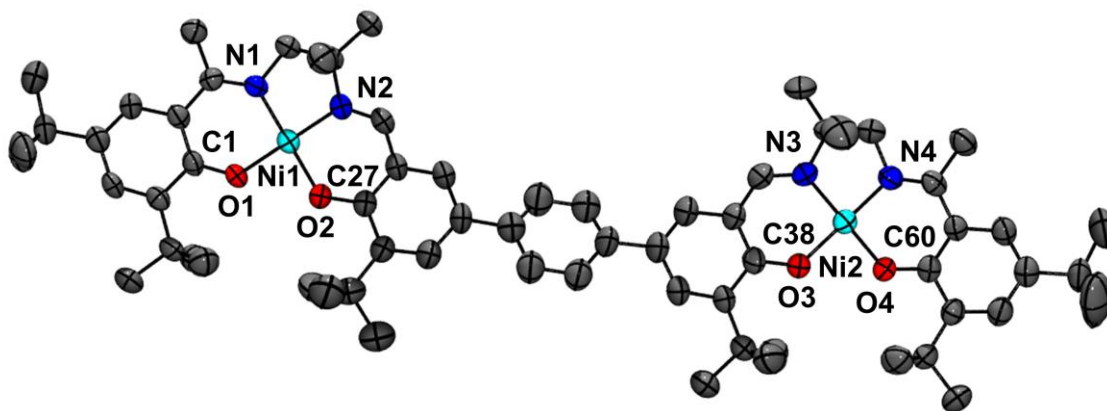


Figure 2.5. POV-Ray representation of **5**.

Thermal ellipsoids shown at 50% probability level. Hydrogen atoms and solvent omitted for clarity. Ni, cyan; C, gray; O, red; N, blue. Selected interatomic distances [Å] and angles [deg]: Ni(1)-O(1): 1.822(3), Ni(1)-O(2): 1.855(3), Ni(1)-N(1): 1.856(3), Ni(1)-N(2): 1.844(4), O(1)-C(1): 1.316(5), O(2)-C(27): 1.318(6), Ni(2)-O(3): 1.865(3), Ni(2)-O(4): 1.831(3), Ni(2)-N(3): 1.842(4), Ni(2)-N(4): 1.854(4), O(3)-C(38): 1.317(6), O(4)-C(60): 1.307(6); Angles: O(1)-Ni(1)-N(1): 93.4(1), O(1)-Ni(1)-O(2): 86.2(1), O(1)-Ni(1)-N(2): 178.5(1), N(1)-Ni(1)-N(2): 87.0(2), N(1)-Ni(1)-O(2): 176.5(2), O(2)-Ni(1)-N(2): 93.5(2), O(3)-Ni(2)-N(3): 93.4(1), O(3)-Ni(2)-O(4): 86.3(1), O(3)-Ni(2)-N(4): 176.5(1), N(3)-Ni(2)-N(4): 86.9(2), N(3)-Ni(2)-O(4): 179.4(1), O(4)-Ni(2)-N(4): 93.4(1).

Table 2.1. Selected crystallographic data for **2**, **4**, and **5**.

	2	4	5
Formula	C ₉₂ H ₁₃₀ N ₄ Ni ₂ O ₅	C ₇₂ H ₉₆ N ₆ Ni ₂ O ₄	C ₈₉ H ₁₃₉ N ₄ Ni ₂ O ₄
Formula weight	1560.31	1226.93	1446.45
Space group	P 21/n	P -1	P b c a
a (Å)	15.5829(11)	11.4567(7)	29.9305(5)
b (Å)	39.582(3)	13.1358(10)	12.1234(2)
c (Å)	16.2027(11)	25.5529(16)	47.9429(8)
α (deg)	90	82.482(5)	90
β (deg)	110.448(2)	89.480(4)	90
γ (deg)	90	67.190(5)	90
V [Å³]	9364.0(11)	3510.7(4)	17396.5(5)
Z	4	2	8
T (K)	150	150	296
ρ_{calcd} (g cm⁻³)	1.107	1.161	1.105
λ (Å)	0.77490	1.54178	1.54178
μ (cm⁻¹)	0.6370	1.043	0.898
R indices^a with I > 2.0σ(I) (data)	0.0439	0.0599	0.0555
wR₂	0.1126	0.1685	0.1250
R₁	0.0626	0.07934	0.0893
Goodness-of-fit on F²	1.033	1.044	1.080

^aGoodness-of-fit on *F*.**Table 2.2.** Experimental and calculated (in parentheses)^a coordination sphere metrical parameters for the complexes [Å].

Complex	Ni(1)- O(1)	Ni(1)- O(2)	Ni(1)- N(1)	Ni(1)- N(2)	Ni(2)- O(3)	Ni(2)- O(4)	Ni(2)- N(3)	Ni(2)- N(3)
2	1.827 (1.844)	1.871 (1.857)	1.863 (1.858)	1.842 (1.850)	1.854 (1.853)	1.836 (1.846)	1.841 (1.851)	1.861 (1.857)
[2^{••}]²⁺ (broken symmetry)	(1.819)	(1.845)	(1.851)	(1.845)	(1.843)	(1.819)	(1.844)	(1.851)
[2^{••}]²⁺ (triplet)	(1.824)	(1.840)	(1.850)	(1.845)	(1.846)	(1.821)	(1.846)	(1.850)
4	1.832 (1.836)	1.854 (1.857)	1.859 (1.857)	1.845 (1.852)	1.858 (1.851)	1.833 (1.830)	1.851 (1.848)	1.855 (1.852)
[4^{••}]²⁺ (broken symmetry)	(1.823)	(1.833)	(1.857)	(1.840)	(1.828)	(1.814)	(1.837)	(1.847)
[4^{••}]²⁺ (triplet)	(1.823)	(1.833)	(1.857)	(1.840)	(1.828)	(1.814)	(1.837)	(1.847)
5	1.822 (1.830)	1.855 (1.852)	1.856 (1.852)	1.844 (1.848)	1.865 (1.852)	1.831 (1.830)	1.842 (1.848)	1.854 (1.852)
[5^{••}]²⁺ (broken symmetry)	(1.814)	(1.829)	(1.848)	(1.838)	(1.829)	(1.814)	(1.838)	(1.848)
[5^{••}]²⁺ (triplet)	(1.814)	(1.829)	(1.848)	(1.838)	(1.829)	(1.814)	(1.838)	(1.848)

^aSee the Experimental Section for calculation details.

2.2.3. Electrochemistry

The electrochemical behaviour of new bimetallic Ni(Sal) complexes **2**, **4**, and **5** was studied by cyclic voltammetry (CV) in CH₂Cl₂ at 230 K and compared to the electrochemical behaviour of **1** and **3** (Figure 2.6).²¹⁶ All three new complexes are easily oxidized in similar ranges to the previously investigated **1** and **3**, reflecting the common oxidation of the Ni(Sal) units to form a delocalized ligand radical. Both **2** and **5** exhibit two closely spaced reversible one-electron redox couples at $E_{1/2} = 330$ mV and $E_{1/2} = 470$ mV for **2** and $E_{1/2} = 300$ mV and $E_{1/2} = 410$ mV for **5**; as well as irreversible oxidation events at approximately 800 – 850 mV (Table 2.3). In contrast to the closely spaced first two oxidation events for **2** and **5**, **4** displays only one reversible oxidation event at low potential ($E_{1/2} = 380$ mV), albeit a two-electron process reflected in a doubling of the current intensity in comparison to **2**, **3**, and **5**, which is further emphasized in the differential pulse voltammetry (DPV) data (Figure 2.7).^{108, 286} This is likely due to the *meta* 1,3-phenylene linker in **4** in comparison to the *ortho* and *para* connectors in **3** and **5** which facilitate communication between the salen units through the bridge.²⁸⁷⁻²⁸⁸ The splitting of the first two redox processes in **2** is therefore attributable to a small through space interaction between the redox-active salen moieties dictated by the xanthene spacer. The electronic coupling between the two redox-active salen moieties in [**2**]^{•+}, [**4**]^{•+}, and [**5**]^{•+} was investigated via the difference between the first and second oxidation events (ΔE_{ox}) and the comproportionation constant, K_c [Eqns. (1) – (3)].¹⁰² In the absence of electronic coupling, two redox processes separated by a theoretical value of $\Delta E_{1/2} = [RT/F] \ln 4$ ($\Delta E_{1/2} = 28$ mV at 233 K) will be observed. This is typically not observed experimentally, instead a doubling of current intensity at a single potential is observed.^{108, 286} Larger separations are often indicative of more strongly delocalized one-electron oxidized species.¹⁰² The small separation between the first two redox events in **2** and **5**, as well as the corresponding values of K_c suggests limited coupling between the two redox-active salen moieties, and that each salen unit is oxidized individually. In comparison, the unresolvable value of ΔE_{ox} for **4**, as well as the doubling of current intensity, suggests negligible coupling in this derivative.



$$K_c = \frac{[(\text{Sal})\text{L}(\text{Sal}^\bullet)]^2}{[(\text{Sal})\text{L}(\text{Sal})][(\text{Sal}^\bullet)\text{L}(\text{Sal}^\bullet)]} \quad (2)$$

$$K_c = \exp\left(\frac{\Delta E_{\text{ox}} F}{RT}\right) \quad (3)$$

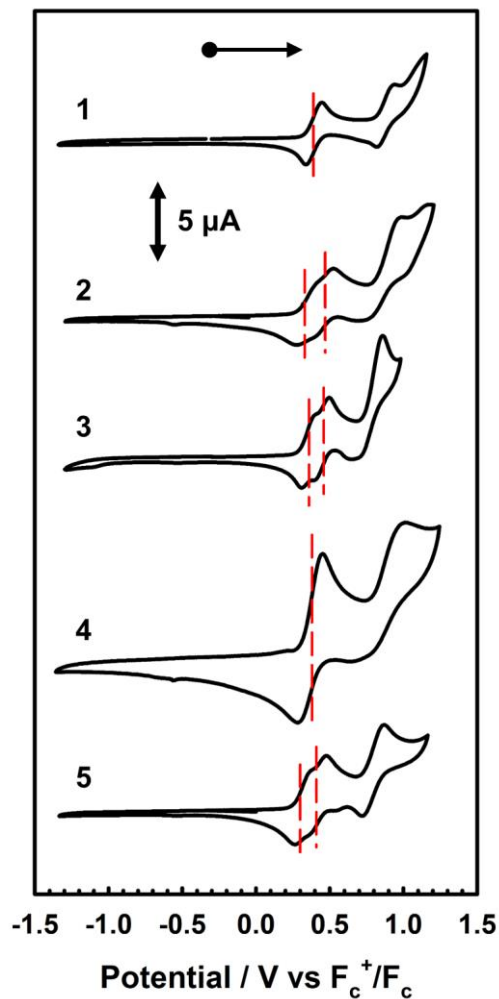


Figure 2.6. Cyclic voltammograms of 1-5 (top to bottom).
 Conditions: 1 mM complex, 0.1 M $n\text{Bu}_4\text{NClO}_4$, scan rate 100 mV s^{-1} , CH_2Cl_2 , 230 K.

Table 2.3. Redox potentials for **1-5** vs. $\text{Fc}^+/\text{Fc}^{a,b}$, and the comproportionation constant (K_c).

Complex	$E_{1/2}^1$ / mV	$E_{1/2}^2$ / mV	$E_{1/2}^3$ / mV	ΔE_{ox} ($E_{1/2}^2 - E_{1/2}^1$)	K_c (230K) ^c
1 ^c	390 (106)	890 (116)	-	500	9.04×10^{10}
2	330 (115)	470 (110)	850 (230)	140	1.17×10^3
3	360 (100)	460 (100)	800 (200)	100	1.55×10^2
4	380 (140)	-	875 (210)	495	-
5	300 (90)	410 (95)	795 (150)	110	2.57×10^2

^aGiven in volts, peak-to-peak separation given in parentheses. ^bPeak-to-peak difference for Fc^+/Fc couple at 233 K is 0.15 V. ^c K_c for **1** is *within* a salen unit, while K_c for **2-5** is *between* salen fragments. ^d[216].

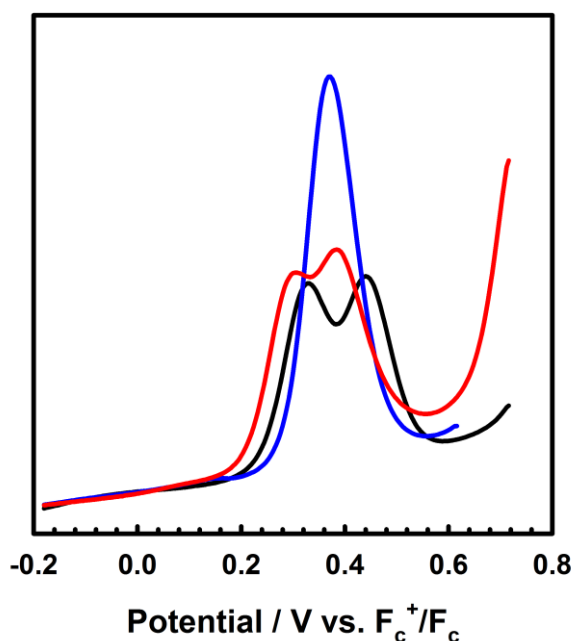


Figure 2.7. Differential pulse voltammetry (DPV) scans of **2** (black line), **4** (blue line), and **5** (red line).

Conditions: 1 mM complex, 0.1 M $n\text{Bu}_4\text{NClO}_4$, CH_2Cl_2 , 230 K.

The K_c values for **2**, **3**, and **5** are much smaller than the value for **1** (Table 2.3), which corresponds to the coupling between the redox-active phenolates *within* a salen unit. While not further investigated, we presume the redox events at high potential for **2-5** are due to the formation of bis-ligand radical species on the salen units.²⁸⁹

2.2.4. Electron Paramagnetic Resonance Spectroscopy

The X-band EPR spectra of $[\mathbf{1}^{\bullet}]^+$ and $[\mathbf{2-4}^{\bullet}]^{2+}$ are presented in Figure 2.8, and that of $[\mathbf{5}^{\bullet}]^{2+}$ is shown in Figure 2.10. EPR is an effective tool to study the degree of delocalization, and metal participation in the singly occupied molecular orbital (SOMO), in transition-metal complexes incorporating redox-active ligands. Furthermore, in this work, EPR is a sensitive probe for detecting spin-spin interactions in the bis-ligand radical species $[\mathbf{2-5}^{\bullet}]^{2+}$. All five complexes exhibit g values close to that of the free electron, indicating a ligand radical species (Table 2.4). The g values are slightly higher than expected for purely ligand based radicals ($g_{\text{ave}} > g_e \sim 2.0023$), which suggests non-negligible contribution of the Ni centres to the SOMOs. The ligand radical $[\mathbf{1}^{\bullet}]^+$ was previously investigated and exhibits a rhombic spectrum ($g_{\text{ave}} = 2.048$, Table 2.4) with ca. 13% Ni d_{xz} character in the SOMO (based on DFT).²¹⁶

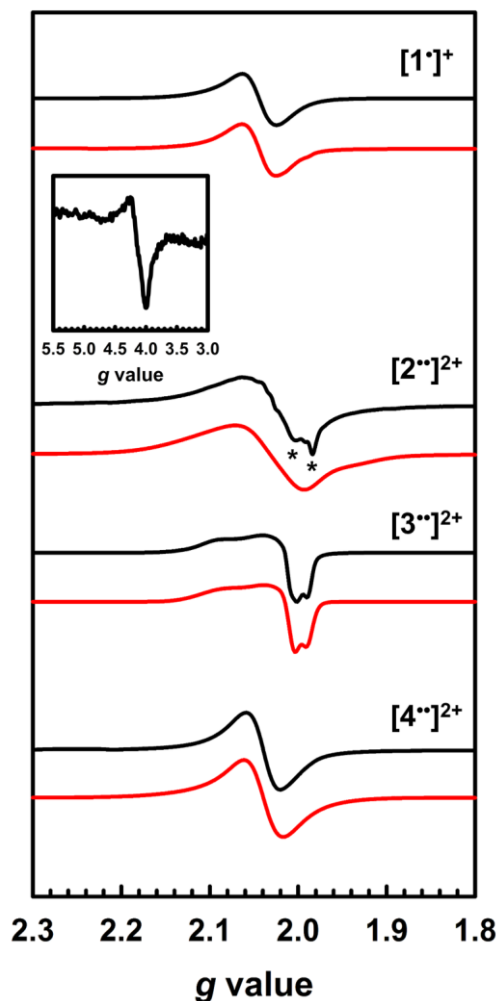


Figure 2.8. X-band EPR spectra (black) of $[1^\bullet]^+$ and $[2-4^{\bullet}]^{2+}$ recorded in frozen CH_2Cl_2 at 0.33 mM. Red lines represent simulations of the experimental data. Inset: weak half-field $\Delta M_s = 2$ transition for $[2^{\bullet}]^{2+}$. Conditions: frequency = 9.38 GHz ($[1^\bullet]^+$ and $[3^{\bullet}]^{2+}$), 9.64 GHz ($[2^{\bullet}]^{2+}$ and $[4^{\bullet}]^{2+}$); power = 2 mW; modulation frequency = 100 kHz; modulation amplitude = 0.4 mT; $T = 6$ K. Asterisks denote the monoradical $[2^\bullet]^+$ impurity (*vide infra*).

Table 2.4. EPR simulation parameters for $[1^\bullet]^+$ and $[2-5^{\bullet}]^{2+}$

Complex	g_{xx}	g_{yy}	g_{zz}	g_{ave}	$D / 10^{-4} \text{ cm}^{-1}$	E/D
$[1^\bullet]^+$ ^a	2.061	2.046	2.037	2.048	-	-
$[2^{\bullet}]^{2+}$	2.120	2.020	1.980	2.035	75	<0.05
$[3^{\bullet}]^{2+}$ ^a	2.090	2.019	2.000	2.036	13	<0.04
$[4^{\bullet}]^{2+}$	2.047	2.036	2.033	2.038	-	-
$[5^{\bullet}]^{2+}$		2.014			-	-

^a[216].

The X-band EPR spectrum of $[2^{\bullet}]^{2+}$ differs substantially from that of $[1^\bullet]^+$, exhibiting a low field resonance at $g = 4$ in addition to the features at ca. $g = 2$. This low field

resonance is attributed to a half-field transition (Figure 2.8 – inset), which suggests significant population of the triplet spin state. Both the weak intensity and position suggest that the zero-field splitting (ZFS) parameters are small.²⁹⁰ The signal at ca. $g = 2$ contains two contributions. The minor component originates from an $S = \frac{1}{2}$ monoradical **[2]^{•+}** impurity, which is manifest as a relatively sharp rhombic feature at $g_1 = 2.115$, $g_2 = 2.012$, and $g_3 = 1.987$ (Figure 2.9). The main spectrum is significantly broader and displays outermost resonances assigned to the $\Delta M_s = 1$ transitions of the triplet species. This assignment is corroborated by EPR measurements at the Q-band frequency, which shows a global evolution of the spectrum with frequency that is inconsistent with the presence of simple rhombic $S = \frac{1}{2}$ systems (Appendix A – Figure A8). The low resolution of the triplet spectrum complicates the determination of accurate ZFS parameters by simulation. By using the g values determined for **[2]^{•+}** as an initial guess for the simulation of the triplet spectra at both X- and Q-band frequencies (Appendix A – Figure A8), the ZFS parameters are estimated as $|D| = 0.0075 \text{ cm}^{-1}$ with an $E/D < 0.05$. By using the point dipole approximation (Eqn. 4)²⁹¹ these ZFS parameters afford an interspin distance of 6.9 Å, which exceeds the distance between the two mean N₂O₂ planes measured in the crystal structure of **2** (3.98 Å). Such discrepancy is not unexpected for organic diradicals and can be taken as evidence of substantial delocalization of the unpaired electrons.²⁹²⁻²⁹³ We further investigated the magnetic interaction in **[2^{••}]²⁺** via the temperature dependence of the $\Delta M_s = 2$ signal. A plot of the intensity of the $\Delta M_s = 2$ signal as a function of $1/T$ results in a straight line (Appendix A – Figure A9), suggesting a weak interaction between the two salen radical units. The magnetic coupling for **[2^{••}]²⁺** is comparable to that reported for paracyclophane,²⁹⁴ and Ni(II)-thiazyl p-stacked radical dimers,²⁹⁵ and could be further interpreted in terms of a McConnell-I mechanism involving delocalized radicals.²⁹⁶

$$|D| = \frac{3 g_e^2 \mu_B^2}{2 r^3} \quad (4)$$

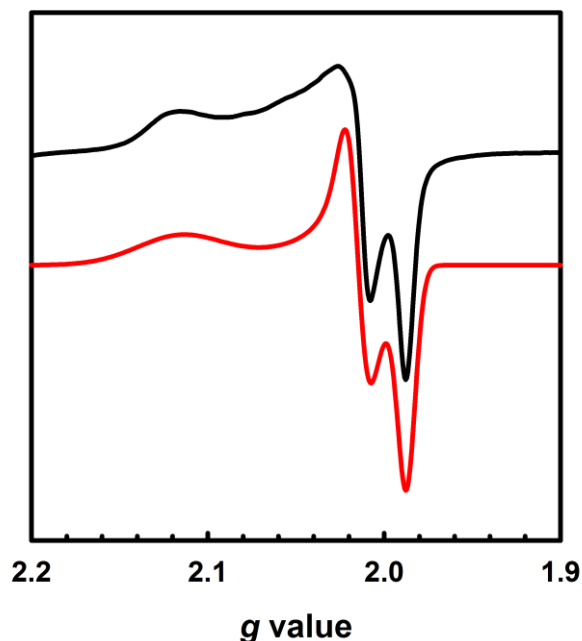


Figure 2.9. X-band EPR spectrum of $[2^{\bullet}]^{2+}$ recorded in frozen CH_2Cl_2 at 1.2 mM. Conditions: frequency = 9.64 GHz; power = 2 mW; modulation frequency = 100 kHz; modulation amplitude = 0.4 mT; $T = 8$ K. The red line represents simulation to the experimental data using the parameters given in the text.

The EPR spectrum for $[3^{\bullet}]^{2+}$ was previously simulated as a diradical²⁹⁷ by considering the individual salen moieties in *cis* and *trans* conformations relative to one another, with the observed experimental data a combination of the two sub-spectra.²¹⁶ Although a half-field transition is not observed, based on the analysis of $[2^{\bullet}]^{2+}$, the data for $[3^{\bullet}]^{2+}$ was simulated as a triplet species instead of two conformers, with small ZFS parameters (Table 2.4). The lack of an observable half-field transition, coupled with the small ZFS parameters suggest limited coupling in $[3^{\bullet}]^{2+}$.²⁹⁷ Using the point dipole approximation (Eqn. 4), an interspin distance is calculated as 12.5 Å. This value is again larger than the 9.8 Å distance between the Ni centres in the crystal structure of **3**, and similarly to the analysis of $[2^{\bullet}]^{2+}$, suggests extensive delocalization of the unpaired electrons. It must be stressed that the D values are small for both $[2^{\bullet}]^{2+}$ and $[3^{\bullet}]^{2+}$, confirming that the spin-spin interactions are weak in both complexes.

The EPR spectrum of $[4^{\bullet}]^{2+}$ exhibits a broad signal at $g_{\text{ave}} = 2.038$, consistent with the other oxidized complexes. A half-field transition was not observed, likely due to the large separation between the salen moieties in $[4^{\bullet}]^{2+}$. In agreement with the above

structural and electrochemical data, the EPR spectrum of mono-oxidized $[4^{\bullet}]^+$ (Appendix A – Figure A10) is very similar to $[4^{\bullet}]^{2+}$, but with ca. $\frac{1}{2}$ the intensity.

Oxidation of **5** to $[5^{\bullet}]^{2+}$ at low temperature resulted in a very weak EPR signal (Figure 2.10 – bottom) with ca. 3% intensity in comparison to a concentration matched sample of $[4^{\bullet}]^{2+}$. It was hypothesized that the lack of signal was either due to sample decomposition, or spin-spin interactions due to intermolecular interaction of $[5^{\bullet}]^{2+}$ at low temperature (*vide infra*). EPR analysis of a solution of $[5^{\bullet}]^{2+}$ at 298 K affords an isotropic signal with a $g_{\text{iso}} = 2.014$, supporting the assignment as a bis-ligand radical species, although with less contribution of the central Ni atoms to the SOMO. The intensity of the doubly integrated signal of $[5^{\bullet}]^{2+}$ under non-saturating conditions is plotted against the concentration in the inset of Figure 2.10. A clear saturation is observed after ca. 0.5 mM, indicative of dimerization/aggregation processes above this concentration.

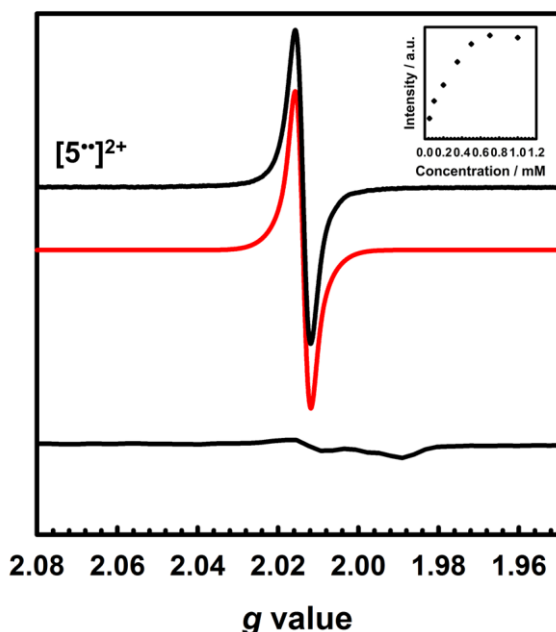


Figure 2.10. Top: Room temperature X-band EPR spectrum of $[5^{\bullet}]^{2+}$ (black) recorded in CH_2Cl_2 at 0.35 mM (simulation in red). Inset: Saturation curve of the signal at $g_{\text{iso}} = 2.014$ with increasing concentration suggesting aggregation above 0.5 mM. Bottom: X-band EPR spectrum of $[5^{\bullet}]^{2+}$ oxidized at 77 K. Conditions: (Top) frequency = 9.44 GHz; power = 2 mW; modulation frequency = 100 kHz; modulation amplitude = 0.15 mT; $T = 298$ K. (Bottom) frequency = 9.38 GHz; power = 2 mW; modulation frequency = 100 kHz; modulation amplitude = 0.6 mT; $T = 77$ K.

2.2.5. Electronic Absorption Spectroscopy

Chemical oxidation of **2**, **4**, and **5** with two equivalents of $[\text{N}(\text{C}_6\text{H}_3\text{Br}_2)_3][\text{SbF}_6]$ at 198 K resulted in the appearance of intense transitions in the NIR region of the absorption spectra (Figure 2.11). In all cases, isosbestic points are observed during the sequential addition of oxidant from 0-2 equivalents indicating clean conversion to the respective oxidized product (Figure 2.12). For $[\mathbf{2}^{\bullet}]^{2+}$, in which the salen moieties are cofacially aligned, the exciton model predicts a blue-shifted and doubly intense band relative to the monomeric analogue $[\mathbf{1}^{\bullet}]^+$. Indeed, a blue-shifted band by ca. 330 cm^{-1} relative to the IVCT transition observed in $[\mathbf{1}^{\bullet}]^+$ is observed. The IVCT band for $[\mathbf{2}^{\bullet}]^{2+}$ is nearly double the intensity of the band observed in $[\mathbf{1}^{\bullet}]^+$ ($42,900$ vs. $27,700\text{ M}^{-1}\text{ cm}^{-1}$), with the slightly diminished intensity in $[\mathbf{2}^{\bullet}]^{2+}$ likely due to minimal symmetry perturbations resulting in the low energy forbidden transition gaining weak intensity.²⁹⁸ Indeed, the low energy transition in $[\mathbf{2}^{\bullet}]^{2+}$ is evident as a shoulder in Figure 2.11B. For oblique systems such as $[\mathbf{3}^{\bullet}]^{2+}$ and $[\mathbf{4}^{\bullet}]^{2+}$, the exciton model predicts a splitting of bands as both transitions at high and low energy are partially allowed (Figure 2.11A and 2.11C). The intensity of the observed bands is dependent on the distance and angle between the transition moment dipole moments. For $[\mathbf{3}^{\bullet}]^{2+}$, which has an approximate angle of 60° between the two salen units, two NIR transitions are observed equally split about the IVCT band in $[\mathbf{1}^{\bullet}]^+$.²¹⁶ For $[\mathbf{4}^{\bullet}]^{2+}$ which has a significantly larger angle between the two salen units (120°) and is closer to the parallel system, we observe a prominent low energy band red-shifted by ca. 190 cm^{-1} as well as a lower-intensity shoulder corresponding to the higher energy transition predicted by the exciton model.

Finally, the exciton model predicts that $[\mathbf{5}^{\bullet}]^{2+}$ will afford a red-shifted band relative to the monomeric analogue. At low temperature, we do not observe a red-shifted IVCT band, but a broad transition ranging from $20,000\text{ cm}^{-1}$ to $10,000\text{ cm}^{-1}$ ($\epsilon = 30,000\text{ M}^{-1}\text{ cm}^{-1}$), alongside a broad blue-shifted NIR band ($\lambda_{\text{max}} = 5,100\text{ cm}^{-1}$, $\epsilon = 29,000\text{ M}^{-1}\text{ cm}^{-1}$, Figure 2.12D). Heating/sonication of this solution did not change the absorption profile and dynamic light scattering (DLS) experiments confirm the presence of large aggregates (mean size $\sim 145\text{ nm}$ – Appendix A – Figure A14), likely formed via π -interactions between radical cations.²⁹⁹ Oxidation of a dilute solution (0.08 mM) of **5** to $[\mathbf{5}^{\bullet}]^{2+}$ at 298 K did however afford a red-shifted band as predicted by the exciton model (Figure 2.11). Concentration-dependent EPR studies at 298 K show saturation of the main resonance at $g = 2$ beginning at 0.5 mM, suggesting aggregation above this concentration, and the

broadness of the band depicted in Figure 2.11 is likely due to partial aggregation of $[5^{••}]^{2+}$ even at room temperature. Overall, the shifting and/or splitting of the intense IVCT bands in the bimetallic bis-ligand radical species is correctly predicted by the exciton model.

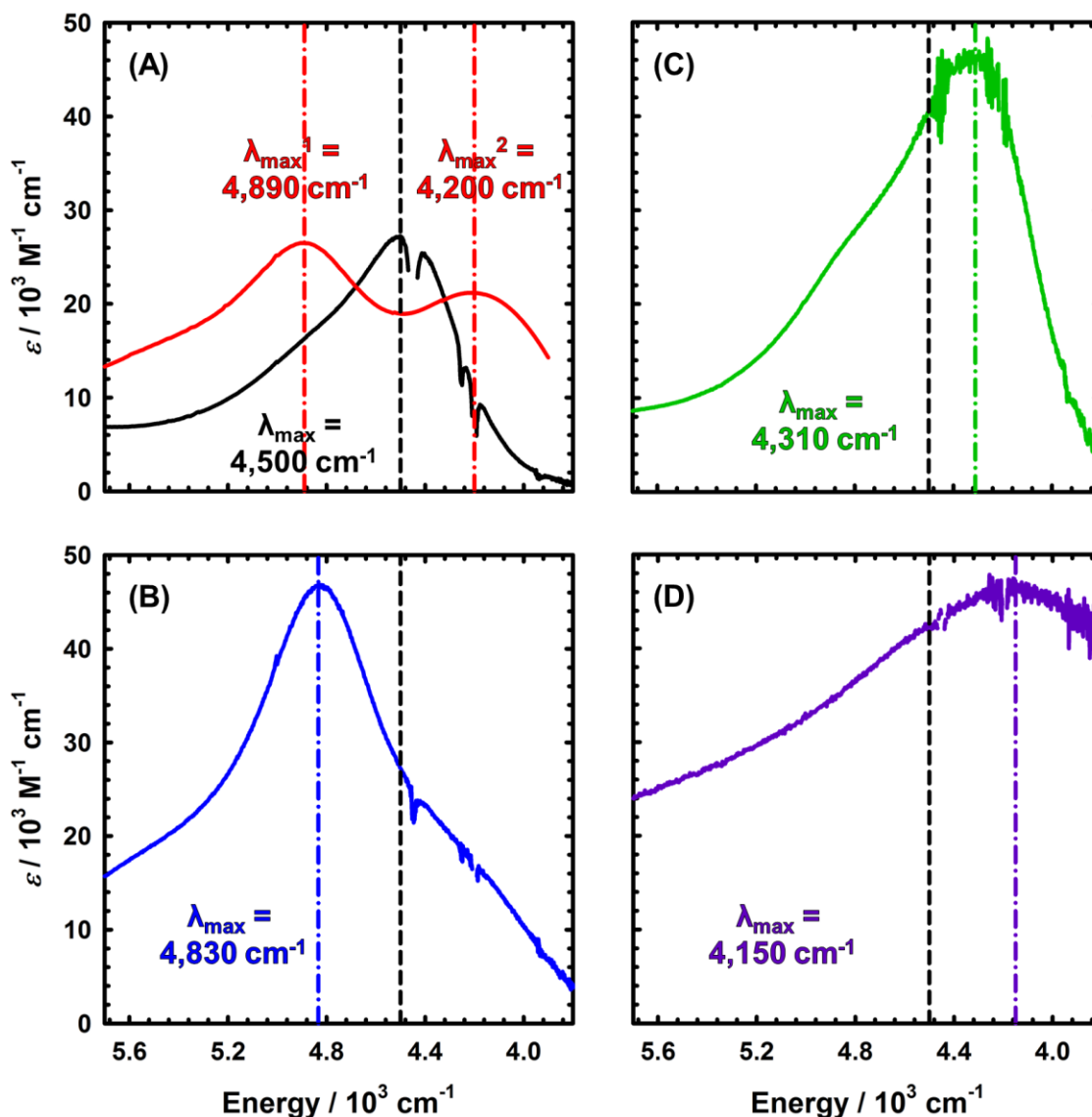


Figure 2.11. NIR region in the absorption spectra of $[1^{\bullet+}]$ and $[2-5^{\bullet\bullet}]^{2+}$. (A) Black line: $[1^{\bullet+}]$, red line: $[3^{\bullet\bullet}]^{2+}$; (B) $[2^{\bullet\bullet}]^{2+}$; (C) $[4^{\bullet\bullet}]^{2+}$; (D) $[5^{\bullet\bullet}]^{2+}$. The dashed black line represents λ_{max} for $[1^{\bullet+}]$. Coloured dashed lines represent λ_{max} for the respective bis-ligand radical complex.

Conditions: CH_2Cl_2 , 0.33 mM complex (A-C), 0.08 mM complex (D), $T = 195 \text{ K}$ (A-C), 298 K (D).

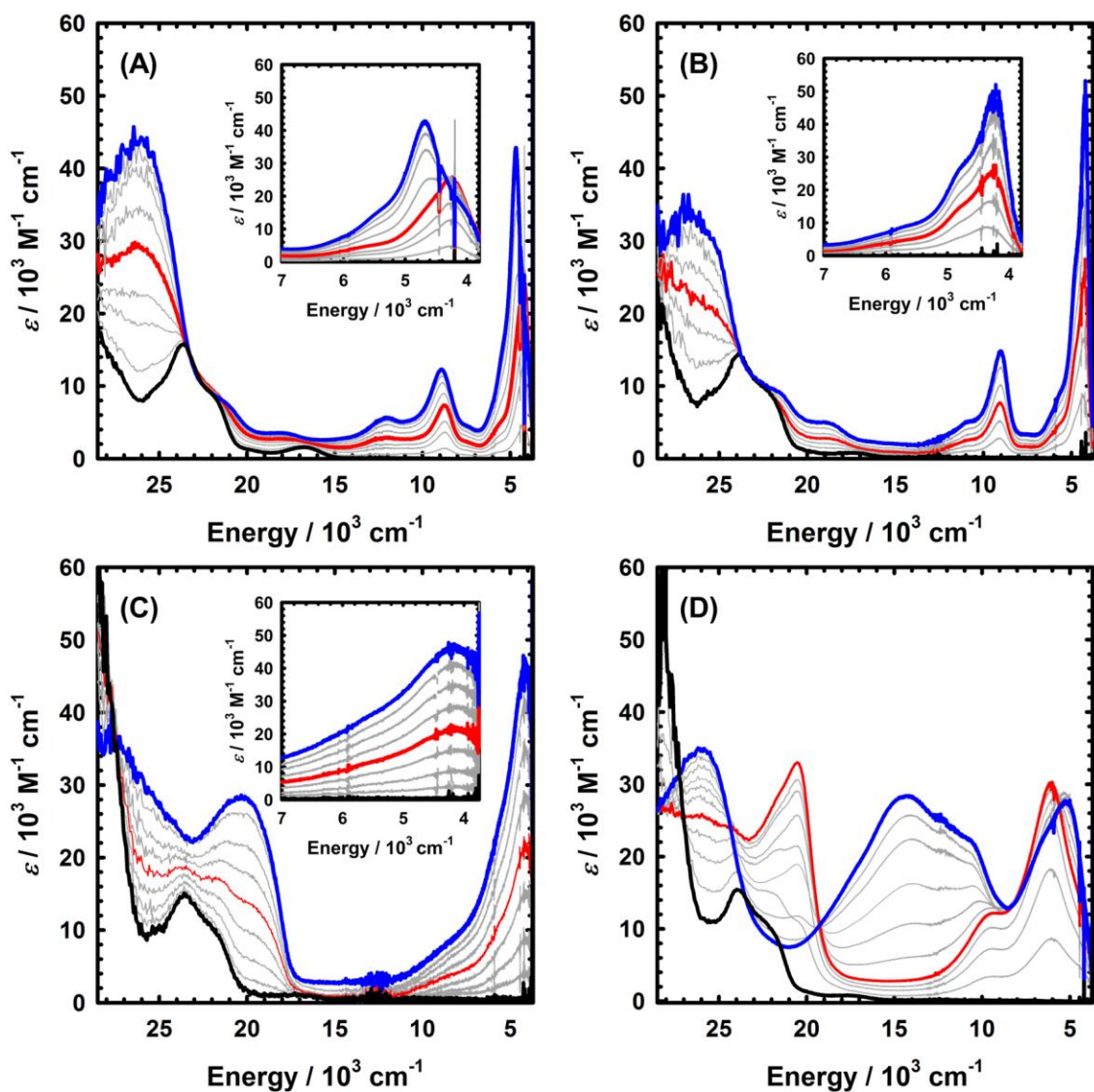


Figure 2.12. Full oxidation titration data for (A) **2** (black) to $[2^{\bullet\bullet}]^{2+}$ (blue), 0.33 mM; (B) **4** (black) to $[4^{\bullet\bullet}]^{2+}$ (blue), 0.33 mM; (C) **5** (black) to $[5^{\bullet\bullet}]^{2+}$ (blue), 298 K, 0.08 mM; (D) **5** to $[5^{\bullet\bullet}]^{2+}$, 195 K, 0.33 mM. Red lines represent the addition of one equivalent of oxidant. Intermediate grey lines measured during the oxidation titration with $[N(C_6H_3Br_2)_3][SbF_6]$.

Table 2.5. Spectroscopic properties of the Ni complexes in CH₂Cl₂ solution.^a

Complex ^b	λ_{\max} [cm ⁻¹] ($\epsilon \times 10^3$ [M ⁻¹ cm ⁻¹])
1^c	25,400 sh (4.7), 23,900 (8.2), 22,300 sh (5.3), 17,400 w (0.36)
[1^{•+}]^c	32,000 (100), 26,500 (14.6), 25,000 (10.6), 21,700 (7.1), 19,100 (4.1), 11,000 (3.0), 9,100 (9.2), 5,900 sh (7.1), 4,500 (27.7)
2	23,800 (15.6), 21,800 sh (8.6), 16,700 w (1.7)
[2^{•+}]²⁺	21,000 sh (7.2), 17,800 (3.4), 12,100 (5.8), 8,970 (12.3), 4,830 (42.9)
3^c	23,800 (13.4), 22,300 sh (9.1), 17,400 w (0.42)
[3^{•+}]²⁺ c	32,000 (100), 26,500 (19.7), 25,000 (16.4), 21,700 (9.9), 19,100 (4.8), 9,260 (10.4), 4,890 (26.5), 4,200 (21.1)
4	23,500 (14.5), 21,850 sh (8.8), 17,500 w (0.8)
[4^{•+}]²⁺	21,500 (9.5), 18,500 (4.4), 9,100 (14.0), 5,850 sh (8.2), 4,850 sh (26.1), 4,310 (46.1)
5	23,500 (14.4), 21,600 sh (9.2), 17,400 w (1.1)
[5^{•+}]²⁺	20,200 (28.6), 8,700 sh (8.0), 5,400 sh (27), 4,150 (46.6)

^aNIR transitions in bold. ^bConditions: 0.33 mM (1-4), 0.08 mM (5), CH₂Cl₂, 198 K (1-4), 298 K (5); sh = shoulder, w = weak. ^c[215].

2.2.6. Theoretical Calculations

Geometry optimization for both triplet ($S = 1$) and broken symmetry (BS, $S = 0$) electronic structures for **[2^{•+}]²⁺**, **[4^{•+}]²⁺**, and **[5^{•+}]²⁺** show a pronounced coordination sphere contraction when compared to the neutral analogues (Table 2.2), matching the predicted coordination sphere changes for **[1^{•+}]** and **[3^{•+}]²⁺**.²¹⁶ The two spin states are nearly isoenergetic for both **[4^{•+}]²⁺** (BS lower in energy by 0.2 kcal mol⁻¹) and **[5^{•+}]²⁺** (triplet lower in energy by 0.05 kcal mol⁻¹). Interestingly, the BS solution for **[2^{•+}]²⁺** is 2.8 kcal mol⁻¹ lower in energy in comparison to the triplet solution, thus predicting the most significant spin-interaction for this species. In all cases, the spin density plots show that the radicals are delocalized across the salen moieties, with minimal spin density on the bridging unit (Figure 2.13 and Appendix A – Figure A15).

Time-dependent DFT (TD-DFT) calculations on both triplet and BS solutions for the bis-ligand radical species were employed to gain insight into the donor and acceptor orbitals, and energy shifts associated with the experimentally observed NIR features. The TD-DFT results are similar for both electronic structures, predicting low energy transitions with an intensity pattern in line with the exciton model (Table 2.6). For the triplet calculations, extensive mixing of the donor and acceptor orbitals results in orbitals delocalized over both salen units. For the BS calculations, the donor and acceptor orbitals are confined to the individual salen units and match the orbitals associated with the predicted low energy transition for the monomer **[1^{•+}]**.²¹⁶ The predicted low energy bands from the BS TD-DFT calculations are symmetric and antisymmetric linear combinations of

the α HOMO \rightarrow α LUMO and β HOMO \rightarrow β LUMO local transitions on the individual salen radicals, providing further evidence of excited state mixing of the salen chromophores in the doubly oxidized dimers (Figure 2.14).

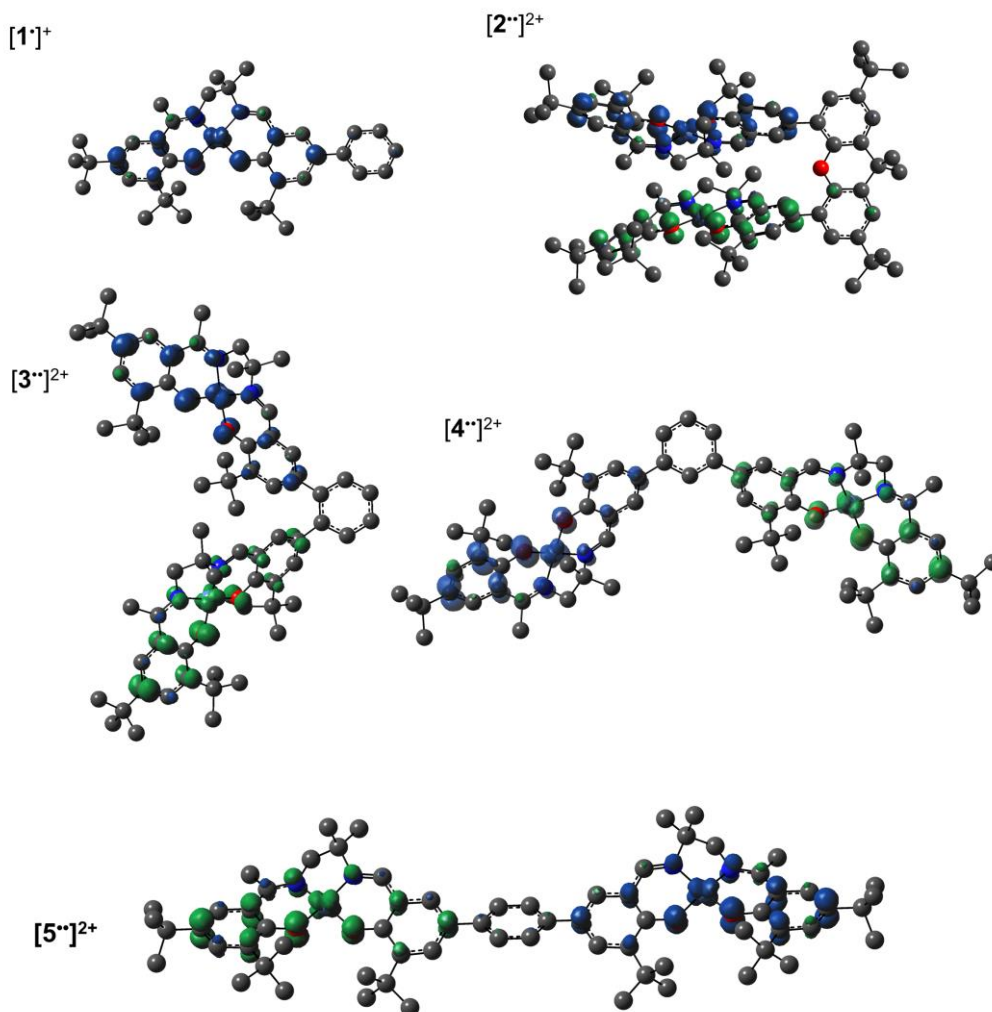


Figure 2.13. Spin density plots for $[1\bullet]^+$ and the broken symmetry ($S = 0$) solution for $[2\bullet\bullet]^{2+}$. See the experimental section for calculation details.

Table 2.6. TD-DFT predicted energies and oscillator strengths for the broken symmetry ($S = 0$) solution for the doubly oxidized dimers.^{a,b,c}

	Low Energy Band		High Energy Band	
	Energy (cm ⁻¹)	Oscillator Strength (<i>f</i>)	Energy (cm ⁻¹)	Oscillator Strength (<i>f</i>)
$[2\bullet\bullet]^{2+}$	3,590	0.055	4,995	0.406
$[3\bullet\bullet]^{2+}$	4,708	0.270	5,675	0.196
$[4\bullet\bullet]^{2+}$	4,935	0.395	5,570	0.092
$[5\bullet\bullet]^{2+}$	4,390	0.744	5,495	0.002

^aSee the experimental section for calculation details. ^bThe TD-DFT predicted NIR band for $[1\bullet]^+$ is at $\lambda_{\max} = 5,260$ cm⁻¹, $f = 0.2450$. ^cThe predicted band energies for the triplet ($S = 1$) solutions match the BS ($S = 0$) results.

For the co-facial orientation in $[2^{**}]^{2+}$ ($S = 0$), the high energy band is predicted to have significantly increased oscillator strength in comparison to the low energy band ($f = 0.406$ vs. $f = 0.055$, see Table 2.6), in accordance with the experimental results and the exciton coupling model. We had previously hypothesized that the NIR band splitting in $[3^{**}]^{2+}$ was a result of exciton coupling of the radical salen units in an oblique geometry,²¹⁶ and the data presented herein for the full series of dimers provides confirmation of this interpretation. The increased inter-chromophore angle in $[4^{**}]^{2+}$ relative to $[3^{**}]^{2+}$, results in the low energy band exhibiting significantly greater intensity in comparison to the high energy band (Figure 2.11), and this is correctly predicted by the TD-DFT calculations ($f = 0.395$ vs. $f = 0.092$, see Table 2.6). Finally, for the parallel orientation in $[5^{**}]^{2+}$, only the low energy band is predicted to exhibit significant intensity (Table 2.6), reflecting the limited capacity of the forbidden transition to gain intensity via symmetry perturbations in this chromophore geometry.²⁹⁸

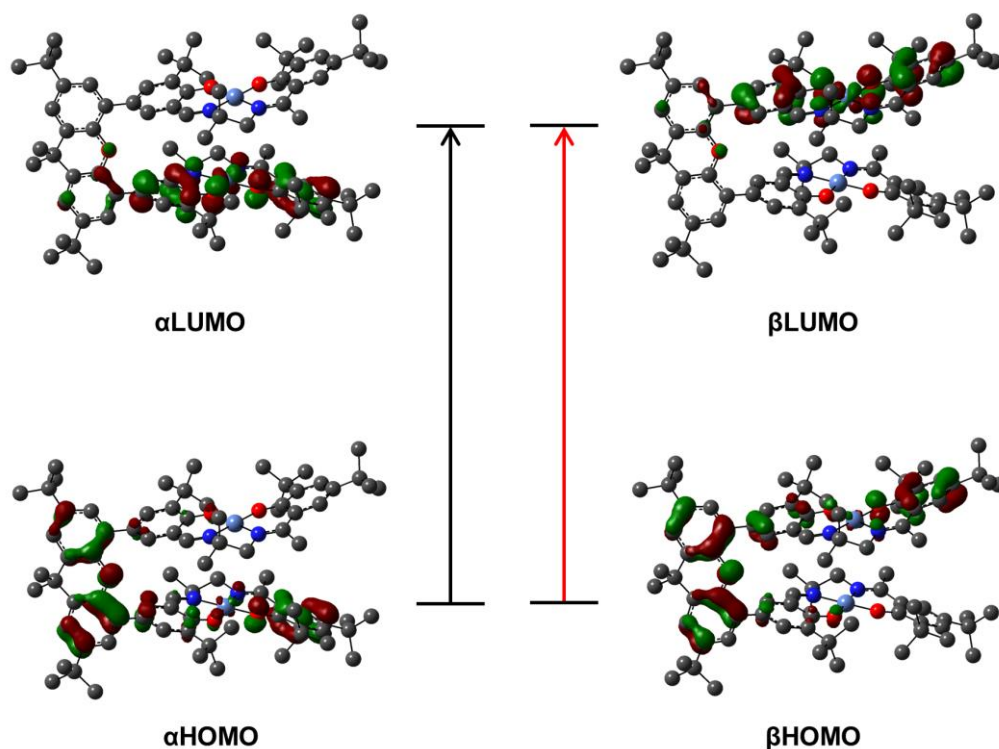


Figure 2.14. Kohn-Sham molecular orbitals for the broken symmetry ($S = 0$) of $[2^{**}]^{2+}$ associated with the calculated NIR transitions at $4,995$ and $3,590$ cm^{-1} . The predicted low energy bands are symmetric and antisymmetric linear combinations of the $\alpha\text{HOMO} \rightarrow \alpha\text{LUMO}$ (black arrow), and $\beta\text{HOMO} \rightarrow \beta\text{LUMO}$ (red arrow) local transitions on the individual salen radicals.

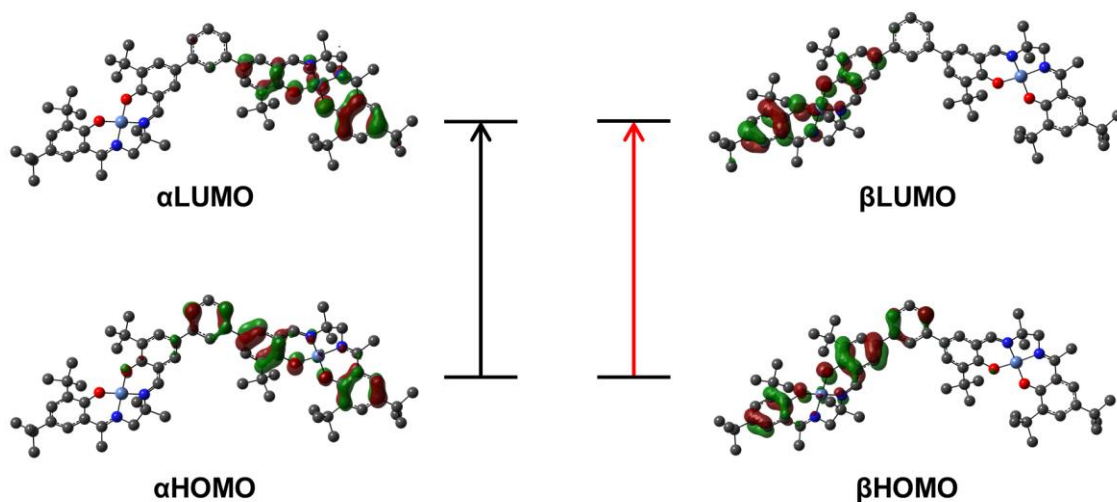


Figure 2.15. Kohn-Sham molecular orbitals for the broken symmetry ($S = 0$) solution of $[4^{**}]^{2+}$ associated with the calculated NIR transitions at 5,570 and 4,935 cm^{-1} (black and red arrows; $\alpha/\beta\text{HOMO} \rightarrow \alpha/\beta\text{LUMO}$). Predicted transitions are a result of symmetric and asymmetric linear combinations of the orbitals shown.

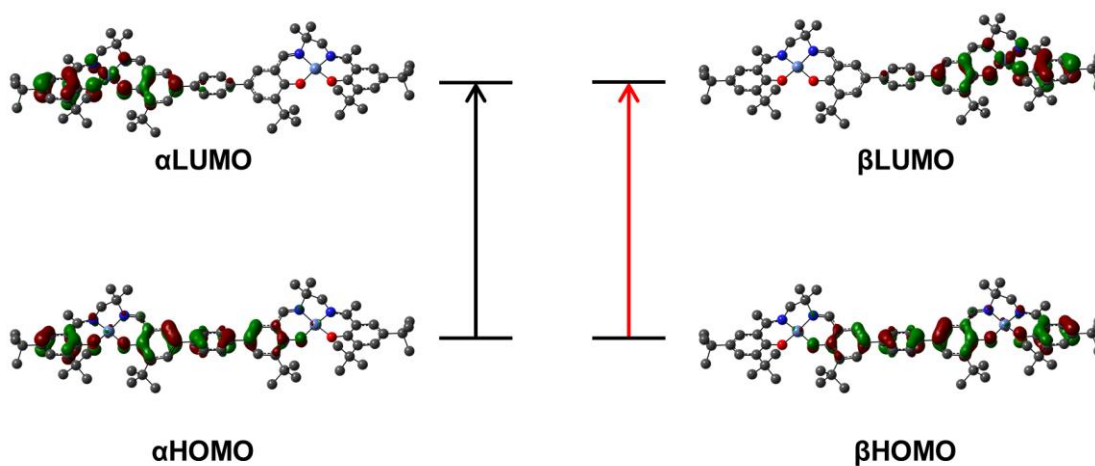


Figure 2.16. Kohn-Sham molecular orbitals for the broken symmetry ($S = 0$) solution of $[5^{**}]^{2+}$ associated with the calculated NIR transitions at 5,495 and 4,390 cm^{-1} (black and red arrows; $\alpha/\beta\text{HOMO} \rightarrow \alpha/\beta\text{LUMO}$). Predicted transitions are a result of symmetric and asymmetric linear combinations of the orbitals shown.

2.3. Discussion and Summary

Investigation of the influence of inter-chromophore distance and relative geometry on photophysical properties in discrete dimers provides a mechanism to understand the absorption and emission properties in aggregated systems.³⁰⁰⁻³⁰³ In this context, a series of bimetallic Ni(Sal) complexes were prepared and studied (**2-5**), in which the relative geometry of the salen units has been systematically varied from coplanar to parallel. All complexes are easily oxidized to the corresponding bis-ligand radical species, in which the ligand radicals are confined to the individual salen units. The xanthene spacer of **2** has previously been employed in photophysical studies of chromophore interactions,²⁸⁴⁻²⁸⁵ and the close Ni--Ni distance of 3.98 Å is within a range for the observation of strong interactions via direct wave-function overlap.²⁵⁸ Interestingly, a weak spin-spin interaction of the ligand radical units in [**2**^{••}]²⁺ is observed via X- and Q-band EPR spectroscopy, and this is further corroborated by DFT calculations. EPR simulation of the oblique dimer [**3**^{••}]²⁺ as a triplet affords very small ZFS parameters, demonstrating that a non-interacting diradical description is appropriate for this derivative.^{291, 297} Most interestingly, for the doubly oxidized species, significant shifts in the IVCT bands in the NIR are observed, matching that predicted by the exciton model. This study shows, for the first time, the applicability of the exciton model to bis-ligand radical systems absorbing in the NIR, and demonstrates the ability to tune the energy of absorption by nearly 400 nm in this low energy region. We plan to further study the interesting aggregation process and associated photophysical properties of the *para* dimer [**5**^{••}]²⁺, which under the current conditions is irreversible.

2.4. Experimental

2.4.1. Materials

All chemicals used were of the highest grade available and were purified whenever necessary. Literature methods were followed in order to prepare 5,5'-(2,7-di-*tert*-butyl-9,9-dimethyl-9*H*-xanthene-4,5-diyl)bis(3-(*tert*-butyl)-2-hydroxybenzaldehyde) (**6**),³⁰⁴ (*E*)-2-(1((2-amino-2-methylpropyl)imino)ethyl)-4,6-di-*tert*-butylphenol (**7**),²¹⁴ and 5,5''-di-*tert*-butyl-4,4''-dihydroxy-[1,1':4'1''-terphenyl]-3,3''-dicarbaldehyde (**12**).³⁰⁵ The tris(2,4-dibromophenyl) aminium hexafluoroantimonate radical chemical oxidant [N(C₆H₃Br₂)₃][SbF₆] ($E_{1/2} = 1.14$ V vs. Fc⁺/Fc, MeCN)¹⁰⁷ was synthesized according to

published protocols.³⁰⁶ Electronic spectra were recorded on a Cary 5000 spectrophotometer with variable pathlength (1 and 10 mm, Hellma, Inc.). Constant temperatures were maintained by a dry ice/acetone bath. Cyclic voltammetry (CV) was performed on a PAR-263A potentiometer, equipped with a Ag wire reference electrode, a Pt disk working electrode, and a Pt counter electrode with ⁿBu₄NClO₄ (0.1 M) solution in CH₂Cl₂. Decamethylferrocene was used as an internal standard.³⁰⁷ ¹H NMR spectra were recorded on a Bruker AV-400 instrument. Mass spectra (positive ion) were obtained on a Bruker Microflex LT MALDI-TOF MS instrument. Elemental analyses (C, H, N) were performed by Mr. Paul Mulyk at Simon Fraser University on a Carlo Erba EA1110 CHN elemental analyzer. Electron paramagnet resonance (EPR) spectra were collected using a Bruker EMXplus spectrometer with a premiumX X-band microwave bridge and a dual mode resonator connected to an Oxford Instruments He flow cryostat. Samples for X-band EPR measurements were placed in 4 mm outer diameter tubes with sample volumes of ~250 μ L. For the Q-band measurements, the same apparatus was used; with a 33.9 GHz microwave bridge and a qwt resonator. EPR spectra were simulated using the EasySpin package in MATLAB.³⁰⁸

2.4.2. X-ray Structure Determination

All crystal structure plots were produced using ORTEP-3³⁰⁹ and rendered with POV-Ray (v.3.6.2).³¹⁰ A summary of the crystal data and experimental parameters for structure determinations is given in Table 2.1.

2.4.2.1. X-ray Structure Determination of **2**

Single crystal X-ray crystallographic analysis of **2** was performed at 150 K on a D8 goniostat equipped with a Bruker PHOTON100 CMOS detector at Beamline 11.3.1 at the Advanced Light Source (Lawrence Berkeley National Laboratory) using synchrotron radiation tuned to $\lambda = 0.7749 \text{ \AA}$. For data collection, frames were measured for a duration of 2 s at 0.5° intervals of ω . The data frames were collected using the program APEX2 and processed using the program SAINT routine within APEX2. The data were corrected for absorption and beam corrections based on the multiscan technique as implemented in SADABS. The structure was solved using the intrinsic phasing method³¹¹ and refined with ShelXL within ShelXle.³¹² The structure contained heavily disordered solvent that could not be successfully modelled, thus, the PLATON/SQUEEZE³¹³ program was used to generate

a 'solvent-free' HKLF5 format data set. The equivalent of 4 molecules of hexane and 4 molecules of CH₂Cl₂ was removed from the unit cell. All non-hydrogen atoms were refined anisotropically. All C-H hydrogen atoms were placed in calculated positions but were not refined. CCDC number: 1579266.

2.4.2.2. X-ray Structure Determination of 4 and 5

Single crystal X-ray crystallographic analysis of **4** and **5** was performed on a Bruker SMART diffractometer equipped with an APEX II CCD detector and I μ SCuK α (λ = 1.54184 nm) microfocus sealed X-ray tube fitted with HELIOS multilayer optics. Crystals were mounted on a MiTeGen dual-thickness MicroMounts using parabar oil. The data was collected at room temperature (approximated to 296 K) (**5**) and 150(2) K (via an Oxford Cryosystems cold-stream) (**4**). Data was collected in a series of ϕ and ω scans with 1.00° image widths and 60 s exposures. The crystal-to-detector distance was 40 mm. Data was processed using the Bruker APEX II software suite. Structures were solved using the intrinsic phasing method³¹¹ and refined with ShelXL within ShelXle.³¹² The structure of **5** contained heavily disordered solvent that could not be successfully modelled, thus, the PLATON/SQUEEZE³¹³ program was used to generate a 'solvent-free' HKLF5 format data set. The equivalent of 28 molecules of hexane was removed from the unit cell. All non-hydrogen atoms were refined anisotropically. All C-H hydrogen atoms were placed in calculated positions but were not refined. CCDC number: 1579267 (**4**), 1579268 (**5**).

2.4.3. Oxidation Protocol

Under an inert atmosphere at 195 K, 500 μ L of a CH₂Cl₂ solution of the metal complex (4.6 mM) was added to 3.0 mL of dry CH₂Cl₂. Monitored by UV-vis-NIR spectroscopy, a saturated solution of [N(C₆H₃Br₂)₃][SbF₆] in CH₂Cl₂ was added in 60 μ L aliquots resulting in clean conversion to the respective one- and two-electron oxidized species.

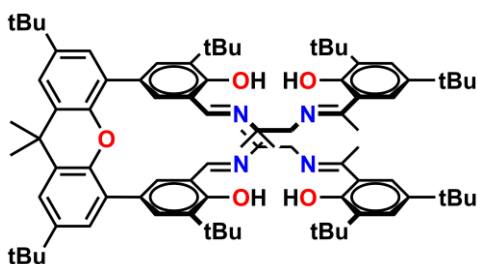
2.4.4. Theoretical Calculations

Geometry optimizations were performed using the Gaussian 09 program (Revision D.01),³¹⁴ the B3LYP functional,³¹⁵⁻³¹⁶ and 6-31G(d) basis set on all atoms as this functional/basis set combination has afforded a good match to experimental metrical parameters in similar salen systems.²¹⁴⁻²¹⁷ Frequency calculations at the same level of

theory confirmed that the optimized structures were located at a minimum on the potential energy surface. Single-point calculations for energetic analysis were performed using the B3LYP functional and the TZVP basis set of Ahlrichs on all atoms.³¹⁷⁻³¹⁸ The intensities of the 10 lowest energy electronic transitions were calculated by time-dependent density functional theory (TD-DFT)³¹⁹⁻³²⁰ at the B3LYP/TZVP level with a polarized continuum model (PCM) for CH₂Cl₂ (dielectric $\epsilon = 8.94$).³²¹⁻³²⁴

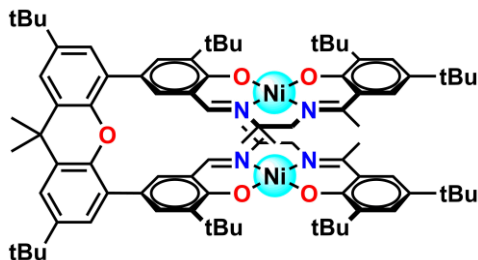
2.4.5. Synthesis

6-6'-((1*E*,1'*E*)-((((1*E*,1'*E*)-((2,7-di-*tert*-butyl-9,9-dimethyl-9*H*-xanthene-4,5-diyl)bis(5-(*tert*-butyl)-6-hydroxy-3,1-phenylene))bis(methaneylylidene))bis(azaneylylidene))bis(2-methylpropane-2,1-diyl))bis(azaneylylidene))bis(ethan-1-yl-1-ylidene))bis(2,4-di-*tert*-butylphenol) (**8**):



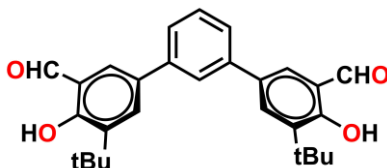
A 10 mL degassed dichloroethane solution of **6** (0.49 g, 0.73 mmol) was added to a refluxing 10 mL degassed dichloroethane solution of **7** (0.47 g, 1.5 mmol). The yellow mixture was refluxed for 24 hours, after which the mixture was cooled and the solvent was removed *in vacuo* until only 5 mL remained. Cold methanol was added to the mixture (20 mL) and a bright yellow precipitate formed which was collected via suction filtration and washed with cold methanol (3x5 mL) and pentane (3x5 mL). Yield: 0.48 g, 52%. MALDI-MS $m/z = 1275.51$ (100%). ¹H NMR (400 MHz, CDCl₃): $\delta = 8.12$ (s, 2H), 7.46 (d, $J = 2.3$ Hz, 2H), 7.41 (d, $J = 2.4$ Hz, 2H), 7.35 (m, 4H), 7.32 (d, $J = 2.2$ Hz, 2H), 7.17 (d, $J = 2.4$ Hz, 2H), 3.61 (s, 4H), 2.31 (s, 6H), 1.78 (s, 6H), 1.39 (s, 18H), 1.38 (s, 12H), 1.37 (s, 18H), 1.29 (s, 18H), 1.17 (s, 18H).

6-6'-((1*E*,1'*E*)-((((1*E*,1'*E*)-((2,7-di-*tert*-butyl-9,9-dimethyl-9*H*-xanthene-4,5-diyl)bis(5-(*tert*-butyl)-6-hydroxy-3,1-phenylene))bis(methaneylylidene))bis(azaneylylidene))bis(2-methylpropane-2,1-diyl))bis(azaneylylidene))bis(ethan-1-yl-1-ylidene))bis(2,4-di-*tert*-butylphenol)-di-nickel(II) (**2**):



To a solution of **8** (50 mg, 0.039 mmol) in 3 mL dry dimethylformamide (DMF) was added a 3 mL dry DMF Ni(OAc)₂•4H₂O solution (40 mg, 0.16 mmol). The mixture turned deep brown upon addition of the metal salt, and was stirred at reflux for 16 hours. The mixture was then cooled to room temperature and placed in an ice bath. The brown solid precipitate was collected via suction filtration. The crude material was recrystallized in CH₂Cl₂/hexanes (1:1) to obtain light brown crystals suitable for X-ray analysis. Yield: 45 mg, 82%. MALDI-MS *m/z* = 1389.51 (100%). ¹H NMR (400 MHz, CD₂Cl₂): δ = 7.52 (s, 2H), 7.51 (s, 2H), 7.35 (d, *J* = 2.4 Hz, 2H), 7.27 (d, *J* = 2.5 Hz, 2H), 7.24 (d, *J* = 2.4 Hz, 2H), 7.03 (d, *J* = 2.4 Hz, 2H), 6.89 (s, 2H), 1.71 (s, 6H), 1.61 (s, 6H), 1.50 (s, 4H), 1.44 (s, 18H), 1.42 (s, 18H), 1.40 (s, 12 H), 1.35 (s, 18H), 1.24 (s, 18H). Anal. Calcd. (%) for C₈₅H₁₁₄N₄O₅Ni₂: C 70.82, H 8.40, N, 3.59; Found: C 70.77, H 8.56, N 3.71.

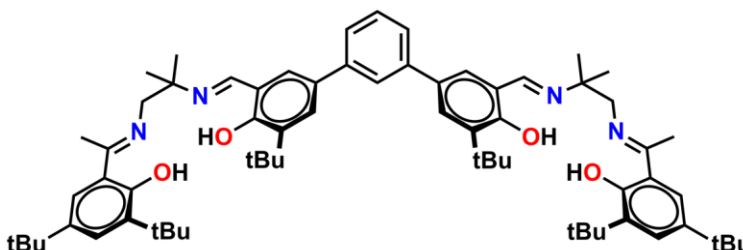
5,5''-di-*tert*-butyl-4,4''-dihydroxy-[1,1':3',1''-terphenyl]-3,3''-dicarbaldehyde (**10**):



A 2-neck flask was charged with 2-hydroxy-3-*tert*-butyl-5-'Bpin'-benzaldehyde (**9**) (500 mg, 1.63 mmol), K₂CO₃ (215 mg, 1.56 mmol), and Pd(PPh₃)₄ (55 mg, 0.048 mmol) and subjected to three evacuation/refill cycles. 10 mL of degassed DME/H₂O (5:1) was added to the solids. 1,3-dibromobenzene (93 μL, 0.78 mmol) was added and the mixture was heated at reflux for 24 hours, after which the mixture was allowed to cool to room temperature. The mixture was extracted with CH₂Cl₂ (3x20 mL). The solvent was removed *in vacuo* and the crude material was purified via flash column chromatography (2.5% EtOAc in hexanes) to afford the title compound as a yellow solid. Yield: 78 mg, 53%. MALDI-MS *m/z* = 430.92 (100%). ¹H NMR (400 MHz, CDCl₃): δ = 11.83 (s, 2H), 9.99 (s, 2H), 7.80 (d, *J* = 2.3 Hz, 2H), 7.70-7.66 (m, 1H), 7.65 (d, *J* = 2.3 Hz, 2H), 7.55-7.53 (m,

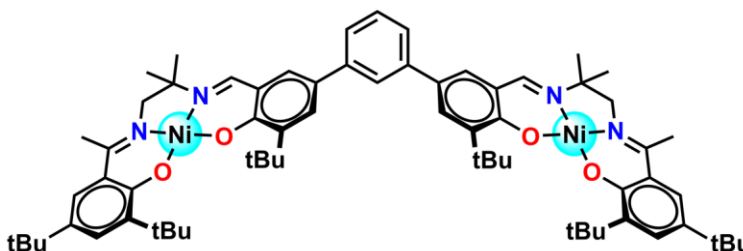
3H), 1.49 (s, 18H). Anal. Calcd. (%) for $C_{28}H_{30}O_4$: C 78.11, H 7.02; Found (%): C 78.31, H 7.18.

3,3''-di-*tert*-butyl-5,5''-bis((*E*-((1-(((*E*-1-(3,5-di-*tert*-butyl-2-hydroxyphenyl)ethylidene)amino)-2-methylpropan-2-yl)imino)methyl)-[1,1':3',1''-terphenyl]-4,4''-diol (**11**):



To a stirring solution of **10** (140 mg, 0.33 mmol) in THF (40 mL) was added **7** (217 mg, 0.68 mmol). The mixture was heated at reflux for 24 hours, after which it was cooled to room temperature. The solvent was removed *in vacuo* and the crude material was recrystallized in hot MeOH. Yield: 250 mg, 75%. MALDI-MS m/z : 1031.95 (100%). 1H NMR (500 MHz, $CDCl_3$): δ = 8.55 (s, 2H), 7.66 (d, J = 2.1 Hz, 1H), 7.58 (d, J = 2.3 Hz, 2H), 7.45 (d, J = 1.3 Hz, 3H), 7.42 (d, J = 2.2 Hz, 2H), 7.38 (d, J = 2.4 Hz, 2H), 7.35 (d, J = 2.4 Hz, 2H), 3.71 (s, 4H), 2.36 (s, 6H), 1.52 (s, 12H), 1.48 (s, 18H), 1.38 (s, 18H), 1.29 (s, 18H). Anal. Calcd. (%) for $C_{68}H_{94}N_4O_4$: C 79.18, H 9.19, N 5.43; Found (%): C 79.31, H 9.28, N 5.20.

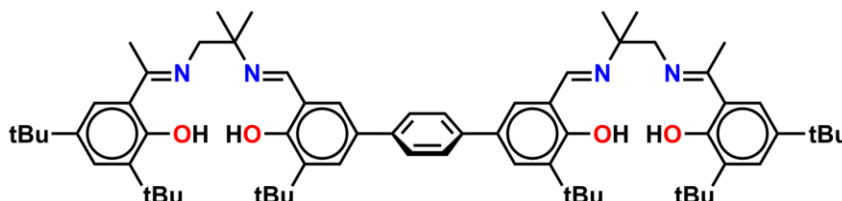
3,3''-di-*tert*-butyl-5,5''-bis((*E*-((1-(((*E*-1-(3,5-di-*tert*-butyl-2-hydroxyphenyl)ethylidene)amino)-2-methylpropan-2-yl)imino)methyl)-[1,1':3',1''-terphenyl]-4,4''-diol-di-nickel(II) (**4**):



To a stirring solution of **11** (50 mg, 0.05 mmol) in DMF (5 mL) was added $Ni(OAc)_2 \cdot 4H_2O$ (48 mg, 0.2 mmol) in DMF (5 mL). The mixture was heated at reflux for 5 hours, after which it was cooled to room temperature and the dark brown precipitate collected via suction filtration. The solid material was washed with H_2O (3x5 mL) and

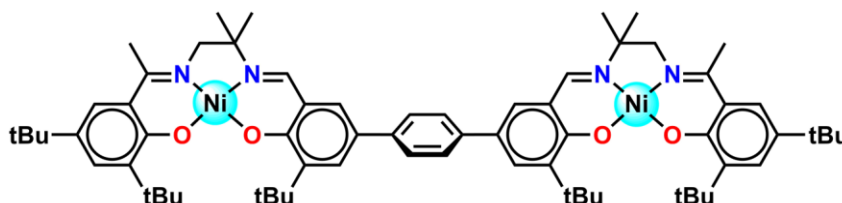
recrystallized in CH₂Cl₂/MeCN at -40°C to yield brown crystals suitable for X-ray analysis. Yield: 51 mg, 91%. MALDI-MS *m/z* = 1143.19 (100%). ¹H NMR (500 MHz, CDCl₃): δ = 7.60 (s, 1H), 7.53 (d, *J* = 2.5 Hz, 2H), 7.45 (s, 2H), 7.34 (m, 3H), 7.30 (d, *J* = 2.5 Hz, 2H), 7.21 (d, *J* = 2.4 Hz, 2H), 7.19 (d, *J* = 2.5 Hz, 2H), 3.23 (s, 4H), 2.34 (s, 6H), 1.46 (s, 12H), 1.45 (s, 18H), 1.43 (s, 18H), 1.29 (s, 18H). Anal. Cald. (%) for C₆₈H₉₀N₄O₄Ni₂: C 71.34, H 7.92, N 4.89; Found (%): C 71.60, H 8.11, N 4.58.

3,3'-di-*tert*-butyl-5,5'-bis((*E*)-((1-(((*E*)-1-(3,5-di-*tert*-butyl-2-hydroxyphenyl)ethylidene)amino)-2-methylpropan-2-yl)imino)methyl)-[1,1':4'1''-terphenyl]-4,4''-diol (**13**):



To a stirring solution of **12** (100 mg, 0.23 mmol) in THF (40 mL) was added **7** (150 mg, 0.49 mmol). The mixture was heated at reflux for 24 hours, after which it was cooled to room temperature. The solvent was removed *in vacuo* and the crude material was recrystallized in hot MeOH. Yield: 210 mg, 87%. MALDI-MS *m/z*: 1031.31 (100%). ¹H NMR (500 MHz, CDCl₃): δ = 8.56 (s, 2H), 7.58 (m, 6H), 7.43 (d, *J* = 2.3 Hz, 2H), 7.39-7.35 (m, 4H), 3.72 (s, 4H), 2.37 (s, 6H), 1.53 (s, 12H), 1.49 (s, 18H), 1.42 (s, 18H), 1.29 (s, 18H). Anal. Cald. (%) for C₆₈H₉₄N₄O₄: C 79.18, H 9.19, N 5.20; Found (%): C 79.40, H 9.33, N 4.96.

3,3'-di-*tert*-butyl-5,5'-bis((*E*)-((1-(((*E*)-1-(3,5-di-*tert*-butyl-2-hydroxyphenyl)ethylidene)amino)-2-methylpropan-2-yl)imino)methyl)-[1,1':4'1''-terphenyl]-4,4''-diol-di-nickel(II) (**5**):



To a stirring solution of **13** (50 mg, 0.05 mmol) in DMF (5 mL) was added Ni(OAc)₂•4H₂O (48 mg, 0.2 mmol) in DMF (5 mL). The mixture was heated at reflux for 5 hours, after which it was cooled to room temperature. The brown precipitate was collected

via suction filtration and washed with cold H₂O (3x5 mL). X-ray quality crystals were grown from concentrated pyridine solutions. Yield: 50 mg, 88%. MALDI-MS m/z = 1144.31 (100%). ¹H NMR (400 MHz, CDCl₃): δ = 7.68 (s, 4H), 7.60 (d, J = 2.5 Hz, 2H), 7.37 (s, 2H), 7.31 (d, J = 2.3 Hz, 2H), 7.29 (d, J = 2.4 Hz, 2H), 7.09 (d, J = 2.4 Hz, 2H), 3.50 (s, 4H), 2.07 (s, 6H), 1.46 (s, 18H), 1.45 (s, 18H), 1.39 (s, 12H), 1.26 (s, 18H). Anal. Calcd. (%) for C₆₈H₉₀N₄O₄Ni₂: C 71.34, H 7.92, N 4.89; Found (%): C 71.55, H 8.09, N 4.71.

Chapter 3. Electronic Structure Description of a Doubly Oxidized Bimetallic Cobalt Complex with a Proradical Ligand

Adapted from: Clarke, R.M.; Hazin, K.; Thompson, J.R.; Savard, D.; Prosser, K.E.; and Storr, T. *Inorg. Chem.*, **2016**, *55*, 762-774.

RMC and KH performed the synthesis. RMC carried out the chemical oxidation, solution magnetic susceptibility, electrochemistry, UV-Vis-NIR, EPR analysis and theoretical calculations. JRT performed the crystallography. DS collected and interpreted the solid-state magnetics data. KEP collected the EPR data.

3.1. Introduction

50 years ago Balch and Holm reported that reaction of *o*-phenylenediamine with $\text{CoCl}_2 \cdot 6\text{H}_2\text{O}$ in aqueous ammonia in the presence of air affords a violet precipitate of the formula $\text{Co}(\text{C}_6\text{H}_4(\text{NH})_2)_2$.³²⁵ The X-ray structure was subsequently solved 20 years later in 1985 by Peng and co-workers,³²⁶ although there remains persistent debate over the ground state electronic structure as the spectroscopic oxidation state describing a d^6 Co(III) or a d^7 Co(II) electron configuration cannot be unambiguously defined (Figure 3.1).³²⁷

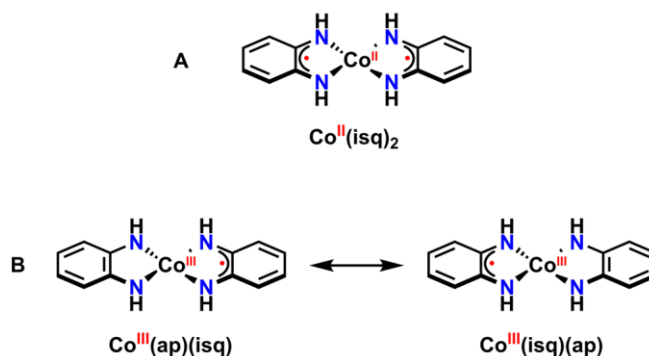


Figure 3.1. Possible electronic structures for $\text{Co}(\text{C}_6\text{H}_4(\text{NH})_2)_2$.

In the ensuing years, Co complexes involving pro-radical ligands have been investigated extensively due to the interesting electronic structures of both neutral and oxidized species. Examples include work by Benisvy and co-workers in which they demonstrate the first example of a phenoxy radical ligand involved in a tetracoordinated

Co(II) complex *via* ligand-based oxidation of one imidazole-phenolate ligand.³²⁸ Both tetracoordinated Co(II) and square pyramidal Co(III) complexes with radical *o*-iminobenzosemiquinonate-type ligands have been prepared,^{327, 329-330} as well as complexes with dithiosemiquinato and *o*-diiminobenzosemiquinato radical ligands (Figure 3.2).^{266, 331-334}

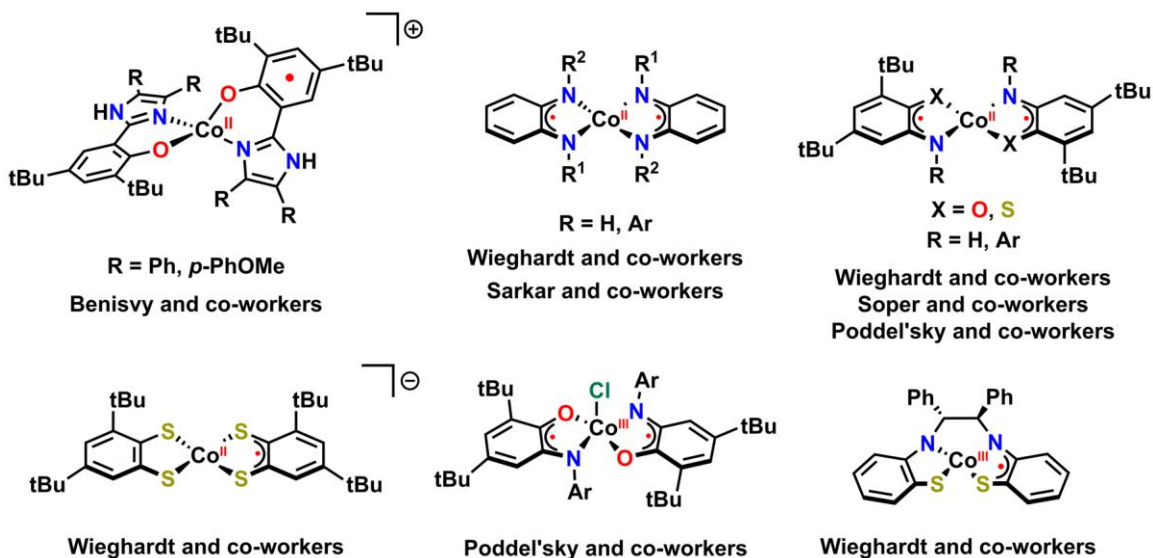
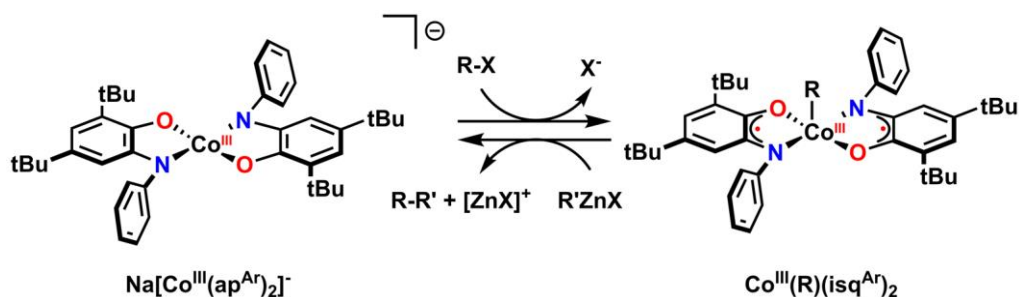


Figure 3.2. Selected examples of Co(II) and Co(III) complexes with pro-radical ligands. Only resonance forms with radical character are shown.

Elegant work by Soper and co-workers demonstrated the utility of *o*-amidophenolate ligands in the mediation of oxidative addition and reductive elimination reactions at Co(III) in a well-defined cycle for Negishi-like cross-coupling of alkyl halides with organozinc reagents (Scheme 3.1).³³⁵⁻³³⁶ Both oxidative addition and reductive elimination steps require a formal 2 electron oxidation/reduction of the metal centre, however in this case, the oxidizing and reducing equivalents come from the *o*-amidophenolate ligands as they shuttle between *o*-amidophenolate (ap) and *o*-iminosemiquinone (isq) oxidation states.

Scheme 3.1. Redox-active ligand-mediated oxidative addition and reductive elimination reactions at Co(III) investigated by Soper and co-workers.



Co(Sal) complexes find broad utility in a variety of catalytic transformations, including the ring opening of epoxides developed by Jacobsen,³³⁷⁻³⁴⁰ and the oxidation of alcohols.³⁴¹⁻³⁴³ As with many other examples of metallosalen catalysis (see Chapter 1, Section 1.4.1), a number of groups have investigated the activity of bimetallic Co(Sal) complexes in comparison to monomeric analogues. Coates and co-workers have developed covalently linked bimetallic systems for the synthesis of highly isotactic polyethers from meso-epoxides in which the selectivity is determined by the helicity of the binaphthol bond. Racemic catalyst mixtures are able to selectively polymerize each enantiomer to produce highly isotactic polyethers in >99% yield (Figure 3.3).^{179, 344-346} Lu and co-workers have employed similar bimetallic catalysts for the copolymerization of CO₂ with meso-epoxides,³⁴⁷⁻³⁴⁸ while Kleij and co-workers have developed rigid and flexible spacers for the construction of 'strapped' bimetallic cobalt complexes for the asymmetric ring opening (ARO) of epoxides (Figure 3.3).³⁴⁹ In addition to covalent linkage of salen complexes, Hong and co-workers reported bimetallic Co(Sal) complexes linked via hydrogen bonds for the asymmetric nitro-aldol (Henry) reaction between aryl aldehydes and nitromethane (Figure 3.3).¹⁷⁴ Low yields and enantioselectivities were observed when using monomeric analogues incapable of self-assembly. Modification of the hydrogen-bonding motifs to urea functionalities on both sides of the cobalt complexes led to drastically improved yields and enantioselectivities with a broader substrate scope.³⁵⁰ Furthermore, the second generation self-assembled catalyst was also employed in the HKR of terminal epoxides with excellent results. With catalyst loadings as low as 0.03 mol%, enantioselectivities of 99% were reported under solvent-free conditions after 8-14 hours.³⁵¹

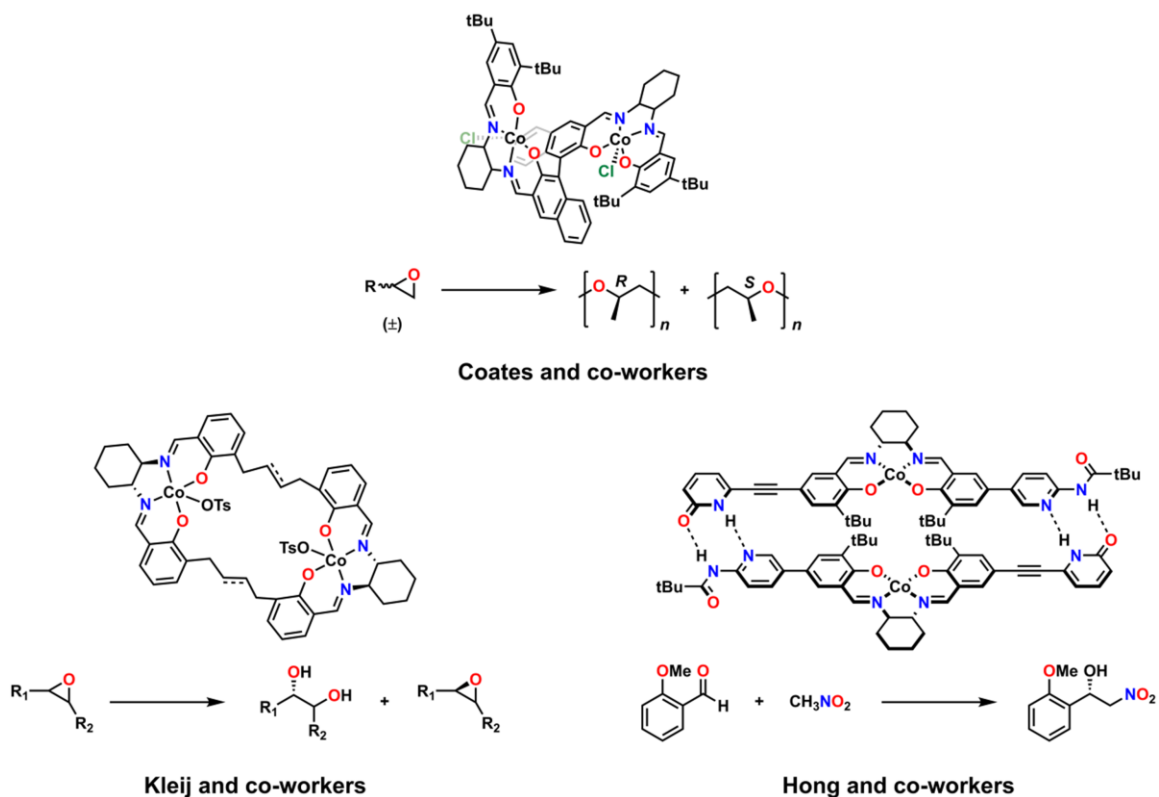


Figure 3.3. Select examples of bimetallic Co(Sal) complexes investigated by Coates and co-workers,¹⁷⁹ Kleij and co-workers,³⁴⁹ and Hong and co-workers¹⁷⁴ for epoxide polymerizations, ARO of epoxides, and nitro-aldol reactions, respectively.

Although studied extensively in the context of catalysis, the ligand radical chemistry of multimetallic salen complexes has received comparatively little attention. We have previously studied the geometric and electronic structures of a monometallic Ni(Sal) complex and its bimetallic analogue (See Chapter 2, Figure 3.4).²¹⁶ Upon oxidation with a suitable chemical oxidant, the bimetallic Ni(Sal) complex can be oxidized to a bis-ligand radical species. In this chapter, this work is extended to the analogous Co complexes as a means to study the interplay between pro-radical salen ligands and more easily oxidizable metal centres. The structure of the bimetallic Co complex bears resemblance to the cofacial porphyrins studied by Collman and co-workers,¹⁵³ Nocera and co-workers,¹⁶⁰⁻¹⁶¹ and the Co calixpyrroles studied by Love and co-workers^{163-165, 352} for dioxygen reduction (Figure 1.15). In this work, through extensive experimental and theoretical characterization techniques, we show that upon one- and two-electron oxidation, respectively, monometallic and bimetallic Co(Sal) complexes form species with ligand radical character. However, significant metal contribution to the singly occupied molecular orbitals (SOMOs) results in a less delocalized electronic structure in comparison

to the Ni analogues, resulting in a much broader low-energy absorption band in the vis-NIR spectrum lacking observable splitting due to exciton coupling.

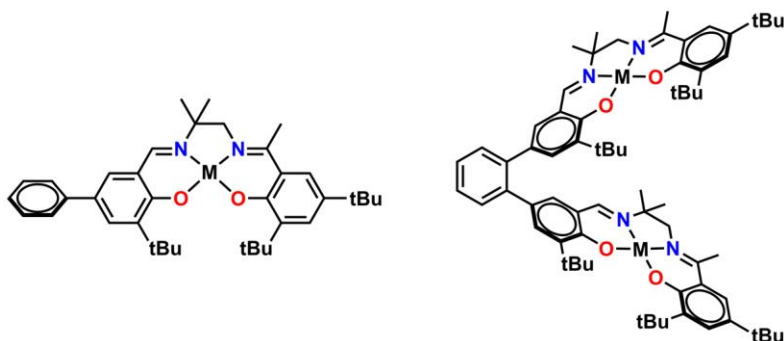


Figure 3.4. Monometallic and bimetallic salen complexes studied. M = Ni, previous work;²¹⁶ M = Co, this work.

3.2. Results

3.2.1. Synthesis and Solution-State Characterization

The complexes **CoL**¹ and **Co**₂**L**² were prepared in moderate yields by treating diethyl ether solutions of **H**₂**L**¹ and **H**₄**L**² with Co(OAc₂)•4H₂O dissolved in MeOH under anaerobic conditions. The asymmetric ligand **H**₂**L**¹ is used as it allows **CoL**¹ to more closely resemble a metal binding unit of **Co**₂**L**². The electronic difference between a phenyl substituent and a *tert*-butyl substituent are minor based on the Hammett parameters ($\sigma_p = -0.01$ vs -0.20)³⁵³ but will need to be considered when determining the locus of oxidation in this asymmetric system. Recrystallization of **CoL**¹ and **Co**₂**L**² afforded X-ray quality crystals (*vide infra*). Solution magnetic susceptibility measurements (¹H NMR Evans method¹¹²⁻¹¹³) revealed the presence of a low-spin, $S = \frac{1}{2}$ d⁷ Co(II) ground state for **CoL**¹ ($\mu_{\text{eff}} = 1.75 \mu_B$) and an $S = 1$ ground state for **Co**₂**L**² ($\mu_{\text{eff}} = 2.75 \mu_B$), originating from two independent $S = \frac{1}{2}$ d⁷ Co (II) centres (*vide infra*). Both complexes display paramagnetically shifted ¹H NMR spectra, with **CoL**¹ exhibiting two sets of discernible signals originating from the asymmetric salen ligand.²⁶⁰ Despite being less soluble, **Co**₂**L**² has a similar paramagnetically shifted ¹H NMR spectrum, albeit with only one set of resonances, likely due to fast rotation on the NMR time-scale about the 1,2-phenylene linker at room temperature. The solution structure of **Co**₂**L**² was further investigated by VT ¹H NMR spectroscopy, and while the results are not as definitive as similar data for the analogous Ni complex (**3** in Chapter 2),²¹⁶ splitting of the upfield resonance at -11 ppm (attributed to

the iminic proton) and increased signal broadening in the aromatic region suggests rotational restriction at low temperature (^1H NMR data can be found in Appendix B – Figures B1 – 3).

3.2.2. Solid-State Characterization of CoL^1 and Co_2L^2

The solid-state structures of CoL^1 and Co_2L^2 are presented in Figure 3.5 and Figure 3.6, respectively. Crystallographic data for both complexes can be found in Table 3.1. Both complexes exhibit slightly distorted square planar geometries with the expected N_2O_2 coordination sphere of the salen ligand. The slight distortion of the trigonal planar geometry is likely due to the sterically demanding *tert*-butyl groups in the *ortho* positions of the complexes. Co_2L^2 crystallizes with two molecules of Co_2L^2 in the asymmetric unit and an average intramolecular Co---Co distance of 10 Å. Furthermore, the bimetallic complex exists in a *cis* conformation in the solid-state, with the bulky *tert*-butyl groups on the same side of the molecule, in agreement with the analogous Ni complex.²¹⁶ This is in contrast however, to the Cu complex of H_4L^2 in which the *tert*-butyl groups are aligned on opposing sides of the complex in the solid-state.³⁵⁴

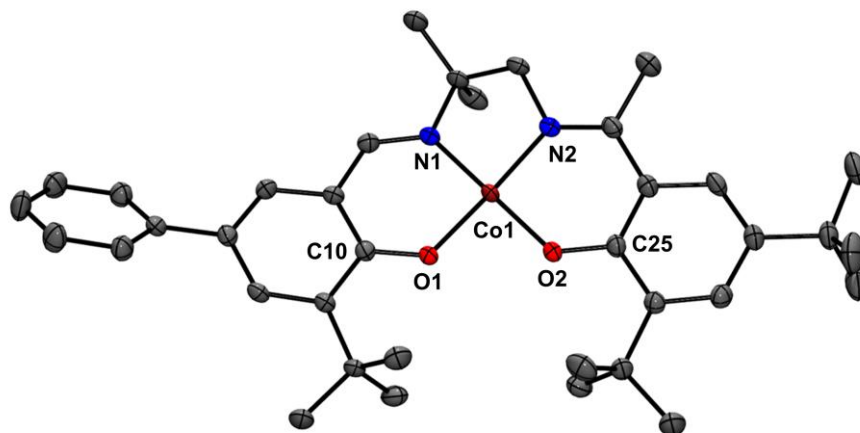


Figure 3.5. POV-Ray representation of CoL^1 .

Thermal ellipsoids shown at 50% probability level. Hydrogen atoms omitted for clarity. Co, scarlet; C, grey; O, red; N, blue. Selected interatomic distances [Å] and angles [deg]: Co(1)-O(1): 1.875(2), Co(1)-O(2): 1.835(2), Co(1)-N(1): 1.860(2), Co(1)-N(2): 1.872(2), C(10)-O(1): 1.315(3), C(25)-O(2): 1.322(3); Angles: O(1)-Co(1)-O(2): 87.7(7), O(1)-Co(1)-N(2): 172.0(9), O(1)-Co(1)-N(1): 93.5(8), O(2)-Co(1)-N(2): 93.0(9), O(2)-Co(1)-N(1): 174.9(9), N(2)-Co(1)-N(1): 86.6(9).

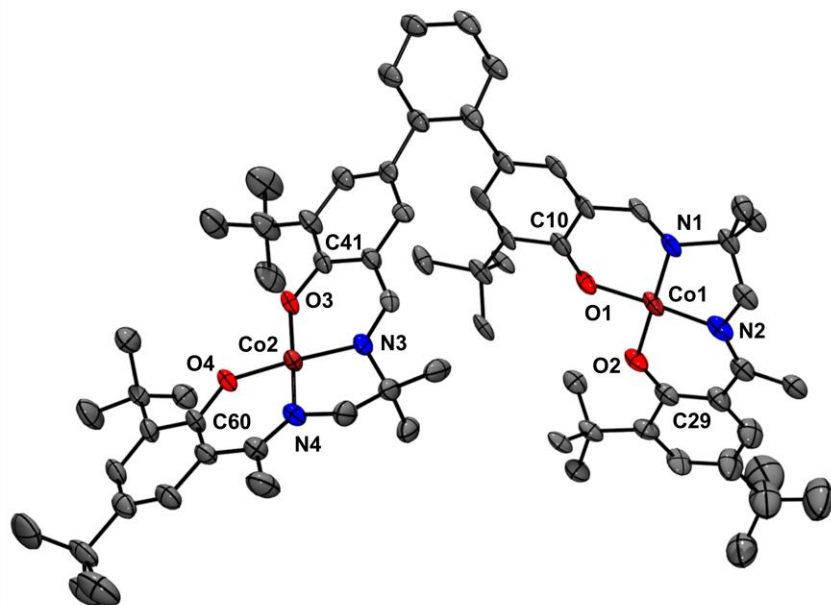


Figure 3.6. POV-Ray representation of Co_2L^2 .

Thermal ellipsoids shown at 50% probability level. Hydrogen atoms and solvent omitted for clarity. Co, scarlet; C, grey; O, red; N, blue. Selected interatomic distances [Å] and angles [deg]: Co(1)-O(1): 1.873(6), Co(1)-O(2): 1.830(5), Co(1)-N(1): 1.842(6), Co(1)-N(2): 1.870(9), C(10)-O(1): 1.317(1), C(29)-O(2): 1.321(1), Co(2)-O(3): 1.858(7), Co(2)-O(4): 1.839(6), Co(2)-N(3): 1.856(7), Co(2)-N(4): 1.894(8), C(41)-O(3): 1.331(1), C(60)-O(4): 1.310(1), Co(1)-Co(2): 10.04; Angles: O(1)-Co(1)-N(1): 92.7(3), O(1)-Co(1)-O(2): 87.8(3), O(1)-Co(1)-N(2): 173.2(3), O(2)-Co(1)-N(2): 92.9(3), O(2)-Co(1)-N(1): 176.2(3), N(1)-Co(1)-N(2): 87.1(3), O(3)-Co(2)-N(3): 92.3(3), O(3)-Co(2)-O(4): 87.6(3), O(3)-Co(2)-N(4): 178.0(3), O(4)-Co(2)-N(4): 92.5(3), O(4)-Co(2)-N(3): 177.3(3), N(3)-Co(2)-N(4): 87.5(3).

Table 3.1. Selected crystallographic data for **CoL¹**, **Co₂L²**, and **[CoL¹-H₂O]⁺**.

	CoL¹	Co₂L²	[CoL¹-H₂O]⁺
Formula	C ₃₇ H ₄₈ N ₂ O ₂ Co	C ₆₈ H ₉₀ N ₄ O ₄ Co ₂	C ₃₇ H ₅₂ CoN ₂ O ₃ Cl ₂ SbF ₆
Formula weight	611.7	1145.3	950.4
Space group	P -1	P -1	P2 ₁ /c
a (Å)	11.18(2)	16.09(13)	14.60(9)
b (Å)	11.63(2)	19.86(2)	9.12(7)
c (Å)	13.73(3)	25.86(3)	32.64(2)
α (deg)	93	98	90
β (deg)	97	106	94
γ (deg)	108	103	90
V [Å³]	1675	7516	4332
Z	2	4	4
T (K)	296	103	293
ρ_{calcd} (g cm⁻³)	1.213	1.012	1.457
λ (Å)	0.7749	0.71073	1.54180
μ (cm⁻¹)	0.684	0.482	9.610
R indices^a with I > 2.0σ(I) (data)	0.0379	0.0790	0.0529
wR₂	0.1201	0.2055	0.0569
R₁	0.0589	0.1811	0.0750
Goodness-of-fit on F²	1.109	0.959	1.1071

^aGoodness-of-fit on *F*.

3.2.3. Electrochemistry

The redox processes for **CoL¹** and **Co₂L²** were probed by cyclic voltammetry (CV) in CH₂Cl₂ using tetra-*n*-butyl-ammonium perchlorate (^{*n*}Bu₄NClO₄) as the supporting electrolyte (Figure 3.7). The redox processes vs. ferrocenium/ferrocene (F_c⁺/F_c) are reported in Table 3.2. A quasi-reversible one-electron redox process is observed for **CoL¹** at 0.16 V versus F_c⁺/F_c. An additional two-electron quasi-reversible redox-process is observed at 0.76 V (see Section 3.2.9 for further discussion). The redox processes are similar to those reported by Thomas and co-workers for a symmetric tBu-substituted Co(Sal) complex (0.01 and 0.70 V vs F_c⁺/F_c) albeit shifted to slightly more positive potentials, likely due to the slight changes in ligand electronics between the symmetric and tBu-substituted ligand and **H₂L¹**.³⁵⁵ Thomas and co-workers also report a third redox process at 0.74 V, which nearly overlaps the second wave at 0.70 V. In the case of **CoL¹**, we could not further resolve the two-electron process at 0.76 V (assigned in comparison to the internal standard F_c⁺). Fujii and co-workers have also investigated the electronic structure of a symmetric tBu-substituted Co(Sal) complex with an axially bound triflate anion.²⁶⁰ In this case, the first observed redox process was at -0.101 V, which is 0.26 V more negative than that observed for **CoL¹**. A number of factors may play a role in the

more negative potential, including the use of $n\text{Bu}_4\text{OTf}$ as the supporting electrolyte, as well as the use of a pre-oxidized complex in the CV experiment.

Table 3.2. Redox potentials for CoL^1 and Co_2L^2 versus $\text{Fc}^+/\text{Fc}^{a,b}$.

Complex	E_{pa}^1	E_{pc}^1	$E_{1/2}^1$	E_{pa}^2	E_{pc}^2	$E_{1/2}^2$
CoL^1	0.25	0.08	0.16 (0.17)	0.86	0.66	0.76 (0.20)
Co_2L^2	0.25	0.03	0.14 (0.23)	0.94	0.63	0.78 (0.30)

^aGiven in volts, peak-to-peak separation given in parentheses. ^bPeak-to-peak difference for Fc^+/Fc couple at 233 K is 0.15 V.

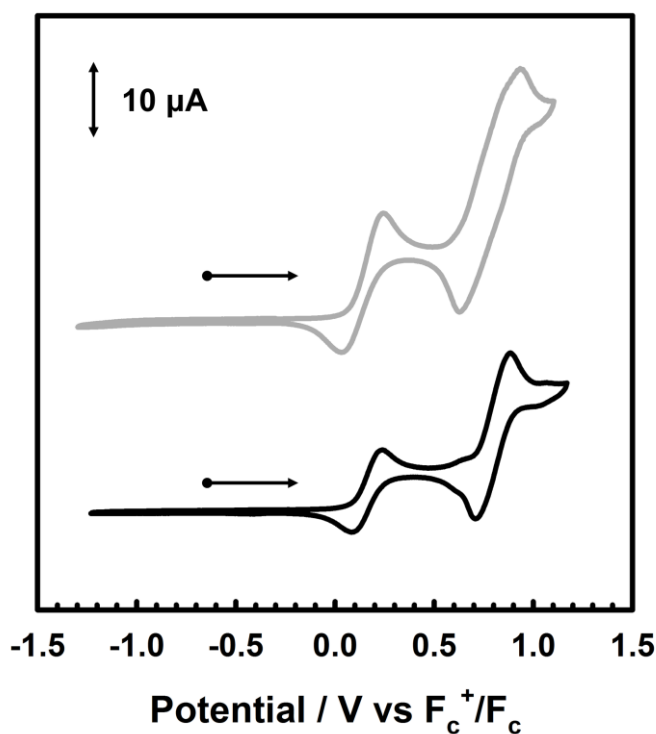


Figure 3.7. Cyclic voltammograms of CoL^1 (black line) and Co_2L^2 (grey line) in CH_2Cl_2 at 233 K.

Conditions: 2.5 mM complex, 0.1 M $n\text{Bu}_4\text{NClO}_4$, scan rate 100 mV s^{-1} .

Co_2L^2 displays very similar oxidation processes in comparison to CoL^1 (Figure 3.7); however, the current intensities are effectively doubled with a two-electron redox process observed at 0.14 V and a four-electron process observed at 0.78 V. These data show that the two Co(Sal) units are effectively isolated, with no observable splitting of the redox process (and as a result no communication between the salen moieties) at the limit of spectral resolution.

3.2.4. Synthesis and Characterization of Oxidized Complexes

Bulk oxidation of neutral complexes was performed under a dinitrogen atmosphere using AgSbF_6 as the oxidant (0.65 V vs. F_c^+/F_c in CH_2Cl_2).¹⁰⁷ $[\text{CoL}^1\text{-H}_2\text{O}][\text{SbF}_6]$ was recrystallized from CH_2Cl_2 /pentane solution, and the molecular structure is presented in Figure 3.8. The crystallographic data can be found in Table 3.1. The solid-state structure of $[\text{CoL}^1\text{-H}_2\text{O}][\text{SbF}_6]$ exhibits a slightly distorted square pyramidal geometry with the N_2O_2 coordination sphere from the salen ligand. The complex also bears an apically bound adventitious water molecule. A close contact exists between a hydrogen of the axially bound water molecule and an F atom of the SbF_6 counterion (F4---O3 distance of 2.844 Å). The Co ion is displaced by 0.147 Å above the plane of the coordinating atoms of the salen ligand toward O3. Upon oxidation, the Co-O bond lengths remain essentially the same in comparison to CoL^1 ; however, the Co-N bonds become slightly elongated (see Table 3.4 in section 3.2.8.1 for a comparison between experimental and computed bond lengths). Similar structural data have been reported by Thomas et al. for a *para* OMe-substituted $\text{Co}(\text{Sal})$ complex.³⁵⁵ The presence of paramagnetically shifted ^1H NMR signals is a strong indication that the electronic structure does not consist of a low-spin $\text{Co}(\text{III})$ central metal ion, as this electronic structure would result in a diamagnetic species with a ^1H NMR spectrum with peaks in the usual spectral window. Furthermore, the paramagnetic effects are enhanced upon complex oxidation with the ^1H NMR spectral window of CoL^1 widening significantly from $-10 \rightarrow 25$ ppm to $-35 \rightarrow 60$ ppm upon oxidation.

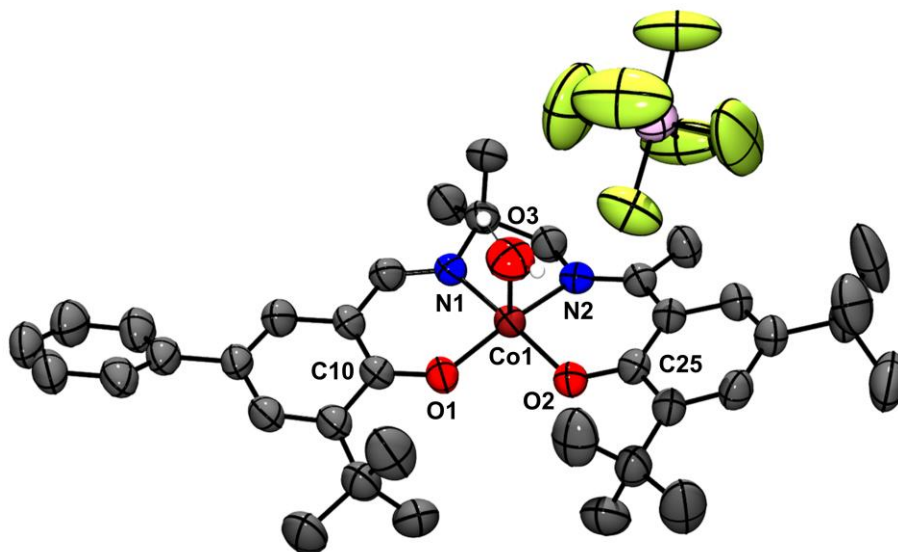


Figure 3.8. POV-Ray representation of **[CoL1-H2O][SbF6]**.

Thermal ellipsoids shown at 50% probability level. Hydrogen atoms (except those bound to O3) and solvent omitted for clarity. Co, scarlet; C, grey; O, red; N, blue; H, white; F, yellow-green; Sb, plum. Selected interatomic distances [Å] and angles [deg]: Co(1)-O(1): 1.868(4), Co(1)-O(2): 1.846(3), Co(1)-N(1): 1.891(4), Co(1)-N(2): 1.892(4), Co(1)-O(3): 2.124(4), C(10)-O(1): 1.324(6), C(25)-O(2): 1.326(6); Angles: O(1)-Co(1)-N(1): 93.4(2), O(1)-Co(1)-O(2): 87.7(2), O(1)-Co(1)-N(2): 170.1(2), O(2)-Co(1)-N(2): 97.1(2), O(2)-Co(1)-N(1): 171.7(2), N(1)-Co(1)-N(2): 85.8(2), O(3)-Co(1)-O(1): 91.7(2), O(3)-Co(1)-N(1): 96.4(2), O(3)-Co(1)-O(2): 91.8(2), O(3)-Co(1)-N(2): 98.1(2).

Similar shifting patterns are observed in the work of Fujii and co-workers, which can be attributed to ligand-based radical contributions to the overall electronic structure of these complexes upon oxidation.^{260, 356} Unfortunately, we were unable to isolate X-ray quality crystals of **[Co₂L²-2H₂O][2SbF₆]**, although the compound was characterized by a number of analytical and spectroscopic methods. Mass spectrometry (MS) analysis of the oxidized complexes did not afford the expected molecular ions (ESI-MS or MALDI-MS) due to loss of the weakly bound, apical water ligand.

3.2.5. Electronic Absorption Spectroscopy

The solution electronic absorption spectra of neutral and oxidized **CoL¹** and **Co₂L²** in the vis-NIR region are shown in Figure 3.9. Both neutral complexes are characterized by intense CT transitions at ca. 27,000 cm⁻¹ (14,700 M⁻¹ cm⁻¹ – **CoL¹**, 24,600 M⁻¹ cm⁻¹ – **Co₂L²**) and 23,000 cm⁻¹ (14,800 M⁻¹ cm⁻¹ – **CoL¹**, 25,800 M⁻¹ cm⁻¹ – **Co₂L²**); which are in good agreement to other reported Co(Sal) systems (Table 3.3).^{260, 355, 357} Both neutral

complexes have the same overall spectral shape, with **Co₂L²** exhibiting double the intensity in comparison to **CoL¹** across all wavelengths, with some minor changes at higher energy which likely arise due to the central phenylene linker. The oxidized complexes display broad high-energy transitions at ca. 27,000 cm⁻¹ (10,700 M⁻¹ cm⁻¹ – **[CoL¹-H₂O]⁺**, 23,200 M⁻¹ cm⁻¹ – **[Co₂L²-2H₂O]²⁺**) and 22,000 cm⁻¹ (5,100 M⁻¹ cm⁻¹ – **[CoL¹-H₂O]⁺**, 12,500 M⁻¹ cm⁻¹ – **[Co₂L²-2H₂O]²⁺**). Low-energy transitions for each complex appear at ca. 11,000 cm⁻¹ (3,600 M⁻¹ cm⁻¹ – **[CoL¹-H₂O]⁺**, 7,700 M⁻¹ cm⁻¹ – **[Co₂L²-2H₂O]²⁺**) and 8,500 cm⁻¹ (8,400 M⁻¹ cm⁻¹ – **[CoL¹-H₂O]⁺**, 17,800 M⁻¹ cm⁻¹ – **[Co₂L²-2H₂O]²⁺**). The low energy transitions are attributed to ligand contributions to the overall electronic structure of the oxidized complexes,^{266, 333} and the nature of the transitions was further analyzed by theoretical calculations (*vide infra*). Thomas and co-workers as well as Fujii and co-workers both observed similar low-energy bands (~10,000 cm⁻¹; ~6,000 M⁻¹ cm⁻¹) in their studies of oxidized monomeric Co(Sal) complexes.^{260, 355} Both groups studied the same salen ligand, the differences in the two complexes being the axially bound ligand (H₂O in the case of Thomas and co-workers and triflate in the case of Fujii and co-workers), as well as the presence of an SbF₆⁻ counterion in the work of Thomas. The low-energy band observed in this work for **[CoL¹-H₂O]⁺** appears at lower energy (8,500 cm⁻¹) and is also more intense (8,400 M⁻¹ cm⁻¹), a result which is attributable to slight differences in ligand electronics. Furthermore, we investigated the temperature dependence of the low energy band (Figure 3.10) at 298 and 195 K. No differences in the band were observed in this temperature range, suggesting that the complex is best described as a single electronic isomer in the temperature range studied.

Table 3.3. Spectroscopic properties of the Co complexes in CH₂Cl₂ solution.

Complex	λ_{\max} [cm ⁻¹] ($\epsilon \times 10^3$ [M ⁻¹ cm ⁻¹])
CoL¹	27 700 sh (14.3), 26 900 (14.7), 25 600 sh (13.1), 23 400 (14.8), 20 100 sh (3.1)
[CoL¹-H₂O]⁺	27 000 (10.7), 21 900 (5.1), 11 400 (3.6), 8500 (8.4)
Co₂L²	27 600 sh (24.0), 26 600 (24.6), 25 300 sh (23.0), 23 300 (25.8), 20 100 sh (6.4)
[Co₂L²-2H₂O]²⁺	27 000 (23.2), 22 600 sh (12.5), 11 200 sh (7.7), 8600 (17.8)

^aConditions: 1 mM complex, CH₂Cl₂, 298 K, sh = shoulder

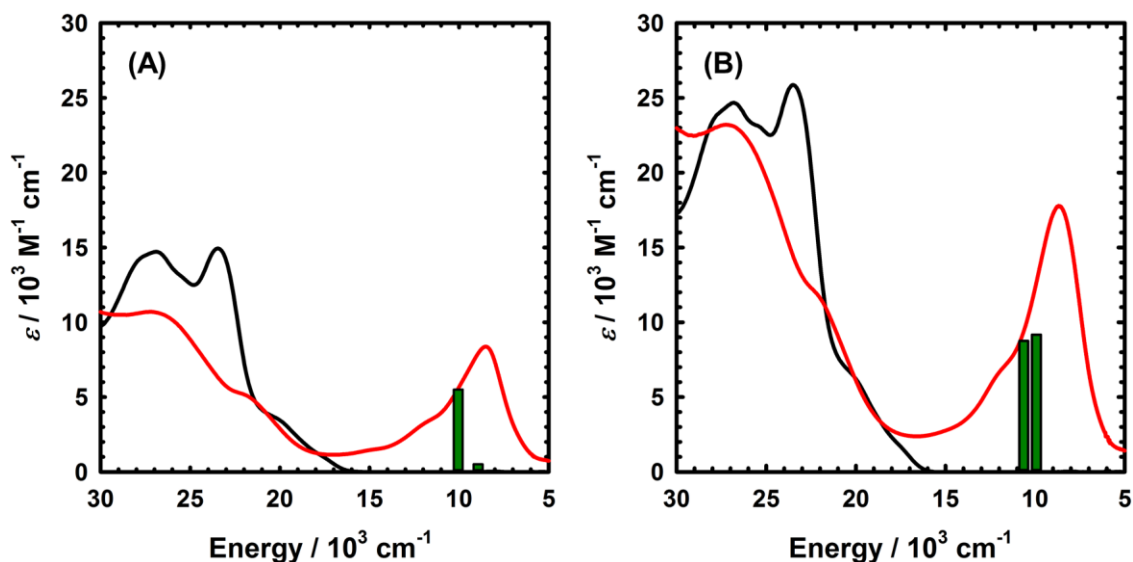


Figure 3.9. (A) vis-NIR spectra of CoL^1 (black line) and $[\text{CoL}^1\text{-H}_2\text{O}]^+$ (red line). (B) vis-NIR spectra of Co_2L^2 (black line) and $[\text{Co}_2\text{L}^2\text{-2H}_2\text{O}]^{2+}$ (red line). DFT transitions are shown as vertical green lines (*vide infra*).

Conditions: 1 mM complex, CH_2Cl_2 , 298 K.

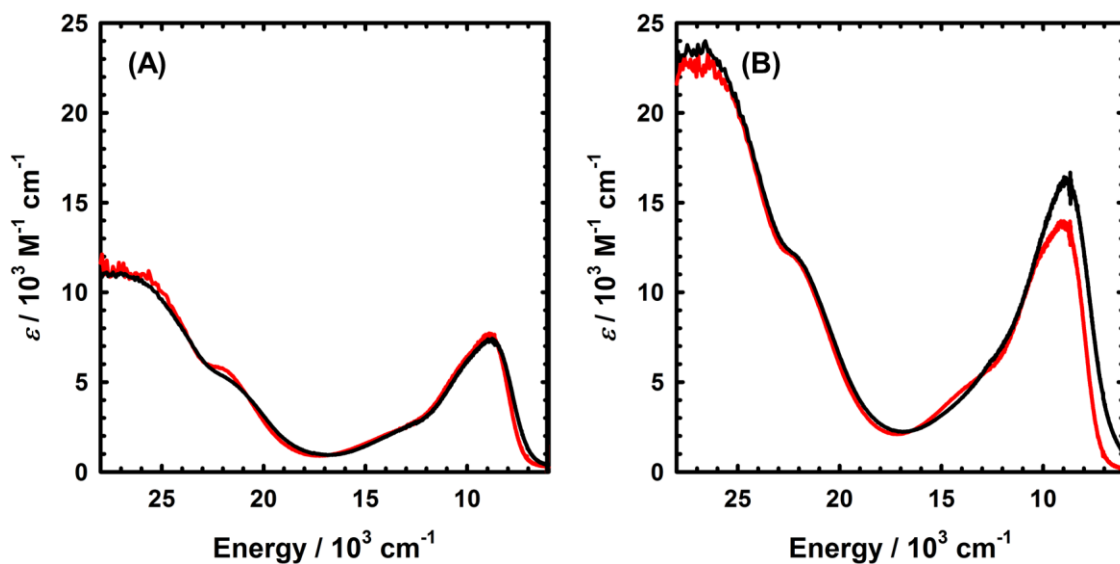


Figure 3.10. Temperature dependant Vis-NIR spectra of: (A) $[\text{CoL}^1\text{-H}_2\text{O}]^+$ and (B) $[\text{Co}_2\text{L}^2\text{-2H}_2\text{O}]^{2+}$ at 298 K (black lines) and 195 K (red lines).

Conditions: 1 mM complex, CH_2Cl_2 , spectra corrected for solvent contraction at low temperature.

Similar to the spectra of the neutral complexes, the oxidized dimer species $[\text{Co}_2\text{L}^2\text{-2H}_2\text{O}]^{2+}$ displays a doubling of spectral features across all wavelengths, further enforcing that the two salen units are isolated in the neutral and oxidized bimetallic complexes. The

low energy band in $[\text{Co}_2\text{L}^2\text{-2H}_2\text{O}]^{2+}$ exhibits a ~15% decrease in the overall intensity at 190 K; however, in the absence of any other characterization data to support a temperature-dependent change in electronic structure, this is likely due to factors such as lower solubility at decreased temperature.³⁵⁸

3.2.6. Electron Paramagnetic Resonance Spectroscopy

The X-band EPR spectra of the neutral and oxidized complexes is presented in Figure 3.11. CoL^1 displays an EPR spectrum that is consistent with a low-spin Co(II) ($S = \frac{1}{2}$) ground state. On the basis of reports by our group³⁵⁹ and others,³⁶⁰⁻³⁶¹ CoL^1 exhibits a $|yz, {}^2A_2\rangle$ ground state in frozen CH_2Cl_2 with hyperfine splitting originating from the $I = 7/2$ Co nucleus and the $I = 1$ ${}^{14}\text{N}$ nuclei of the salen ligand. The EPR spectrum of the dimeric complex Co_2L^2 , exhibits a similar shape which can be attributed to two four-coordinate Co(II) ($S = \frac{1}{2}$) metal centres, both with $|yz, {}^2A_2\rangle$ ground states in frozen CH_2Cl_2 .³⁵⁹⁻³⁶¹ Co_2L^2 displays a resolvable eight-line pattern at low field ($g \sim 3.35$). Further evidence for a lack of metal-metal interaction between the two cobalt centres in Co_2L^2 can be found from the EPR spin integration ratio of Co_2L^2 to CoL^1 of ~2.2; indicating minimal coupling between metal centres. The above EPR analysis is further corroborated by theoretical calculations and solid-state magnetic studies (*vide infra*).

The X-band EPR spectra of the oxidized analogues $[\text{CoL}^1\text{-H}_2\text{O}]^+$ and $[\text{Co}_2\text{L}^2\text{-2H}_2\text{O}]^{2+}$ are also displayed in Figure 3.11. Both oxidized complexes display paramagnetically shifted ${}^1\text{H}$ NMR signals, however both are EPR silent in the X-band frequency range to temperatures as low as 10 K. Spin states (triplet and higher spin multiplicities) with large zero-field splitting (ZFS) parameters ($|D| > \sim 0.3 \text{ cm}^{-1}$) will have EPR allowed transitions outside the energy range of X-band EPR and will thus appear silent in this frequency mode (see Section 3.3.7 on solid-state magnetism and Section 3.2.8.2 for an in-depth DFT investigation of potential spin-states). Thomas and co-workers do observe a signal in the Q-band frequency range, which is interpreted as an allowed transition within the $|-\frac{1}{2}, +\frac{1}{2}\rangle$ doublet for a high-spin ($S_{\text{Co}} = 3/2$) Co ion weakly interacting with a ligand-based radical in a structurally similar oxidized monomeric complex.³⁵⁵

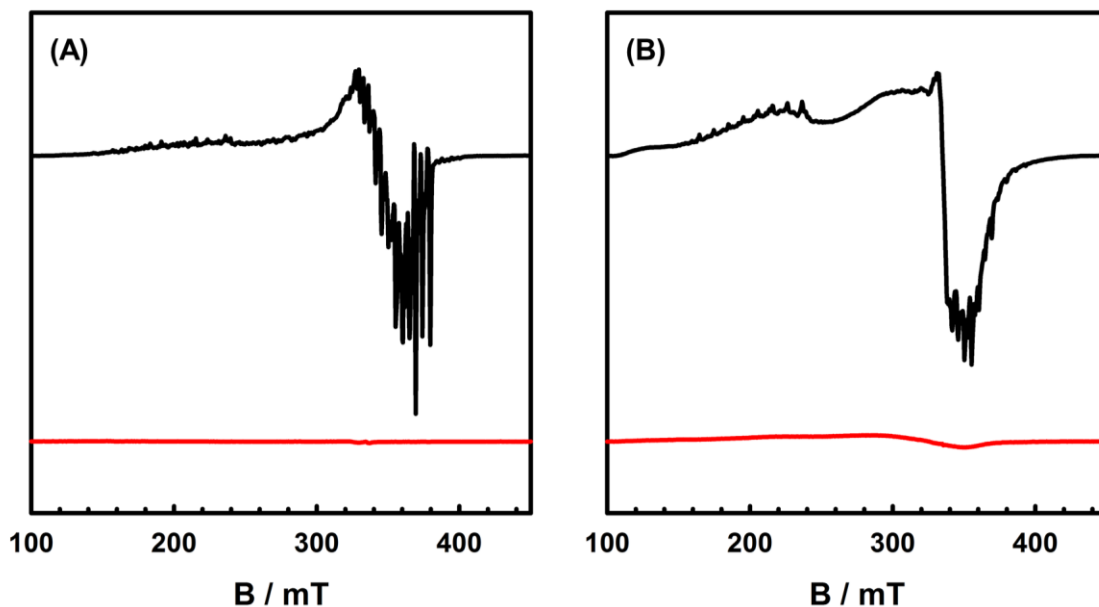


Figure 3.11. X-band EPR spectra of 0.3 mM solutions of: (A) CoL^1 (black line) and $[\text{CoL}^1\text{-H}_2\text{O}]^+$ (red line) and (B) Co_2L^2 (black line) and $[\text{Co}_2\text{L}^2\text{-2H}_2\text{O}]^{2+}$ (red line).

Conditions: frequency = 9.383 GHz; power = 2.0 mW; modulation frequency = 100 kHz; modulation amplitude = 0.6 mT; $T = 20$ K (neutral), 10 K (oxidized).

3.2.7. Solid-State Magnetism

The magnetic susceptibility (χ_M) vs temperature (T) data for Co_2L^2 , $[\text{CoL}^1\text{-H}_2\text{O}][\text{SbF}_6]$, and $[\text{Co}_2\text{L}^2\text{-2H}_2\text{O}][2\text{SbF}_6]$ were obtained between 1.8 and 300 K under a dc applied field of 10,000 Oe, and the $\chi_M T$ vs T plots are presented in Figure 3.12 and Figure 3.14. For Co_2L^2 , at room temperature, the $\chi_M T$ vs T product (Figure 3.12) of $1.06 \text{ cm}^3 \text{ K mol}^{-1}$ corresponds closely to a value of $1.08 \text{ cm}^3 \text{ K mol}^{-1}$ (given $g \sim 2.40$; $S = \frac{1}{2}$; $C = 0.54 \text{ cm}^3 \text{ K mol}^{-1}$) for two non-interacting square planar Co(II) centres.³⁶²⁻³⁶³ A g value of 2.40 was used for all solid-state magnetism analyses herein as this corresponds closely to an average g value reported for a number of square-planar Co(II) complexes with N_2O_2 coordination environments.^{260, 359-361, 364} The spin-only value is lower (0.75), demonstrating orbital contributions to the magnetic moment.³⁶⁵ As the temperature is decreased, the $\chi_M T$ versus T product increases slowly to a maximum of $1.20 \text{ cm}^3 \text{ K mol}^{-1}$ at 70 K followed by a sharp decrease to $0.63 \text{ cm}^3 \text{ K mol}^{-1}$ at 1.8 K. The change in $\chi_M T$ versus T with temperature suggests the presence of a combination of both weak ferromagnetic and antiferromagnetic interactions in the system. The $\chi_M T$ versus T data above 40 K was fit; however, the full temperature range could not be adequately modelled using a standard

Ising-Heisenberg model.³⁶⁶ The sharp decrease at low temperature can be caused by the presence of magnetic anisotropy and/or thermal depopulation of the low-lying excited states. The field dependence of the magnetization was also measured for Co_2L^2 at 1.8, 3, 5, and 8 K and is shown in Figure 3.13. At 1.8 K, the magnetization increases to a maximum of $2.27(1) \mu_B$ and does not saturate, which suggests the presence of anisotropy in the system.

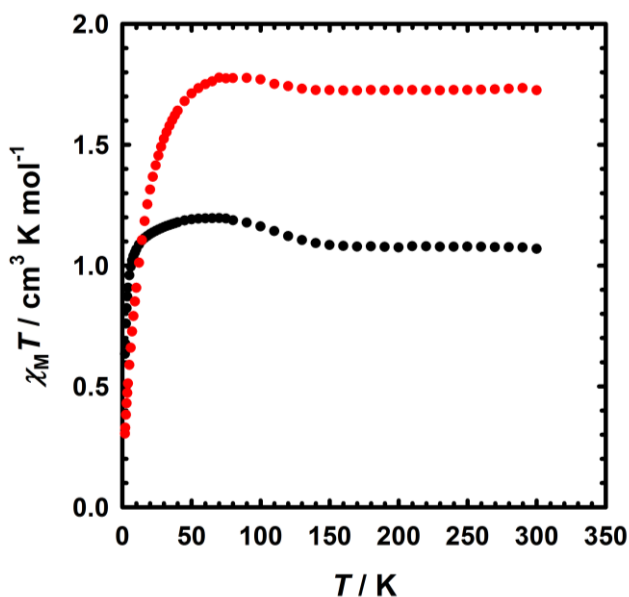


Figure 3.12. $\chi_M T$ vs T data for Co_2L^2 (black) and $[\text{Co}_2\text{L}^2\text{-}2\text{H}_2\text{O}][2\text{SbF}_6]$ (red) at 10,000 Oe between 1.8 and 300 K.

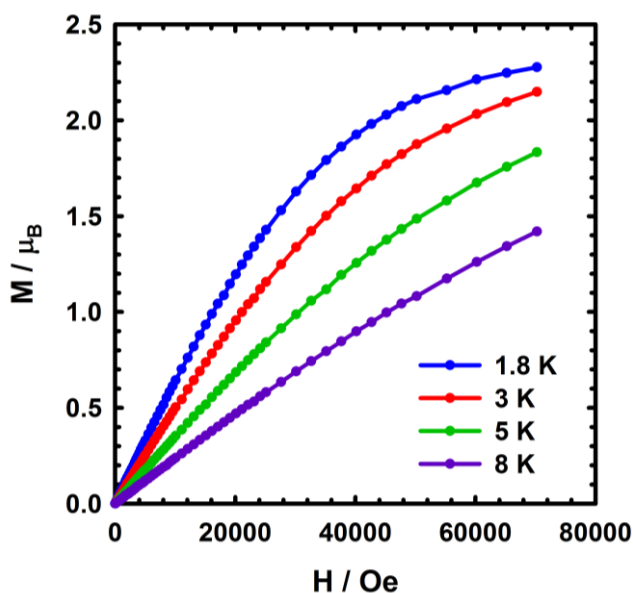


Figure 3.13. Field dependence of the magnetization for Co_2L^2 at 1.8, 3, 5, and 8 K between 0 and 7 T.

For $[\text{CoL}^1\text{-H}_2\text{O}][\text{SbF}_6]$, the $\chi_M T$ versus T product (Figure 3.14) at room temperature is $1.08 \text{ cm}^3 \text{ K mol}^{-1}$, which is slightly higher than the product ($0.915 \text{ cm}^3 \text{ K mol}^{-1}$) for an $S = 1$ system. Fits of the data were compared for both a d^7 Co(II) ligand radical electronic structure and a high-spin Co(III) complex. For the d^7 Co(II) system, this includes one non-interacting $S = \frac{1}{2}$ Co(II) unit ($g \sim 2.40$; $C = 0.54 \text{ cm}^3 \text{ K mol}^{-1}$) and one $S = \frac{1}{2}$ ligand radical with a fixed $g = 2.00$ ($C = 0.375 \text{ cm}^3 \text{ K mol}^{-1}$) at 298 K. As the temperature decreases, the $\chi_M T$ versus T product slowly decreases to a minimum of $0.12(1) \text{ cm}^3 \text{ K mol}^{-1}$ at 1.8 K suggesting the presence of antiferromagnetic interactions in the system. The field dependence of the magnetization data (Figure 3.15) was measured between 0 and 7 T and increases steadily to a maximum of $0.68 \mu_B$ at 7 T, which indicates the presence of anisotropy. The $\chi_M T$ versus T data was well modelled with the Bleaney-Bowers equation³⁶⁷ (Equations 1 and 2) resulting in the fitting parameters of $g = 2.41(1)$ and $J = -5.2(1) \text{ cm}^{-1}$ (Figure 3.14, red). This result suggests a weak antiferromagnetic interaction between the Co(II) centre and the ligand radical for $[\text{CoL}^1\text{-H}_2\text{O}][\text{SbF}_6]$.

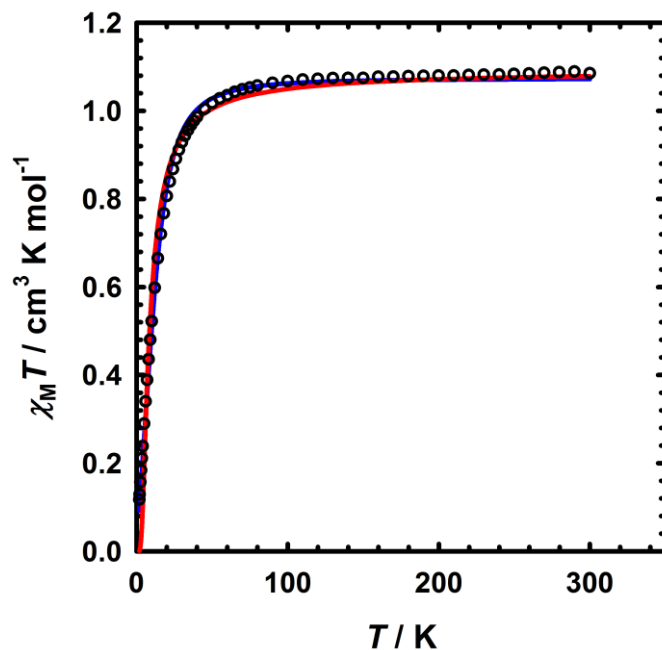


Figure 3.14. $\chi_M T$ versus T data for $[\text{CoL}^1\text{-H}_2\text{O}]^+$ at 10,000 Oe between 1.8 and 300 K (o).

The solid red line represents the fit to the data for an $S = \frac{1}{2}$ Co(II) unit ($g \sim 2.40$, $C = 0.54 \text{ cm}^3 \text{ K mol}^{-1}$) antiferromagnetically coupled ($J = -5.2(1) \text{ cm}^{-1}$) to an $S = \frac{1}{2}$ ligand radical with a fixed $g = 2.00$ ($C = 0.375 \text{ cm}^3 \text{ K mol}^{-1}$). The solid blue line represents the fit to an $S = 1$ Co(III) complex ($[D] = 32.3 \text{ cm}^{-1}$, $g = 2.079$, $\chi_{\text{TIP}} < 1 \times 10^{-9} \text{ emu}$).

The $\chi_M T$ versus T data could also be well modelled to an $S = 1$ system of an intermediate-spin Co(III) centre ($[D] = 32.3 \text{ cm}^{-1}$; $g = 2.079$; $\chi_{\text{TIP}} < 1 \times 10^{-9} \text{ emu}$; Figure 3.14, blue), showing that both electronic descriptions satisfy the solid-state magnetism data. This analysis is in agreement with a similar oxidized Co(Sal) complex (triflate axial ligand) recently reported by Kurahashi and Fujii.²⁶⁰

$$H = -2J[\widehat{S}_1\widehat{S}_2] \quad (1)$$

$$\chi_M T = \frac{2N\beta^2 g^2}{k} \frac{[1]}{\left[3 + \exp\left(-\frac{2J}{kT}\right)\right]} \quad (2)$$

Interestingly, in work reported by Thomas and co-workers.,³⁵⁵ solid-state magnetic data ($1.47 \text{ cm}^3 \text{ K mol}^{-1}$) supports a high-spin Co(II) centre strongly antiferromagnetically coupled to a phenoxyl radical for a structurally similar oxidized Co salen complex with an axial water ligand. These results suggest that the electronic structure of oxidized Co salen complexes is sensitive to packing in the solid-state, in addition to the donating ability of both the salen and the axial ligand.

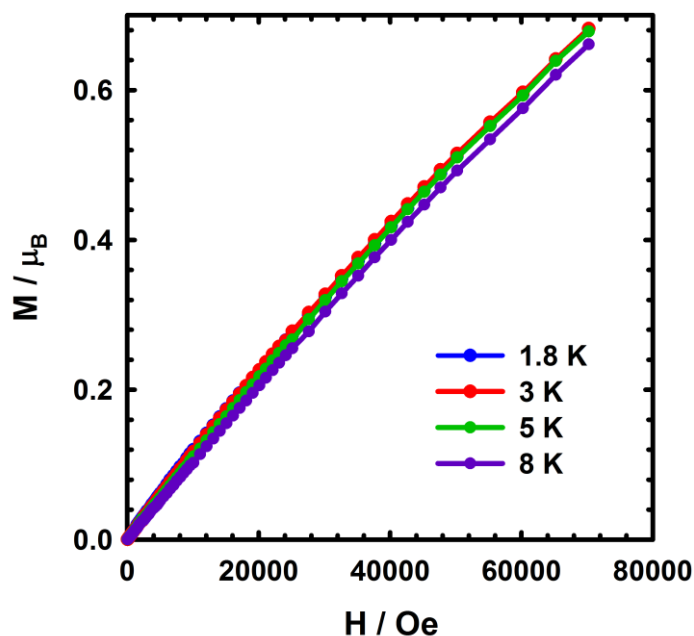


Figure 3.15. Field dependence of the magnetization for $[\text{CoL}^1\text{-H}_2\text{O}]^+$ at 1.8, 3, 5 and 8 K between 0 and 7 T.

For $[\text{Co}_2\text{L}^2\text{-}2\text{H}_2\text{O}]^{2+}$, the $\chi_M T$ versus T product (Figure 3.12) at room temperature is $1.72(1) \text{ cm}^3 \text{ K mol}^{-1}$, which is close to the value of $1.83 \text{ cm}^3 \text{ K mol}^{-1}$ for two non-interacting $S = \frac{1}{2} \text{ Co(II)}$ metal centres ($g \sim 2.40$; $C = 0.54 \text{ cm}^3 \text{ K mol}^{-1}$) and two non-interacting $S = \frac{1}{2}$ ligand radicals ($g \sim 2.00$, $C = 0.375 \text{ cm}^3 \text{ K mol}^{-1}$). Similarly to Co_2L^2 , as the temperature decreases, the $\chi_M T$ versus T product increases to a maximum of $1.77(1) \text{ cm}^3 \text{ K mol}^{-1}$ at 90 K and then sharply decreases to a value of $0.29(1) \text{ cm}^3 \text{ K mol}^{-1}$ at 1.8 K. This suggests the presence of at least one ferromagnetic and one anti-ferromagnetic interaction in the system, similarly to Co_2L^2 . The data, however, could not be modelled to a standard Ising-Heisenberg model,³⁶⁶ most likely due to the presence of high anisotropy in the system as supported by the absence of saturation in the M versus H data (Figure 3.16), which increases steadily to the maximum value of $1.23 \mu_B$ at 7 T.

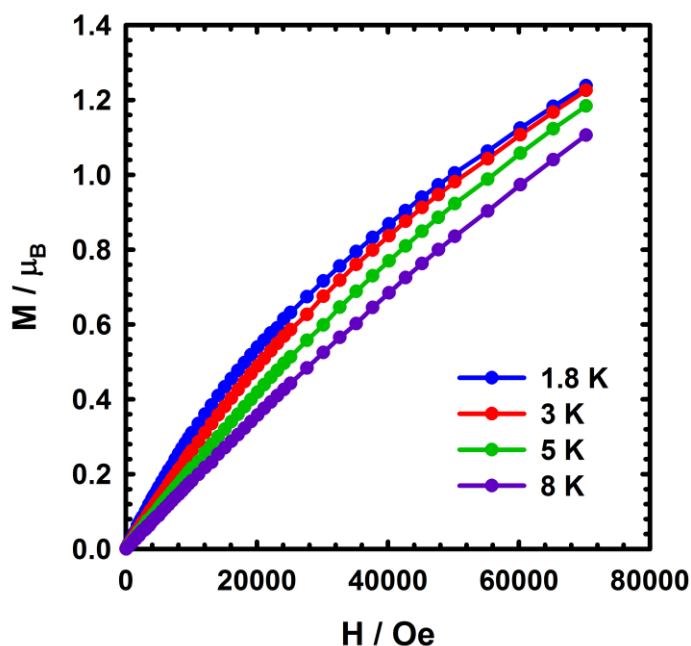


Figure 3.16. Field dependence of the magnetization for $[\text{Co}_2\text{L}^2\text{-}2\text{H}_2\text{O}]^{2+}$ at 1.8, 3, 5, and 8 K between 0 and 7 T.

3.2.8. Theoretical Analysis

3.2.8.1. Neutral CoL^1 and Co_2L^2

Density functional theory (DFT) calculations on both neutral and oxidized complexes provided further insight into their geometric and electronic structures. First, we compared the optimized geometry of neutral CoL^1 and Co_2L^2 with the experimental

metrical data. The calculations reproduce the coordination sphere bond lengths to within 0.03 Å (Table 3.4). In addition, the calculations correctly predict the slight asymmetry in the coordination sphere due to the asymmetric salen ligands. The VT ¹H NMR spectroscopy results suggest that **Co₂L²** is able to freely rotate about the phenylene linker, and thus we calculated the energy of the *cis* and *trans* conformers. The *trans* orientation is predicted to be 0.42 kcal mol⁻¹ lower in energy in comparison to the *cis* orientation, demonstrating the nearly isoenergetic nature of the two conformers; however, due to the solid-state structure of **Co₂L²** exhibiting the *cis* conformation, we performed all further calculations using this orientation. The electronic structure of the neutral complexes and, in particular, the SOMOs, were further investigated, and the DFT calculations accurately predict the metal-based character (*d_{yz}*, *d_{z²}*) of the SOMOs for both complexes (Figure 3.17), highlighting the [*yz*, ²A₂) ground states as determined by EPR spectroscopy (Figure 3.11).³⁶⁰⁻³⁶¹ Further evidence for a lack of electronic communication between Co centres in **Co₂L²** is exemplified by the isoenergetic nature of the triplet and BS electronic solutions ($\Delta E = 0.005$ kcal mol⁻¹) (Figure 3.18).

Table 3.4. Experimental^a and calculated (in parentheses)^b coordination sphere metrical parameters for the neutral complexes (in Å).

Bond	CoL ¹	Co ₂ L ² (S = 1)	Co ₂ L ² (S = 0)
Co1-O1	1.875 (1.853)	1.869 (1.861)	1.869 (1.861)
Co1-O2	1.835 (1.832)	1.827 (1.840)	1.827 (1.840)
Co1-N1	1.860 (1.863)	1.848 (1.870)	1.848 (1.870)
Co1-N2	1.872 (1.866)	1.857 (1.875)	1.857 (1.875)
Co2-O3	-	1.861 (1.854)	1.861 (1.853)
Co2-O4	-	1.838 (1.832)	1.838 (1.856)
Co2-N3	-	1.856 (1.862)	1.856 (1.862)
Co2-N4	-	1.888 (1.867)	1.888 (1.866)
Co1-Co2	-	10.03 (9.382)	10.03 (9.383)

^aAverage of two values for experimental data. ^bSee the Experimental Section for calculation details.

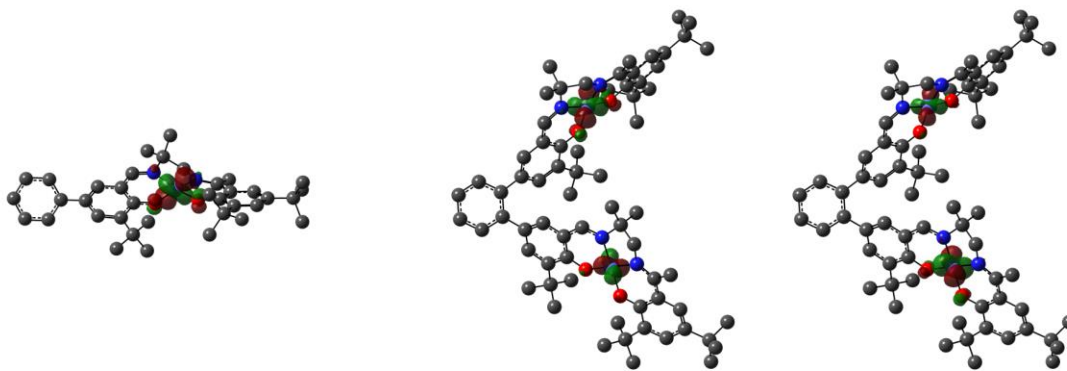


Figure 3.17. DFT-predicted SOMOs for CoL^1 and Co_2L^2 .

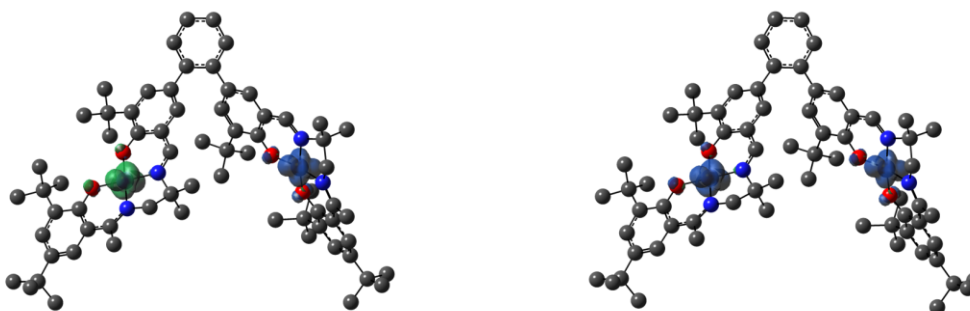


Figure 3.18. (left) Predicted spin-density plot for the BS solution of Co_2L^2 . (right) Predicted spin-density plot for the triplet solution of Co_2L^2 . The two electronic structure solutions are isoenergetic ($\Delta E = 0.005 \text{ kcal mol}^{-1}$).

3.2.8.2. $[\text{CoL}^1\text{-H}_2\text{O}]^+$ and $[\text{Co}_2\text{L}^2\text{-2H}_2\text{O}]^{2+}$

Upon oxidation, a number of potential electronic structures are possible, and we sought to determine a computational model that accurately predicted experimental results for $[\text{CoL}^1\text{-H}_2\text{O}]^+$ to apply to the more computationally taxing $[\text{Co}_2\text{L}^2\text{-2H}_2\text{O}]^{2+}$. Possible electronic structure descriptions of one-electron oxidized $[\text{CoL}^1\text{-H}_2\text{O}]^+$ include diamagnetic $\text{Co(III)(Sal)} - (\text{Co}^{3+}\text{-L})$, and intermediate-spin $\text{Co(III)(Sal)} - (\uparrow\uparrow\text{Co}^{3+}\text{-L})$ which would both result from metal-based oxidation. Ligand-based oxidations would result in one of four electronic structures, low-spin Co(II) coupled antiferromagnetically or ferromagnetically to a salen ligand radical, $(\uparrow\text{Co}^{2+}\text{-}\downarrow\text{L}^{\cdot})$ or $(\uparrow\text{Co}^{2+}\text{-}\uparrow\text{L}^{\cdot})$ and the high-spin states of the previous descriptions, $(\uparrow\uparrow\uparrow\text{Co}^{2+}\text{-}\downarrow\text{L}^{\cdot})$ or $(\uparrow\uparrow\uparrow\text{Co}^{2+}\text{-}\uparrow\text{L}^{\cdot})$. The Co(III) singlet electronic structure is much higher in relative energy in comparison to all other calculated electronic structures, matching the experimental evidence supporting an alternative electronic structure with paramagnetic character (Table 3.5). Interestingly, the

intermediate-spin Co(III)-salen ($\uparrow\uparrow\text{Co}^{3+}\text{-L}$), low-spin Co(II) ligand radical ($\uparrow\text{Co}^{2+}\text{-}\uparrow\text{L}^{\cdot}$), and high-spin ($\uparrow\uparrow\uparrow\text{Co}^{2+}\text{-}\downarrow\text{L}^{\cdot}$) initial guesses all converge to the same electronic structure solution, referred to as the ‘triplet solution’ for the remainder of this chapter. This solution is predicted to be lowest in energy (Table 3.5) and supports strong metal and ligand frontier molecular orbital mixing in the oxidized complex. Geometrically, the coordination sphere is best replicated by the triplet and BS singlet ($\uparrow\text{Co}^{2+}\text{-}\downarrow\text{L}^{\cdot}$) solutions with the bond lengths of the four coordinate salen atoms reproduced within 0.02 Å (Table 3.6). Table 3.5 outlines the relative energies of the possible spin states described above. The spin-density plots for the two lowest-energy electronic structures are presented in Figure 3.19. As is evident in the spin-density plots, binding of an axial water ligand reorders the Co-based d orbitals such that the ground-state orbital is now predominantly d_{z^2} in character, in excellent agreement with results obtained in other DFT studies on Co salen complexes.^{355, 359} The majority of unpaired spin is localized to the central metal ion in the triplet (~75%), with the remaining unpaired spin density delocalized across the ligand framework,³⁵⁵ highlighting the contributions of the intermediate-spin Co(III) and low spin Co(II)L[·] electronic states. Significantly less spin-density is localized at the metal centre in the BS singlet $\uparrow\text{Co}^{2+}\text{-}\downarrow\text{L}^{\cdot}$ (ca. one electron), with the remaining spin-density delocalized across the ligand framework.

Table 3.5. DFT-calculated energy differences of possible spin states for **[CoL¹-H₂O]⁺**

Solution	Relative Energy (kcal mol ⁻¹)
Co ³⁺ -L (closed-shell singlet)	+17
‘Triplet solution’	0
Broken symmetry (open-shell) singlet	+2.6
$\uparrow\uparrow\uparrow\text{Co}^{2+}\text{-}\uparrow\text{L}^{\cdot}$	+6.5

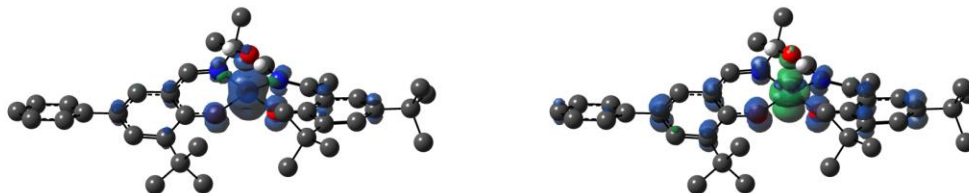


Figure 3.19. (left) Predicted spin-density plot for the triplet solution. (right) Predicted spin-density plot for the BS anti-ferromagnetically coupled ligand radical solution, $\uparrow\text{Co}^{2+}\text{-}\downarrow\text{L}^{\cdot}$.

Table 3.6. Experimental and calculated^a coordination sphere metrical parameters for **[CoL¹-H₂O]⁺** (in Å).

Bond ^b	[CoL ¹ -H ₂ O] ⁺ (X-ray)	[CoL ¹ -H ₂ O] ⁺ (S = 1)	[CoL ¹ -H ₂ O] ⁺ (S = 0)
Co1-O1	1.868	1.848	1.873
Co1-O2	1.846	1.837	1.852
Co1-N1	1.891	1.884	1.880
Co1-N2	1.892	1.883	1.885
Co1-O3	2.124	2.186	2.235

^aSee the Experimental Section for calculation details. ^bFor number scheme see Figure 3.10.

Time-dependent DFT (TD-DFT) accurately predicts the absence of low-energy spectral features for **CoL¹**, while correctly predicting the presence of low-energy electronic transitions for **[CoL¹-H₂O]⁺**. One band of significant intensity is predicted (10,050 cm⁻¹; $f = 0.2908$), which is slightly blue-shifted in comparison to the maximum of the broad low-energy transition observed experimentally (Figure 3.9 and Figure 3.20). The predicted band is a β HOMO \rightarrow β LUMO transition, and AOMix³⁶⁸ decomposition of relevant MOs into constituent components indicates that the predicted transition is predominantly a ligand-to-metal charge transfer band (LMCT) with a shift in electron density from the salen ligand to the metal d_{yz} orbital. However, even though there is a significant shift in electron density to the Co centre, the salen ligand remains the dominant component in both donor and acceptor orbitals. The BS solution predicts an intense NIR band at low energy ($\sim 4,200$ cm⁻¹; $f = 0.1395$); however, this band is not observed experimentally.

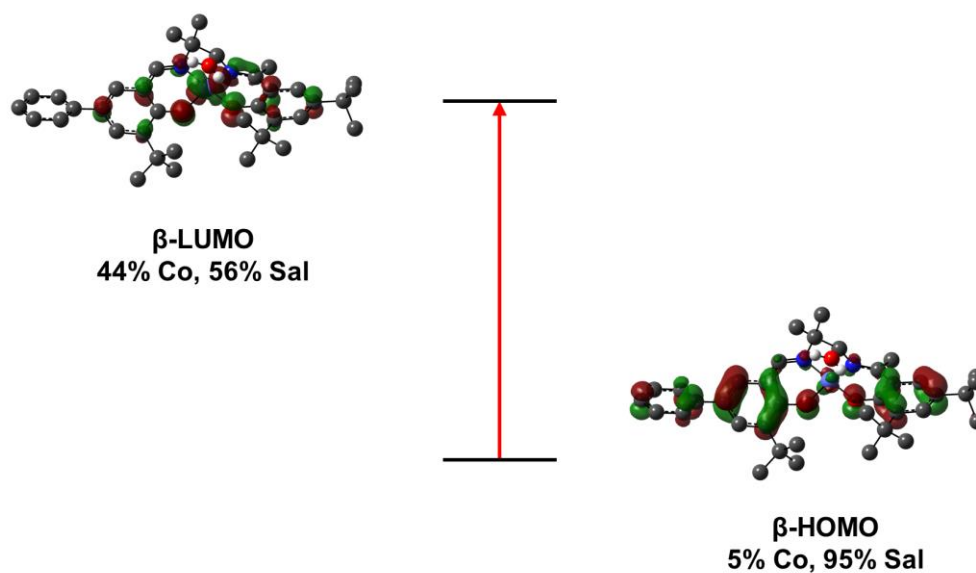


Figure 3.20. Kohn-Sham molecular orbitals for the triplet solution of $[\text{CoL}^1\text{-H}_2\text{O}]^+$ associated with the calculated NIR transition at $10,050\text{ cm}^{-1}$ ($\beta\text{HOMO} \rightarrow \beta\text{LUMO}$).

MO breakdown calculated using AOMix;³⁶⁸ see the Experimental Section for details.

We then applied the same calculation protocol to $[\text{Co}_2\text{L}^2\text{-2H}_2\text{O}]^{2+}$, ignoring high-spin Co(II) spin states as they are predicted to be much higher in energy in comparison to the low spin states for $[\text{CoL}^1\text{-H}_2\text{O}]^+$. The two electronic solutions of lowest energy include an overall quintet electronic structure, incorporating two ‘triplet’ Co salen units, as well as a BS singlet electronic structure in which ligand radicals and metal-based electrons are antiferromagnetically coupled on each salen arm to afford an overall singlet electronic structure. The spin-density plots of the two electronic structures are presented in Figure 3.21. The quintet solution is $\sim 8.5\text{ kcal mol}^{-1}$ lower in energy in comparison to the BS electronic structure solution, in line with expected results from the monomer calculations, as well as the experimental magnetic data. Whereas the ligand spin density is equally distributed between both phenolate rings in $[\text{CoL}^1\text{-H}_2\text{O}]^+$, the ligand spin density shifts *slightly* to the outermost phenolate rings in $[\text{Co}_2\text{L}^2\text{-2H}_2\text{O}]^{2+}$. Despite this, in both cases the majority ($\sim 90\%$) of spin density is localized to the central Co ions and N_2O_2 coordination sphere. For $[\text{Co}_2\text{L}^2\text{-2H}_2\text{O}]^{2+}$, TD-DFT analysis on the quintet electronic structure solution predicts two low-energy transitions that are 353 cm^{-1} apart (Figure 3.9 and Figure 3.22). These transitions are $\beta\text{HOMO} \rightarrow \beta\text{LUMO}$ and $\beta\text{HOMO} \rightarrow \beta\text{LUMO}+1$ transitions, respectively and are shown in Figure 3.22. These transitions, like those of $[\text{CoL}^1\text{-H}_2\text{O}]^+$, are both predominantly LMCT in character (as determined by AOMix analysis) in which

charge transfers from the phenylene linker to one of the salen units. However, despite these predicted transitions, we do not observe splitting of the low-energy band experimentally. We also investigated the TD-DFT transitions of the BS singlet solution, in which two lower-energy bands ($\sim 3,900\text{ cm}^{-1}$; $f = 0.1298$ and $\sim 4,600\text{ cm}^{-1}$; $f = 0.1115$) are predicted. These bands, however, are not observed experimentally, and our characterization data together with the data for $[\text{CoL}^1\text{-H}_2\text{O}]^+$ strongly supports a quintet electronic structure for $[\text{Co}_2\text{L}^2\text{-2H}_2\text{O}]^{2+}$.

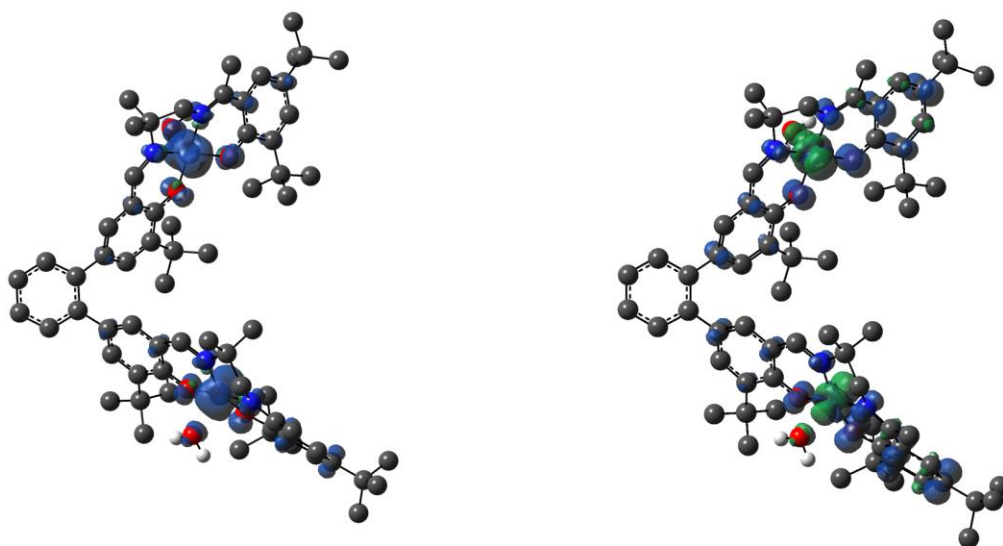


Figure 3.21. (left) Predicted spin-density plot for the quintet (bis-triplet) spin state. (right) Predicted spin-density plot for the bis-BS singlet solution.

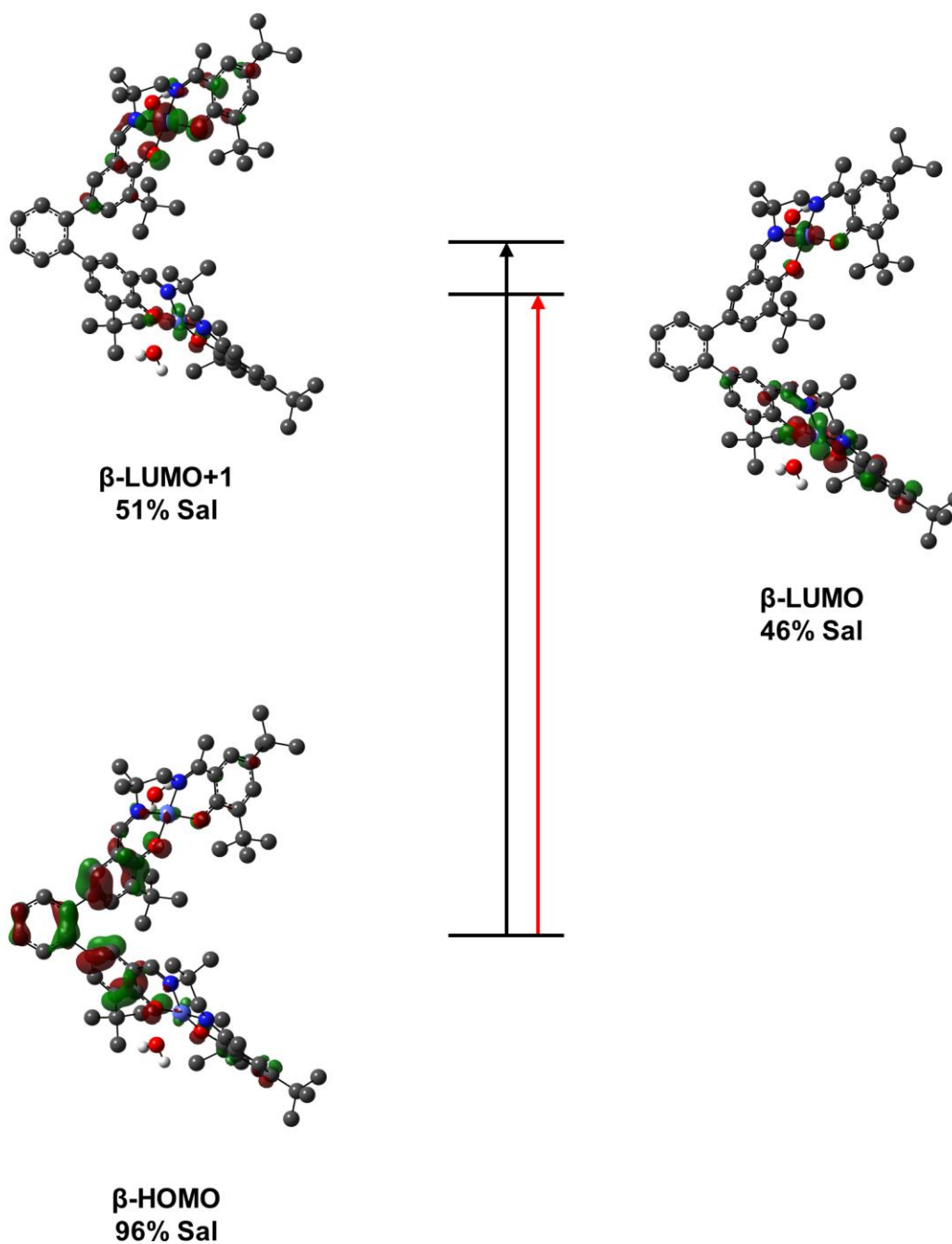


Figure 3.22. Kohn-Sham molecular orbitals for the quintet solution of $[\text{Co}_2\text{L}^2\text{-2H}_2\text{O}]^{2+}$ associated with the calculated NIR transitions at $10\,403\text{ cm}^{-1}$ ($\beta\text{HOMO} \rightarrow \beta\text{LUMO}$; black line) and $10\,757\text{ cm}^{-1}$ ($\beta\text{HOMO} \rightarrow \beta\text{LUMO}+1$; red line). MO breakdown calculated using AOMix, see the Experimental Section for details.

3.2.9. Double Oxidation of CoL¹

Investigation of the CV spectrum of isolated [CoL¹-H₂O]⁺ reveals splitting of the higher-potential, two-electron redox process into independent one-electron processes separated by ~200 mV at 233 K (Figure 3.23). This splitting allowed us to investigate the oxidation of CoL¹ to the bis-oxidized form using the aminium radical chemical oxidant [N(C₆H₃Br₂)₃][SbF₆] ($E_{\text{ox}} = 1.14$ V vs F_c⁺/F_c in MeCN).

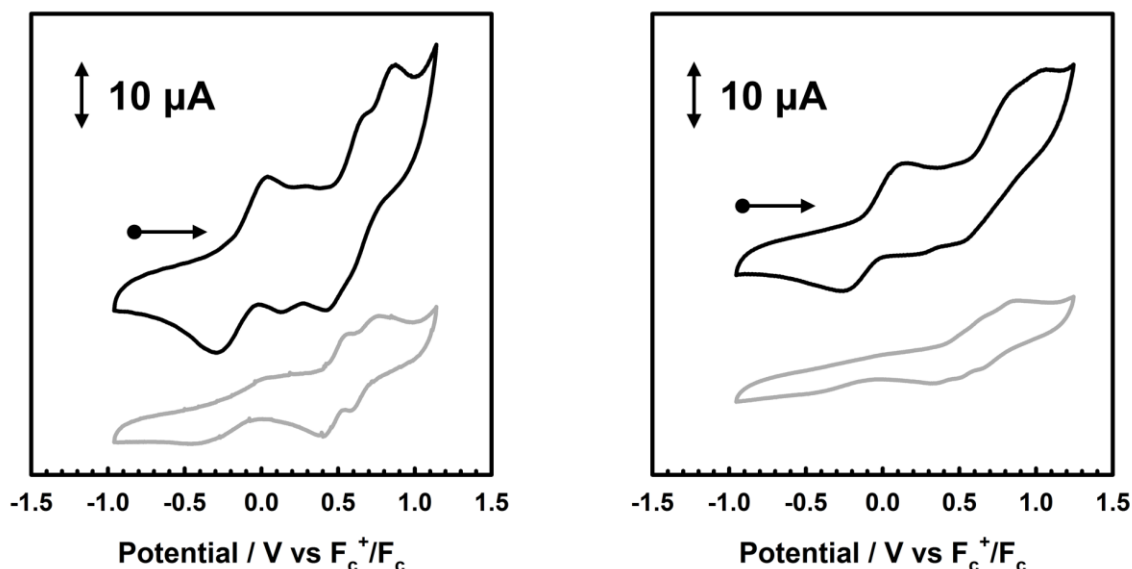


Figure 3.23. Cyclic voltammograms of: (left) [CoL¹-H₂O]⁺ and (right) [Co₂L²-2H₂O]²⁺ at 298 K (black) and 233 (grey). Conditions: 1 mM complex, 0.1 M ⁿBu₄NClO₄, scan rate 100 mV s⁻¹, CH₂Cl₂.

Sequential addition of oxidant under an inert atmosphere at 198 K resulted in clean conversion to the doubly oxidized species with isosbestic points at 12,000, 20,000, and 23,000 cm⁻¹ (Figure 3.24). The doubly oxidized species exhibits a broad shoulder at ~8,700 cm⁻¹ ($\epsilon = 1,700$ M⁻¹ cm⁻¹) and a more intense band at 15,000 cm⁻¹ ($\epsilon = 6,800$ M⁻¹ cm⁻¹), similar to the electronic spectra observed in other reports on Co(III)-phenoxyl radical species.³⁶⁹⁻³⁷¹ The overall spectral shape is in good agreement with that observed by Thomas and co-workers for an electrochemically generated doubly oxidized Co(Sal) complex.³⁵⁵ Furthermore, the EPR spectra for the doubly oxidized species consists of an $S = \frac{1}{2}$ signal centered at $g = 2.00$ (Figure 3.25). A g value that is slightly lower than the free electron g value ($g_e = 2.0023$) is common in Co(III) complexes bearing a phenoxyl radical, and thus lends support to this electronic structure description for the doubly

oxidized complex herein.^{369, 372-374} This is further emphasized by the appearance of a ^{57}Co hyperfine interaction, observed as shoulders on the $S = \frac{1}{2}$ peak, although not fully resolved due to broadening of the experimental spectrum. The hyperfine coupling is on the order of ~ 1.2 mT, which is in good agreement with hyperfine coupling constants observed in the EPR spectra of other Co(III)-phenoxy radical complexes.^{369, 371}

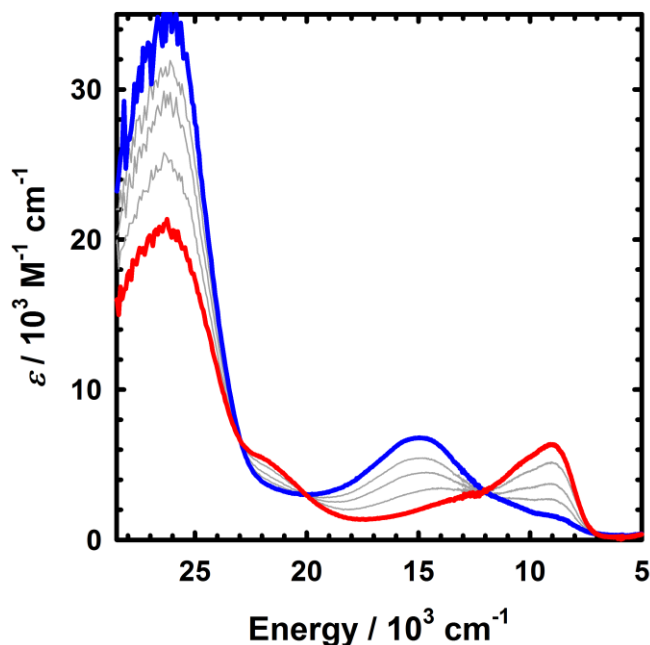


Figure 3.24. Oxidation titration of $[\text{CoL}^1\text{-H}_2\text{O}]^+$ (red) to the doubly oxidized species (blue) with the chemical oxidant $[\text{N}(\text{C}_6\text{H}_3\text{Br}_2)_3][\text{SbF}_6]$. Intermediate grey lines are measured upon sequential addition of oxidant during the titration. Conditions: CH_2Cl_2 and 198 K.

The experimental evidence for an electronic structure consisting of a Co(III) metal centre bound to a phenoxy radical is further corroborated by DFT analysis on the doubly oxidized species with two axially bound water molecules, $[\text{CoL}^1\text{-2H}_2\text{O}]^{2+}$. The spin-density plot of DFT-optimized $[\text{CoL}^1\text{-2H}_2\text{O}]^{2+}$ is depicted in Figure 3.26, 98% of which is localized to the phenyl substituted side of the salen ligand. This is interesting as the Hammett parameters would suggest that the tBu substituted side of the molecule would be easiest to oxidize ($\sigma_{para} = -0.20$ for tBu vs. -0.01 for phenyl). It may be that the phenyl substituent stabilizes the ensuing electron hole through extended ‘delocalization’ despite the higher Hammett parameter. This result further emphasizes that double oxidation of CoL^1 results in a genuine Co(III)-phenoxy radical electronic structure.

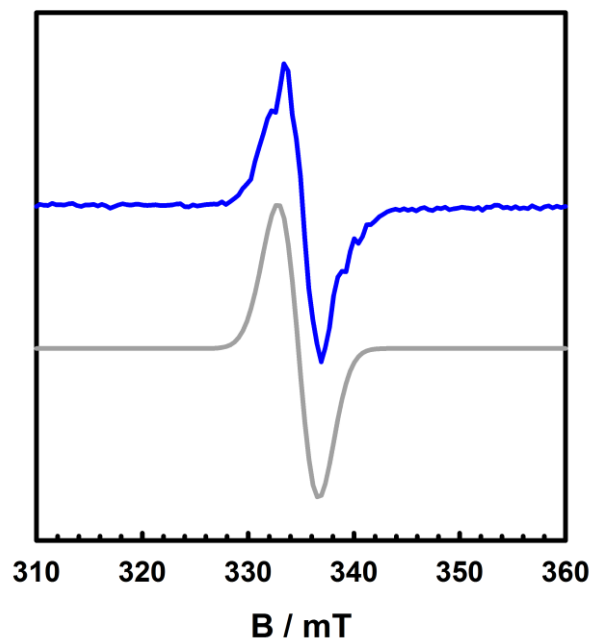


Figure 3.25. X-band EPR spectrum of doubly oxidized **CoL¹** (blue) in frozen CH₂Cl₂ with $g = 2.00$ (blue). Simulation (grey).

Conditions: frequency = 9.378; power = 2.0 mW; modulation frequency = 100 kHz; modulation amplitude = 0.6 mT; $T = 100$ K.

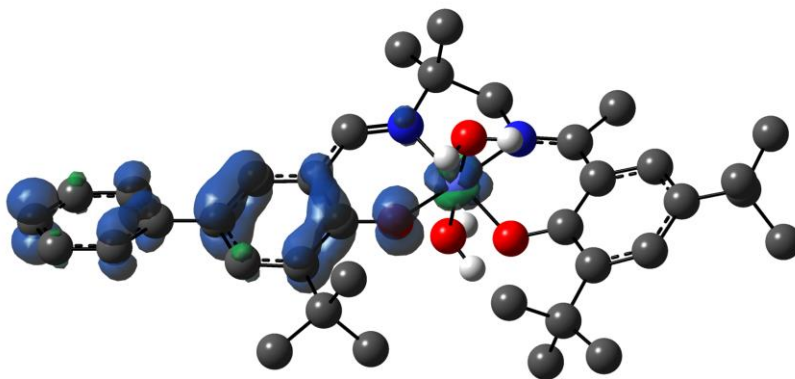


Figure 3.26. Spin-density plot of the dication **[CoL¹-2H₂O]²⁺**, 98% spin-density localized to the salen ligand.

3.3. Discussion and Summary

Neutral complexes **CoL**¹ and **Co₂L**² were prepared, and characterization of both complexes is consistent with the formation of low-spin d⁷ Co(II) centres bound to dianionic, closed-shell salen ligands on the basis of EPR, NMR and X-ray diffraction techniques. The central Co ion in **CoL**¹ exists in a slightly distorted square planar environment in the solid state. This distortion is also present in the bimetallic complex **Co₂L**². Of particular interest is the lack of spin-spin coupling between the two metal-localized unpaired spins in **Co₂L**². Characterization techniques such as CV, vis-NIR, and EPR all display a doubling of spectral intensities relative to **CoL**¹, consistent with a description of **Co₂L**² having two independent metal-salen units. Although solid-state magnetic SQUID data do suggest limited coupling at low temperature, the high magnetic anisotropy in the system prevents more detailed analysis. These results agree well with the expected findings based on the large intramolecular metal-metal separation distance of ca. 10 Å between the two Co centres in the complex.

The geometric and electronic structure of oxidized analogues were studied, using [**CoL**¹-H₂O]⁺ to aid in the characterization of [**Co₂L**²-2H₂O]²⁺. Upon oxidation **CoL**¹ gains an apically bound water molecule, in similar fashion to the structure reported by Thomas and co-workers.³⁵⁵ Unfortunately, we were unable to obtain X-ray quality crystals of [**Co₂L**²-2H₂O]²⁺ likely due to the many possible conformers the molecule can adopt as well as the presence of two SbF₆⁻ counterions. However, on the basis of characterization data, **Co₂L**² also gains two water molecules upon oxidation, presumably one apically bound to each of the two Co centres in the complex.

Oxidation of **CoL**¹ to [**CoL**¹-H₂O]⁺ affords a complex with significant ligand radical character. Solid-state magnetism data for [**CoL**¹-H₂O][SbF₆] can be fit to either an intermediate-spin Co(III) complex or a low-spin d⁷ Co(II) ligand radical complex with weak antiferromagnetic coupling ($J = -5.2(1) \text{ cm}^{-1}$) between the metal and ligand (Figure 3.14). DFT calculations predict the triplet state to be slightly lower in energy (2.6 kcal mol⁻¹) in comparison to the BS antiferromagnetically coupled solution. Interestingly, the intermediate-spin Co(III) complex (↑↑Co³⁺-L), low-spin Co(II) ligand radical (↑Co²⁺-↑L[•]), and high-spin (↑↑↑Co²⁺-↓L[•]) initial guesses converge to the same triplet electronic solution. Further analysis of the DFT triplet solution shows this to be a mixture of both the (↑↑Co³⁺-L) and (↑Co²⁺-↑L[•]) electronic isomers with ca. 75% of the spin density residing on Co. This

result is in agreement with paramagnetic ^1H NMR data analysis by Kurahashi and Fujii.²⁶⁰ Further oxidation of $[\text{CoL}^1\text{-H}_2\text{O}]^+$ affords the doubly oxidized species with an electronic structure that is best described as a low spin Co(III) ion bound to a phenoxyl radical. Isosbestic points in the vis-NIR indicate clean conversion from the singly to doubly oxidized species, while EPR and DFT analyses confirm the presence of a Co(III)-phenoxyl radical electronic structure.

While two separate one-electron processes were observed in the CV spectrum of Ni_2L^2 (**3** in Chapter 2),²¹⁶ a single two electron process is observed for Co_2L^2 (Figure 3.7). This result suggests that the locus of oxidation in these approximately geometrically equivalent systems differs, facilitating weak coupling in the case of Ni_2L^2 . Comparison of the predicted spin-densities of the doubly oxidized $[\text{Ni}_2\text{L}^2]^{2+}$ and $[\text{Co}_2\text{L}^2]^{2+}$ systems shows that the locus of oxidation is more contracted in the case of the Co derivative with the majority of the spin-density centered on the Co and coordinating atoms. In the case of Ni, the spin density is extensively delocalized across the salen moieties, providing a mechanism for increased communication between the two salen units.²¹⁶

Further evidence for ligand radical character in these systems is evident from the low-energy transitions of moderate intensity in the vis-NIR spectrum of both $[\text{CoL}^1\text{-H}_2\text{O}]^+$ and $[\text{Co}_2\text{L}^2\text{-2H}_2\text{O}]^{2+}$. TD-DFT calculations were employed to further investigate the nature of these electronic transitions. For $[\text{CoL}^1\text{-H}_2\text{O}]^+$ the predicted band is predominantly LMCT in character with significant ligand contribution to both donor and acceptor orbitals (Figure 3.20). The analogous one-electron oxidized Ni complex (**1** in Chapter 2)²¹⁶ displays two much more intense low-energy bands ($\lambda_{\text{max}} = 9,100 \text{ cm}^{-1}$, $\epsilon = 9,200 \text{ M}^{-1} \text{ cm}^{-1}$ and $\lambda_{\text{max}} = 4,500 \text{ cm}^{-1}$, $\epsilon = 27,700 \text{ M}^{-1} \text{ cm}^{-1}$) assigned as ligand-ligand charge transfer (LLCT) bands. The LMCT character of the low-energy band for $[\text{CoL}^1\text{-H}_2\text{O}]^+$ results in less overlap between the donor and acceptor orbitals in comparison to the Ni derivative, resulting in lower intensity.³⁷⁵

The electronic spectrum of $[\text{Co}_2\text{L}^2\text{-2H}_2\text{O}]^{2+}$ displays a doubling of spectral intensities across all wavelengths in comparison to $[\text{CoL}^1\text{-H}_2\text{O}]^+$. The low-energy envelope of transitions was also investigated by TD-DFT calculations. Two low-energy transitions are predicted, which fall under the experimentally broad band (Figure 3.9 and Figure 3.22), and like $[\text{CoL}^1\text{-H}_2\text{O}]^+$, both transitions are best described as LMCT transitions on the basis of AOMix decompositions analysis. The analogous Ni dimer

complex exhibits two intense bands ($\lambda_{\max} = 4,890 \text{ cm}^{-1}$, $\epsilon = 26\,500 \text{ M}^{-1} \text{ cm}^{-1}$ and $\lambda_{\max} = 4,200 \text{ cm}^{-1}$, $\epsilon = 21,200 \text{ M}^{-1} \text{ cm}^{-1}$) in place of the single low-energy band in the oxidized monomeric Ni complex (Chapter 2).²¹⁶ These bands are equally spaced in comparison to the band observed for the oxidized monomeric complex ($\sim 4,500 \text{ cm}^{-1}$) and are attributed to exciton coupling in the excited state.^{238-239, 376} The broad low-energy band observed in the spectrum of $[\text{Co}_2\text{L}^2\text{-2H}_2\text{O}]^{2+}$ does not display resolvable splitting, despite two closely spaced transitions predicted by TD-DFT calculations. The interaction between chromophores, leading to exciton coupling, is a function of the transition moment dipole of the monomer and the angle and distance between the transition moment dipoles in the dimer (see Chapter 2).^{238-239, 377} For an oblique dimer arrangement, as in this case, two bands are expected if certain criteria can be met.^{238, 377-378} The low band intensity, a result of the LMCT character and contracted donor and acceptor orbitals, likely limits exciton coupling in the case of $[\text{Co}_2\text{L}^2\text{-2H}_2\text{O}]^{2+}$. Overall, we have shown in this chapter that the bimetallic Co complex, Co_2L^2 , can be doubly oxidized to the dication and that each salen unit remains effectively isolated in both the neutral and oxidized structures.

3.4. Experimental

3.4.1. Materials

All chemicals used were of the highest grade available and were further purified whenever necessary.³⁷⁹ Literature methods were followed to prepare the ligands, 1-(2-hydroxy-3,5-di-*tert*-butylphenyl)methyl-2,5-diimine-4,4-dimethyl-6-(2-hydroxy-3-*tert*-butyl-5-phenyl)phenyl (H_2L^1) and 1,2-bis(1-(2-hydroxy-3,5-di-*tert*-butylphenyl)methyl-2,5-diimine-4,4-dimethyl-6-(2-hydroxy-3,5-di-*tert*-butylphenyl))benzene (H_4L^2)²¹⁶ as well as the aminium radical chemical oxidant $[\text{N}(\text{C}_6\text{H}_3\text{Br}_2)_3][\text{SbF}_6]$.³⁰⁶

3.4.2. Instrumentation

^1H NMR spectra were recorded on a Bruker AV-500 instrument. Solution paramagnetic susceptibilities were calculated using the Evans method.¹¹²⁻¹¹³ Mass spectra (positive ion) were obtained on a Bruker Microflex LT MALDI-TOF MS instrument. Elemental analyses (C, H, N) were performed by Mr. Farzad Haftbaradaran and Mr. Paul Mulyk at Simon Fraser University on a Carlo Erba EA1110 CHN elemental analyzer. Electronic spectra were recorded on a Cary 5000 spectrophotometer with a custom-

designed immersion fiber-optic probe with variable path-length (1 and 10 mm; Hellma, Inc.). Constant temperatures were maintained by a dry ice/acetone bath. Solvent contraction was accounted for in all variable-temperature (VT) studies. Cyclic voltammetry (CV) was performed on a PAR-263A potentiometer, equipped with a Ag wire reference electrode, a Pt disk working electrode, and a Pt counter electrode with ${}^n\text{Bu}_4\text{NClO}_4$ (0.1 M) solution in CH_2Cl_2 . Decamethylferrocene was used as an internal standard. Electron paramagnetic resonance (EPR) spectra were collected using a Bruker EMXplus spectrometer operating with a premiumX X-band microwave bridge and an HS resonator. Low-temperature measurements of frozen solutions used a Bruker ER 4112HV helium temperature-control system and continuous flow cryostat. Samples for X-band EPR measurements were placed in 4 mm outer-diameter sample tubes with sample volumes of $\sim 250 \mu\text{L}$.

3.4.3. X-ray Structure Determination

All crystal structure plots were produced using ORTEP-3³⁰⁹ and rendered with POV-Ray (v.3.6.2).³¹⁰ A summary of the crystal data and experimental parameters for structure determinations is given in Table 3.1.

3.4.3.1. CoL¹

Single-crystal X-ray crystallographic analysis of a block-red crystal of **CoL¹** was performed at the Advanced Light Source (Lawrence Berkeley National Laboratory) using synchrotron radiation tuned to $\lambda = 0.7749 \text{ \AA}$. Intensity data were collected at 296 K on a D8 goniostat equipped with a Bruker APEXII CCD detector at Beamline 11.3.1. For data collection frames were measured for a duration of 1 s at 0.3° intervals of ω with a maximum 2θ value of $\sim 60^\circ$. The data frames were collected using the program APEX2 and processed using the program SAINT routine within APEX2. The data were corrected for absorption and beam corrections based on the multiscan technique as implemented in SADABS. The structure was solved by the intrinsic phasing method,³¹¹ and subsequent refinements were performed using ShelXle.³¹² All non-hydrogen atoms were refined anisotropically. All C-H hydrogen atoms were placed in calculated positions but were not refined. CCDC number: 1448640.

3.4.3.2. [CoL¹-H₂O]⁺

Crystallographic analysis of [CoL¹-H₂O]⁺ was performed on a Bruker APEX II Duo diffractometer with graphite monochromated Cu K α radiation. A dark green block crystal was mounted on a 150 μ m MiteGen sample holder. The data were collected at 293 K to a maximum 2 θ value of \sim 60°. Data were collected in a series of ϕ and ω scans in 0.50° widths with 10.0 s exposures. The crystal-to-detector distance was 50 mm. The structure was solved by intrinsic phasing³¹¹ and refined by least-squares procedures using Crystals.³⁸⁰ [CoL¹-H₂O]⁺ crystallizes with one molecule of CH₂Cl₂ solvent in the asymmetric unit. All non-hydrogen atoms were refined anisotropically. All C-H hydrogen atoms were placed in calculated positions but were not refined. CCDC number: 1448642.

3.4.3.3. Co₂L²

Crystallographic analysis of Co₂L² was performed on a Bruker X8 APEX II diffractometer with graphite monochromated Mo K α radiation. An irregular red crystal was mounted on a glass fiber. The data were collected at a temperature of 103.15 \pm 0.1 K to a maximum 2 θ value of 45.0°. Data were collected in a series of ϕ and ω scans in 0.50° widths with 30.0 s exposures. The crystal-to-detector distance was 40 mm. The complex crystallizes as a two-component twin with the two components related by a 180° rotation about the (0–0.5 1) reciprocal axis. Data were integrated for both twin components, including both overlapped and non-overlapped reflections. The structure was solved by direct methods using non-overlapped data from the major twin component. Subsequent refinements were performed using an HKLF5 format data set containing complete data from component 1 and any overlapped reflections from component 2. The material crystallizes with two Co₂L² complexes and hexane solvent in the asymmetric unit. The solvent molecules are disordered and cannot be modelled properly; thus the PLATON/SQUEEZE³¹³ program was used to generate a “solvent-free” HKLF5 format data set. The equivalent of four molecules of hexane were removed from the asymmetric unit. All non-hydrogen atoms were refined anisotropically. All hydrogen atoms were included in calculated positions but were not refined. The batch scale refinement showed a roughly 57:43 ratio between major and minor twin components. CCDC number: 1448641.

3.4.4. Solid-State Magnetism

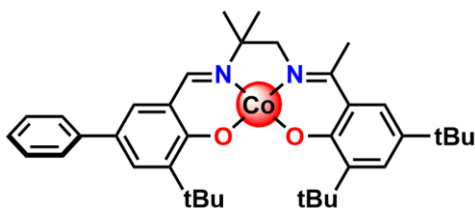
The magnetic properties of Co_2L^2 , $[\text{CoL}^1\text{-H}_2\text{O}]^+$, and $[\text{Co}_2\text{L}^2\text{-2H}_2\text{O}]^{2+}$ were measured using a Quantum Design MPMS-XL7 SQUID magnetometer operating between 1.8 and 300 K for direct-current (dc) applied fields ranging between -7 and 7 T. The measurements were performed on polycrystalline samples of 16.2, 23.7, and 20.4 mg, for Co_2L^2 , $[\text{CoL}^1\text{-H}_2\text{O}]^+$, and $[\text{Co}_2\text{L}^2\text{-2H}_2\text{O}]^{2+}$ respectively, wrapped in a polyethylene membrane. The data were corrected for the diamagnetic contribution of the sample holder and of the complexes.

3.4.5. Theoretical Calculations

Geometry optimizations were performed using the Gaussian 09 program (Revision D.01),³¹⁴ the B3LYP functional,³¹⁵⁻³¹⁶ and the 6-31g(d) basis set on all atoms as this functional/basis set combination has afforded a good match to experimental metrical data in similar salen systems.²¹⁴⁻²¹⁶ Frequency calculations at the same level of theory confirmed that the optimized structures were located at a minimum on the potential energy surface. Single-point calculations for energetic analysis were performed with the B3LYP functional and the TZVP basis set of Ahlrichs on all atoms.³¹⁷⁻³¹⁸ Broken-symmetry (BS) density functional theory (DFT) calculations were performed with the same functional and basis set.³⁸¹⁻³⁸² The intensities of the 30 lowest-energy electronic transitions were calculated by TD-DFT³¹⁹⁻³²⁰ at the B3LYP/TZVP level with a polarized continuum model (PCM) for CH_2Cl_2 .³²¹⁻³²⁴ AOMix was used for determining atomic orbital compositions employing Mulliken population analysis.³⁶⁸

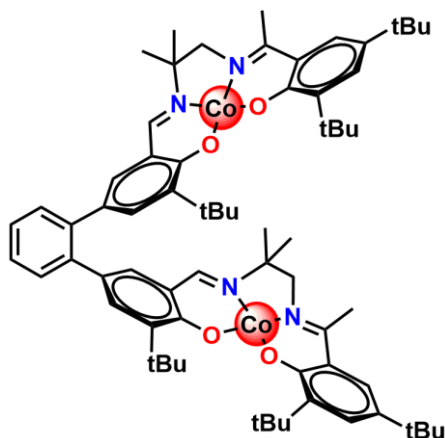
3.4.6. Synthesis

1-(2-hydroxy-3,5-di-*tert*-butylphenyl)methyl-2,5-diimine-4,4-dimethyl-6-(2-hydroxy-3-*tert*-butyl-5-phenyl)phenyl cobalt (II) (CoL^1):



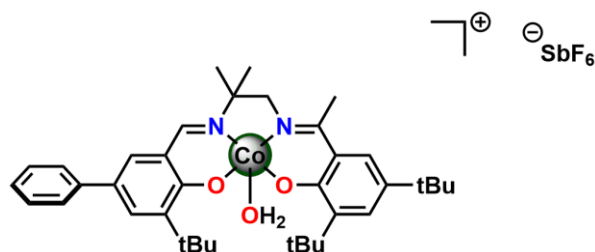
To a solution of **H₂L¹** (340 mg, 0.6 mmol) in diethyl ether (4 mL) was added a Co(OAc)₂·4H₂O solution (155 mg, 0.6 mmol) in methanol (4 mL) under anaerobic conditions. The yellow solution immediately changed colour to dark red upon addition of the metal salt. The mixture was stirred at room temperature until a dark red precipitate formed, which was collected *via* suction filtration and dried *in vacuo*. The precipitate was recrystallized by slow diffusion of methanol into a concentrated CH₂Cl₂ solution to afford block red crystals. Yield: 290 mg, 74%. Anal. Cald. (%) for C₃₇H₄₈N₂O₂Co: C 72.65; H 7.91; N 4.58; found: C 72.97; H 7.63; N 4.64. MALDI-MS *m/z*: 611.30 (100%). Solution magnetic moment (¹H Evans method): $\mu_{\text{eff}} = 1.75 \mu_{\text{B}}$.

1,2-bis(1-(2-hydroxy-3,5-di-*tert*-butylphenyl)methyl-2,5-diimine-4,4-dimethyl-6-(2-hydroxy-3,5-di-*tert*-butylphenyl))benzene-di-cobalt (II) (**Co₂L²**):



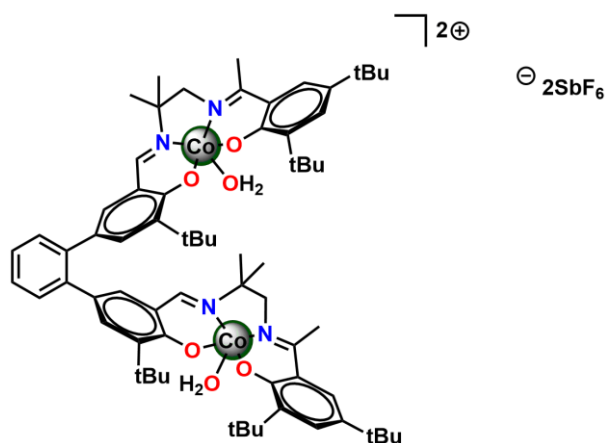
To a solution of **H₄L²** (400 mg, 0.4 mmol) in diethyl ether (5 mL) was added a Co(OAc)₂·4H₂O solution (190 mg, 0.8 mmol) in methanol (5 mL) under anaerobic conditions. The solution immediately turned from yellow to red upon addition of the metal salt. The mixture was stirred at room temperature until a dark red precipitate formed which was collected *via* suction filtration and dried *in vacuo*. The precipitate was recrystallized by slow diffusion of methanol into a concentrated CH₂Cl₂ solution to afford block red crystals. Yield: 200 mg, 45%. MALDI-MS *m/z*: 1144.48 (100%). Anal. Cald. (%) for C₆₈H₉₀N₄O₄Co₂: C 67.36; H 7.54; N 4.55; found: C 67.25; H 7.61; N 4.27. Solution magnetic moment (¹H Evans method): $\mu_{\text{eff}} = 2.75 \mu_{\text{B}}$.

1-(2-hydroxy-3,5-di-*tert*-butylphenyl)methyl-2,5-diimine-4,4-dimethyl-6-(2-hydroxy-3-*tert*-butyl-5-phenyl)phenyl aqua cobalt ([**CoL¹-H₂O**]⁺):



To a solution of **CoL**¹ (110 mg, 0.18 mmol) in CH₂Cl₂ (3 mL) was added a AgSbF₆ solution (60 mg, 0.18 mmol) in CH₂Cl₂ (3 mL) under anaerobic conditions. The solution immediately turned from red to dark green upon addition of oxidant and was stirred at room temperature for 30 minutes until a silver mirror formed. The reaction mixture was filtered through celite and concentrated *in vacuo*. The crude material was redissolved in CH₂Cl₂ (2 mL), and pentane was added (2 mL) to precipitate a dark green powder. Crystals suitable for X-ray diffraction analysis were grown by slow diffusion of pentane into a concentrated CH₂Cl₂ solution. Yield: 132 mg, 85%. Anal. Cald (%) for C₃₇H₅₀N₂O₃CoSbF₆•H₂O: C 50.30; H 5.93; N 3.17; found: C 49.92; H 5.90; N 2.97. Solution magnetic moment (¹H Evans method) $\mu_{\text{eff}} = 2.62 \mu_{\text{B}}$.

1,2-bis(1-(2-hydroxy-3,5-di-*tert*-butylphenyl)methyl-2,5-diimine-4,4-dimethyl-6-(2-hydroxy-3,5-di-*tert*-butylphenyl))benzene-di-cobalt ([Co₂L²-2H₂O]²⁺):



To a solution of **Co₂L²** (150 mg, 0.13 mmol) in CH₂Cl₂ (5 mL) was added a AgSbF₆ solution (90 mg, 0.26 mmol) in CH₂Cl₂ (5 mL) under anaerobic conditions. The solution immediately turned from red to dark green upon addition of oxidant and was stirred at room temperature for 30 minutes until a silver mirror formed. The reaction mixture was filtered through celite and concentrated *in vacuo*. The crude solid was redissolved in

CH₂Cl₂ (2 mL), and pentane was added (2 mL) to afford a green precipitate. Yield: 168 mg, 70%. Anal. Calcd. (%) for C₆₈H₉₀N₄O₄Co₂Sb₂F₁₂•2H₂O: C 49.41; H 5.73; N 3.39; found: C 49.12; H 5.47; N 3.40.

Chapter 4. Tuning Electronic Structure to Control Manganese Nitride Activation

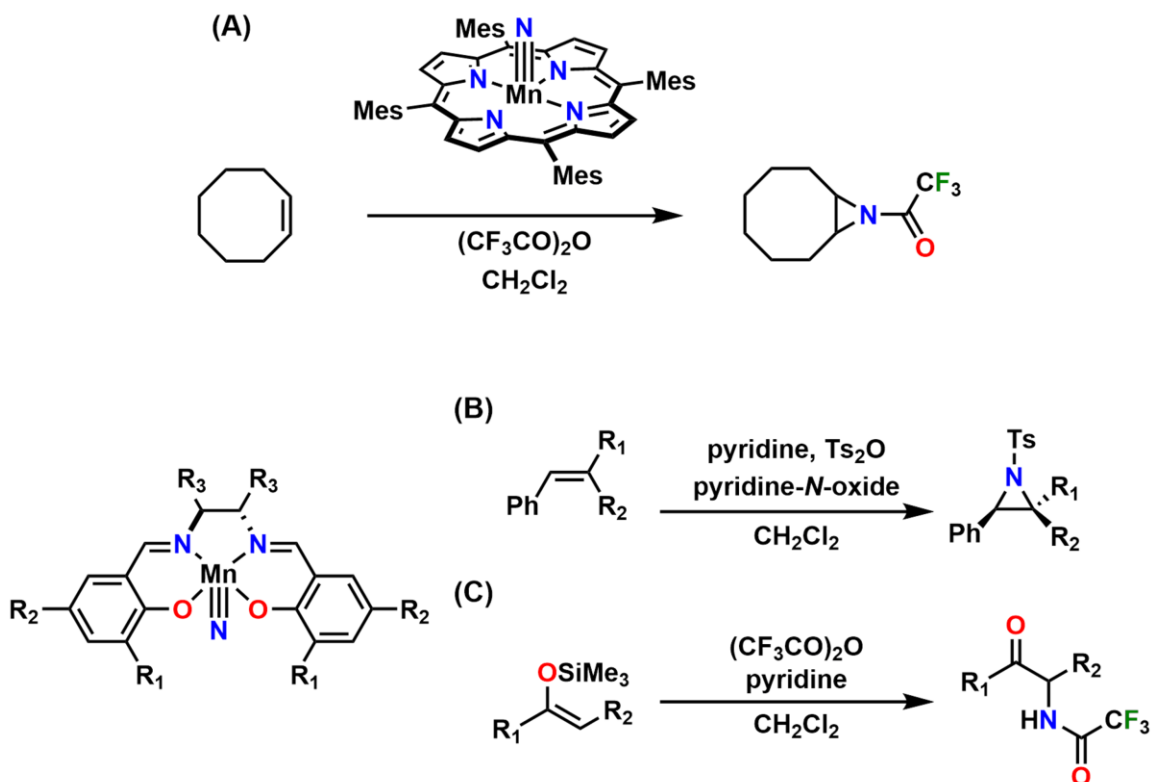
Adapted from: Clarke, R.M.; and Storr, T. *J. Am. Chem. Soc.*, **2016**, *138*, 15299-15302.

4.1. Introduction

Transition metal complexes bearing terminal nitride (N^{3-}) ligands are of significant interest due to the key role they may play in the nitrogen fixation process,³⁸³⁻³⁸⁴ their importance in stoichiometric nitrene transfer reactions,³⁸⁵⁻³⁸⁶ and their utility as catalysts.³⁸⁷⁻³⁸⁸ In the context of nitrogen fixation (both biological and industrial),³⁸⁹ there have been a number of important reports of Fe nitride complexes in oxidation states IV,³⁹⁰⁻³⁹⁶ V,³⁹⁷⁻³⁹⁹ and VI,⁴⁰⁰ and their reactivities are well documented.^{394, 396, 401} In many cases the reactivity of terminal nitride complexes can be rationalized by the nucleophilicity (or electrophilicity) of the nitride ligand, which is determined by the metal, oxidation state, and ancillary ligands.⁴⁰² Group 8 nitrides of Ru(VI) and Os(VI) react with a variety of nucleophiles as a result of population of $\text{M}\equiv\text{N} \pi^*$ antibonding orbitals in the transition state.⁴⁰³⁻⁴¹¹ In addition, reactive electrophilic group 9 terminal nitride complexes of Co,⁴¹² Rh,⁴¹³ and Ir⁴¹⁴⁻⁴¹⁵ have been reported, and a transient terminal nitride of Ni has recently been described.⁴¹⁶ In contrast to the reactivity of late metal nitrides, early metal nitrides are generally more stable and are often a product of N_2 activation reactions.⁴¹⁷⁻⁴¹⁹ In some cases, early transition metal nitrides have been demonstrated to react as nucleophiles.⁴²⁰⁻⁴²¹ Terminal nitrides of Mn(V) exhibit reactivity intermediate between their early and late transition metal analogues, and have found utility as nitrene transfer reagents.³⁸⁶ Seminal work by Groves and co-workers demonstrated nitrene transfer from a nitridomanganese(V) porphyrin complex to cyclooctene upon activation with trifluoroacetic anhydride (TFAA),⁴²² and subsequent studies demonstrated the utility of nitridomanganese(V) salen complexes in the transfer of nitrene groups to alkenes and silyl enol ethers (Scheme 4.1).⁴²³⁻⁴²⁶ Despite the synthetic utility of nitridomanganese(V) complexes, all examples require the addition of a Lewis acid such as TFAA or *p*-toluenesulfonic anhydride, likely to activate the nitride by conversion to the corresponding imide before group transfer to the substrate.⁴²⁷ Nitridomanganese(V) salen complexes have found further utility as reagents in the synthesis of other metal-nitrido fragments.⁴²⁸⁻

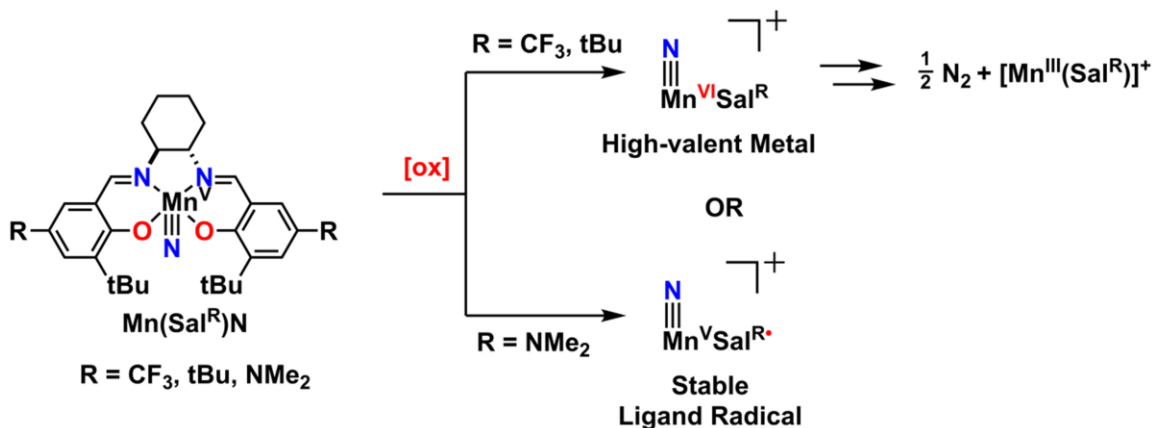
433

Scheme 4.1. Select examples of nitrene transfer reactions from nitridomanganese(V) complexes. (A) nitridomanganese(V) porphyrins for the aziridination of cyclooctene; (B-C) nitridomanganese(V) salens for nitrene transfer to alkenes and silyl enol ethers.



In this chapter, the oxidative activation of a series of Mn(V) nitrides is investigated in which the resulting reactivity is tuned by the electronic properties of the ancillary ligand (Scheme 4.2). Metal complexes of salen-type ligands have the potential for redox-activity at either the metal or the ligand upon one-electron oxidation, permitting investigation of the resultant reactivity upon oxidation of either the metal or ligand in this series of nitridomanganese(V) complexes.

Scheme 4.2. Oxidation of Mn(V) nitride complexes to afford high-valent metal or ligand radical electronic structures; subsequent homocoupling affords N₂ in the case of the Mn(VI) complexes.



Initial oxidation experiments on **Mn(Sal^{tBu})N** in the presence of 1 equivalent of AgSbF₆ resulted in an immediate colour change from green to orange-brown, and characterization of the recrystallized product showed quantitative formation of the high-spin Mn(III) complex **[Mn(Sal^{tBu})]⁺[SbF₆⁻]** (see Section 4.4.3), suggesting that oxidation of **Mn(Sal^{tBu})N** resulted in rapid loss of the nitride ligand to afford the crystallographically characterized **[Mn(Sal^{tBu})]⁺[SbF₆⁻]** product. Lau has extensively studied the N-N homocoupling reactivity of various complexes of Ru(VI), Os(VI), and Mn(V) with Schiff base ligands.⁴³⁴ While both Ru(VI) and Os(VI) complexes undergo N-N coupling in the presence of N-heterocyclic ligands,^{410, 435-436} Mn nitrides have not been observed to couple N₂ directly.⁴³⁷ Additional examples of dinitrogen coupling reactions from transition metal nitrides include Fe(IV/V) complexes,^{391, 438} an open-shell Ir complex and its analogous Rh complex,⁴¹³⁻⁴¹⁵ as well as Os and Mo complexes (Figure 4.1).⁴³⁹

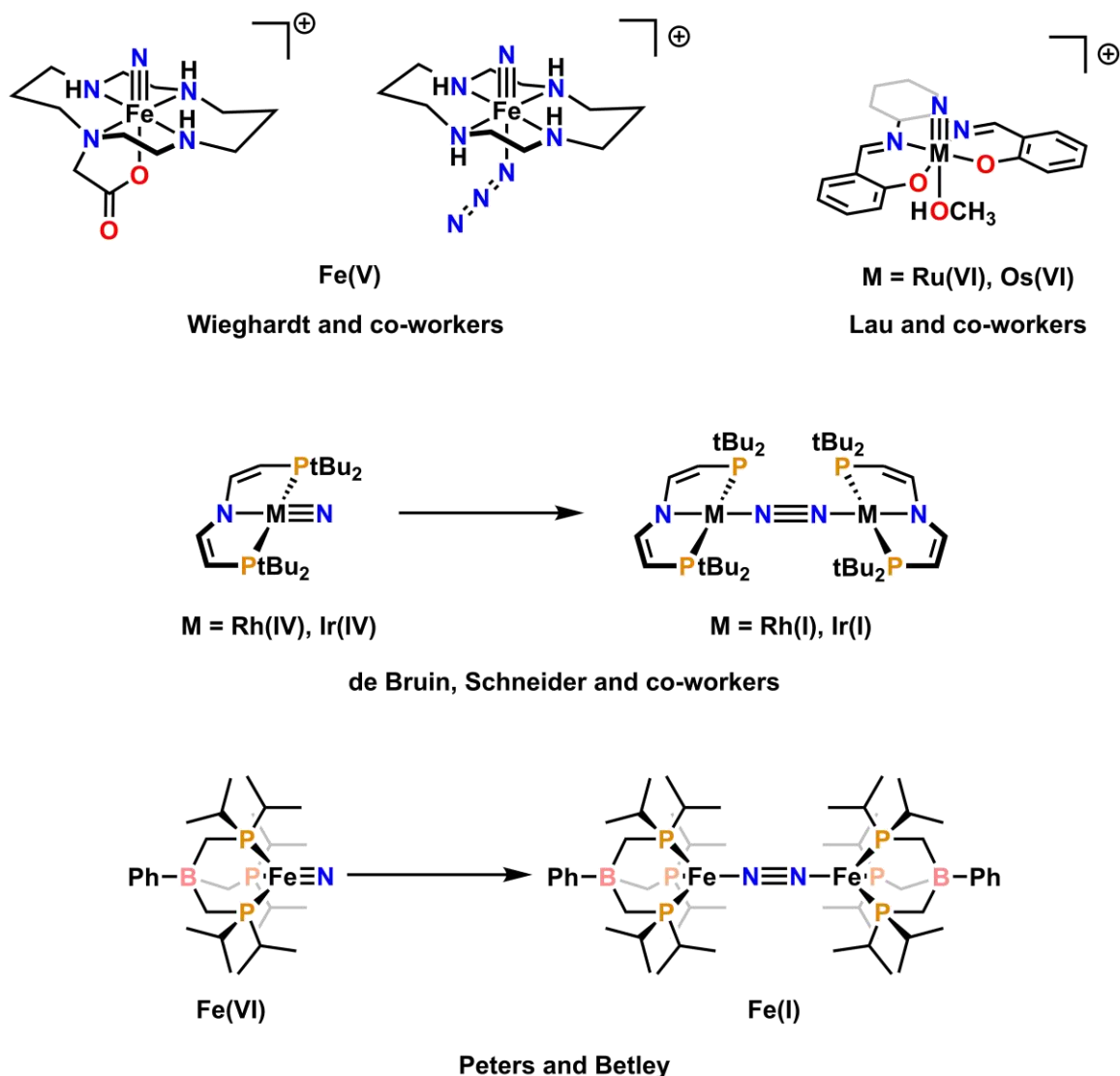


Figure 4.1. Select examples of coupling of terminal nitrido ligands to yield N₂ or μ -N₂ bridged dimeric species.

4.2. Results

4.2.1. Synthesis

Mn(Sal^{tBu})N and **Mn(Sal^{CF₃})N** were prepared via oxidation of the corresponding Mn chloride complexes with NaOCl in the presence of NH₄OH according to the method reported by Carreira and co-workers (Scheme 4.3).⁴²⁶ While **Mn(Sal^{NMe₂})N** could also be prepared following this procedure, isolated yields were low (<20%), and thus photolysis of the precursor azido complex was employed, which afforded **Mn(Sal^{NMe₂})N** in higher yields (Scheme 4.4).⁴⁴⁰ All three complexes are isolated as microcrystalline solids with

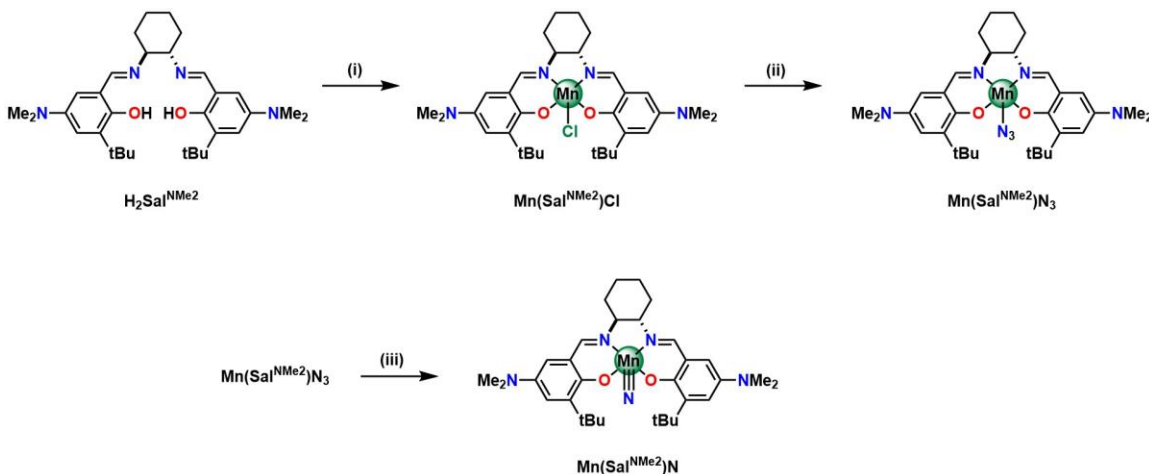
diamagnetic d^2 ($|^1A_1, d_{xy}\rangle$)⁴⁴¹ ground states, typical of Mn(V) nitrides in (pseudo)tetragonal ligand fields (see Appendix C – Figure C1 for ¹H NMR spectra).⁴⁴²⁻⁴⁴³

Scheme 4.3. Synthesis of Mn(Sal^{CF3})N.



Reaction conditions: (i) 2 equivalents Mn(OAc)₂·4H₂O, LiCl, EtOH; (ii) NH₄OH, NaOCl, 4:1 CH₂Cl₂/MeOH.

Scheme 4.4. Synthesis of Mn(Sal^{NMe2})N.



Reaction conditions: (i) 2 equivalents Mn(OAc)₂·4H₂O, LiCl, EtOH; (ii) NaN₃ (aq), 1:1 CH₂Cl₂/MeOH; (iii) hv, C₆H₆.

4.2.2. Solid-State Characterization

The solid-state structures of the two new nitridomanganese(V) complexes **Mn(Sal^{CF3})N** and **Mn(Sal^{NMe2})N** are presented in Figure 4.2 and Figure 4.3, respectively; while the solid-state structure of **Mn(Sal^{tBu})N** was previously reported by Jørgensen.⁴⁴⁴ Select crystallographic data is presented in Table 4.1. All three complexes adopt a pseudo-square pyramidal geometry with the nitride ligand adopting the apical position and the central manganese ion puckered out of the N₂O₂ salen plane by ~0.5 Å (R = tBu, 0.507 Å; R = CF₃, 0.431 Å; R = NMe₂, 0.496 Å). As described in an analogous Cu salen complex with the CF₃ ligand, the O-Mn bond lengths are slightly elongated in this derivative due to

the reduced donating ability of the electron-deficient CF₃ salen ligand.¹²⁶ The Mn≡N bond lengths for both **Mn(Sal^{CF₃})N** (1.526 Å) and **Mn(Sal^{NMe₂})N** (1.514 Å) are in agreement with other reported nitridomanganese complexes with terminal nitride ligands. The shorter Mn≡N bond in **Mn(Sal^{NMe₂})N** could be a consequence of the increased electron density at the metal centre due to the strongly donating NMe₂ groups in this derivative.

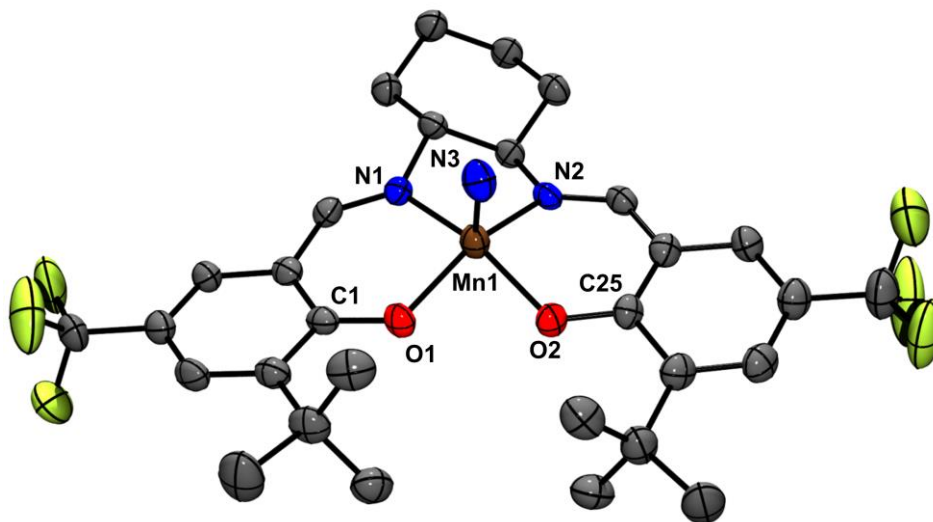


Figure 4.2. POV-Ray representation of **Mn(Sal^{CF₃})N**.

Thermal ellipsoids shown at 50% probability level. Hydrogen atoms omitted for clarity. Mn, brown; C, grey; O, red; N, blue; F, yellow-green. Selected interatomic distances [Å] and angles [deg]: Mn(1)-O(1): 1.917(3), Mn(1)-O(2): 1.922(3), Mn(1)-N(1): 1.950(4), Mn(1)-N(2): 1.961(4), Mn(1)-N(3): 1.526(5), O(1)-C(1): 1.297(6), O(2)-C(25): 1.303(6); Angles: O(1)-Mn(1)-O(2): 84.8(1), O(1)-Mn(1)-N(1): 91.2(2), O(1)-Mn(1)-N(2): 152.9(2), O(1)-Mn(1)-N(3): 106.0(2), O(2)-Mn(1)-N(2): 90.4(2), O(2)-Mn(1)-N(1): 155.6(2), O(2)-Mn(1)-N(3): 103.5(2), N(1)-Mn(1)-N(2): 82.3(2), N(1)-Mn(1)-N(3): 100.8(2), N(2)-Mn(1)-N(3): 101.0(2).

The solid-state structure of the reduced **[Mn(Sal^{tBu})]⁺[SbF₆]⁻** formed quantitatively via one-electron oxidation of **Mn(Sal^{tBu})N** is presented in Figure 4.4. The Mn(III) ion adopts a square planar geometry with the salen ligand, with a short Mn-F contact with the SbF₆⁻ counterion (2.255 Å).

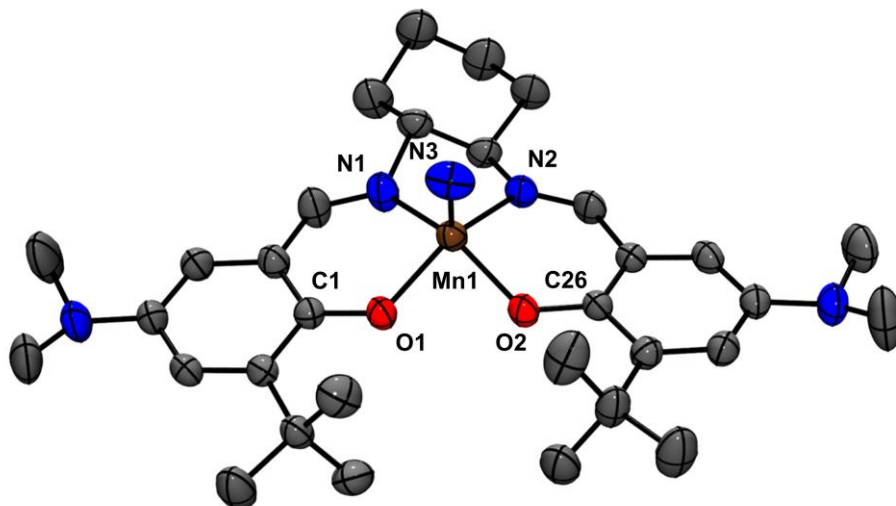


Figure 4.3. POV-Ray representation of $\text{Mn}(\text{Sal}^{\text{NMe}_2})\text{N}$.

Thermal ellipsoids shown at 50% probability level. Hydrogen atoms omitted for clarity. Mn, brown; C, grey; O, red; N, blue. Selected interatomic distances [Å] and angles [deg]: Mn(1)-O(1): 1.914(3), Mn(1)-O(2): 1.909(3), Mn(1)-N(1): 1.960(4), Mn(1)-N(2): 1.958(3), Mn(1)-N(3): 1.514(5), O(1)-C(1): 1.311(5), O(2)-C(26): 1.332(5); Angles: O(1)-Mn(1)-O(2): 83.2(1), O(1)-Mn(1)-N(1): 90.4(1), O(1)-Mn(1)-N(2): 149.4(1), O(1)-Mn(1)-N(3): 107.3(2), O(2)-Mn(1)-N(2): 90.3(1), O(2)-Mn(1)-N(1): 151.1(1), O(2)-Mn(1)-N(3): 106.6(2), N(1)-Mn(1)-N(2): 80.9(2), N(1)-Mn(1)-N(3): 102.2(2), N(2)-Mn(1)-N(3): 103.2(2).

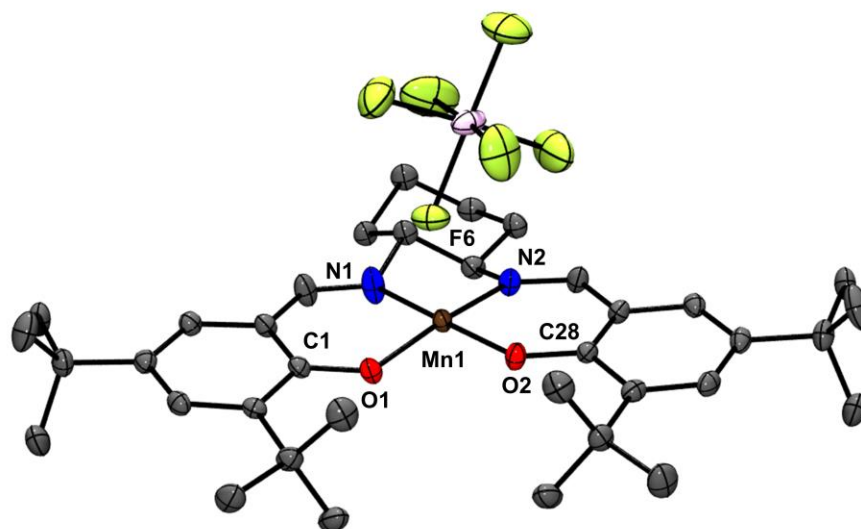


Figure 4.4. POV-Ray representation of $[\text{Mn}(\text{Sal}^{\text{tBu}})][\text{SbF}_6]$.

Thermal ellipsoids shown at 50% probability level. Hydrogen atoms and solvent omitted for clarity. Mn, brown; C, grey; O, red; N, blue; F, yellow-green; Sb, plum. Selected interatomic distances [Å] and angles [deg]: Mn(1)-O(1): 1.850(3), Mn(1)-O(2): 1.846(2), Mn(1)-N(1): 1.959(3), Mn(1)-N(2): 1.959(4), Mn(1)-F(6): 2.255(2), O(1)-C(1): 1.326(4), O(2)-C(28): 1.328(4); Angles: O(1)-Mn(1)-O(2): 93.0(1), O(1)-Mn(1)-N(1): 91.4(1), O(1)-Mn(1)-N(2): 167.6(1), O(1)-Mn(1)-F(6): 95.3(1), O(2)-Mn(1)-N(1): 92.2(1), O(2)-Mn(1)-N(1): 174.1(1), O(2)-Mn(1)-F(6): 93.5(1), N(1)-Mn(1)-N(2): 82.7(1), N(1)-Mn(1)-F(6): 90.0(1), N(2)-Mn(1)-F(6): 95.5(1).

Table 4.1. Selected crystallographic data for **Mn(Sal^{CF3})N**, **Mn(Sal^{NMe2})N**, and **[Mn(Sal^{tBu})]^{II}[SbF₆]**.

	Mn(Sal^{CF3})N	Mn(Sal^{NMe2})N	[Mn^{II}(Sal^{tBu})]^{II}[SbF₆]•CH₂Cl₂
Formula	C ₃₀ H ₃₄ F ₆ MnN ₃ O ₂	C ₃₂ H ₄₆ MnN ₅ O ₂	C ₃₇ H ₅₄ Cl ₂ F ₆ MnN ₂ O ₂ Sb
Formula weight	637.54	587.68	920.41
Space group	P2 ₁	P2 ₁ /n	P2 ₁ /c
a (Å)	13.66(2)	9.31(4)	17.49(14)
b (Å)	26.85(4)	28.13(11)	10.14(9)
c (Å)	24.51(4)	12.19(5)	24.39(2)
α (deg)	90	90	90
β (deg)	90.3(13)	102.81(15)	108.6(2)
γ (deg)	90	90	90
V [Å³]	8983.8(2)	3114(2)	4098.49
Z	12	4	4
T (K)	150	150	150
ρ_{calcd} (g cm⁻³)	1.414	1.253	1.492
λ (Å)	1.54178	0.71073	0.71073
μ (cm⁻¹)	4.199	0.460	1.158
R indices^a with I > 2.0σ(I) (data)	0.0514	0.0778	0.0461
wR₂	0.1223	0.1681	0.1059
R₁	0.0646	0.0940	0.0513
Goodness-of-fit on F²	0.976	1.267	1.051

^aGoodness-of-fit on *F*.

4.2.3. Electrochemistry

The redox processes of the three nitridomanganese(V) complexes were probed electrochemically (CV) in CH₂Cl₂ using tetra-*n*-butyl-ammonium perchlorate (^{*n*}Bu₄NClO₄) as the supporting electrolyte (Figure 4.5). The redox processes vs. ferrocenium/ferrocene (F_c⁺/F_c) are reported in Table 4.2. All three complexes display oxidation events at low potential, the first of which is tunable by ca. 490 mV and correlates well with the respective Hammett parameters of the *para* substituent (Figure 4.5 – inset).^{353, 445-446} Analysis of the scan-rate dependence suggested an electrochemical reaction mechanism (EC) for both the CF₃ and *t*Bu derivatives, while the NMe₂ redox couple remained quasi-reversible at all scan rates investigated (Figure 4.6). The full CV spectrum of **Mn(Sal^{tBu})N** exhibits an additional redox process at high potential (~0.75 V), however this process is not associated with the parent nitridomanganese(V) complex, but rather the reduced **[Mn(Sal^{tBu})]^{II}[SbF₆]** complex upon nitride loss after electrochemical oxidation (Appendix C – Figure C2). For the CF₃ derivative, this process is not observed in the electrochemical region accessible in CH₂Cl₂, likely due to the electron withdrawing CF₃ group. Both CF₃ and *t*Bu derivatives exhibit additional low potential reduction processes (~-0.66 V for R = CF₃ and ~-0.8 V for R = *t*Bu) which are attributed to reduction of the N₂ homocoupling

product (Appendix C – Figure C3). Interestingly, these potentials also scale according to the electron donating ability of the *para* substituent, with the more electron withdrawing CF₃ group, now *easier* to reduce, appearing at higher potentials than the more electron donating tBu substituent.

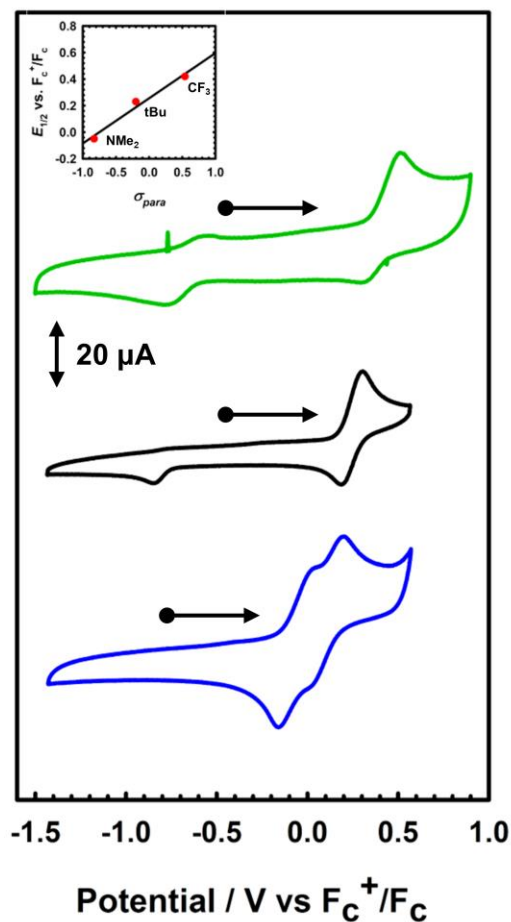


Figure 4.5. Cyclic voltammograms of **Mn(Sal^R)N**. R = CF₃ (green); R = tBu (black); and R = NMe₂ (blue). The first oxidation potential is tunable by ca. 490 mV. Inset: Hammett plot of the redox potentials of **Mn(Sal^R)N** vs σ_{para} of the *para* ring substituent.

Conditions: 1 mM complex, 0.1 M ⁿBu₄NClO₄, scan rate 100 mV s⁻¹, CH₂Cl₂, 233 K.

Table 4.2. Redox potentials for **Mn(Sal^{tBu})N**, **Mn(Sal^{CF3})N**, and **Mn(Sal^{NMe2})N** versus F_c⁺/F_c^{a,b}.

R	E_{pa}^1	E_{pc}^1	$E_{1/2}^1$	E_{pa}^2	E_{pc}^2	$E_{1/2}^2$
tBu	0.30	0.19	0.25 (0.11)	-	-	-
CF ₃	0.51	0.33	0.42 (0.18)	-	-	-
NMe ₂	0.03	-0.21	-0.07 (0.19)	0.20	0.00	0.10 (0.20)

^aGiven in volts, peak-to-peak separation in parentheses. ^bPeak-to-peak difference for F_c⁺/F_c couple at 233 K is 0.13 V.

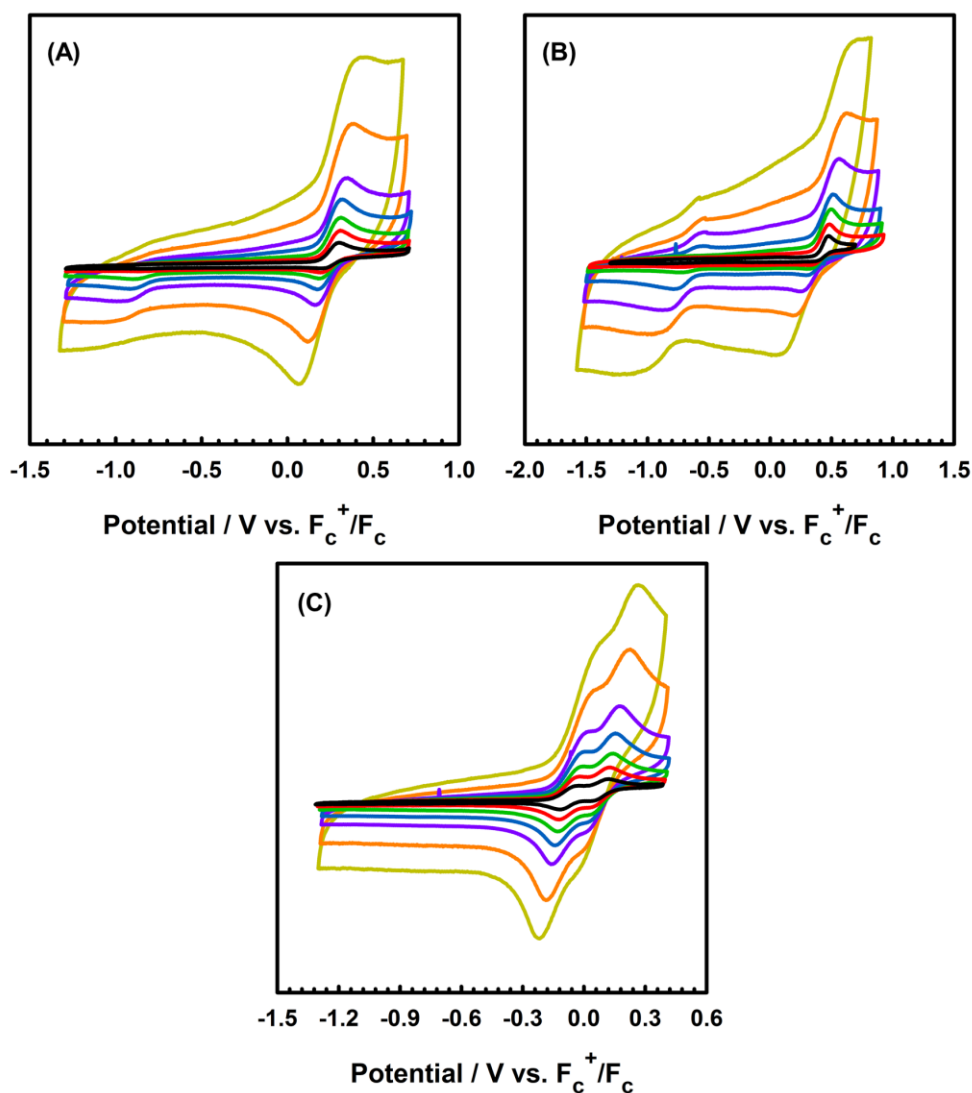
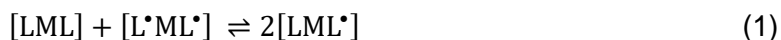


Figure 4.6. Scan rate dependence of **Mn(Sal^R)N**. (A) R = tBu; (B) R = CF₃; (C) R = NMe₂.

Conditions: 1 mM complex, 0.1 M ⁿBu₄NClO₄, CH₂Cl₂, 233 K. Black: 10 mV s⁻¹; red: 25 mV s⁻¹; green: 50 mV s⁻¹; blue: 100 mV s⁻¹; purple: 200 mV s⁻¹; orange: 500 mV s⁻¹; yellow: 1000 mV s⁻¹.

The CV spectrum of the electron-rich NMe₂ derivative displays two closely-spaced redox processes at -0.07 V and 0.10 V vs. F_c⁺/F_c that remain quasi-reversible at all scan rates investigated, suggesting that oxidation of **Mn(Sal^{NMe2})N** results in a different electronic structure in comparison to the more electron-poor CF₃ and tBu derivatives. These potentials were difficult to resolve with cyclic voltammetry, and thus differential pulse voltammetry (DPV) was employed in order to better resolve the two oxidation events (Figure 4.7). The difference in the first and second oxidation potentials in symmetric

oxidized metal salen complexes can provide information on the degree of electronic coupling, and the extent of electronic delocalization between two identical redox-active phenolates. This of course assumes that both redox events are ligand-based. With the first and second oxidation events resolved, the degree of delocalization and a comproportionation constant (K_c) can be calculated for **Mn(Sal^{NMe2})N** using Eqns. 1-3, where L represents one phenolate of the salen ligand, and M the Mn metal centre.



$$K_c = \frac{[\text{LML}^{\bullet}]^2}{[\text{LML}][\text{L}^{\bullet}\text{ML}^{\bullet}]} \quad (2)$$

$$K_c = \exp\left(\frac{\Delta E_{1/2} F}{RT}\right) \quad (3)$$

The $\Delta E_{1/2}$ value for **Mn(Sal^{NMe2})N** is small (~170 mV) which indicates that there is limited coupling between the two redox-active phenolate rings and results in a comproportionation constant at 298 K of ~350. This relatively small comproportionation constant warrants calculation of the degree of disproportionation of **[Mn(Sal^{NMe2})N]⁺** in solution. Using the K_c value at 298 K and Eqn. 3 above, the solution composition is calculated to be ~90% **[Mn(Sal^{NMe2})N]⁺**, ~5% **Mn(Sal^{NMe2})N**, and ~5% **[Mn(Sal^{NMe2})N]²⁺**. This increases to 99.9% **[Mn(Sal^{NMe2})N]⁺** at 198 K.

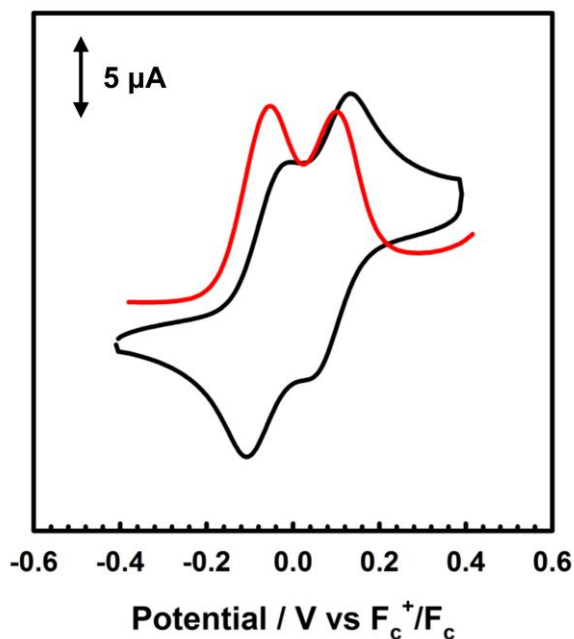


Figure 4.7. CV curve of **Mn(Sal^{NMe2})N** (black) overlaid with a differential pulse voltammetry (DPV) scan (red) which better resolves the two closely spaced oxidation events.

Conditions: 0.5 mM complex, 0.1 M ⁿBu₄NClO₄, CH₂Cl₂, 298 K.

4.2.4. Electronic Absorption Spectroscopy

The electronic absorption spectra of neutral **Mn(Sal^R)N** are typical of nitridomanganese(V) salen complexes with a d_{xy} ground state (Figure 4.8 - Figure 4.10). The weak, broad absorption peak at $\lambda_{\max} \sim 16,000 \text{ cm}^{-1}$ ($\epsilon \sim 300 \text{ M}^{-1} \text{ cm}^{-1}$) is assigned as a forbidden non-bonding $\rightarrow d\pi^*$ transition between the occupied d_{xy} non-bonding orbital and the empty π antibonding orbitals ($d_{xz/yz}$).⁴⁴² The intense transition at high energy is assigned to intraligand azomethine transitions.⁴⁴⁷ Confirmation of these assignments as metal, and ligand-based respectively, is the substituent independent energy of the first transition, while the energy of the intense, ligand-based transition is dependent on the substituent (CF_3 : $27,000 \text{ cm}^{-1}$ > $t\text{Bu}$: $25,800 \text{ cm}^{-1}$ > NMe_2 : $23,000 \text{ cm}^{-1}$).

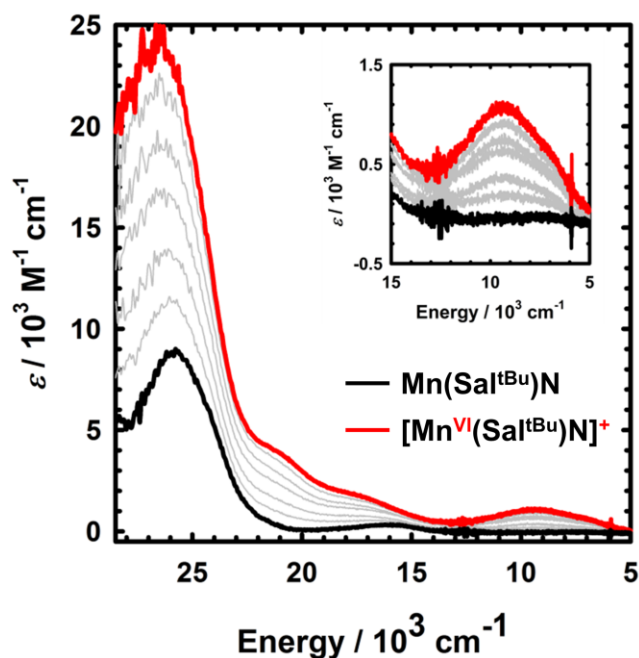


Figure 4.8. UV-vis-NiR spectrum of **Mn(Sal^{tBu})N** (black), and **[Mn^{VI}(Sal^{tBu})N]⁺** (red) at 0.2 mM in CH₂Cl₂ at 195 K. Intermediate grey lines measured during the oxidation titration with [N(C₆H₃Br₂)₃][SbF₆].

The room temperature oxidation of **Mn(Sal^{tBu})N** results in the crystallographically characterized **[Mn(Sal^{tBu})]⁺[SbF₆]⁻** with a distinct absorption spectrum to that of the parent nitride (Appendix C – Figure C4). In order to potentially trap the reactive N-N homocoupling species, oxidation was carried out at 198 K with the aminium radical chemical oxidant [N(C₆H₃Br₂)₃][SbF₆] ($E_{1/2} = 1.14$ V vs F_c^+/F_c)¹⁰⁷. Sequential addition of oxidant affords a species with a UV-vis-NiR spectrum that differs from those of both the starting material and the decay product (Figure 4.8). The formation of a low-intensity band was observed at $\lambda_{\max} = 9,300$ cm⁻¹ ($\epsilon = 1,100$ M⁻¹ cm⁻¹). While broad, weak transitions in the NIR are often indicative of localized ligand-based radicals,^{102-103, 236} EPR analysis of a frozen sample of the oxidized product was characteristic of a metal-based, Mn(V) → Mn(VI) oxidation (*vide infra*). The low-energy band was thus assigned as a ligand-to-metal charge transfer (LMCT) transition. This assignment was further corroborated by DFT calculations (*vide infra*).

Oxidation of the electron deficient **Mn(Sal^{CF₃})N** resulted in similar spectral features to the tBu derivative (Figure 4.9) with the position of the low-energy LMCT transition blue-

shifting relative to the tBu derivative ($\lambda_{\text{max}} = 11,600 \text{ cm}^{-1}$, $\epsilon = 1,000 \text{ M}^{-1} \text{ cm}^{-1}$). A blue-shift in the LMCT band is expected due to the electron withdrawing CF_3 group in this derivative.

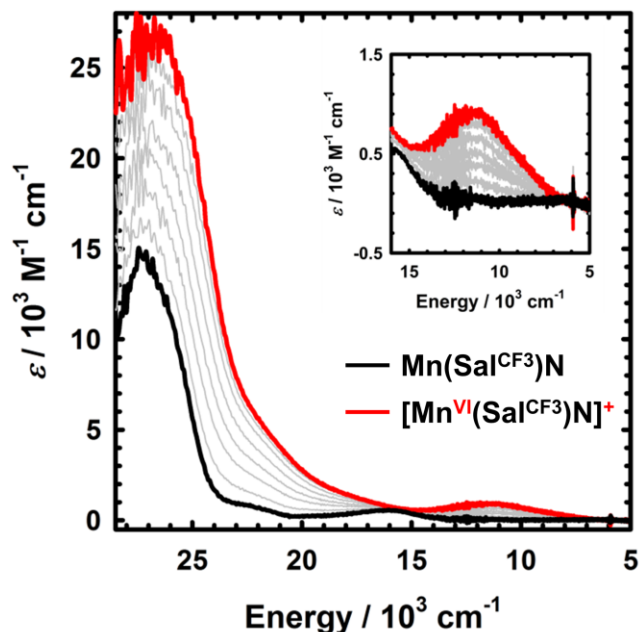


Figure 4.9. UV-vis-NIR spectrum of $\text{Mn}(\text{Sal}^{\text{CF}_3})\text{N}$ (black), and $[\text{Mn}^{\text{VI}}(\text{Sal}^{\text{CF}_3})\text{N}]^+$ (red) at 0.2 mM in CH_2Cl_2 at 195 K. Intermediate grey lines measured during the oxidation titration with $[\text{N}(\text{C}_6\text{H}_3\text{Br}_2)_3][\text{SbF}_6]$.

Low-temperature oxidation of $\text{Mn}(\text{Sal}^{\text{NMe}_2})\text{N}$ results in unique UV-vis-NIR spectral features in comparison with the tBu and CF_3 derivatives. Isosbestic points at $22,800 \text{ cm}^{-1}$ and $23,700 \text{ cm}^{-1}$ indicate clean conversion from neutral to oxidized species in this derivative. Two broad, low energy transitions at $\lambda_{\text{max}} = 6,500 \text{ cm}^{-1}$ ($\epsilon = 800 \text{ M}^{-1} \text{ cm}^{-1}$) and $\lambda_{\text{max}} = 9,500 \text{ cm}^{-1}$ ($\epsilon = 1,000 \text{ M}^{-1} \text{ cm}^{-1}$) are present in the spectrum as well as an envelope of transitions between $15,000$ and $22,000 \text{ cm}^{-1}$ (Figure 4.10). This envelope of transitions is also observed in other oxidized metal salen complexes bearing the NMe_2 substituent,¹¹⁴⁻¹¹⁵ and thus these transitions are predicted to be largely ligand based, and their absence in the spectra of the previous derivatives suggests a change in electronic structure. Indeed, the EPR spectrum of a frozen solution of $[\text{Mn}^{\text{V}}(\text{Sal}^{\text{NMe}_2})\text{N}]^{\cdot+}$ revealed a ligand-based oxidation (*vide infra*). Analysis of the energy, shape, and intensity of NIR bands can reveal information pertinent to the degree of delocalization in mixed-valence systems.¹⁰² According to the Robin-Day classification system,⁹⁹ Class III fully delocalized systems exhibit NIR bands with $\Delta\nu_{1/2} \leq 2,000 \text{ cm}^{-1}$ and intensities $\epsilon \geq 5,000 \text{ M}^{-1} \text{ cm}^{-1}$, with Class II

mixed-valence species exhibiting NIR features that are broader ($\Delta\nu_{1/2} \geq 2,000 \text{ cm}^{-1}$) and less intense ($\epsilon \leq 5,000 \text{ M}^{-1} \text{ cm}^{-1}$). Based on this classification, and the low-energy transitions at $\lambda_{\text{max}} = 6,500 \text{ cm}^{-1}$ and $9,500 \text{ cm}^{-1}$, $[\text{Mn}^{\text{V}}(\text{Sal}^{\text{NMe}_2})\text{N}]^{++}$ is assigned as a Class II mixed-valence species. It should be noted that based on the similarities of the low energy transitions between the Mn(VI) and Mn(V)-ligand radical species described, one must be extremely cautious in assigning oxidation locus in the absence of EPR data.

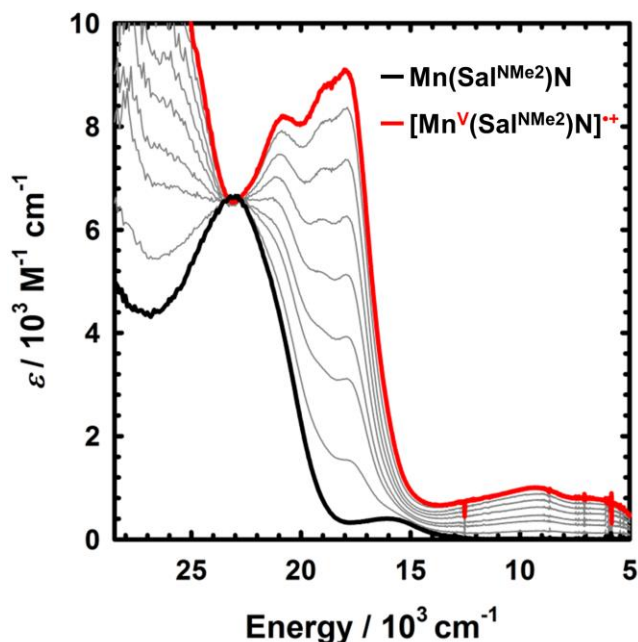


Figure 4.10. UV-vis-NIR spectrum of $\text{Mn}(\text{Sal}^{\text{NMe}_2})\text{N}$ (black), and $[\text{Mn}^{\text{V}}(\text{Sal}^{\text{NMe}_2})\text{N}]^{++}$ (red) at 0.2 mM in CH_2Cl_2 at 195 K. Intermediate gray lines measured during the oxidation titration with $[\text{N}(\text{C}_6\text{H}_3\text{Br}_2)_3][\text{SbF}_6]$.

4.2.5. Electron Paramagnetic Resonance Spectroscopy

EPR spectroscopy was employed in order to unambiguously identify the locus of oxidation in the three oxidized nitridomanganese(V) complexes. The EPR spectra of one-electron oxidized $[\text{Mn}(\text{Sal}^{\text{R}})\text{N}]^+$ recorded at 100 K in frozen CH_2Cl_2 are presented in Figure 4.11. The spectra of both $[\text{Mn}(\text{Sal}^{\text{tBu}})\text{N}]^+$ and $[\text{Mn}(\text{Sal}^{\text{CF}_3})\text{N}]^+$ reveals the locus of oxidation to be metal centered ($\text{Mn}(\text{V}) \rightarrow \text{Mn}(\text{VI})$) in these derivatives. Both spectra display typical axial splitting patterns for a d^1 metal ion (d_{xy}^1 ground state) with hyperfine coupling to a single ^{55}Mn ($I = 5/2$) nucleus. The g values and hyperfine coupling constants for each derivative are presented in Table 4.3, and agree well with two nitridomanganese(VI) complexes previously reported by Wieghardt and co-workers.⁴⁴⁸⁻⁴⁴⁹

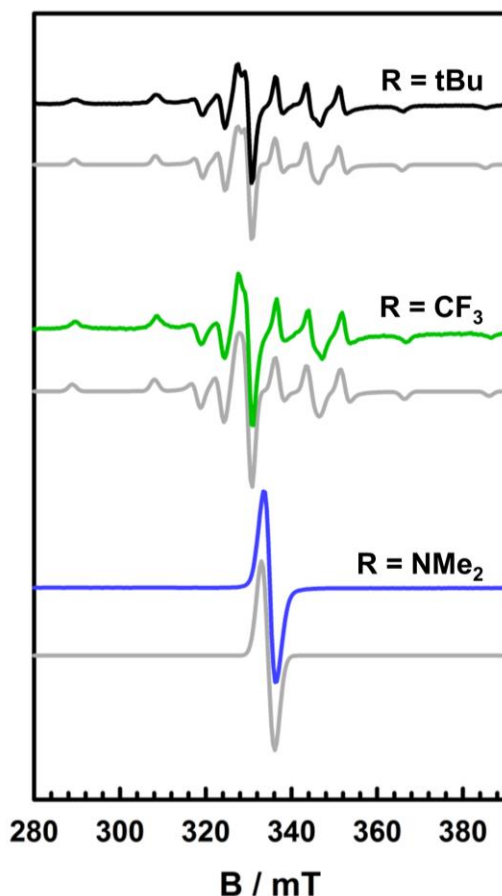


Figure 4.11. X-band EPR spectra of $[\text{Mn}(\text{Sal}^{\text{R}})\text{N}]^+$ recorded in frozen CH_2Cl_2 at 0.4 mM. (top) $\text{R} = \text{tBu}$; (middle) $\text{R} = \text{CF}_3$; (bottom) $\text{R} = \text{NMe}_2$. Grey lines represent simulations of the experimental data.

Conditions: frequency = 9.38 GHz; power = 2.0 mW; modulation frequency = 100 kHz; modulation amplitude = 0.6 mT; $T = 100$ K.

Table 4.3. EPR simulation parameters for $[\text{Mn}(\text{Sal}^{\text{R}})\text{N}]^{+a}$.

	g_{zz}	$g_{xx} = g_{yy}$	A_{zz}	$A_{xx} = A_{yy}$
$\text{R} = \text{tBu}$	1.985	1.995	533	181
$\text{R} = \text{CF}_3$	1.984	1.995	540	187
$\text{R} = \text{NMe}_2$ (100 K)	2.003			
$\text{R} = \text{NMe}_2$ (298 K)	2.003	$A_{\text{N1}} = 13.5$; $6 \times A_{\text{H1}} = 16.7$; $A_{\text{H2}} = 2.8$; $A_{\text{H3}} = 0.8$; $A_{\text{Mn}} = 4.2$		

^aHyperfine values (A) are in MHz

The EPR spectrum of the one-electron oxidized $\text{Mn}(\text{Sal}^{\text{NMe}_2})\text{N}$ reveals the locus of oxidation in this derivative to be the electron-rich salen ligand as evidenced by the isotropic signal centered at $g_{\text{iso}} = 2.003$ (Figure 4.11). This demonstrates that sufficiently electron-donating *para* substituents are capable of reordering the relative energies of redox-active orbitals such that oxidation is no longer metal-centered, but rather ligand-centered in this derivative. In addition, unlike the tBu and CF_3 derivatives which decay even at low

temperature to give half an equivalent of N₂ and a reduced Mn(III) product (*vide infra*, Section 4.2.6), the oxidized NMe₂ derivative is resistant to homocoupling, as the oxidized complex is stable at 195 K and decays only minimally over a 48 h period at 298 K (Appendix C – Figure C5). The room temperature stability of **[Mn^V(Sal^{NMe2})N]^{•+}** allowed for the analysis of its EPR spectrum at room temperature in order to gain insight into the degree of localization in this derivative. Based on the NIR bands in Figure 4.10 as well as similarity to other radical salen complexes with the NMe₂ substituent,¹¹⁴⁻¹¹⁵ this derivative was tentatively assigned as a Class II mixed-valence species. The room temperature spectrum of **[Mn^V(Sal^{NMe2})N]^{•+}** recorded in toluene is presented in Figure 4.12 and was simulated by considering significant hyperfine interactions to one NMe₂ group (1 x N, 6 x H) with smaller hyperfine couplings to the central Mn ion and two phenoxyl protons (Table 4.3). The room-temperature EPR spectrum, and its simulation, thus provide additional verification of a localized ligand radical electronic structure for **[Mn^V(Sal^{NMe2})N]^{•+}**.

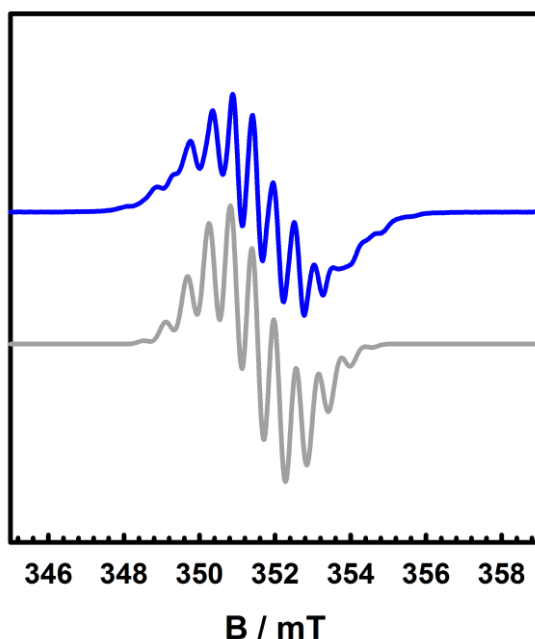


Figure 4.12. X-band EPR spectrum of **[Mn(Sal^{NMe2})N]^{•+}** (0.4 mM) recorded in toluene at room temperature (blue line). The gray line represents simulation of the experimental spectrum.

Conditions: frequency = 9.86 GHz; power = 2.0 mW; modulation frequency = 100 kHz; modulation amplitude = 0.2 mT; $T = 298$ K.

4.2.6. Decay Kinetics

Despite being able to characterize the reactive Mn(VI) intermediates, slow decay of the low energy LMCT bands was observed even at low temperatures (195 K) for both tBu and CF₃ derivatives ($t_{1/2}$ tBu = 4 hours; $t_{1/2}$ CF₃ = 1.6 hours). In accordance with the crystallographically characterized **[Mn(Sal^{tBu})[SbF₆]**, we postulated that a bimolecular reaction involving two molecules of **[Mn^{VI}(Sal^R)N]⁺** was responsible for the observed decay. The decay of the low-energy absorption bands was well modelled to a second order kinetic dependence, suggestive of the proposed bimolecular mechanism, which would result in 2 molecules of the crystallographically characterized Mn(III) product, as well as half an equivalent of N₂ (Figure 4.13). The rate constant for the CF₃ derivative ($k_2 = 0.86 \pm 0.09 \text{ M}^{-1} \text{ s}^{-1}$) is approximately 2.5 times larger in comparison to the tBu derivative ($k_2 = 0.34 \pm 0.04 \text{ M}^{-1} \text{ s}^{-1}$), which can be attributed to the change in peripheral ligand electronics (*vide infra*). Strikingly, the NMe₂ derivative is stable under the experimental conditions at 195 K and decays only minimally over a 48 hour period at 298 K. The Mn≡N stretching band at 1045 cm⁻¹ persists after oxidation with AgSbF₆. Furthermore, the slight decay at 298 K is not well modelled by second-order kinetics, suggesting that the instability of **[Mn^V(Sal^{NMe2})N]⁺** is due to a mechanism other than N-N coupling of the nitrides (Figure 4.13).⁴⁵⁰ Unfortunately, X-ray quality crystals of the oxidized complex have thus far not been isolated. In a recent report, van der Vlugt and co-workers described the preparation of a Ru trimer with bridging nitrido ligands, highlighting the alternative reactivity pathways that redox-active ligands may impose on transition metal nitrido complexes.⁴⁵¹

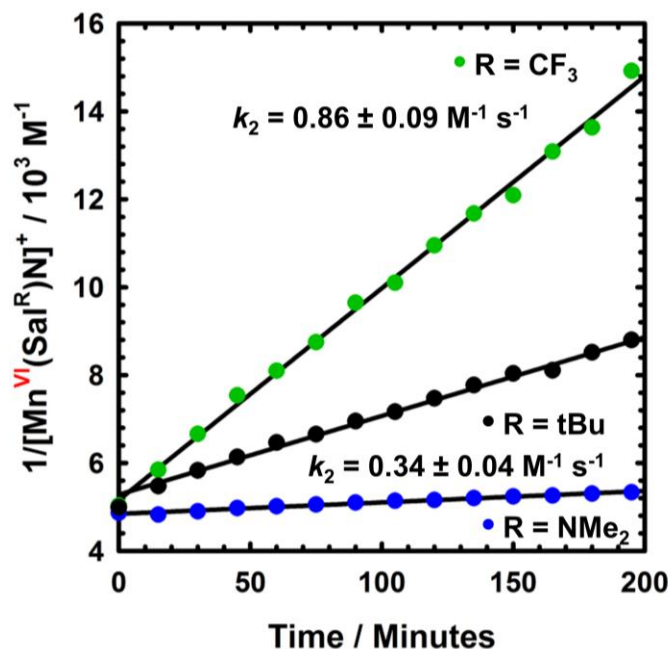


Figure 4.13. Second order kinetic decay plots for $[\text{Mn}^{\text{VI}}(\text{Sal}^{\text{R}})\text{N}]^+$ (R = tBu and CF₃, 195 K; R = NMe₂, 298 K).

Conditions: CH₂Cl₂, 0.2 mM complex. See Appendix C – Figures C6 & 7 for full triplicate kinetic analysis.

In order to confirm that the mechanism for nitride loss involves an intermolecular reaction between two molecules of $[\text{Mn}^{\text{VI}}(\text{Sal}^{\text{R}})\text{N}]^+$, the 50% ¹⁵N-labeled complexes were prepared. GC-MS measurements were performed on the headspace to monitor the gas evolved after oxidation of $\text{Mn}(\text{Sal}^{\text{R}})^{14/15}\text{N}$. Although it was difficult to eliminate atmospheric N₂ (¹⁴N¹⁴N, *m/z* = 28) from the inlet of the instrument,⁴³⁸ we detected ¹⁴N¹⁵N (*m/z* = 29) and ¹⁵N¹⁵N (*m/z* = 30) in a 2:1 ratio, as expected for an intermolecular reaction mechanism involving two molecules of 50% ¹⁵N-labeled $\text{Mn}(\text{Sal}^{\text{R}})^{14/15}\text{N}$ (Table 4.4 and 4.5, Figure 4.14 and 4.15).

Table 4.4. Headspace gas analysis results for the room temperature oxidation of $\text{Mn}(\text{Sal}^{\text{tBu}})^{14/15}\text{N}$ 10 minutes after addition of AgSbF_6 .

m/z	Blank	Vial 1 Run1	Vial 1 Run 2	Vial 1 Run 3	Vial 2 Run 1	Vial 2 Run 2	Vial 2 Run 3
25	0.06	0.03	0.03	0.05	0.04	0.01	0.02
26	0.04	0.05	0.07	0.03	0.05	0.04	0.04
27	0.01	0.00	0.00	0.00	0.00	0.01	0.00
28 ($^{14}\text{N}^{14}\text{N}$)	100.00	100.00	100.00	100.00	100.00	100.00	100.00
29 ($^{14}\text{N}^{15}\text{N}$)	0.35	17.27	20.65	17.01	13.06	13.72	13.24
30 ($^{15}\text{N}^{15}\text{N}$)	0.10	7.96	9.38	7.56	6.09	6.13	6.75
31	0.00	0.00	0.00	0.00	0.00	0.00	0.00
32 (O_2)	21.22	18.90	18.15	19.34	18.82	18.51	18.40
33	0.03	0.02	0.04	0.04	0.05	0.03	0.04
34	0.10	0.12	0.15	0.10	0.11	0.12	0.10
35	0.17	0.30	0.76	1.29	0.61	0.24	0.50

See the experimental section for details.

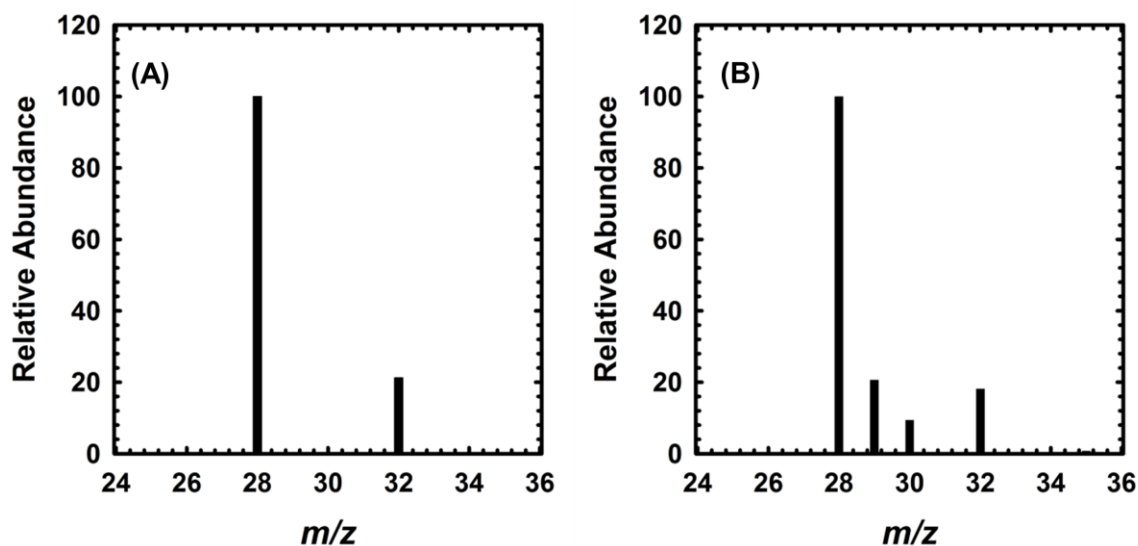


Figure 4.14. Representative GC-MS results (vial 1, run 2 – Table 4.4) for the headspace examination of the $[\text{Mn}^{\text{VI}}(\text{Sal}^{\text{tBu}})^{14/15}\text{N}]^+$ decay. (A) headspace of a blank sample. (B) headspace of a sample of $\text{Mn}(\text{Sal}^{\text{tBu}})^{14/15}\text{N}$ 10 minutes after addition of 1 equivalent of AgSbF_6 at 298 K.

$^{14}\text{N}^{14}\text{N}$ is set at a relative abundance of 100.

Table 4.5. Headspace gas analysis results for the room temperature oxidation of $\text{Mn}(\text{Sal}^{\text{CF}_3})^{14/15}\text{N}$ 10 minutes after addition of AgSbF_6 .

m/z	Blank	Vial 1 Run1	Vial 1 Run 2	Vial 1 Run 3	Vial 2 Run 1	Vial 2 Run 2	Vial 2 Run 3
25	0.03	0.04	0.09	0.04	0.03	0.03	0.03
26	0.05	0.04	0.12	0.07	0.04	0.04	0.04
27	0.01	0.01	0.03	0.00	0.02	0.01	0.02
28 ($^{14}\text{N}^{14}\text{N}$)	100.00	100.00	100.00	100.00	100.00	100.00	100.00
29 ($^{14}\text{N}^{15}\text{N}$)	0.68	17.44	12.47	19.70	14.34	16.72	19.59
30 ($^{15}\text{N}^{15}\text{N}$)	0.15	8.85	6.28	8.83	6.70	7.15	8.98
31	0.00	0.00	0.05	0.05	0.03	0.04	0.00
32 (O_2)	21.76	14.22	16.44	14.46	15.03	16.41	16.32
33	0.06	0.05	0.07	0.02	0.02	0.03	0.07
34	0.13	0.07	0.13	0.05	0.04	0.04	0.09
35	0.25	0.17	0.38	0.34	0.45	0.18	0.31

See the experimental section for details.

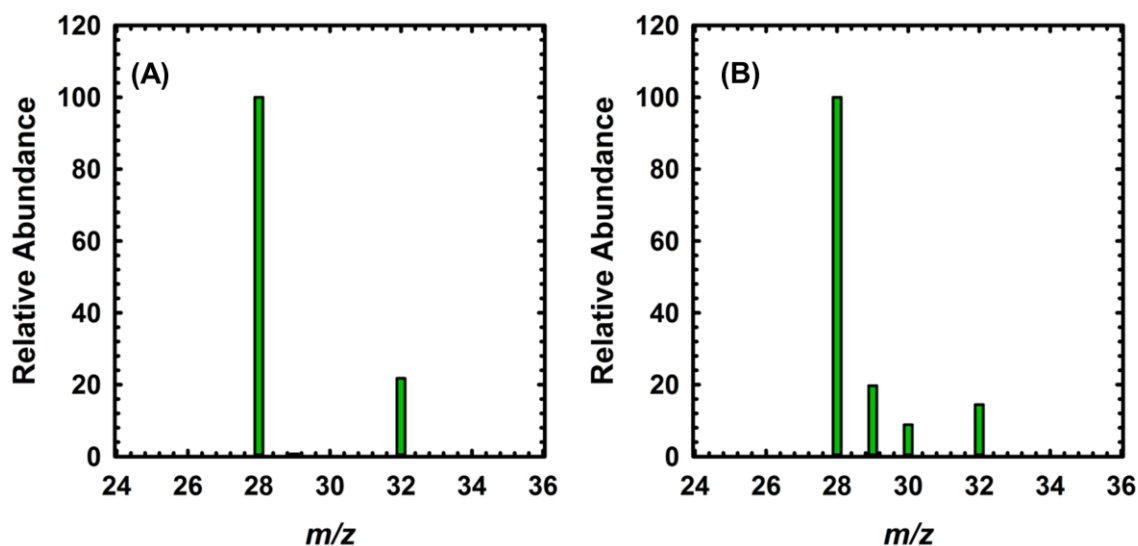


Figure 4.15. Representative GC-MS results (vial 1, run 2 – Table 4.5) for the headspace examination of the $[\text{Mn}^{\text{VI}}(\text{Sal}^{\text{CF}_3})^{14/15}\text{N}]^+$ decay. (A) headspace of a blank sample. (B) headspace of a sample of $\text{Mn}(\text{Sal}^{\text{CF}_3})^{14/15}\text{N}$ 10 minutes after addition of 1 equivalent of AgSbF_6 at 298 K.

$^{14}\text{N}^{14}\text{N}$ is set at a relative abundance of 100.

Finally, GC-MS experiments were performed on the headspace of samples of one-electron oxidized $\text{Mn}(\text{Sal}^{\text{NMe}_2})^{14/15}\text{N}$. Up to 24 hours, no N_2 was detected in the headspace of the reaction vials, again suggesting that the slight room temperature decay of this derivative follows a mechanism other than N-coupling of the terminal nitride ligands (Table 4.6 and 4.7, Figure 4.16).

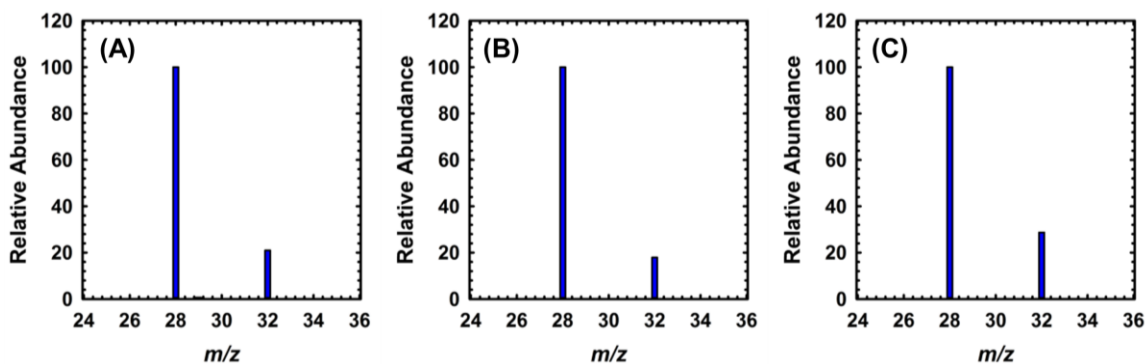


Figure 4.16. Representative GC-MS results for the headspace examination of $[\text{Mn}^{\text{V}}(\text{Sal}^{\text{NMe}_2})^{14/15}\text{N}]^+$. (A) headspace of a blank sample. (B) headspace of a sample of $\text{Mn}(\text{Sal}^{\text{NMe}_2})^{14/15}\text{N}$ 10 minutes after addition of oxidant. (C) headspace of the sample in (B) 24 hours after the addition of oxidant.

Table 4.6. Headspace gas analysis results for the room temperature oxidation of $\text{Mn}(\text{Sal}^{\text{NMe}_2})^{14/15}\text{N}$ 10 minutes after addition of AgSbF_6 .

m/z	Blank	Vial 1 Run1	Vial 1 Run 2	Vial 1 Run 3	Vial 2 Run 1	Vial 2 Run 2	Vial 2 Run 3
25	0.01	0.02	0.02	0.03	0.03	0.02	0.05
26	0.02	0.12	0.07	0.05	0.07	0.09	0.11
27	0.00	0.00	0.00	0.01	0.01	0.00	0.01
28 ($^{14}\text{N}^{14}\text{N}$)	100.00	100.00	100.00	100.00	100.00	100.00	100.00
29 ($^{14}\text{N}^{15}\text{N}$)	0.61	0.45	0.61	0.44	0.51	0.72	0.67
30 ($^{15}\text{N}^{15}\text{N}$)	0.11	0.08	0.14	0.12	0.15	0.14	0.14
31	0.00	0.02	0.00	0.01	0.05	0.05	0.03
32 (O_2)	20.94	18.13	18.46	17.91	16.95	16.62	17.41
33	0.01	0.03	0.02	0.02	0.03	0.04	0.01
34	0.08	0.14	0.12	0.11	0.09	0.03	0.10
35	0.25	0.37	0.40	0.48	0.67	0.21	0.71

See the experimental section for details.

Table 4.7. Headspace gas analysis results for the room temperature oxidation of $\text{Mn}(\text{Sal}^{\text{NMe}_2})^{14/15}\text{N}$ 24 hours after addition of AgSbF_6 .

m/z	Blank	Vial 1 Run1	Vial 1 Run 2	Vial 1 Run 3	Vial 2 Run 1	Vial 2 Run 2	Vial 2 Run 3
25	0.02	0.00	0.02	0.01	0.02	0.01	0.01
26	0.03	0.01	0.01	0.03	0.02	0.02	0.01
27	0.00	0.00	0.00	0.01	0.00	0.00	0.00
28 ($^{14}\text{N}^{14}\text{N}$)	100.00	100.00	100.00	100.00	100.00	100.00	100.00
29 ($^{14}\text{N}^{15}\text{N}$)	0.36	0.43	0.47	0.49	0.41	0.39	0.40
30 ($^{15}\text{N}^{15}\text{N}$)	0.04	0.04	0.10	0.10	0.06	0.05	0.06
31	0.01	0.00	0.01	0.00	0.00	0.00	0.00
32 (O_2)	29.69	25.79	30.39	28.67	23.62	23.60	23.67
33	0.02	0.01	0.03	0.03	0.01	0.02	0.01
34	0.10	0.10	0.12	0.07	0.09	0.07	0.05
35	0.09	0.20	0.31	0.20	0.75	0.28	0.14

See the experimental section for details.

4.2.7. Theoretical Calculations

Theoretical calculations on the oxidized species match the experimental findings, predicting a $d^{1_{xy}}$ Mn(VI) ground state for $R = CF_3$ and tBu and the formation of a localized ligand radical for $R = NMe_2$. The singularly occupied molecular orbitals (SOMOs) are depicted in Figure 4.17, while the spin density plots are shown in Figure 4.18. The SOMOs for the Mn(VI) species are primarily of d_{xy} character, which is non-bonding with respect to the nitride ligand. The SOMO for the NMe_2 derivative is ligand-based and localized to one side of the salen framework, as depicted in both the SOMO and spin density plots. Natural bond order (NBO) analysis is consistent with a highly covalent interaction between the Mn and terminal nitride ligand in the oxidized forms (Appendix C – Tables C1 & 2), with the Mayer bond orders decreasing *slightly* in the order $NMe_2 > tBu > CF_3$ (2.868, 2.732, 2.730). The negative spin density localized on the nitride in $R = tBu$ (-0.20) and $R = CF_3$ (-0.24) can be rationalized by considering the Mn-N bond as a combination of $Mn(VI)\equiv N^{3-}$ ($S_{Mn} = \frac{1}{2}$) and $Mn(V)=N^{\cdot}$ ($S_N = \frac{1}{2}$) resonance forms. A nitridyl radical resonance form, which could be slightly favoured for $R = CF_3$, provides support for a radical coupling pathway to produce N_2 .^{413, 415} Recent work by Ménard and co-workers on a similar system is also suggestive of a radical coupling pathway (see Section 5.3.1).⁴⁵²

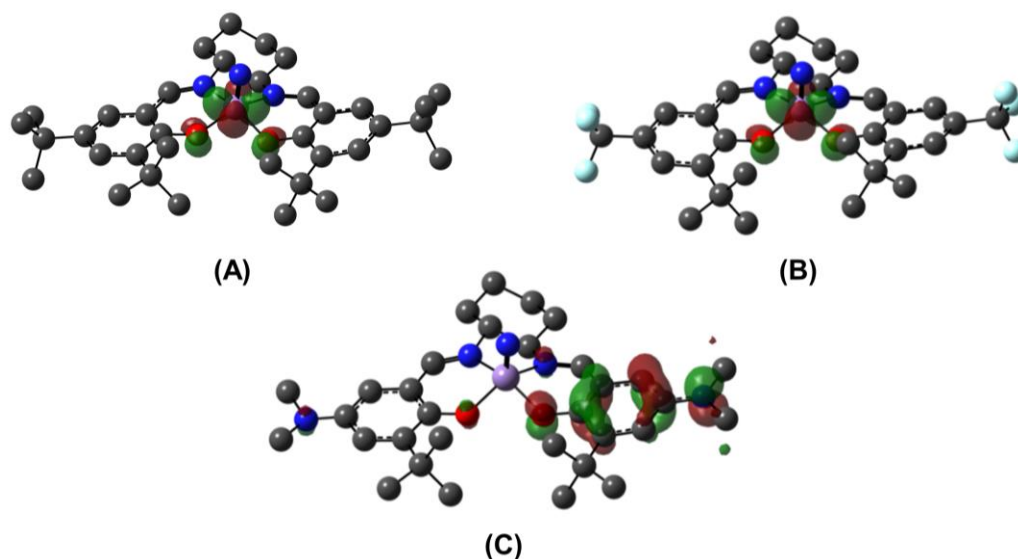


Figure 4.17. DFT predicted SOMOs for $[Mn(Sal^R)N]^+$. (A) $R = tBu$; (B) $R = CF_3$; (C) $R = NMe_2$. Both $R = tBu$ and CF_3 SOMOs are predicted to be of d_{xy} character, while the $R = NMe_2$ SOMO is ligand-based, and localized to one side of the bis-phenoxide salen ligand. See the experimental section for calculation details.

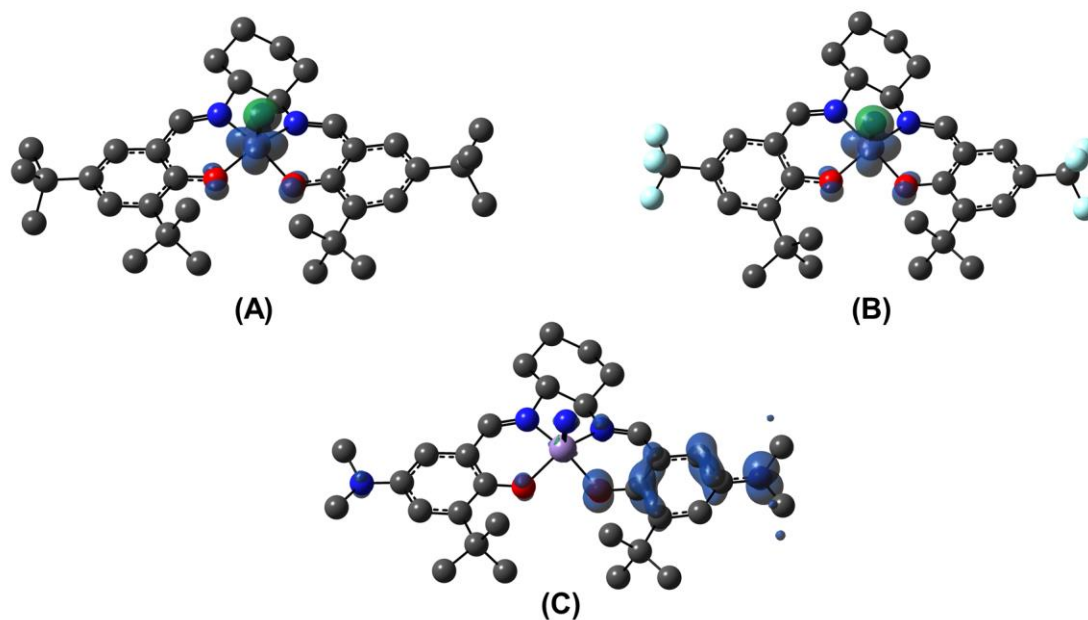


Figure 4.18. Spin density plots for the three oxidized complexes. (A) $[\text{Mn}^{\text{VI}}(\text{Sal}^{\text{tBu}})\text{N}]^+$; (B) $[\text{Mn}^{\text{VI}}(\text{Sal}^{\text{CF}_3})\text{N}]^+$; (C) $[\text{Mn}^{\text{V}}(\text{Sal}^{\text{NMe}_2})\text{N}]^{2+}$. See the experimental section for calculation details.

The spin density plot for $[\text{Mn}^{\text{V}}(\text{Sal}^{\text{NMe}_2})\text{N}]^{2+}$ is in agreement with the results obtained via room temperature EPR spectroscopy. The majority of the unpaired spin resides on a single NMe_2 group, with significantly less spin density located on the central Mn ion. The hyperfine coupling constants to $I_{\text{Mn}} = 5/2$ determined from simulation of the EPR data for $\text{R} = \text{tBu}/\text{CF}_3$ ($A_{\text{zz}} \sim 530$ MHz, $A_{\text{xx}} = A_{\text{yy}} \sim 180$ MHz) vs. NMe_2 ($A_{\text{iso}} = 4.2$ MHz) reflect the different locus of oxidation.

4.3. Discussion and Summary

This study provides key insight into the role of ligand electronics in the nitride activation process, with the nitride precursors readily synthesized from oxidative conditions in the presence of NH_4OH . Remarkably, oxidation of neutral $\text{Mn}(\text{Sal}^{\text{tBu}})\text{N}$ resulted in oxidative nitride coupling to produce N_2 and a crystallographically characterized Mn(III) species. Low temperature experiments (vis-NIR and EPR spectroscopies) reveal the locus of oxidation to be the Mn(V) centre, providing access to a reactive Mn(VI) species. The bimolecular N_2 coupling was suitably modelled to a second order kinetic dependence, and isotopic labelling confirmed that both N atoms are derived from the nitridomanganese(VI) complex. DFT calculations demonstrate that the SOMO is d_{xy} in

character, and non-bonding with respect to the terminal nitride ligand, as expected based on the electronic structure description of the isoelectronic vanadyl ion by Ballhausen and Gray (see Appendix C – Figure C11 for a qualitative molecular orbital diagram of a terminal nitride in a square pyramidal ligand field).⁴⁵³

Substitution of the *para* tBu substituent in **Mn(Sal^{tBu})N** for the strongly electron withdrawing CF₃ substituent unsurprisingly also results in metal-based oxidation to Mn(VI). Interestingly, CF₃ substitution leads to a nearly 2.5-fold increase in the rate of N-N coupling, demonstrating that ligand electronics, along with metal oxidation state, play a key role in the coupling reaction. DFT calculations reveal a slight increase in the spin density localized at the nitride ligand (-0.24 for CF₃ vs -0.20 for tBu) which could potentially explain the enhanced coupling reactivity by considering the Mn-N bond as a combination of Mn(VI)≡N³⁻ ($S_{Mn} = \frac{1}{2}$) and Mn(V)=N• ($S_N = \frac{1}{2}$) resonance forms. A nitridyl radical resonance form, which could be slightly favored for R = CF₃, provides further support for a radical coupling pathway to produce N₂ in this study.

Finally, substitution to an electron donating NMe₂ group at the *para* position resulted in ligand-based oxidation to a localized phenoxyl radical species. This was confirmed via room-temperature EPR analysis, as well as theoretical calculations. This result demonstrated that sufficiently electron donating substituents are able to re-order the relative energies of the redox-active orbitals in nitridomanganese(V) complexes. Remarkably, the ligand-radical species is stable at room temperature, which may further strengthen the radical coupling pathway for the Mn(VI) species described above.

Overall, this chapter demonstrates that nitride activation is dictated by remote ligand electronics. Further efforts are needed to model the reaction pathway and assess the possibility of accessing and activating NH₃ adducts of electron-deficient Mn(Sal) systems for H₂ generation as well as the potential for these systems to activate C-H bonds through radical reaction pathways (see Section 5.3).

4.4. Experimental

4.4.1. Materials

All chemicals used were of the highest grade available and were further purified whenever necessary. Dichloromethane was dried over CaH₂ prior to use. The ligands

$\text{H}_2\text{Sal}^{\text{tBu}}$, $\text{H}_2\text{Sal}^{\text{CF}_3}$, and $\text{H}_2\text{Sal}^{\text{NMe}_2}$, as well as the aminium radical chemical oxidant, $[\text{N}(\text{C}_6\text{H}_3\text{Br}_2)_3][\text{SbF}_6]$, were synthesized according to published protocols.^{114, 126, 306, 454-455} The tBu substituted metal complex $\text{Mn}(\text{Sal}^{\text{tBu}})\text{N}$ was also prepared according to published protocols.^{426, 442}

4.4.2. Instrumentation

Electronic spectra were recorded on a Cary 5000 spectrophotometer with a custom-designed immersion fiber-optic probe with variable pathlength (1 and 10 mm; Hellma, Inc.). Constant temperatures were maintained by a dry ice/acetone bath. Cyclic voltammetry (CV) was performed on a PAR-263A potentiometer, equipped with an Ag wire reference electrode, a glassy carbon working electrode, and a Pt counter electrode with ${}^n\text{Bu}_4\text{NClO}_4$ (0.1 M) solution in CH_2Cl_2 . Decamethylferrocene was used as an internal standard.³⁰⁷ ${}^1\text{H}$ and ${}^{19}\text{F}$ NMR spectra were recorded on a Bruker AV-400 instrument. GC-MS analysis of isotopically labelled N_2 following decay of $[\text{Mn}(\text{Sal}^{\text{R}})\text{N}]^+$ was performed on an Agilent Technologies 6890 series GC system with a 5973 mass selective detector. Elemental analyses (C, H, N) were performed by Mr. Paul Mulyk at Simon Fraser University on a Carlo Erba EA1110 CHN elemental analyzer. Electron paramagnetic resonance (EPR) spectra were collected using a Bruker EMXplus spectrometer operating with a premiumX X-band microwave bridge and an HS resonator. Samples for X-band EPR measurements were placed in 4 mm outer-diameter tubes with sample volumes of ~ 250 μL . EPR spectra were simulated using the EasySpin package in MATLAB.³⁰⁸

4.4.3. X-ray Structure Determination

Single-crystal X-ray crystallographic analysis of a block-green ($\text{Mn}(\text{Sal}^{\text{CF}_3})\text{N}$) or block-brown ($\text{Mn}(\text{Sal}^{\text{NMe}_2})\text{N}$ and $[\text{Mn}(\text{Sal}^{\text{tBu}})][\text{SbF}_6]$) crystal was performed on a Bruker APEX II Duo diffractometer with graphite monochromated Cu K α ($\text{Mn}(\text{Sal}^{\text{CF}_3})\text{N}$) or Mo K α ($\text{Mn}(\text{Sal}^{\text{NMe}_2})\text{N}$ and $[\text{Mn}(\text{Sal}^{\text{tBu}})][\text{SbF}_6]$) radiation. The crystals were mounted on a 150 μm MiteGen sample holder. The data were collected at 293 K ($\text{Mn}(\text{Sal}^{\text{CF}_3})\text{N}$ and $\text{Mn}(\text{Sal}^{\text{NMe}_2})\text{N}$) or 150 K ($[\text{Mn}(\text{Sal}^{\text{tBu}})][\text{SbF}_6]$) to a maximum 2θ of 50° . Data were collected in a series of ϕ and ω scans in 0.5° - 1.0° widths with 10.0 – 60.0 s exposures. The crystal-to-detector distance was 40 mm. The structures were solved by intrinsic phasing³¹¹ and subsequent refinements were performed using ShelXle.³¹² All non-hydrogen atoms were refined anisotropically. All C-H hydrogen atoms were placed in calculated positions but

were not refined. CCDC numbers: 1497761 (**Mn(Sal^{tBu})**)[SbF₆], 1497762 (**Mn(Sal^{NMe2})**N), 1497763 (**Mn(Sal^{CF3})**N).

4.4.4. Oxidation Protocol

Under an inert atmosphere at 195 K, 100 μL of a dry CH_2Cl_2 solution of the metal complex was diluted into 9.0 mL of dry CH_2Cl_2 (0.2 mM final concentration). Monitored by UV-vis-NIR, a solution containing 50 mg of $[\text{N}(\text{C}_6\text{H}_3\text{Br}_2)_3][\text{SbF}_6]$ dissolved in 1 mL of dry CH_2Cl_2 was added in 20 μL additions resulting in clean conversion to the respective one-electron oxidized species.

4.4.5. Kinetics Measurements

Decay experiments for **[Mn(Sal^{tBu})N]⁺** and **[Mn(Sal^{CF3})N]⁺** were monitored after addition of 1 eq. of chemical oxidant to dry CH_2Cl_2 solutions of metal complex under an inert atmosphere. 1 eq. was determined first by adding $[\text{N}(\text{C}_6\text{H}_3\text{Br}_2)_3][\text{SbF}_6]^+$ in 40 μL additions to 0.2 mM solutions of metal complex in 9 mL of dry CH_2Cl_2 . The increase of low energy bands at $\sim 9300\text{ cm}^{-1}$ (**Mn(Sal^{tBu})**N) or $\sim 11\,600\text{ cm}^{-1}$ (**Mn(Sal^{CF3})**N) was monitored until the appearance of a band corresponding to the free $[\text{N}(\text{C}_6\text{H}_3\text{Br}_2)_3][\text{SbF}_6]^+$ was observed. At this point, the reaction vessel was cleaned out and a new 0.2 mM solution of metal complex in 9 mL dry CH_2Cl_2 was prepared. A volume of $[\text{N}(\text{C}_6\text{H}_3\text{Br}_2)_3][\text{SbF}_6]$ corresponding to a value before the appearance of free $[\text{N}(\text{C}_6\text{H}_3\text{Br}_2)_3][\text{SbF}_6]^+$ was added in a single addition and the UV-vis-NIR spectrum was monitored every 15 minutes over a 4 hour period. This experiment was repeated in triplicate for each derivative.

4.4.6. Isotopic Detection by GC-MS

Detection of isotopically labelled N_2 from decay of 50% ^{15}N labelled **Mn(Sal^R)**N was monitored *via* GC-MS on an Agilent Technologies 6890 series GC system equipped with a 5973 mass selective detector using helium as carrier gas, in splitless injection mode. In a glovebox, 2 mg (0.003 mmol) of **Mn(Sal^R)**N was placed into each of three 1.5 mL vials and dissolved in 1 mL dry CH_2Cl_2 . The three vials were sealed with a septum and then flushed with argon for 20 minutes each. Subsequently, a stock AgSbF_6 (0.009 mmol in 1 mL CH_2Cl_2) solution was prepared in a fourth 1.5 mL vial, sealed with a septum and also flushed with argon for 20 minutes. 250 μL of the AgSbF_6 solution was added to two of the

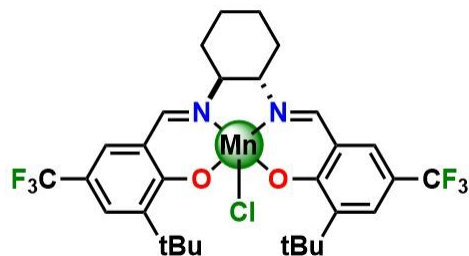
three vials containing 50% ^{15}N labelled $\text{Mn}(\text{Sal}^{\text{R}})\text{N}$. No oxidant was added to the third vial in order to use its headspace as a background. 5 μL of the headspace was injected manually onto the GC-MS and we observed a peak corresponding to the evolved gas at ~ 1.10 minutes. This was done once for the blank and three times each for the two vials containing oxidized complex. The peak corresponding to $^{28}\text{N}_2$ was set at 100% relative abundance.⁴³⁸ We also examined the headspace of the $\text{R} = \text{NMe}_2$ derivative 24 hours after oxidation in order to rule out slow decomposition via N_2 loss.

4.4.7. Theoretical Calculations

Geometry optimizations were performed using the Gaussian 09 program (Revision D.01),³¹⁴ the B3LYP functional,³¹⁵⁻³¹⁶ and the 6-31G(d) basis set on all atoms as this functional/basis set combination has afforded a good match to experimental metrical data in similar salen systems. All calculations employed a polarized continuum model (PCM) for CH_2Cl_2 .³²¹⁻³²⁴ Frequency calculations at the same level of theory confirmed that the optimized structures were located at a minimum on the potential energy surface. Single-point calculations for energetic analysis, as well as NBO computations were performed with the BP86 functional⁴⁵⁶⁻⁴⁵⁹ and the TZVP basis set of Ahlrichs on all atoms.³¹⁷⁻³¹⁸ Attempts to calculate the $\text{Mn}(\text{V})=\text{N}\cdot$ ($S_{\text{N}} = \frac{1}{2}$) resonance form collapsed to the $\text{Mn}(\text{VI})\equiv\text{N}^3-$ ($S_{\text{Mn}} = \frac{1}{2}$) electronic structure. The intensities of the 30 lowest-energy electronic transitions were calculated by TD-DFT at the BP86/TZVP level.³¹⁹⁻³²⁰

4.4.8. Synthesis

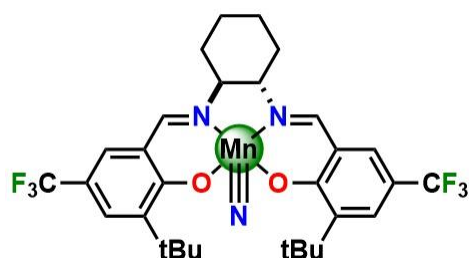
(*N,N'*-bis(3-*tert*-butyl-5-trifluoromethylsalicylidene))-1*R*,2*R*-(-)-1,2-cyclohexanediamine manganese chloride ($\text{Mn}(\text{Sal}^{\text{CF}_3})\text{Cl}$):



$\text{Mn}(\text{OAc})_2 \cdot 4\text{H}_2\text{O}$ (100 mg, 0.4 mmol) was added to a refluxing ethanol solution (2 mL) of $\text{H}_2\text{Sal}^{\text{CF}_3}$ (110 mg, 0.2 mmol). The bright yellow solution immediately turned dark

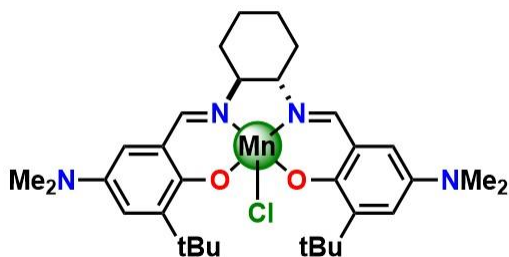
brown and was stirred at reflux for 2 hours. After 2 hours, solid LiCl (25 mg, 0.6 mmol) was added and the solution was refluxed for an additional hour. The solution was removed from heat and the solvent was removed *in vacuo*. The crude material was dissolved in CH₂Cl₂ (15 mL) and passed through a pad of silica. The solvent was again removed *in vacuo* and the crude residue redissolved in EtOH (2 mL). Cold water was added dropwise until a light brown precipitate formed which was collected *via* suction filtration. Yield: 110 mg, 80%. MALDI-MS *m/z*: 658.62 (100%). Anal. Calcd (%) for C₃₀H₃₄ClF₆MnN₂O₂: C 54.68, H 5.20, N 4.25; Found: C 54.92, H 5.05, N 4.50.

(N,N'-bis(3-*tert*-butyl-5-trifluoromethylsalicylidene))-1*R*,2*R*-(-)-1,2-cyclohexanediamine manganese nitride (**Mn(Sal^{CF₃})N**):



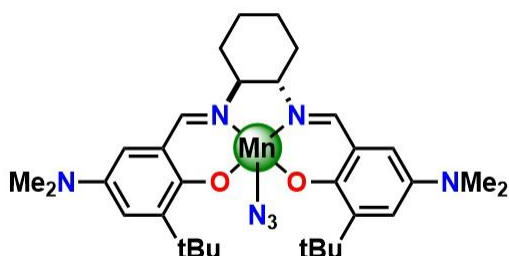
Mn(Sal^{CF₃})Cl (110 mg, 0.17 mmol) was dissolved in a 4:1 mixture of CH₂Cl₂ and MeOH (5 mL total). 5 drops of NH₄OH was added to the mixture, which was stirred vigorously at room temperature for 30 minutes, after which 5 drops of NaOCl was added to the mixture. The mixture was allowed to stir at room temperature for an additional 2 hours. Water was added (5 mL) and extracted into 3x10 mL CH₂Cl₂. The organic phase was dried over MgSO₄ and the solvent was removed *in vacuo*. The crude material was purified by flash column chromatography using CH₂Cl₂/Hexane (1:1) as eluent. The title compound was obtained as a light green powder. Yield: 40 mg, 37%. ATR: $\nu(\text{Mn}\equiv\text{N}) = 1042 \text{ cm}^{-1}$. MALDI-MS *m/z*: 637.79 (100%). ¹H NMR (500 MHz, CDCl₃): $\delta = 8.03$ (s, 1H), 7.97 (s, 1H), 7.56 (d, *J* = 2.0 Hz, 1H), 7.53 (d, *J* = 1.8 Hz, 1H), 7.41 (s, 1H), 7.36 (s, 1H), 3.53 (m, 1H), 3.03 (m, 1H), 2.68 (m, 1H), 2.52 (d, *J* = 11.2 Hz, 1H), 2.07 (d, *J* = 8.1 Hz, 2H), 1.55 (m, 2H), 1.47 (s, 9H), 1.43 (s, 9H), 1.41 (m, 2H); ¹⁹F NMR (400 MHz, CDCl₃): $\delta = -61.45, -61.50$. Anal. Calcd (%) for C₃₀H₃₄F₆MnN₃O₂: C 56.52, H 5.38, N 6.59; Found: C 56.75, H 5.10, N 6.81. Slow evaporation of a concentrated CH₂Cl₂/MeOH solution yielded block green crystals suitable for X-ray analysis.

(N,N'-bis(3-tert-butyl-5-dimethylaminosalicylidene))-1R,2R(-)-1,2-cyclohexanediamine manganese chloride (**Mn(Sal^{NMe₂})Cl**):



Mn(OAc)₂•4H₂O (100 mg, 0.4 mmol) was added to a refluxing EtOH solution (2 mL) of H₂Sal^{NMe₂} (105 mg, 0.2 mmol). The orange solution slowly turned brown and was allowed to stir at reflux for 4 hours, at which point solid LiCl (25 mg, 0.6 mmol) was added and the mixture was refluxed for an additional 2 hours. The mixture was removed from the heat and the solvent was removed *in vacuo*. The crude material was dissolved in CH₂Cl₂ (15 mL) and passed through a pad of silica. The solvent was again removed *in vacuo* and the crude residue was dissolved in hot acetonitrile (2 mL). The hot mixture was placed in an ice bath for 30 minutes and dark brown microcrystals were collected via filtration. Yield: 55 mg, 48%. MALDI-MS *m/z*: 610.69 (100%, [M+H]); Anal. Cald (%) for C₃₂H₄₆ClMnN₄O₂: C 63.10, H 7.61, N 9.20; Found: C 63.20, H 7.40, N 8.98.

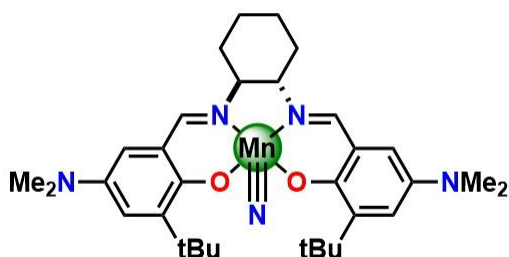
(N,N'-bis(3-tert-butyl-5-dimethylaminosalicylidene))-1R,2R(-)-1,2-cyclohexanediamine manganese azide (**Mn(Sal^{NMe₂})N₃**):



Mn(Sal^{NMe₂})Cl (30 mg, 0.05 mmol) was dissolved in a 1:1 mixture of dichloromethane and methanol (2 mL total). The mixture was stirred at room temperature and an aqueous solution of NaN₃ (6.5 mg, 0.1 mmol, 100 μL) was added. The brown solution was stirred for 1 hour and the solvent was removed *in vacuo*. The crude material was redissolved in dichloromethane (5 mL) and passed through a pad of celite. The solvent was again removed *in vacuo* and the crude material dissolved in hot acetonitrile

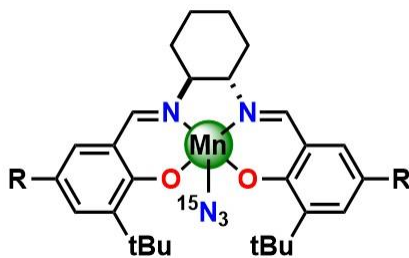
(5 mL). The hot mixture was placed in an ice bath and dark brown microcrystals were collected via filtration. Yield: 30 mg, 98%. IR (neat): $\nu(\text{N}_3) = 2050 \text{ cm}^{-1}$. Anal. Cald (%) for $\text{C}_{32}\text{H}_{46}\text{MnN}_7\text{O}_2$: C 62.42, H 7.53, N 15.92; Found: C 62.06, H 7.70, N 15.77.

(*N,N'*-bis(3-*tert*-butyl-5-dimethylaminosalicylidene))-1*R*,2*R*-(-)-1,2-cyclohexanediamine manganese nitride (**Mn(Sal^{NMe₂})N**):



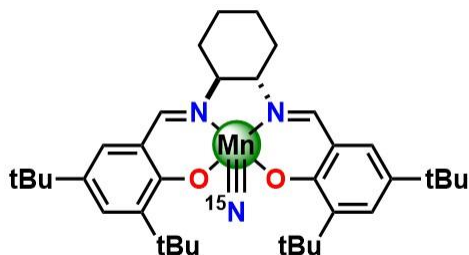
A quartz photolysis chamber was charged with **Mn(Sal^{NMe₂})N₃** (30 mg, 0.05 mmol). 30 mL of benzene was added and the suspension was irradiated for 24 hours with stirring. Following irradiation, the benzene was removed *in vacuo* and the crude material was purified *via* flash column chromatography using dichloromethane/methanol (19:1) as eluent ($R_f = 0.4$). The title compound was obtained as a dark brown powder. Yield: 17 mg, 60%. IR (neat): $\nu(\text{Mn}\equiv\text{N}) = 1045 \text{ cm}^{-1}$. MALDI-MS m/z : 587.06 (100%). ¹H NMR (500 MHz, CD_2Cl_2): $\delta = 7.99$ (d, $J = 1.7 \text{ Hz}$, 1H), 7.93 (d, $J = 1.9 \text{ Hz}$, 1H), 7.13 (d, $J = 3.1 \text{ Hz}$, 1H), 7.11 (d, $J = 3.2 \text{ Hz}$, 1H), 6.48 (d, $J = 3.1 \text{ Hz}$, 1H), 6.43 (d, $J = 3.2 \text{ Hz}$, 1H), 3.48 (m, 1H), 2.99 (t, $J = 11.3 \text{ Hz}$, 1H), 2.79 (s, 6H), 2.78 (s, 6H), 2.65 (d, $J = 9.5 \text{ Hz}$, 1H), 2.48 (d, $J = 12.5 \text{ Hz}$, 1H), 1.98 (d, $J = 8.5 \text{ Hz}$, 2H), 1.44 (s, 9H), 1.39 (s, 9H). Anal. Cald (%) for $\text{C}_{32}\text{H}_{46}\text{MnN}_5\text{O}_2$: C 65.40, H 7.89, N 11.92; Found: C 65.12, H 7.82, N 11.56. Slow evaporation of a concentrated dichloromethane/methanol solution yielded block-brown crystals suitable for X-ray analysis.

Mn(Sal^R)¹⁵N₃:



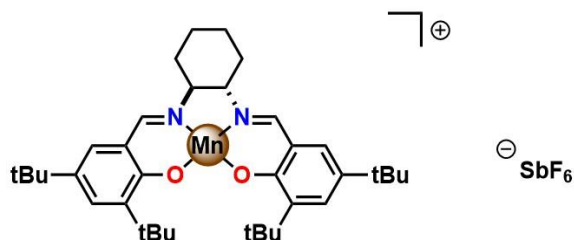
Mn(Sal^{tBu})Cl (100 mg, 0.16 mmol) was dissolved in a 1:1 mixture of dichloromethane and methanol (6 mL total). The mixture was stirred at room temperature and an aqueous solution of terminally labelled Na¹⁵N₃ (20 mg, 0.30 mmol, 300 μL) was added. The brown solution was stirred at room temperature for 1 hour, after which the solvent was removed *in vacuo*. The crude material was then dissolved in dichloromethane (10 mL) and passed through a pad of celite. The solvent was again removed *in vacuo* and the crude material dissolved in hot acetonitrile. The hot mixture was placed in an ice bath and dark brown microcrystals were collected via filtration. Yield: 75 mg, 75%. The ¹⁵N labelled **Mn(Sal^{CF3})¹⁵N₃** and **Mn(Sal^{NMe2})¹⁵N₃** compounds were prepared following the same procedure.

50% ¹⁵N labelled Mn(Sal^{tBu})N:



A quartz photolysis chamber was charged with **Mn(Sal^{tBu})¹⁵N₃** (75 mg, 0.12 mmol). 40 mL of benzene was added and the suspension was irradiated for 24 hours with stirring. Following irradiation, the benzene was removed *in vacuo* and the crude material was purified via flash column chromatography using dichloromethane as eluent ($R_f = 0.6$). The title compound was obtained as a dark green powder. Yield: 50 mg, 70%. IR (neat): $\nu(\text{Mn}\equiv^{14}\text{N}) = 1043 \text{ cm}^{-1}$; $\nu(\text{Mn}\equiv^{15}\text{N}) = 1016 \text{ cm}^{-1}$. The 50% ¹⁵N labelled **Mn(Sal^{CF3})N** and **Mn(Sal^{NMe2})N** compounds were prepared following the same procedure as for the tBu derivative. IR (neat) 50% **Mn(Sal^{CF3})¹⁵N**: $\nu(\text{Mn}\equiv^{14}\text{N}) = 1042 \text{ cm}^{-1}$; $\nu(\text{Mn}\equiv^{15}\text{N}) = 1014 \text{ cm}^{-1}$. IR (neat) 50% **Mn(Sal^{NMe2})¹⁵N**: $\nu(\text{Mn}\equiv^{14}\text{N}) = 1045 \text{ cm}^{-1}$; $\nu(\text{Mn}\equiv^{15}\text{N}) = 1020 \text{ cm}^{-1}$.

$[Mn(Sal^{tBu})][SbF_6]$:



Under an inert atmosphere, **Mn(Sal^{tBu})N** (50 mg, 0.08 mmol) was dissolved in 10 mL dry CH₂Cl₂. AgSbF₆ (27 mg, 0.08 mmol) was added as a 1 mL CH₂Cl₂ solution. The mixture was stirred for 10 minutes, at which point a silver mirror had formed. The mixture was filtered and passed through a pad of celite (9:1 CH₂Cl₂/MeOH) and recrystallized in 1:1 CH₂Cl₂/MeOH mixture to yield **[Mn(Sal^{tBu})][SbF₆]** quantitatively (68 mg). Solution magnetic moment (¹H Evans method):¹¹²⁻¹¹³ $\mu_{\text{eff}} = 4.83 \mu_{\text{B}}$. MALDI-MS $m/z = 599.32$ [M-SbF₆] (100%). Anal. Cald (%) for C₃₆H₅₂F₆MnN₂O₂Sb: C 51.75, H 6.27, N 3.35; Found: C 51.58, H 6.03, N 3.18.

Chapter 5. Ongoing and Future Directions

5.1. Thesis Summary

This thesis presents the results from a number of projects focusing on the design, synthesis, electronic structure determination, and reactivity of oxidized mono and bimetallic complexes employing the salen ligand framework. Through a suite of experimental and theoretical methods, unique spectroscopic handles have been identified which can provide insight into both the geometry and electronic structure of ligand radical species. Outlined below are ongoing and future endeavors that build off of the results obtained and discussed in the previous chapters.

5.2. Chapter 2 and Chapter 3

Chapter 2 describes the photophysical properties of a series of bis-oxidized bimetallic Ni(Sal) complexes as a result of their electronic structure; whereas Chapter 3 discusses the electronic structure of an analogous bimetallic Co(Sal) complex. Future work on the bimetallic salen constructs described could focus on reactivity (catalytic or stoichiometric) as a consequence of electronic structure, as well as the incorporation of NIR absorbing complexes into materials. In particular, the aggregate properties of $[5^{**}]^{2+}$ described in Chapter 2 should be investigated in depth.

5.2.1. Reactivity of Bimetallic Salen Constructs

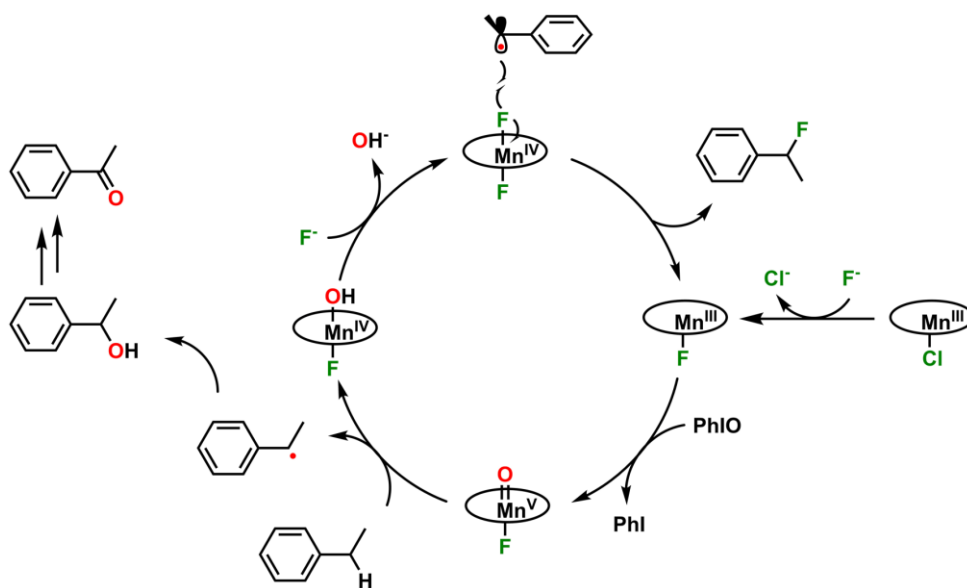
Numerous reactivity studies involving metal-salen complexes have demonstrated second order kinetic dependence with respect to the metallosalen catalyst.¹⁴² As a means to enhance reactivity, multiple catalytic sites have been incorporated into the same molecule, and in many cases cooperativity was observed.¹⁷²⁻¹⁷⁶ Furthermore, bimetallic systems offer advantages over their monomeric counterparts via enhanced substrate binding and the stabilization of reactive intermediates. Rigid or flexible spacers can be used to target specific substrates which can interact with the binding pocket through weak non-covalent interactions. Future work in the area of the bimetallic salen complexes described in Chapters 2 and 3 should focus on reactivity as my current results establish

spectroscopic handles that can be used to identify specific geometries and electronic structures present during reactivity with substrate.

5.2.1.1. C-H Fluorination

Recently, Groves and co-workers developed a series of Mn porphyrin and Mn salen systems for the fluorination of benzylic and aliphatic C-H bonds, that make use of silver fluoride/tetrabutyl ammonium fluoride trihydrate or triethylamine trihydrofluoride as the fluorine source.⁴⁶⁰⁻⁴⁶³ Mn(Sal) systems were also proficient catalysts for late stage benzylic C-H fluorination with [¹⁸F]fluoride, demonstrating the broad applicability of this chemistry.⁴⁶¹ The proposed mechanism follows a reaction pathway similar to that of cytochrome P450 (Scheme 5.1). Mn(III)(L)F (where L = porphyrin or salen) is formed *in situ* and oxidized to a formally Mn(V) species [(L)Mn(V)(O)F] which, analogous to Compound I, abstracts a hydrogen atom from the substrate, forming a Mn(IV) species. Radical rebound with the Mn(IV)(L)F₂ species, which could be formed via displacement of the hydroxyl group by a second equivalent of F⁻, generates the fluorinated product. Immediate radical rebound with the Mn(IV) hydroxylated species before OH⁻ displacement by fluoride results in undesired reactivity resulting in oxygenated species (alcohols and ketones).

Scheme 5.1. Proposed catalytic cycle for the manganese porphyrin/salen-catalyzed C-H fluorination reactions reported by Groves and co-workers.⁴⁶⁰⁻⁴⁶³ The ellipsoid represents the porphyrin/salen ligand. Ethylbenzene is used as an example substrate.



We envision potential improvements to this chemistry through methodologies explored in this thesis. First, employment of bimetallic catalysts may increase the local concentration of Mn-F species for immediate fluorine rebound following hydrogen atom abstraction, reducing the amount of undesired oxygenated products. Second, through careful tuning of the electronics by *para* group substitution (as described in Chapter 4) the reactivity of the hydrogen atom abstracting species may be tunable to enhance rate and selectivity of the fluorination catalysts.

Initial studies have been undertaken, with the preparation of two bimetallic Mn complexes for potential use as C-H fluorination catalysts. We employ the 1,2-phenylene spacer and the xanthene spacer in order to investigate the influence of metal distance and orientation on the reactivity of the catalysts. The achiral diamine backbone employed in Chapters 2 and 3 has been replaced with a chiral cyclohexane backbone for potential asymmetric activity. The monomeric analogue was also prepared in order to compare the activity of bimetallic complexes with monomeric analogues. We also employ the more labile triflate anion as this has been shown to be more active in ^{18}F fluorination studies (Figure 5.1, see Section 5.4 for experimental details).⁴⁶¹

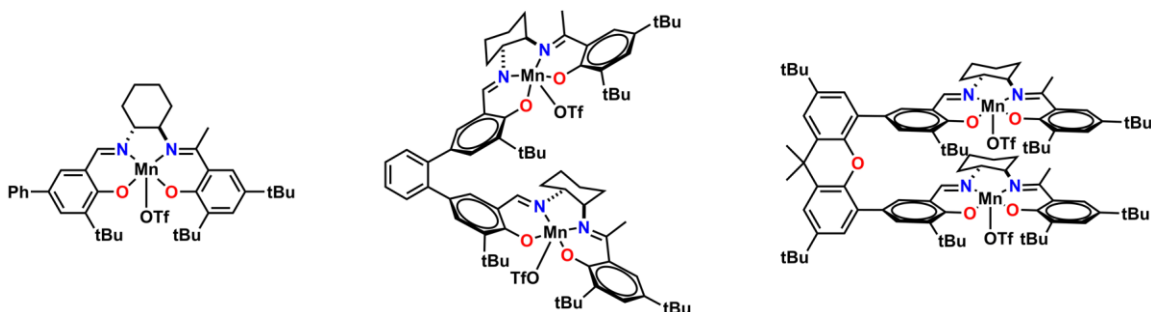


Figure 5.1. Mono and bimetallic Mn complexes prepared for use as fluorination catalysts.

Current results using 4-ethylbiphenyl as substrate show comparable activity to the Groves system for the monomeric complex (~6:1 fluorinated to oxygenated product, as characterized by $^1\text{H}/^{19}\text{F}$ NMR and MALDI-MS, see Section 5.4 for experimental details). Future work should focus on the activity of the bimetallic catalysts, with further modifications to the geometry (different spacer groups) and electronic structure (different *para* substituents) dependent on initial results.

5.2.1.2. Oxidative Transformations

The incorporation of oxidized functions into organic molecules is an inherently difficult challenge; the catalysts that do so often contain precious, rare-earth metals such as rhodium, iridium, and platinum. Nature has developed metalloenzymes capable of selective substrate oxidation using first row transition metals and mild oxidants (O_2/H_2O_2), and many structural and functional small molecule models have been developed.^{59-60, 464} Future reactivity studies employing the binucleating ligands used in Chapters 2 and 3 (and their chiral analogues described above) should be geared towards oxidative transformations such as those depicted in Figure 5.2. The use of different spacer groups allows for the preparation of a small library of complexes with variation of the distance and angle between the metal centres to tune the affinity of the binding pocket to specific substrates. Initial studies on Co complexes for the nitro-aldol (Henry) reaction should be pursued, as this reaction has previously been shown to be enhanced by bimetallic effects.^{174, 351} Further reactivity studies with the bimetallic Co(Sal) complexes include the activation of small molecules such as O_2 and quinones (such as 2,3-dichloro-5,6-dicyano-1,4-benzoquinone, DDQ), both of which are the appropriate size to fit inside the pocket created by the 1,2-phenylene spacer.^{160-161, 163-165, 352} Bimetallic Mn and Fe complexes should be prepared as these species could provide access to high-valent metal-oxo species for thioether oxidation and C-H hydroxylation.⁴⁶⁵⁻⁴⁶⁶ Finally, the addition of bulky monodentate ligands (L, in Figure 5.2) can be used to block peripheral substrate access to the metal centres, restricting substrate reactivity to the binding pocket.

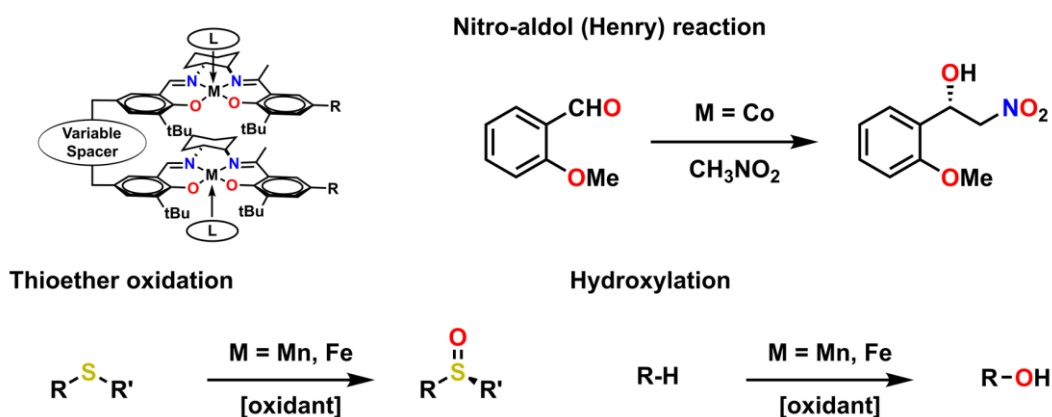


Figure 5.2. Potential oxidative transformations to be targeted by multimetallic complexes employing mild oxidants (O_2/H_2O_2).

5.2.2. Aggregation of $[5^{**}]^{2+}$

Oxidation of the *para* dimer (**5**, Chapter 2) at low temperature or at concentrations above 0.5 mM results in aggregation which under the current experimental conditions is irreversible. While oxidation of dilute solutions of **5** at room temperature did result in the expected NIR transitions, significant broadening of the experimental spectra was observed likely due to minor aggregation occurring even at room temperature (Appendix A – Figure A14). Future studies should focus on understanding the aggregation process for $[5^{**}]^{2+}$, as well as further examination of the interesting photophysical properties of the aggregated species. Transmission electron microscopy (TEM) should be used to understand size and morphology of the aggregates, providing additional insight over the current DLS measurements. My results do suggest a solvent dependence to the observed aggregation (Figure 5.3), and this should be explored in more detail.

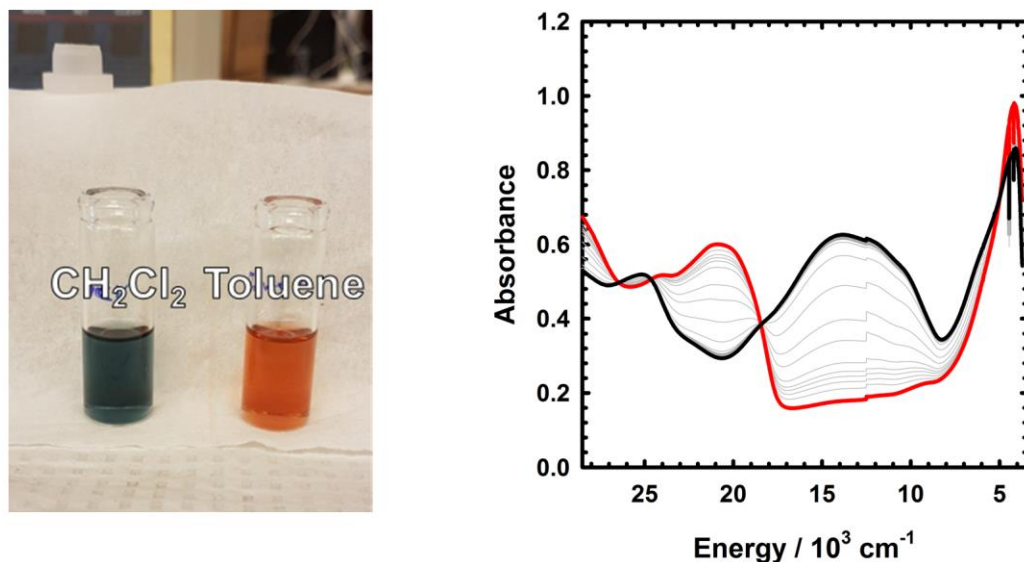


Figure 5.3. (left) 1 mM solutions of $[5^{**}]^{2+}$ in CH_2Cl_2 and toluene; (right) dilution of a CH_2Cl_2 solution (1 mM) of $[5^{**}]^{2+}$ into toluene (0.2 mM final concentration) causes disaggregation of $[5^{**}]^{2+}$. The black spectrum is recorded at time 0, grey lines are recorded every 2.5 minutes until the red spectrum is reached (~25 minutes). Isobestic points at 5,000, 18,500, 24,500, and 26,500 cm^{-1} indicate clean conversion from one species to another.

5.3. Chapter 4

Chapter 4 outlines the preparation of a series of nitridomanganese(V) salen complexes of varying electron donating abilities. Oxidation of these complexes results in oxidative coupling of the nitride ligands or a stable ligand-radical species depending on the *para* substituent. The work described in Chapter 4 provides a starting point for many further studies on transition metal nitride complexes, including N-atom transfer reactions, and C-H bond activation.

5.3.1. Mechanism for N-N Coupling

While a number of reports attribute N-N coupling to nitridyl radical character in open shell systems (Figure 5.4),^{413, 415} our current results do not discount the possibility of coupling initiated by a donor/acceptor pathway, where nitride lone pair electrons are donated into a Mn≡N antibonding orbital (Figure 5.4B).^{439, 467} In isoelectronic Cr(V) systems, Bendix and co-workers demonstrate via elegant EPR studies that spin polarization at the nitride *increases* with elongation of the Cr-N triple bond.⁴⁶⁸ Initial donation from a nitride lone pair into the π^* orbital could cause increased spin density to be shuttled onto the nitride, facilitating the coupling reaction. Why this is observed in the one-electron oxidized species and not the neutral **Mn(Sal^R)N** complexes requires further investigation, and DFT modelling of the reaction pathway in collaboration with Dr. Sam de Visser (Manchester) is currently ongoing, as well as attempts to detect any intermediates along the coupling pathway via parallel mode EPR.⁴⁶⁹⁻⁴⁷⁰

Interestingly, in recent work reported by Ménard and co-workers, oxidation of a similar nitridomanganese complex with an unsubstituted salen ligand resulted in significant formation of an *N*-bridged species analogous to that which we initially set out to prepare.⁴⁵² We do not observe this species in our work and speculate that this could be due to the use of sterically bulky *ortho* and *para* substituents. In addition, the crystallographically characterized Mn(III) species described in Chapter 4 exhibits a strong counterion interaction (2.255 Å Mn-F distance in the solid-state), and the use of the bulky B(C₆F₅)₄⁻ by Ménard and co-workers may limit the stabilization of the Mn(III) adduct observed.

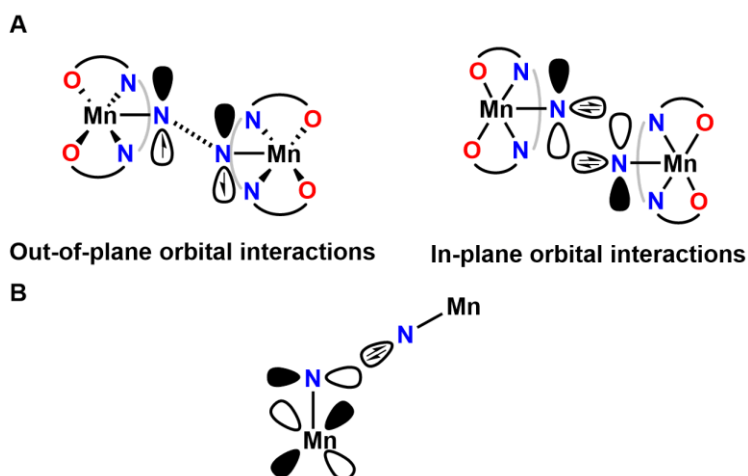


Figure 5.4. (A) Orbital interactions involved in a radical coupling pathway. (B) Orbital interactions involved in a donor/acceptor coupling pathway. Adapted from reference 415.

5.3.2. N-Atom Transfer

Transition metal nitrides have found exceptional utility as nitrene transfer reagents and future studies should be geared toward investigating the applicability of the complexes described in Chapter 4 towards N-atom transfer reactivity. Preliminary reactions with phosphines⁴⁷¹ or alkyl radicals such as Gomberg's dimer ($\text{Ph}_3\text{C}(\text{C}_6\text{H}_5)=\text{CPh}_2$)^{393, 472} may provide insight into the applicability of these systems towards one or two-electron chemistry (Figure 5.5). Gomberg's dimer exists in a temperature dependent equilibrium in which the radical is only ~2% abundant at room temperature.⁴⁷³ Goldberg and co-workers have very recently reported a series of Gomberg's dimer derivatives which exist exclusively as monomers in solution at room temperature for investigation of the oxygen rebound mechanism observed in cytochrome P450 and its models.⁴⁷⁴ Reactivity of these derivatives with the oxidized nitridomanganese complexes should be investigated.

To determine the feasibility of two electron nitrogen transfer chemistry, reaction with phosphines to form phosphoraneiminato ligands should be undertaken. Similar reactivity has been reported for Fe nitride complexes.^{394-395, 471} Depending on the results of phosphine reactivity, nitrogen transfer to other substrates such as CO, isonitriles, and alkenes may be possible under the right conditions. Avenues for minimizing the background N-N coupling reaction through the use of dilute solutions of Mn complex or via addition of large excess of substrate could be explored.

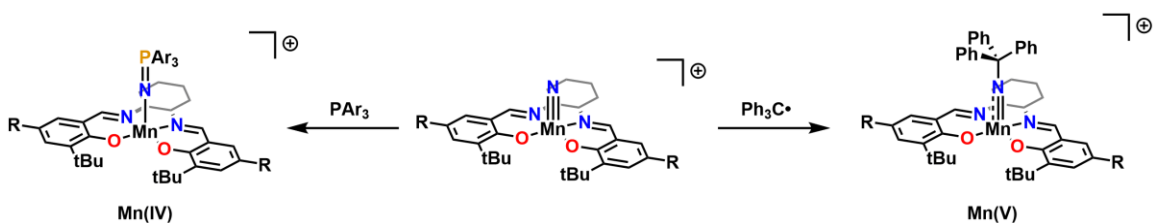


Figure 5.5. Exploratory reactions with phosphines (left) and Gomberg's dimer (right) to investigate the feasibility of one and two-electron reactivity pathways.

5.3.3. C-H Bond Activation

A further goal of the chemistry described in Chapter 4 is the ability to use high-valent Mn nitride compounds for the activation of C-H bonds. Inspired by metalloenzymes such as cytochrome P450, metal-oxo complexes have found great utility for C-H bond activation,^{464, 475-477} and the analogous metal-imido species are also known.⁴⁷⁸⁻⁴⁷⁹ C-H bond activation by metal-nitrido species is rare,^{409, 480-481} however ligand insertion reactions have been reported for nitrides of Ru,⁴⁸²⁻⁴⁸³ Ir,⁴¹⁵ U,⁴⁸⁴ Fe,⁴⁸⁵ Co,^{412, 486} and Ni.⁴¹⁶ Using the well characterized $[\text{Ru}^{\text{VI}}(\text{Sal})(\text{MeOH})\text{N}]^+$,⁴¹⁰⁻⁴¹¹ Lau and co-workers have demonstrated elegant intermolecular C-H bond activation of a number of aliphatic and benzylic C-H bonds in the presence of pyridine through initial hydrogen atom transfer (HAT, Figure 5.6).⁴⁰⁹ Chapter 4 demonstrated the ability to tune the reactivity of the metal nitrido fragment using ligand electronics, and future studies could focus on the applicability of these systems towards intermolecular C-H activation analogous to those reported by Lau and co-workers. Finding conditions that slow or eliminate the current N-N coupling pathway in order to facilitate favorable reactivity is of immediate interest. While the background N-N coupling reactivity of the electron deficient systems described in Chapter 4 (R = tBu and CF₃) may be too fast to be synthetically useful ($t_{1/2}$ of ca. 4 hrs for R = tBu and 1.5 hrs for R = CF₃ at 195 K, and ca. seconds at 298 K) at the current concentrations investigated (0.2 mM),¹²⁵ dilute solutions or reactions carried out with a large excess of substrate (e.g. xanthene, BDE = 75.5 kcal mol⁻¹)⁴⁰⁹ may allow for competitive reaction over the N-N background decay. Based on initial results, mechanistic details of the C-H activation process should be investigated and the role of peripheral ligand electronics assessed for their influence on the product profile. DFT calculations should be used to investigate the mechanisms of C-H bond activation reactions, with future nitridomanganese complex modifications being informed by the computed reactivity pathways.

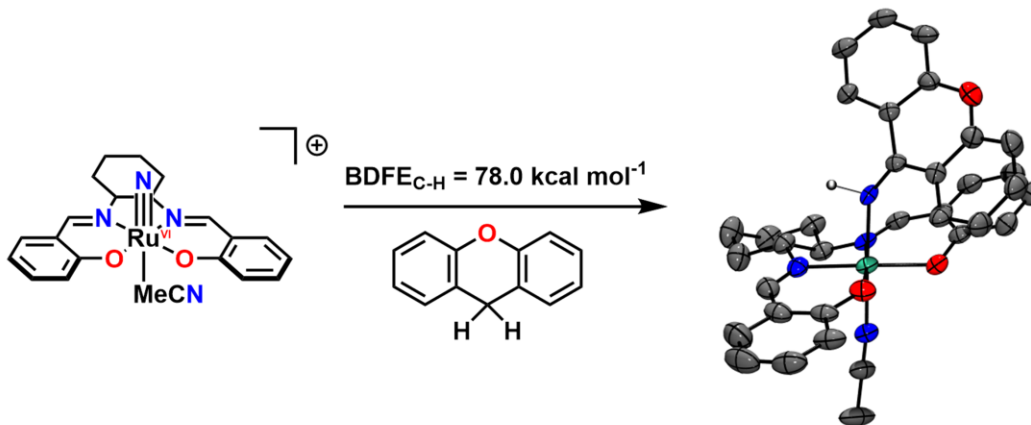


Figure 5.6. Intermolecular C-H bond activation with a Ru nitride supported by the salen framework reported by Lau and co-workers.⁴⁰⁹

Finally, the electron rich R = NMe₂ derivative (which upon oxidation is stable in solution at 298 K) may also allow for interesting reactivity under the right conditions. Although stable as a ligand-radical at 298 K, strategies for activation of **[Mn(Sal^{NMe2})N]^{•+}** in the presence of substrate include photoactivation, and protonation of the *para* NMe₂ groups.

5.3.3.1. Photolysis of **[Mn^V(Sal^{NMe2})N]^{•+}**

Previous work by other groups demonstrates that photoactivation of transition metal nitrides can result in activation reactions at the ancillary ligands or solvent.^{412, 416, 484, 486-487} Initial photolysis experiments with **[Mn^V(Sal^{NMe2})N]^{•+}** suggest that exposure to 365 nm UV light induces homocoupling of the nitrides on the basis of UV-vis data and MALDI-MS data (**Mn^{III}(Sal^{NMe2})** *m/z* = 573.30; Figure 5.7). This could occur via a metal-to-ligand charge transfer mechanism, although direct activation of the nitride cannot be discounted at this time. As detailed in Chapter 4 for the *t*Bu and CF₃ derivatives, detection of ¹⁵N₂ in the headspace of **[Mn^V(Sal^{NMe2})N]^{•+}** following oxidation should be undertaken. Strikingly, if the photolysis reaction is carried out in toluene, MS data suggests **[Mn^V(Sal^{NMe2})N]^{•+}** activates the C-H bonds of the solvent (*m/z* = 678.36, BDE = 89.8 kcal mol⁻¹). Like the N-atom transfer chemistry described above, of immediate concern is finding conditions that slow or eliminate the background N-N coupling pathway in order for reaction with substrate to occur competitively. It is possible that highly dilute solutions of **[Mn(Sal^{NMe2})N]^{•+}** with excess substrate may allow for C-H bond activation chemistry once subjected to photolysis. The product profile and mechanistic details of potential C-H bond reactivity via

photolysis should be explored, as this may provide a method for the direct amination of unreactive C-H bonds.⁴⁸⁸

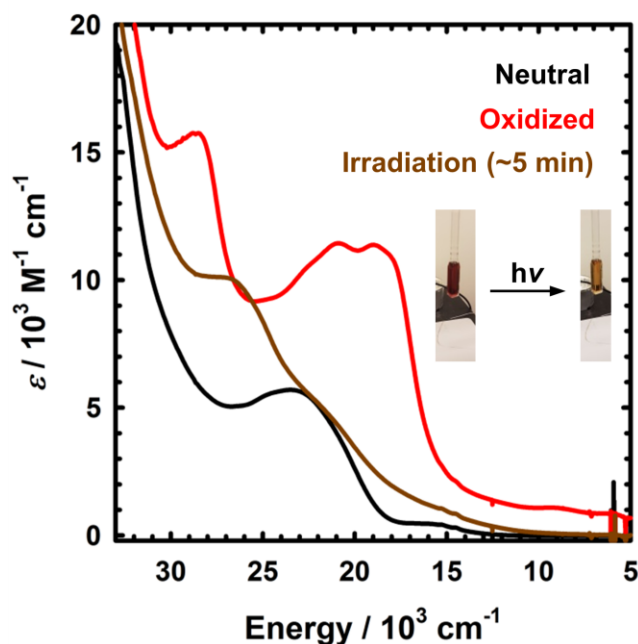


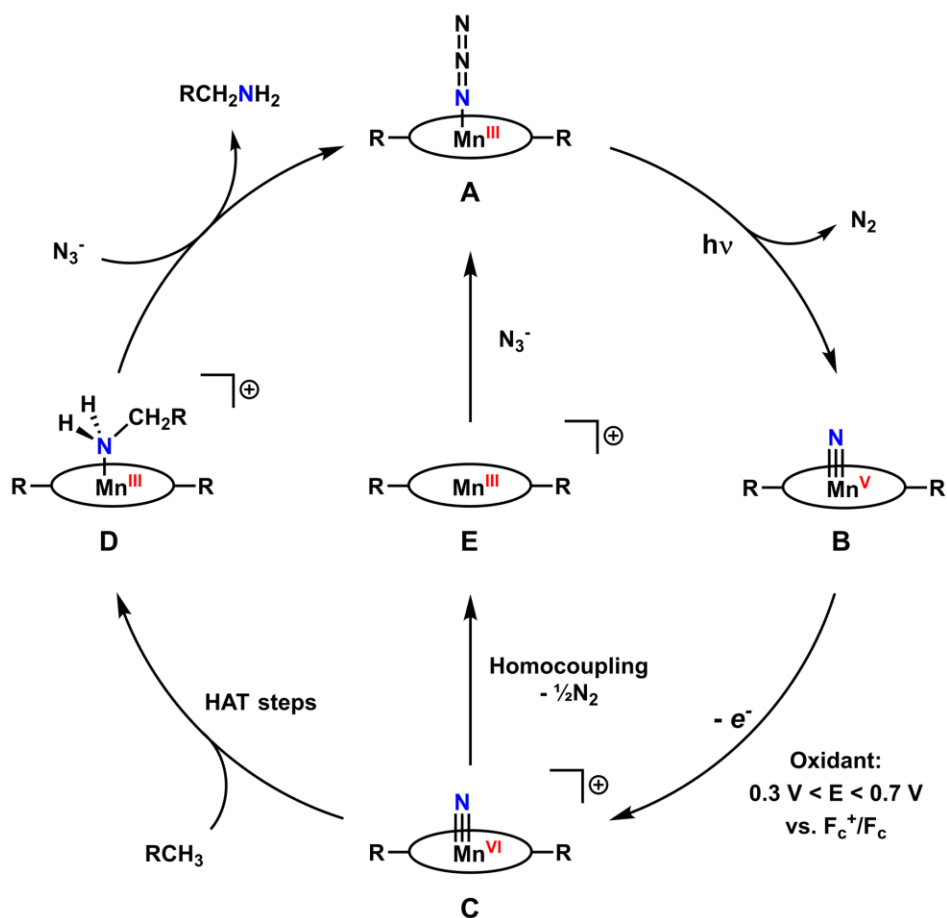
Figure 5.7. UV-vis-NIR spectra of $\text{Mn}(\text{Sal}^{\text{NMe}_2})\text{N}$ (black), $[\text{Mn}^{\text{V}}(\text{Sal}^{\text{NMe}_2})\text{N}]^{+\bullet}$ (red), and after irradiation for ~5 minutes with a long wavelength UV lamp ($\lambda_{\text{ex}} = 365$ nm). Inset: photographs of $[\text{Mn}^{\text{V}}(\text{Sal}^{\text{NMe}_2})\text{N}]^{+\bullet}$ before and after irradiation. Conditions: 1 mM complex, oxidized with 1 eq. of AgSbF_6 and filtered, 1 cm pathlength, CH_2Cl_2 , 298 K.

Due to the ability to prepare $\text{Mn}(\text{Sal}^{\text{R}})\text{N}$ via photolysis of the corresponding azido complexes, and depending on the initial reactivity results in the presence of substrate, it may be possible to combine photoactivation of $\text{Mn}^{\text{III}}(\text{Sal}^{\text{R}})\text{N}_3$ ($E_{1/2} \sim 0.8$ V vs F_c^+/F_c) with *in situ* oxidation of the resultant $\text{Mn}^{\text{V}}(\text{Sal}^{\text{R}})\text{N}$ ($E_{1/2} = 0.0 - 0.4$ V vs F_c^+/F_c) to $[\text{Mn}(\text{Sal}^{\text{R}})\text{N}]^{+\bullet}$ into a photoelectrocatalytic cycle for the activation of C-H bonds (Scheme 5.2). This is made possible due to the lower oxidation potential of the nitridomanganese complex formed after photolysis relative to the oxidation potential of the parent azido complex. Selection of a chemical oxidant with an oxidation potential higher than $\text{Mn}^{\text{V}}(\text{Sal}^{\text{R}})\text{N}$ but lower than $\text{Mn}^{\text{III}}(\text{Sal}^{\text{R}})\text{N}_3$ will selectively oxidize the photogenerated $\text{Mn}^{\text{V}}(\text{Sal}^{\text{R}})\text{N}$. This could be done with either a chemical oxidant ($[\text{N}(\text{C}_6\text{H}_4\text{Br})_3]^+$, Ag^+)¹⁰⁷ or with a large surface area electrode at a set potential. With a suitable choice of oxidant, this proposed cycle is applicable to all $\text{Mn}(\text{Sal}^{\text{R}})\text{N}$ species.

Before reactivity in the presence of substrates is studied, azide photolysis followed by nitride coupling in the presence of a suitable oxidant and excess azide should be undertaken to determine the feasibility of Scheme 5.2 ($A \rightarrow B \rightarrow C \rightarrow E \rightarrow A \dots$). Addition of a large excess of azide to Mn(III) solutions and monitoring the loss of the azide stretch in the IR during photoelectrolysis should provide a spectroscopic handle to monitor this reactivity.

For reactions with substrate, N-N homocoupling in this case would not present a major disadvantage so long as the azide is added in significant excess. This reactivity would present a major advancement in the direct amination of C-H bonds using a photoelectrocatalytic cycle. Stoichiometric C-H activation studies investigated previously will inform the initial substrate scope as well as the conditions required for efficient hydrogen atom transfer (HAT) steps.

Scheme 5.2. Proposed photoelectrochemical catalytic cycle for the activation of C-H bonds with **Mn(Sal^R)N**. The ellipsoid represents the salen ligand.



5.3.3.2. Protonolysis of $[\text{Mn}^{\text{V}}(\text{Sal}^{\text{NMe}_2})\text{N}]^{2+}$

DFT calculations suggest a shift in the oxidation locus from ligand to metal via the addition of two equivalents of H^+ (Figure 5.8). The cyclic voltammograms of $\text{Mn}(\text{Sal}^{\text{NMe}_2})\text{N}$ in the presence of 1 and 2 equivalents of $[\text{H}(\text{Et}_2\text{O})_2][\text{BF}_4]$ are presented in Figure 5.9. The separation of the first two redox events in $\text{Mn}(\text{Sal}^{\text{NMe}_2})\text{N}$ changes from 170 mV to 630 mV upon the addition of one equivalent of acid, as after protonation of one NMe_2 group the corresponding phenoxide is more difficult to oxidize (Table 5.1). Addition of a second equivalent of acid results in significant changes to the CV spectrum. The first oxidation event shifts to more positive potentials, and an irreversible reduction process appears at ca. -0.5 mV. Analysis of the scan-rate dependence (Figure 5.10) suggests a change in electronic structure due to the lack of reversibility in the first oxidation process, and its similarity to the scan rate dependence of both $\text{R} = \text{tBu}$ and CF_3 derivatives (Chapter 4) is suggestive of N-N homocoupling. $\text{Mn}(\text{Sal}^{\text{NMe}_2})\text{N}$ remains quasi-reversible in the absence of acid at all scan rates studied as shown on the right of Figure 5.10. Protonation of the terminal NMe_2 groups may provide a mechanism to activate $[\text{Mn}(\text{Sal}^{\text{NMe}_2})\text{N}]^{2+}$ towards reactivity with substrates as a triply charged species may be less likely to undergo homocoupling reactivity to yield N_2 . Experiments should be undertaken to determine the degree of background N-N homocoupling (if any) in the presence of 2 equivalents of acid at both 195 and 298 K. Following these experiments, reactivity in the presence of substrate should be investigated.

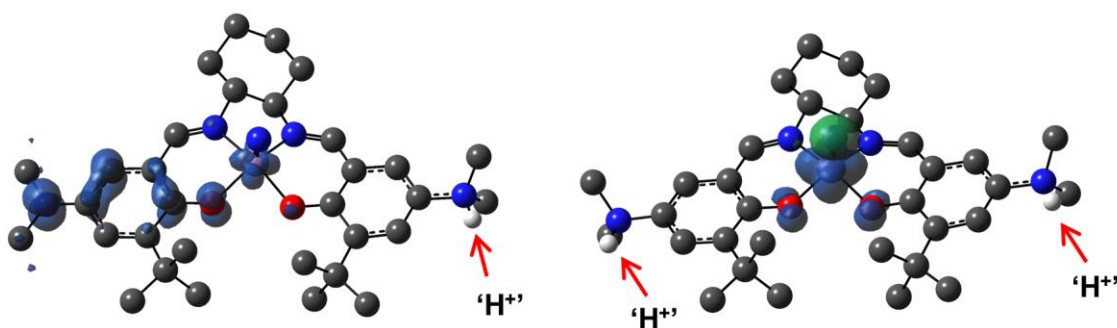


Figure 5.8. Spin density plots for $[\text{Mn}(\text{Sal}^{\text{NHMe}_2}(\text{NMe}_2)\text{N})]^{2+}$ and $[\text{Mn}(\text{Sal}^{\text{NHMe}_2})\text{N}]^{3+}$. See the Experimental Section in Chapter 4 for calculation details.

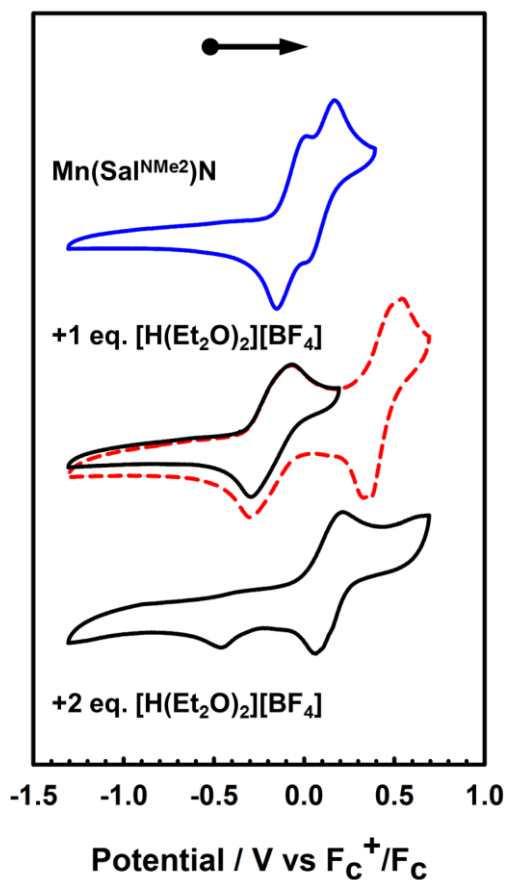


Figure 5.9. Cyclic voltammograms of $\text{Mn}(\text{Sal}^{\text{NMe}_2})\text{N}$ in the presence of 1 and 2 equivalents of $[\text{H}(\text{Et}_2\text{O})_2][\text{BF}_4]$. Conditions: 1 mM complex, 0.1 M $n\text{Bu}_4\text{NClO}_4$, scan rate 100 mV s^{-1} , CH_2Cl_2 , 233 K.

Table 5.1. Redox potentials for $\text{Mn}(\text{Sal}^{\text{tBu}})\text{N}$ (+ 1 and 2 eq. $[\text{H}(\text{Et}_2\text{O})_2][\text{BF}_4]$) versus Fc^+/Fc ^{a,b}.

	E_{pa}^1	E_{pc}^2	$E_{1/2}^1$	E_{pa}^2	E_{pc}^2	$E_{1/2}^2$	$\Delta E_{1/2}$
$\text{Mn}(\text{Sal}^{\text{NMe}_2})$	0.03	-0.21	-0.07 (0.19)	0.20	0.00	0.10 (0.20)	0.170
+ 1 eq. $[\text{H}(\text{Et}_2\text{O})_2][\text{BF}_4]$	-0.3	-0.07	-0.19 (0.23)	0.54	0.34	0.44 (0.20)	0.630
+ 2 eq. $[\text{H}(\text{Et}_2\text{O})_2][\text{BF}_4]$	0.07	0.2	0.14	-	-	-	-

^aGiven in volts, peak-to-peak separation in parentheses. ^bPeak-to-peak difference for Fc^+/Fc couple at 233 K is 0.16 V.

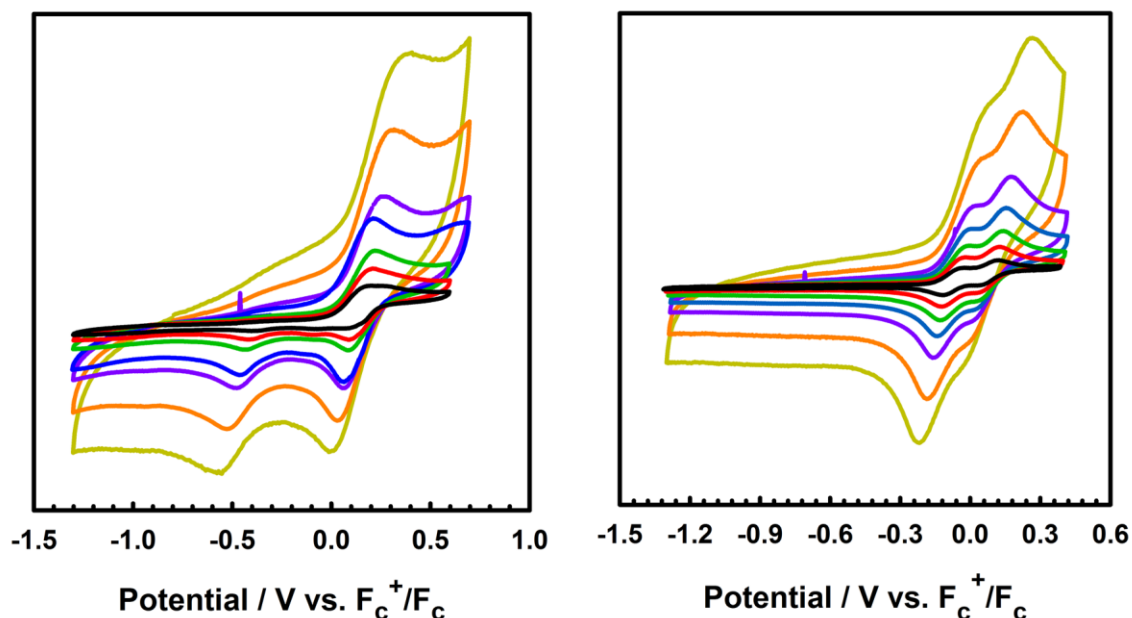
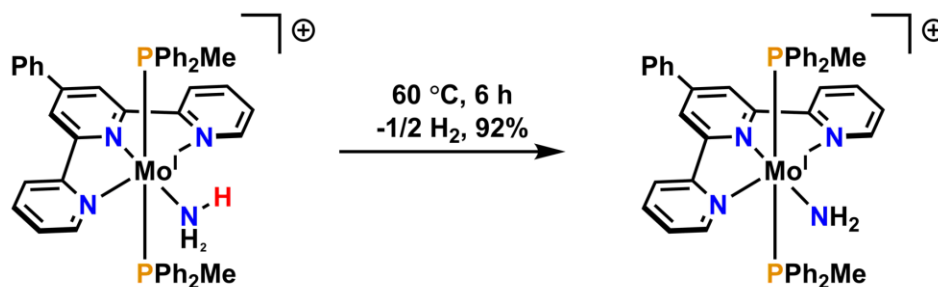


Figure 5.10. Scan rate dependence of **Mn(Sal^{NMe2})N** with two equivalents of [H(Et₂O)₂][BF₄] (left) and without (right). Conditions: 1 mM complex, 0.1 M ^tBu₄NClO₄, CH₂Cl₂, 233 K. Black: 10 mV s⁻¹; red: 25 mV s⁻¹; green: 50 mV s⁻¹; blue: 100 mV s⁻¹; purple: 200 mV s⁻¹; orange: 500 mV s⁻¹; yellow: 1000 mV s⁻¹.

5.3.4. Oxidation of Ammonia to H₂ and N₂

Ammonia production from its elements H₂ and N₂, as well as the reverse reaction (oxidation of ammonia) represent fundamental steps in the development of NH₃ as a nitrogen-based fuel and hydrogen storage medium.⁴⁸⁹⁻⁴⁹² Despite the successes of homogenous transition-metal-catalyzed N₂ reduction chemistry by the groups of Schrock,³⁸³ Nishibayashi,^{384, 493-495} Peters,⁴⁹⁶⁻⁴⁹⁸ and others,⁴⁹⁹⁻⁵⁰⁰ much less is known about H₂ formation following NH₃ activation. NH₃ represents an ideal hydrogen storage medium due to its high capacity (17.6% wt. H₂), low cost (~\$1.5 kg⁻¹ H₂), and ease of handling (-33 °C b.p.).⁵⁰¹⁻⁵⁰² Activation of the N-H bonds in NH₃ has been achieved through oxidative addition,⁵⁰³⁻⁵⁰⁶ deprotonation,⁵⁰⁷ cooperative reactions between the ligand and the metal,⁵⁰⁸⁻⁵¹⁰ or through multimetallic reaction pathways;⁵¹¹ however, in many cases formation of H₂ is not observed following N-H bond cleavage.⁵⁰⁶ Recent efforts in the Chirik group demonstrate that upon coordination to low-valent Mo(I/II), the N-H bonds in NH₃ are weakened from ~100 kcal mol⁻¹ to ~45 kcal mol⁻¹ allowing for the spontaneous evolution of H₂ upon gentle heating in benzene (Scheme 5.3).⁵¹²⁻⁵¹³

Scheme 5.3. Spontaneous hydrogen evolution from a low-valent Mo-NH₃ complex reported by Chirik and co-workers.⁵¹²



The work described in Chapter 4 represents the final step in the ammonia oxidation sequence and future efforts should be geared toward accessing and activating NH₃ adducts of electron-deficient Mn-salen systems (and other ligand platforms) for H₂ generation.

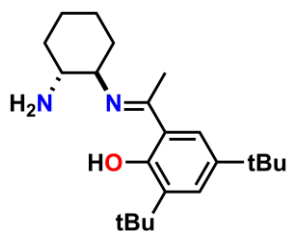
5.4. Experimental

5.4.1. Protocol for C-H Fluorination of 4-Ethylbiphenyl

The protocol for C-H fluorination reactions follows that outlined by Groves and co-workers.⁵¹⁴ To a Schlenk flask was added the substrate (4-ethylbiphenyl), catalyst (20 mol%), and 3 equivalents of AgF. The flask was then filled and evacuated with N₂ three times and a MeCN solution of triethylamine trihydrofluoride was added via syringe. The mixture was then heated at 50 °C with stirring. An equivalent of PhIO (as prepared according to reference 454) was added slowly while the reaction mixture was under a positive flow of N₂. A further equivalent of PhIO was added every hour during the fluorination reaction until no further product was detected by TLC. The reaction mixture was then removed from the heat, diluted with CH₂Cl₂ and filtered through a short pad of silica. Finally, the solvent was removed *in vacuo* and the crude material purified via flash column chromatography using 2.5% ethyl acetate in hexanes as eluent.

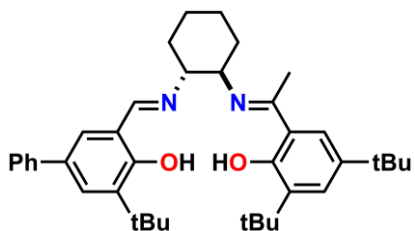
5.4.2. Synthesis

2-((*E*)-1-(((1*R*,2*R*)-2-aminocyclohexyl)imino)ethyl)-4,6-di-*tert*-butylphenol (**1**):



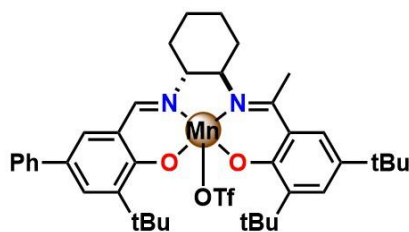
1-(3,5-di-*tert*-butyl-2-hydroxyphenyl)ethan-1-one (500 mg, 2 mmol) was added to a stirring ethanol solution (25 mL) of 1,2-diaminocyclohexane (350 mg, 3 mmol). The mixture was stirred vigorously for 48 hours, during which it changed to a bright yellow colour. The solvent was removed *in vacuo* and the crude material was passed through a pad of silica. Ethyl acetate was used to elute the high R_f fractions, followed by 10% MeOH in ethyl acetate to elute the product. The solvent was removed and the product was collected as a fine yellow powder. Yield: 450 mg, 65%. MALDI-MS m/z : 344.28 (100%). $^1\text{H NMR}$ (500 MHz, CDCl_3): δ = 7.41 (d, J = 2.4 Hz, 1 H), 7.39 (d, J = 2.4 Hz, 1H), 3.35 (ddd, J = 11.1, 8.9, 4.2 Hz, 1H), 3.01 (ddd, J = 11.0, 8.9, 4.0 Hz, 1H), 2.41 (s, 3H), 1.45 (s, 9H), 1.32 (s, 9H).

3-(*tert*-butyl)-5-((*E*)-(((1*R*,2*R*)-2-(((*E*)-1-(3,5-di-*tert*-butyl-2-hydroxyphenyl)ethylidene)amino)cyclohexyl)imino)methyl)-[1,1'-biphenyl]-4-ol (**2**):



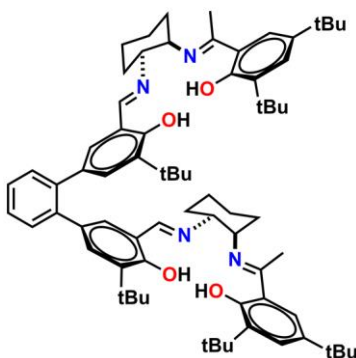
To a solution of **1** (40 mg, 0.12 mmol) in MeOH (5 mL) was added solid 5-(*tert*-butyl)-4-hydroxy-[1,1'-biphenyl]-3-carbaldehyde (30 mg, 0.12 mmol; prepared according to reference 206). The mixture was stirred at reflux for 1 hour during which time a fine yellow precipitate formed. The powder was collected by suction filtration and washed with cold MeOH (3x2 mL). Yield: 68 mg, 98%. MALDI-MS m/z : 580.41 (100%). $^1\text{H NMR}$ (500 MHz, CD_2Cl_2): δ = 8.41 (s, 1H), 7.47 (d, J = 2.3 Hz, 1H), 7.43 (m, 1H), 7.41 (d, J = 1.2 Hz, 1H), 7.37 (m, 2H), 7.31 (d, J = 2.4 Hz, 1H), 7.26 (m, 2H) 7.18 (d, J = 2.3 Hz, 1H), 3.89 – 3.74 (m, 1H), 3.49 – 3.38 (m, 1H), 2.30 (s, 3H), 1.44 (s, 9H), 1.42 (s, 9H), 1.22 (s, 9H).

3-(*tert*-butyl)-5-((*E*-(((1*R*,2*R*)-2-(((*E*-1-(3,5-di-*tert*-butyl-2-hydroxyphenyl)ethylidene)amino)cyclohexyl)imino)methyl)-[1,1'-biphenyl]-4-ol manganese (III) triflate (**3**):



To a refluxing solution of **2** (100 mg, 0.17 mmol) in EtOH (5 mL) was added solid Mn(OAc)₂•4H₂O (127 mg, 0.52 mmol). The mixture slowly turned from yellow to dark brown and was stirred at reflux for 2 hours, after which it was removed from the heat and the solvent was removed *in vacuo*. The crude residue was dissolved in an acetone/MeOH solution (4 mL:3 mL) and passed through a plug of Celite. To the brown solution was added 6 mL of 0.5 M triflic acid and the mixture was stirred vigorously for 30 minutes, after which point the organic layer was separated, and concentrated *in vacuo* to result in a brown powder. The crude powder was recrystallized from CHCl₃/hexanes to yield **3** as a microcrystalline material. Yield: 110 mg, 81%. MALDI-MS *m/z*: 782.29 (100%). Anal. Calcd (%) for C₄₀H₅₀F₃MnN₂O₅S: C 61.37, H 6.44, N 3.58, S 4.10; Found: C 61.02, H 6.21, N 3.42, S 4.48. Solution magnetic moment (¹H Evans' Method¹¹²⁻¹¹³): $\mu_{\text{eff}} = 4.88 \mu_{\text{B}}$.

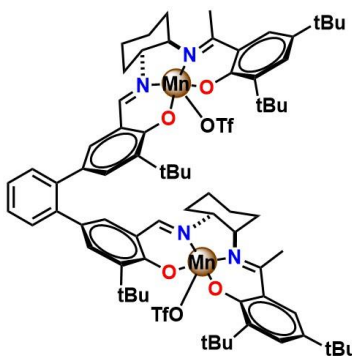
3,3''-di-*tert*-butyl-5,5''-bis((*E*-(((1*R*,2*R*)-2-(((*E*-1-(3,5-di-*tert*-butyl-2-hydroxyphenyl)ethylidene)amino)cyclohexyl)imino)methyl)-[1,1':2',1''-terphenyl]-4,4''-diol (**4**):



To a stirring solution of **1** (88 mg, 0.25 mmol) in dichloroethane (2 mL, 3 Å mol. sieves) under N₂ was added a solution of 5,5''-di-*tert*-butyl-4,4''-dihydroxy-[1,1':2',1''-terphenyl]-3,3''-dicarbaldehyde (50 mg, 0.12 mmol; prepared according to reference 206)

in dichloroethane (2 mL). The mixture was stirred at reflux for 20 hours, after which point it was removed from the heat and the mol. sieves filtered off. The solvent was removed *in vacuo* and the crude material was purified by flash column chromatography using 10% ether in petroleum ether as eluent. Yield: 98 mg, 78%. MALDI-MS *m/z*: 1082.73 (100%). ¹H NMR (500 MHz, CD₂Cl₂): δ = 8.31 (s, 2H), 7.34 (d, *J* = 2.3 Hz, 2H), 7.29 (m, 2H), 7.28 (d, *J* = 2.4 Hz, 2H), 7.20 (dd, *J* = 5.7, 3.2 Hz, 2H), 6.96 (d, *J* = 2.2 Hz, 2H), 6.72 (d, *J* = 2.2 Hz, 2H), 3.81 (m, 2H), 3.39 (m, 2H), 2.30 (s, 6H), 1.43 (s, 18H), 1.24 (s, 18H), 1.03 (s, 18H).

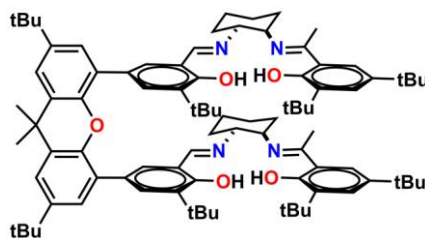
3,3''-di-*tert*-butyl-5,5''-bis((*E*-(((1*R*,2*R*)-2-(((*E*-1-(3,5-di-*tert*-butyl-2-hydroxyphenyl)ethylidene)amino)cyclohexyl)imino)methyl)-[1,1':2',1''-terphenyl]-4,4''-diol manganese (III) triflate (**5**):



To a refluxing solution of **4** (100 mg, 0.09 mmol) in EtOH (5 mL) was added solid Mn(OAc)₂•4H₂O (55 mg, 0.21 mmol). The mixture slowly turned from yellow to brown and was stirred at reflux for 4 hours. The mixture was then removed from the heat, concentrated *in vacuo* and the crude residue redissolved in a mixture of acetone/MeOH (4:3, 7 mL total). Triflic acid (30 equivalents, 0.25 mL in 5.5 mL H₂O) was added and the mixture was stirred vigorously for 30 minutes, and then extracted into CH₂Cl₂. The solvent was reduced and pentane added dropwise to precipitate a fine brown powder which was collected by suction filtration. Yield: 88 mg, 61%. MALDI-MS *m/z*: 1486.57 (100%). Anal. Cald (%) for C₇₄H₉₄F₆Mn₂N₄O₁₀S₂: C 59.75, H 6.37, N 3.77, S 4.31; Found: C 59.46, H 6.12, N 3.72, S 4.68.

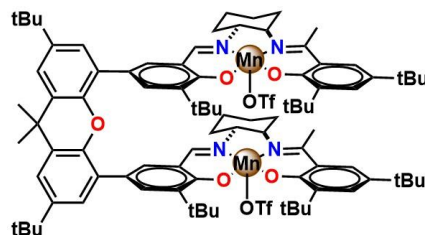
6-6'-((1*E*,1'*E*-(((1*R*,1'*R*)-(((1*E*,1'*E*-((2,7-di-*tert*-butyl-9,9-dimethyl-9*H*-xanthene-4,5-diyl)bis(5-(*tert*-butyl)-6-hydroxy-3,1-phenylene))bis(methaneylydiene))bis

(azaneylydene))bis(cyclohexane-2,1-diyl))bis(azaneylydene))bis(ethan-1-yl-1-ylidene))bis(2,4-di-*tert*-butylphenol) (**6**):



To a stirring solution of **1** (100 mg, 0.29 mmol) in dichloroethane (4 mL, 3 Å mol. sieves) was added a dichloroethane solution (4 mL) of 5,5'-(2,7-di-*tert*-butyl-9,9-dimethyl-9*H*-xanthene-4,5-diyl)bis(3-(*tert*-butyl)-2-hydroxybenzaldehyde) (98 mg, 0.14 mmol; see Chapter 2, Scheme 2.1 – Compound **6**). The mixture was stirred at reflux for 20 hours, at which point it was removed from the heat and the mol. sieves filtered off. The solvent was removed *in vacuo* and the crude material was purified by flash column chromatography using 3% ether in petroleum ether as eluent. Yield: 168 mg, 87%. MALDI-MS *m/z*: 1326.99 (100%). ¹H NMR (500 MHz, CD₂Cl₂): δ = 7.33 (d, *J* = 2.4 Hz, 2H), 7.24 (q, *J* = 2.4 Hz, 4H), 7.14 (d, *J* = 2.2 Hz, 2H), 7.05 (d, *J* = 2.2 Hz, 2H), 7.02 (d, *J* = 2.4 Hz, 2H), 3.91 (m, 2H), 3.67 (m, 2H), 2.32 (s, 6H), 1.67 (s, 6H), 1.35 (s, 18H), 1.29 (s, 18H), 1.19 (s, 18H), 1.14 (s, 18H).

6-6'-((1*E*,1'*E*)-(((1*R*,1'*R*)-(((1*E*,1'*E*)-((2,7-di-*tert*-butyl-9,9-dimethyl-9*H*-xanthene-4,5-diyl)bis(5-(*tert*-butyl)-6-hydroxy-3,1-phenylene))bis(methaneylydene))bis(azaneylydene))bis(cyclohexane-2,1-diyl))bis(azaneylydene))bis(ethan-1-yl-1-ylidene))bis(2,4-di-*tert*-butylphenol) manganese (III) triflate (**7**):



To a refluxing solution of **6** (120 mg, 0.09 mmol) in EtOH (10 mL) was added solid Mn(OAc)₂•4H₂O (60 mg, 0.21 mmol). The mixture slowly turned from yellow to brown and was stirred at reflux for 4 hours. The mixture was then removed from the heat,

concentrated *in vacuo* and the crude residue redissolved in a mixture of acetone/MeOH (4:3, 7 mL total). Triflic acid (30 equivalents, 0.25 mL in 5.5 mL H₂O) was added and the mixture was stirred vigorously for 30 minutes, and then extracted into CH₂Cl₂. The solvent was reduced and pentane added dropwise to precipitate a fine brown powder which was collected by suction filtration. Yield: 86 mg, 55%. MALDI-MS *m/z*: 1730.64 (100%). Anal. Cald (%) for C₉₁H₁₁₈F₆Mn₂N₄O₁₁S₂: C 63.11, H 6.87, N 3.23, S 3.70; Found: C 62.99, H 6.59, N 3.02, S 3.92.

5.4.3. Photolysis of [Mn(Sal^{NMe2})N]^{•+}

To a solution containing 2.5 mg Mn(Sal^{NMe2})N in 2 mL dry CH₂Cl₂ (2.15 mM) was added 0.9 equivalents of AgSbF₆ as a CH₂Cl₂ solution (7 mg AgSbF₆ dissolved in 1 mL, injected 40 μL). The mixture turned from brown to red/purple and was stirred for 10 minutes at room temperature before being filtered through a pad of celite to remove the Ag(0) precipitate. 500 μL of this solution was added to 500 μL of dry CH₂Cl₂ in a quartz UV-vis cell equipped with a Teflon cap. The solution was irradiated with UV light for approximately 5 minutes during which it changed from red to brown.

References

1. Chirik, P. J.; Wieghardt, K., *Science* 2010, **327**, 794-795.
2. Ward, M. D.; McCleverty, J. A., *J. Chem. Soc. Dalton Trans.* 2002, 275-288.
3. Jørgensen, C. K., *Coord. Chem. Rev.* 1966, **1**, 164-178.
4. Kaim, W.; Schwederski, B., *Pure Appl. Chem.* 2004, **76**, 651-364.
5. McCleverty, J. A., *Chem. Rev.* 2004, **104**, 403-418.
6. Pauling, L., *Nature* 1964, **203**, 182.
7. Weiss, J. J., *Nature* 1964, **202**, 83.
8. Chen, H.; Ikeda-Saito, M.; Shaik, S., *J. Am. Chem. Soc.* 2008, **130**, 14778-14790.
9. Sono, M.; Roach, M. P.; Coulter, E. D.; Dawson, J. H., *Chem. Rev.* 1996, **96**, 2841-2888.
10. Solomon, E. I.; Brunold, T. C.; Davis, M. I.; Kemsley, J. N.; Lee, S.-K.; Lehnert, N.; Neese, F.; Skulan, A. J.; Yang, Y.-S.; Zhou, J., *Chem. Rev.* 2000, **100**, 235-350.
11. Jones, R. D.; Summerville, D. A.; Basolo, F., *Chem. Rev.* 1979, **79**, 139-179.
12. Meunier, B.; de Visser, S. P.; Shaik, S., *Chem. Rev.* 2004, **104**, 3947-3980.
13. Praneeth, V. K. K.; Ringenberg, M. R.; Ward, T. R., *Angew. Chem. Int. Ed.* 2012, **51**, 10228-10234.
14. Chirik, P. J., *Inorg. Chem.* 2011, **50**, 9737-9740.
15. Luca, O. R.; Crabtree, R. H., *Chem. Soc. Rev.* 2013, **42**, 1440-1459.
16. Kaim, W., *Eur. J. Inorg. Chem.* 2012, **2012**, 343-348.
17. Lyaskovskyy, V.; de Bruin, B., *ACS Catalysis* 2012, **2**, 270-279.
18. Stubbe, J.; van der Donk, W. A., *Chem. Rev.* 1998, **98**, 705-762.
19. Pujols-Ayala, I.; Barry, B. A., *Biochim. Biophys. Acta* 2004, **1655**, 205-216.
20. Barry, B. A.; Babcock, G. T., *Proc. Natl. Acad. Sci. U. S. A.* 1987, **84**, 7099-7103.
21. Rogers, M. S.; Dooley, D. M., *Curr. Opin. Chem. Biol.* 2003, **7**, 189-196.
22. Slep, L. D.; Neese, F., *Angew. Chem. Int. Ed.* 2003, **42**, 2942-2945.

23. Whittaker, M. M.; Kersten, P. J.; Nakamura, N.; Sanders-Loehr, J.; Schweizer, E. S.; Whittaker, J. W., *J. Biol. Chem.* 1996, **271**, 681-687.
24. Whittaker, J. W., *Chem. Rev.* 2003, **103**, 2347-2364.
25. Whittaker, M. M.; DeVito, V. L.; Asher, S. A.; Whittaker, J. W., *J. Biol. Chem.* 1989, **264**, 7104-7106.
26. Whittaker, M. M.; Whittaker, J. W., *J. Biol. Chem.* 1990, **265**, 9610-9613.
27. *The PyMOL Molecular Graphics System*, 2.0; Schrodinger, LLC.
28. Denisov, I. G.; Makris, T. M.; Sligar, S. G.; Schlichting, I., *Chem. Rev.* 2005, **105**, 2253-2278.
29. Nelson, D. R., *Hum. Genomics* 2009, **4**, 59-65.
30. Hasemann, C. A.; Kurumbail, R. G.; Boddupalli, S. S.; Peterson, J. A.; Deisenhofer, J., *Structure* **3**, 41-62.
31. Dawson, J. H.; Holm, R. H.; Trudell, J. R.; Barth, G.; Linder, R. E.; Bunnenberg, E.; Djerassi, C.; Tang, S. C., *J. Am. Chem. Soc.* 1976, **98**, 3707-3709.
32. Rittle, J.; Green, M. T., *Science* 2010, **330**, 933-937.
33. Dunford, H. B.; Stillman, J. S., *Coord. Chem. Rev.* 1976, **19**, 187-251.
34. Shaik, S.; Kumar, D.; de Visser, S. P.; Altun, A.; Thiel, W., *Chem. Rev.* 2005, **105**, 2279-2328.
35. Groves, J. T., *Proc. Natl. Acad. Sci. U. S. A.* 2003, **100**, 3569-3574.
36. Schrauzer, G. N.; Mayweg, V., *J. Am. Chem. Soc.* 1962, **84**, 3221-3221.
37. Gray, H. B.; Williams, R.; Bernal, I.; Billig, E., *J. Am. Chem. Soc.* 1962, **84**, 3596-3597.
38. Gray, H. B.; Billig, E., *J. Am. Chem. Soc.* 1963, **85**, 2019-2020.
39. Davison, A.; Edelstein, N.; Holm, R. H.; Maki, A. H., *Inorg. Chem.* 1963, **2**, 1227-1232.
40. Locke, J.; McCleverty, J. A.; Wharton, E. J.; Winscom, C. J., *Chemical Communications (London)* 1966, 677-678.
41. McCleverty, J. A., Metal 1,2-Dithiolene and Related Complexes. In *Prog. Inorg. Chem.*, John Wiley & Sons, Inc.: 2007; pp 49-221.
42. Sproules, S.; Wieghardt, K., *Coord. Chem. Rev.* 2011, **255**, 837-860.
43. Eisenberg, R.; Gray, H. B., *Inorg. Chem.* 2011, **50**, 9741-9751.
44. Poddel'sky, A. I.; Cherkasov, V. K.; Abakumov, G. A., *Coord. Chem. Rev.* 2009, **253**, 291-324.

45. Blackmore, K. J.; Ziller, J. W.; Heyduk, A. F., *Inorg. Chem.* 2005, **44**, 5559-5561.
46. Haneline, M. R.; Heyduk, A. F., *J. Am. Chem. Soc.* 2006, **128**, 8410-8411.
47. Brown, S. N., *Inorg. Chem.* 2012, **51**, 1251-1260.
48. Small, B. L.; Brookhart, M.; Bennett, A. M. A., *J. Am. Chem. Soc.* 1998, **120**, 4049-4050.
49. J. P. Britovsek, G.; C. Gibson, V.; J. McTavish, S.; A. Solan, G.; J. P. White, A.; J. Williams, D.; J. P. Britovsek, G.; S. Kimberley, B.; J. Maddox, P., *Chem. Commun.* 1998, 849-850.
50. de Bruin, B.; Bill, E.; Bothe, E.; Weyhermüller, T.; Wieghardt, K., *Inorg. Chem.* 2000, **39**, 2936-2947.
51. Budzelaar, P. H. M.; de Bruin, B.; Gal, A. W.; Wieghardt, K.; van Lenthe, J. H., *Inorg. Chem.* 2001, **40**, 4649-4655.
52. Bart, S. C.; Lobkovsky, E.; Chirik, P. J., *J. Am. Chem. Soc.* 2004, **126**, 13794-13807.
53. Archer, A. M.; Bouwkamp, M. W.; Cortez, M.-P.; Lobkovsky, E.; Chirik, P. J., *Organometallics* 2006, **25**, 4269-4278.
54. Bart, S. C.; Lobkovsky, E.; Bill, E.; Chirik, P. J., *J. Am. Chem. Soc.* 2006, **128**, 5302-5303.
55. Bart, S. C.; Chłopek, K.; Bill, E.; Bouwkamp, M. W.; Lobkovsky, E.; Neese, F.; Wieghardt, K.; Chirik, P. J., *J. Am. Chem. Soc.* 2006, **128**, 13901-13912.
56. Bouwkamp, M. W.; Bowman, A. C.; Lobkovsky, E.; Chirik, P. J., *J. Am. Chem. Soc.* 2006, **128**, 13340-13341.
57. Sylvester, K. T.; Chirik, P. J., *J. Am. Chem. Soc.* 2009, **131**, 8772-8774.
58. Knijnenburg, Q.; Gambarotta, S.; Budzelaar, P. H. M., *Dalton Trans.* 2006, 5442-5448.
59. Que, L.; Tolman, W. B., *Nature* 2008, **455**, 333-340.
60. Nam, W., *Acc. Chem. Res.* 2007, **40**, 465-465.
61. Swiegers, G. F.; Chen, J.; Wagner, P., Bioinspired Catalysis. In *Bioinspiration and Biomimicry in Chemistry*, John Wiley & Sons, Inc.: 2012; pp 165-208.
62. Wang, Y.; DuBois, J. L.; Hedman, B.; Hodgson, K. O.; Stack, T. D. P., *Science* 1998, **279**, 537-540.
63. Chen, M. S.; White, M. C., *Science* 2007, **318**, 783-787.
64. Kudrik, E. V.; Afanasiev, P.; Alvarez, L. X.; Dubourdeaux, P.; Clémancey, M.; Latour, J.-M.; Blondin, G.; Bouchu, D.; Albrieux, F.; Nefedov, S. E.; Sorokin, A. B., *Nat Chem* 2012, **4**, 1024-1029.

65. Alaji, Z.; Safaei, E.; Chiang, L.; Clarke, R. M.; Mu, C. H.; Storr, T., *Eur. J. Inorg. Chem.* 2014, 6066-6074.
66. Balaghi, S. E.; Safaei, E.; Chiang, L.; Wong, E. W. Y.; Savard, D.; Clarke, R. M.; Storr, T., *Dalton Trans.* 2013, **42**, 6829-6839.
67. Wang, Y.; Stack, T. D. P., *J. Am. Chem. Soc.* 1996, **118**, 13097-13098.
68. Huang, X.; Groves, J. T., *Chem. Rev.* 2017.
69. Baglia, R. A.; Zaragoza, J. P. T.; Goldberg, D. P., *Chem. Rev.* 2017, **117**, 13320-13352.
70. Sahu, S.; Goldberg, D. P., *J. Am. Chem. Soc.* 2016, **138**, 11410-11428.
71. Zhang, W.; Lai, W.; Cao, R., *Chem. Rev.* 2017, **117**, 3717-3797.
72. Costas, M., *Coord. Chem. Rev.* 2011, **255**, 2912-2932.
73. Groves, J. T.; Haushalter, R. C.; Nakamura, M.; Nemo, T. E.; Evans, B. J., *J. Am. Chem. Soc.* 1981, **103**, 2884-2886.
74. Dolphin, D.; Traylor, T. G.; Xie, L. Y., *Acc. Chem. Res.* 1997, **30**, 251-259.
75. McGarrigle, E. M.; Gilheany, D. G., *Chem. Rev.* 2005, **105**, 1563-1602.
76. Canali, L.; C. Sherrington, D., *Chem. Soc. Rev.* 1999, **28**, 85-93.
77. Darensbourg, D. J., *Chem. Rev.* 2007, **107**, 2388-2410.
78. Irie, R.; Noda, K.; Ito, Y.; Matsumoto, N.; Katsuki, T., *Tetrahedron Lett.* 1990, **31**, 7345-7348.
79. Jacobsen, E. N.; Zhang, W.; Muci, A. R.; Ecker, J. R.; Deng, L., *J. Am. Chem. Soc.* 1991, **113**, 7063-7064.
80. Lyons, C. T.; Stack, T. D. P., *Coord. Chem. Rev.* 2013, **257**, 528-540.
81. Cozzi, P. G., *Chem. Soc. Rev.* 2004, **33**, 410-421.
82. Clarke, R. M.; Storr, T., *Dalton Trans.* 2014, **43**, 9380-9391.
83. Pratt, R. C.; Stack, T. D. P., *J. Am. Chem. Soc.* 2003, **125**, 8716-8717.
84. Pratt, R. C.; Lyons, C. T.; Wasinger, E. C.; Stack, T. D. P., *J. Am. Chem. Soc.* 2012, **134**, 7367-7377.
85. Saint-Aman, E.; Menage, S.; Pierre, J.-L.; Defrancq, E.; Gellon, G., *New J. Chem.* 1998, **22**, 393-394.
86. Thomas, F.; Jarjayes, O.; Duboc, C.; Philouze, C.; Saint-Aman, E.; Pierre, J.-L., *Dalton Trans.* 2004, 2662-2669.

87. Campbell, E. J.; Nguyen, S. T., *Tetrahedron Lett.* 2001, **42**, 1221-1225.
88. Audebert, P.; Capdevielle, P.; Maumy, M., *New J. Chem.* 1991, **15**, 235-237.
89. Pasini, A.; Bernini, E.; Scaglia, M.; de Santis, G., *Polyhedron* 1996, **15**, 4461-4467.
90. Abu-El-Wafa, S. M.; Issa, R. M.; McAuliffe, C. A., *Inorg. Chim. Acta* 1985, **99**, 103-106.
91. Bottcher, A.; Elias, H.; Jager, E. G.; Langfelderova, H.; Mazur, M.; Muller, L.; Paulus, H.; Pelikan, P.; Rudolph, M.; Valko, M., *Inorg. Chem.* 1993, **32**, 4131-4138.
92. Freire, C.; de Castro, B., *J. Chem. Soc. Dalton Trans.* 1998, 1491-1497.
93. Andrez, J.; Guidal, V.; Scopelliti, R.; Pécaut, J.; Gambarelli, S.; Mazzanti, M., *J. Am. Chem. Soc.* 2017, **139**, 8628-8638.
94. Kaim, W.; Klein, A.; Glöckle, M., *Acc. Chem. Res.* 2000, **33**, 755-763.
95. Demadis, K. D.; Hartshorn, C. M.; Meyer, T. J., *Chem. Rev.* 2001, **101**, 2655-2686.
96. Creutz, C.; Taube, H., *J. Am. Chem. Soc.* 1969, **91**, 3988-3989.
97. Chaudhuri, P.; Verani, C. N.; Bill, E.; Bothe, E.; Weyhermüller, T.; Wieghardt, K., *J. Am. Chem. Soc.* 2001, **123**, 2213-2223.
98. Lu, C. C.; Bill, E.; Weyhermüller, T.; Bothe, E.; Wieghardt, K., *J. Am. Chem. Soc.* 2008, **130**, 3181-3197.
99. Robin, M. B.; Day, P., *Adv. Inorg. Chem. Radiochem.* 1967, **10**, 247.
100. Hush, N. S., Intervalence-Transfer Absorption. Part 2. Theoretical Considerations and Spectroscopic Data. In *Prog. Inorg. Chem.*, John Wiley & Sons, Inc.: 2007; pp 391-444.
101. Fuerholz, U.; Joss, S.; Buergi, H. B.; Ludi, A., *Inorg. Chem.* 1985, **24**, 943-948.
102. D'Alessandro, D. M.; Keene, F. R., *Chem. Soc. Rev.* 2006, **35**, 424-440.
103. Parthey, M.; Kaupp, M., *Chem. Soc. Rev.* 2014, **43**, 5067-5088.
104. Brunschwig, B. S.; Creutz, C.; Sutin, N., *Chem. Soc. Rev.* 2002, **31**, 168-184.
105. Launay, J.-P., *Chem. Soc. Rev.* 2001, **30**, 386-397.
106. Balzani, V.; Juris, A.; Venturi, M.; Campagna, S.; Serroni, S., *Chem. Rev.* 1996, **96**, 759-834.
107. Connelly, N. G.; Geiger, W. E., *Chem. Rev.* 1996, **96**, 877-910.
108. Flanagan, J. B.; Margel, S.; Bard, A. J.; Anson, F. C., *J. Am. Chem. Soc.* 1978, **100**, 4248-4253.

109. Creutz, C., Mixed Valence Complexes of d5-d6 Metal Centers. In *Prog. Inorg. Chem.*, John Wiley & Sons, Inc.: 2007; pp 1-73.
110. Kalyanasundaram, K.; Nazeeruddin, M. K., *Inorg. Chim. Acta* 1994, **226**, 213-230.
111. Ward, M. D., *Chem. Soc. Rev.* 1995, **24**, 121-134.
112. Evans, D. F., *J. Chem. Soc.* 1959, 2003-2005.
113. Evans, D. F.; Fazakerley, G. V.; Phillips, R. F., *J. Chem. Soc. A* 1971, 1931-1934.
114. Chiang, L.; Kochem, A.; Jarjayes, O.; Dunn, T. J.; Vezin, H.; Sakaguchi, M.; Ogura, T.; Orio, M.; Shimazaki, Y.; Thomas, F.; Storr, T., *Chem. Eur. J.* 2012, **18**, 14117-14127.
115. Herasymchuk, K.; Chiang, L.; Hayes, C. E.; Brown, M. L.; Ovens, J. S.; Patrick, B. O.; Leznoff, D. B.; Storr, T., *Dalton Trans.* 2016, **45**, 12576-12586.
116. Storr, T.; Verma, P.; Shimazaki, Y.; Wasinger, E. C.; Stack, T. D. P., *Chem. Eur. J.* 2010, **16**, 8980-8983.
117. Shimazaki, Y.; Tani, F.; Fukui, K.; Naruta, Y.; Yamauchi, O., *J. Am. Chem. Soc.* 2003, **125**, 10512-10513.
118. Radziszewski, J. G.; Gil, M.; Gorski, A.; Spanget-Larsen, J.; Waluk, J.; Mróz, B. J., *J. Chem. Phys.* 2002, **116**, 5912-5912.
119. Spanget-Larsen, J.; Gil, M.; Gorski, A.; Blake, D. M.; Waluk, J.; Radziszewski, J. G., *J. Am. Chem. Soc.* 2001, **123**, 11253-11261.
120. Storr, T.; Wasinger, E. C.; Pratt, R. C.; Stack, T. D. P., *Angew. Chem. Int. Ed.* 2007, **46**, 5198-5201.
121. Storr, T.; Verma, P.; Pratt, R. C.; Wasinger, E. C.; Shimazaki, Y.; Stack, T. D. P., *J. Am. Chem. Soc.* 2008, **130**, 15448-15459.
122. Cramer, C. J., *Essentials of Computational Chemistry: Theories and Models*. 2 ed.; John Wiley & Sons Ltd: 2004.
123. Aono, S.; Nakagaki, M.; Kurahashi, T.; Fujii, H.; Sakaki, S., *J. Chem. Theory Comput.* 2014, **10**, 1062-1073.
124. Kurahashi, T.; Fujii, H., *J. Am. Chem. Soc.* 2011, **133**, 8307-8316.
125. Clarke, R. M.; Storr, T., *J. Am. Chem. Soc.* 2016, **138**, 15299-15302.
126. Chiang, L.; Herasymchuk, K.; Thomas, F.; Storr, T., *Inorg. Chem.* 2015, **54**, 5970-5980.
127. Chiang, L.; Clarke, R. M.; Herasymchuk, K.; Sutherland, M.; Prosser, K. E.; Shimazaki, Y.; Storr, T., *Eur. J. Inorg. Chem.* 2016, **2016**, 49-55.

128. Verma, P.; Pratt, R. C.; Storr, T.; Wasinger, E. C.; Stack, T. D. P., *Proc. Natl. Acad. Sci. U. S. A.* 2011, **108**, 18600-18605.
129. De Castro, B.; Freire, C., *Inorg. Chem.* 1990, **29**, 5113-5119.
130. Santos, I. C.; Vilas-Boas, M.; Piedade, M. F. M.; Freire, C.; Duarte, M. T.; de Castro, B., *Polyhedron* 2000, **19**, 655-664.
131. Leung, W.-H.; Chan, E. Y. Y.; Chow, E. K. F.; Williams, I. D.; Peng, S.-M., *J. Chem. Soc. Dalton Trans.* 1996, 1229-1236.
132. Rotthaus, O.; Jarjays, O.; Thomas, F.; Philouze, C.; Del Valle, C. P.; Saint-Aman, E.; Pierre, J. L., *Chem. Eur. J.* 2006, **12**, 2293-2302.
133. Rotthaus, O.; Thomas, F.; Jarjays, O.; Philouze, C.; Saint-Aman, E.; Pierre, J.-L., *Chem. Eur. J.* 2006, **12**, 6953-6962.
134. Benisvy, L.; Kannappan, R.; Song, Y.-F.; Milikisyants, S.; Huber, M.; Mutikainen, I.; Turpeinen, U.; Gamez, P.; Bernasconi, L.; Baerends, E. J.; Hartl, F.; Reedijk, J., *Eur. J. Inorg. Chem.* 2007, **2007**, 637-642.
135. Pierpont, C. G., *Coord. Chem. Rev.* 2001, **216–217**, 99-125.
136. Adams, D. M.; Noodleman, L.; Hendrickson, D. N., *Inorg. Chem.* 1997, **36**, 3966-3984.
137. Hendrickson, D. N.; Pierpont, C. G., Valence Tautomeric Transition Metal Complexes. In *Spin Crossover in Transition Metal Compounds II*, Springer Berlin Heidelberg: Berlin, Heidelberg, 2004; pp 63-95.
138. Rall, J.; Wanner, M.; Albrecht, M.; Hornung, F. M.; Kaim, W., *Chem. Eur. J.* 1999, **5**, 2802-2809.
139. Speier, G.; Tyeklár, Z.; Tóth, P.; Speier, E.; Tisza, S.; Rockenbauer, A.; Whalen, A. M.; Alkire, N.; Pierpont, C. G., *Inorg. Chem.* 2001, **40**, 5653-5659.
140. Frischmann, P. D.; MacLachlan, M. J., *Chem. Soc. Rev.* 2013, **42**, 871-890.
141. Whiteoak, C. J.; Salassa, G.; Kleij, A. W., *Chem. Soc. Rev.* 2012, **41**, 622-631.
142. Haak, R. M.; Wezenberg, S. J.; Kleij, A. W., *Chem. Commun.* 2010, **46**, 2713-2723.
143. Daumann, L. J.; Schenk, G.; Ollis, D. L.; Gahan, L. R., *Dalton Trans.* 2014, **43**, 910-928.
144. Volbeda, A.; Charon, M.-H.; Piras, C.; Hatchikian, E. C.; Frey, M.; Fontecilla-Camps, J. C., *Nature* 1995, **373**, 580.
145. Peters, J. W.; Lanzilotta, W. N.; Lemon, B. J.; Seefeldt, L. C., *Science* 1998, **282**, 1853-1858.
146. Dey, S.; Das, P. K.; Dey, A., *Coord. Chem. Rev.* 2013, **257**, 42-63.

147. Hiromoto, T.; Ataka, K.; Pilak, O.; Vogt, S.; Stagni, M. S.; Meyer-Klaucke, W.; Warkentin, E.; Thauer, R. K.; Shima, S.; Ermler, U., *FEBS Lett.* 2009, **583**, 585-590.
148. Krahn, E.; Weiss, B.; Kröckel, M.; Groppe, J.; Henkel, G.; Cramer, S.; Trautwein, A.; Schneider, K.; Müller, A., *JBIC Journal of Biological Inorganic Chemistry* 2002, **7**, 37-45.
149. Kentemich, T.; Haverkamp, G.; Bothe, H., The Expression of a Third Nitrogenase in the Cyanobacterium *Anabaena variabilis*. In *Zeitschrift für Naturforschung C*, 1991; Vol. 46, p 217.
150. Einsle, O.; Tezcan, F. A.; Andrade, S. L. A.; Schmid, B.; Yoshida, M.; Howard, J. B.; Rees, D. C., *Science* 2002, **297**, 1696-1700.
151. Smith, S. M.; Rosenzweig, A. C., Particulate Methane Monooxygenase. In *Encyclopedia of Metalloproteins*, Kretsinger, R. H.; Uversky, V. N.; Permyakov, E. A., Eds. Springer New York: New York, NY, 2013; pp 1663-1669.
152. Wallar, B. J.; Lipscomb, J. D., *Chem. Rev.* 1996, **96**, 2625-2658.
153. Collman, J. P.; Wagenknecht, P. S.; Hutchison, J. E., *Angew. Chem. Int. Ed.* 1994, **33**, 1537-1554.
154. Simmons, T. R.; Berggren, G.; Bacchi, M.; Fontecave, M.; Artero, V., *Coord. Chem. Rev.* 2014, **270-271**, 127-150.
155. Schilter, D.; Camara, J. M.; Huynh, M. T.; Hammes-Schiffer, S.; Rauchfuss, T. B., *Chem. Rev.* 2016, **116**, 8693-8749.
156. Wang, N.; Wang, M.; Chen, L.; Sun, L., *Dalton Trans.* 2013, **42**, 12059-12071.
157. Shimazaki, Y.; Nagano, T.; Takesue, H.; Ye, B.-H.; Tani, F.; Naruta, Y., *Angew. Chem. Int. Ed.* 2004, **43**, 98-100.
158. Das, S.; Brudvig, G. W.; Crabtree, R. H., *Chem. Commun.* 2008, 413-424.
159. Collman, J. P.; Zeng, L.; Brauman, J. I., *Inorg. Chem.* 2004, **43**, 2672-2679.
160. Chang, C. J.; Deng, Y.; Heyduk, A. F.; Chang, C. K.; Nocera, D. G., *Inorg. Chem.* 2000, **39**, 959-966.
161. Rosenthal, J.; Nocera, D. G., *Acc. Chem. Res.* 2007, **40**, 543-553.
162. Chang, C. J.; Loh, Z.-H.; Shi, C.; Anson, F. C.; Nocera, D. G., *J. Am. Chem. Soc.* 2004, **126**, 10013-10020.
163. Givaja, G.; Volpe, M.; Edwards, M. A.; Blake, A. J.; Wilson, C.; Schröder, M.; Love, J. B., *Angew. Chem. Int. Ed.* 2007, **46**, 584-586.
164. Askarizadeh, E.; Yaghoob, S. B.; Boghaei, D. M.; Slawin, A. M. Z.; Love, J. B., *Chem. Commun.* 2010, **46**, 710-712.

165. Volpe, M.; Hartnett, H.; Leeland, J. W.; Wills, K.; Ogunshun, M.; Duncombe, B. J.; Wilson, C.; Blake, A. J.; McMaster, J.; Love, J. B., *Inorg. Chem.* 2009, **48**, 5195-5207.
166. Sorokin, A. B.; Kudrik, E. V.; Bouchu, D., *Chem. Commun.* 2008, 2562-2564.
167. Sorokin, A. B.; Kudrik, E. V.; Alvarez, L. X.; Afanasiev, P.; Millet, J. M. M.; Bouchu, D., *Catal. Today* 2010, **157**, 149-154.
168. Bell, S. R.; Groves, J. T., *J. Am. Chem. Soc.* 2009, **131**, 9640-9641.
169. Seo, M. S.; Kim, N. H.; Cho, K.-B.; So, J. E.; Park, S. K.; Clemancey, M.; Garcia-Serres, R.; Latour, J.-M.; Shaik, S.; Nam, W., *Chem. Sci.* 2011, **2**, 1039-1045.
170. Castilla, A. M.; Curreli, S.; Escudero-Adán, E. C.; Belmonte, M. M.; Benet-Buchholz, J.; Kleij, A. W., *Org. Lett.* 2009, **11**, 5218-5221.
171. Escudero-Adán, E. C.; Belmonte, M. M.; Benet-Buchholz, J.; Kleij, A. W., *Org. Lett.* 2010, **12**, 4592-4595.
172. Konsler, R. G.; Karl, J.; Jacobsen, E. N., *J. Am. Chem. Soc.* 1998, **120**, 10780-10781.
173. Mazet, C.; Jacobsen, E. N., *Angew. Chem. Int. Ed.* 2008, **47**, 1762-1765.
174. Park, J.; Lang, K.; Abboud, K. A.; Hong, S., *J. Am. Chem. Soc.* 2008, **130**, 16484-16485.
175. Mouri, S.; Chen, Z.; Mitsunuma, H.; Furutachi, M.; Matsunaga, S.; Shibasaki, M., *J. Am. Chem. Soc.* 2010, **132**, 1255-1257.
176. Handa, S.; Gnanadesikan, V.; Matsunaga, S.; Shibasaki, M., *J. Am. Chem. Soc.* 2010, **132**, 4925-4934.
177. Ready, J. M.; Jacobsen, E. N., *J. Am. Chem. Soc.* 2001, **123**, 2687-2688.
178. Paull, D. H.; Abraham, C. J.; Scerba, M. T.; Alden-Danforth, E.; Lectka, T., *Acc. Chem. Res.* 2008, **41**, 655-663.
179. Hirahata, W.; Thomas, R. M.; Lobkovsky, E. B.; Coates, G. W., *J. Am. Chem. Soc.* 2008, **130**, 17658-17659.
180. Sammis, G. M.; Jacobsen, E. N., *J. Am. Chem. Soc.* 2003, **125**, 4442-4443.
181. Handa, S.; Gnanadesikan, V.; Matsunaga, S.; Shibasaki, M., *J. Am. Chem. Soc.* 2007, **129**, 4900-4901.
182. Chen, Z.; Morimoto, H.; Matsunaga, S.; Shibasaki, M., *J. Am. Chem. Soc.* 2008, **130**, 2170-2171.
183. Sampson, J.; Choi, G.; Akhtar, M. N.; Jaseer, E. A.; Theravalappil, R.; Al-Muallem, H. A.; Agapie, T., *Organometallics* 2017, **36**, 1915-1928.
184. Radlauer, M. R.; Agapie, T., *Organometallics* 2014, **33**, 3247-3250.

185. Radlauer, M. R.; Buckley, A. K.; Henling, L. M.; Agapie, T., *J. Am. Chem. Soc.* 2013, **135**, 3784-3787.
186. Radlauer, M. R.; Day, M. W.; Agapie, T., *Organometallics* 2012, **31**, 2231-2243.
187. Radlauer, M. R.; Day, M. W.; Agapie, T., *J. Am. Chem. Soc.* 2012, **134**, 1478-1481.
188. Miller, J. S.; Calabrese, J. C.; Epstein, A. J.; Bigelow, R. W.; Zhang, J. H.; Reiff, W. M., *J. Chem. Soc., Chem. Commun.* 1986, 1026-1028.
189. Miller, J. S.; Calabrese, J. C.; Rommelmann, H.; Chittipeddi, S. R.; Zhang, J. H.; Reiff, W. M.; Epstein, A. J., *J. Am. Chem. Soc.* 1987, **109**, 769-781.
190. Glaser, T., *Coord. Chem. Rev.* 2013, **257**, 140-152.
191. Glaser, T.; Gerenkamp, M.; Fröhlich, R., *Angew. Chem. Int. Ed.* 2002, **41**, 3823-3825.
192. Glaser, T.; Heidemeier, M.; Grimme, S.; Bill, E., *Inorg. Chem.* 2004, **43**, 5192-5194.
193. Glaser, T.; Heidemeier, M.; Fröhlich, R.; Hildebrandt, P.; Bothe, E.; Bill, E., *Inorg. Chem.* 2005, **44**, 5467-5482.
194. Ratera, I.; Veciana, J., *Chem. Soc. Rev.* 2012, **41**, 303-349.
195. Theil, H.; von Richthofen, C.-G. F.; Stammler, A.; Bögge, H.; Glaser, T., *Inorg. Chim. Acta* 2008, **361**, 916-924.
196. Mukherjee, C.; Stammler, A.; Bögge, H.; Glaser, T., *Inorg. Chem.* 2009, **48**, 9476-9484.
197. Mukherjee, C.; Stammler, A.; Bögge, H.; Glaser, T., *Chem. Eur. J.* 2010, **16**, 10137-10149.
198. Freiherr von Richthofen, C.-G.; Stammler, A.; Bögge, H.; Glaser, T., *Eur. J. Inorg. Chem.* 2011, **2011**, 49-52.
199. Glaser, T.; Heidemeier, M.; Strautmann, J. B. H.; Bögge, H.; Stammler, A.; Krickemeyer, E.; Huenerbein, R.; Grimme, S.; Bothe, E.; Bill, E., *Chem. Eur. J.* 2007, **13**, 9191-9206.
200. Glaser, T.; Heidemeier, M.; Weyhermüller, T.; Hoffmann, R.-D.; Rupp, H.; Müller, P., *Angew. Chem. Int. Ed.* 2006, **45**, 6033-6037.
201. Glaser, T.; Heidemeier, M.; Krickemeyer, E.; Bögge, H.; Stammler, A.; Fröhlich, R.; Bill, E.; Schnack, J., *Inorg. Chem.* 2009, **48**, 607-620.
202. Mukherjee, C.; Hoeke, V.; Stammler, A.; Bögge, H.; Schnack, J.; Glaser, T., *Dalton Trans.* 2014, **43**, 9690-9703.
203. Hoeke, V.; Krickemeyer, E.; Heidemeier, M.; Theil, H.; Stammler, A.; Bögge, H.; Weyhermüller, T.; Schnack, J.; Glaser, T., *Eur. J. Inorg. Chem.* 2013, **2013**, 4398-4409.

204. Krickemeyer, E.; Stammler, A.; Bogge, H.; Schnack, J.; Glaser, T., *Naturforsch., B: Chem. Sci.* 2010, **65**, 295-303.
205. Akine, S.; Taniguchi, T.; Nabeshima, T., *J. Am. Chem. Soc.* 2006, **128**, 15765-15774.
206. Wezenberg, S. J.; Salassa, G.; Escudero-Adan, E. C.; Benet-Buchholz, J.; Kleij, A. W., *Angew. Chem. Int. Ed.* 2011, **50**, 713-716.
207. Frischmann, P. D.; Gallant, A. J.; Chong, J. H.; MacLachlan, M. J., *Inorg. Chem.* 2008, **47**, 101-112.
208. Frischmann, P. D.; Facey, G. A.; Ghi, P. Y.; Gallant, A. J.; Bryce, D. L.; Lelj, F.; MacLachlan, M. J., *J. Am. Chem. Soc.* 2010, **132**, 3893-3908.
209. Gallant, A. J.; Chong, J. H.; MacLachlan, M. J., *Inorg. Chem.* 2006, **45**, 5248-5250.
210. Nabeshima, T.; Miyazaki, H.; Iwasaki, A.; Akine, S.; Saiki, T.; Ikeda, C.; Sato, S., *Chem. Lett.* 2006, **35**, 1070-1071.
211. Guo, Z. Q.; Tong, W. L.; Chan, M. C. W., *Chem. Commun.* 2009, 6189-6191.
212. Guo, Z. Q.; Yiu, S. M.; Chan, M. C. W., *Chem. Eur. J.* 2013, **19**, 8937-8947.
213. Tong, W.-L.; Yiu, S.-M.; Chan, M. C. W., *Inorg. Chem.* 2013, **52**, 7114-7124.
214. Dunn, T. J.; Ramogida, C. F.; Simmonds, C.; Paterson, A.; Wong, E. W. Y.; Chiang, L.; Shimazaki, Y.; Storr, T., *Inorg. Chem.* 2011, **50**, 6746-6755.
215. Dunn, T. J.; Chiang, L.; Ramogida, C. F.; Webb, M. I.; Savard, D.; Sakaguchi, M.; Ogura, T.; Shimazaki, Y.; Storr, T., *Dalton Trans.* 2012, **41**, 7905-7914.
216. Dunn, T. J.; Chiang, L.; Ramogida, C. F.; Hazin, K.; Webb, M. I.; Katz, M. J.; Storr, T., *Chem. Eur. J.* 2013, **19**, 9606-9618.
217. Clarke, R. M.; Hazin, K.; Thompson, J. R.; Savard, D.; Prosser, K. E.; Storr, T., *Inorg. Chem.* 2016, **55**, 762-774.
218. Rotthaus, O.; Jarjayes, O.; Thomas, F.; Philouze, C.; Saint-Aman, E.; Pierre, J.-L., *Dalton Trans.* 2007, 889-895.
219. Rotthaus, O.; Jarjayes, O.; Philouze, C.; Del Valle, C. P.; Thomas, F., *Dalton Trans.* 2009, 1792-1800.
220. Ostroverkhova, O., *Chem. Rev.* 2016, **116**, 13279-13412.
221. Reineke, S.; Thomschke, M.; Lüssem, B.; Leo, K., *Rev. Mod. Phys.* 2013, **85**, 1245-1293.
222. Clarke, T. M.; Durrant, J. R., *Chem. Rev.* 2010, **110**, 6736-6767.
223. Fabian, J.; Nakazumi, H.; Matsuoka, M., *Chem. Rev.* 1992, **92**, 1197-1226.

224. Lu, X.; Lee, S.; Hong, Y.; Phan, H.; Gopalakrishna, T. Y.; Heng, T. S.; Tanaka, T.; Sandoval-Salinas, M. E.; Zeng, W.; Ding, J.; Casanova, D.; Osuka, A.; Kim, D.; Wu, J., *J. Am. Chem. Soc.* 2017.
225. Cai, K.; Xie, J.; Zhao, D., *J. Am. Chem. Soc.* 2014, **136**, 28-31.
226. Yong, G.-P.; Zhao, Y.-M.; Feng, Y.; Zhang, X.-R., *J. Mater. Chem. C* 2013, **1**, 3395-3398.
227. Dou, L.; Liu, Y.; Hong, Z.; Li, G.; Yang, Y., *Chem. Rev.* 2015, **115**, 12633-12665.
228. Cui, B.-B.; Tang, J.-H.; Yao, J.; Zhong, Y.-W., *Angew. Chem. Int. Ed.* 2015, **54**, 9192-9197.
229. Cameron, L. A.; Ziller, J. W.; Heyduk, A. F., *Chem. Sci.* 2016, **7**, 1807-1814.
230. Kramer, W. W.; Cameron, L. A.; Zarkesh, R. A.; Ziller, J. W.; Heyduk, A. F., *Inorg. Chem.* 2014, **53**, 8825-8837.
231. Wong, J. L.; Higgins, R. F.; Bhowmick, I.; Cao, D. X.; Szigethy, G.; Ziller, J. W.; Shores, M. P.; Heyduk, A. F., *Chem. Sci.* 2016, **7**, 1594-1599.
232. Espa, D.; Pilia, L.; Marchio, L.; Mercuri, M. L.; Serpe, A.; Sessini, E.; Deplano, P., *Dalton Trans.* 2013, **42**, 12429-12439.
233. Liu, Y.; Zhang, Z.; Chen, X.; Xu, S.; Cao, S., *Dyes and Pigments* 2016, **128**, 179-189.
234. Pan, Z.; Zhao, K.; Wang, J.; Zhang, H.; Feng, Y.; Zhong, X., *ACS Nano* 2013, **7**, 5215-5222.
235. Cui, B.-B.; Zhong, Y.-W.; Yao, J., *J. Am. Chem. Soc.* 2015, **137**, 4058-4061.
236. Kaim, W., *Coord. Chem. Rev.* 2011, **255**, 2503-2513.
237. Sarkar, B.; Schweinfurth, D.; Deibel, N.; Weisser, F., *Coord. Chem. Rev.* 2015, **293-294**, 250-262.
238. Kasha, M., *Radiat. Res.* 1963, **20**, 55-70.
239. Kasha, M.; Rawls, H. R.; El-Bayoumi, M. A., *Pure Appl. Chem.* 1965, **11**, 371-392.
240. Schellman, J. A., *Acc. Chem. Res.* 1968, **1**, 144-151.
241. Kim, D.; Osuka, A., *Acc. Chem. Res.* 2004, **37**, 735-745.
242. Nakamura, Y.; Hwang, I. W.; Aratani, N.; Ahn, T. K.; Ko, D. M.; Takagi, A.; Kawai, T.; Matsumoto, T.; Kim, D.; Osuka, A., *J. Am. Chem. Soc.* 2005, **127**, 236-246.
243. Urbani, M.; Grätzel, M.; Nazeeruddin, M. K.; Torres, T., *Chem. Rev.* 2014, **114**, 12330-12396.

244. Smalley, S. J.; Waterland, M. R.; Telfer, S. G., *Inorg. Chem.* 2009, **48**, 13-15.
245. Hall, J. D.; McLean, T. M.; Smalley, S. J.; Waterland, M. R.; Telfer, S. G., *Dalton Trans.* 2010, **39**, 437-445.
246. Cohen, S. M.; Halper, S. R., *Inorg. Chim. Acta* 2002, **341**, 12-16.
247. Telfer, S. G.; Wuest, J. D., *Chem. Commun.* 2007, 3166-3168.
248. Thoi, V. S.; Stork, J. R.; Magde, D.; Cohen, S. M., *Inorg. Chem.* 2006, **45**, 10688-10697.
249. Brückner, C.; Zhang, Y.; Rettig, S. J.; Dolphin, D., *Inorg. Chim. Acta* 1997, **263**, 279-286.
250. Sakamoto, R., *et al.*, *Dalton Trans.* 2012, **41**, 14035-14037.
251. Kusaka, S.; Sakamoto, R.; Nishihara, H., *Inorg. Chem.* 2014, **53**, 3275-3277.
252. Filatov, M. A.; Lebedev, A. Y.; Mukhin, S. N.; Vinogradov, S. A.; Cheprakov, A. V., *J. Am. Chem. Soc.* 2010, **132**, 9552-9554.
253. Yu, L.; Muthukumar, K.; Sazanovich, I. V.; Kirmaier, C.; Hindin, E.; Diers, J. R.; Boyle, P. D.; Bocian, D. F.; Holten, D.; Lindsey, J. S., *Inorg. Chem.* 2003, **42**, 6629-6647.
254. Bronner, C.; Baudron, S. A.; Hosseini, M. W.; Strassert, C. A.; Guenet, A.; De Cola, L., *Dalton Trans.* 2010, **39**, 180-184.
255. Halper, S. R.; Cohen, S. M., *Chem. Eur. J.* 2003, **9**, 4661-4669.
256. Palma, A.; Gallagher, J. F.; Muller-Bunz, H.; Wolowska, J.; McInnes, E. J. L.; O'Shea, D. F., *Dalton Trans.* 2009, 273-279.
257. McLean, T. M.; Telfer, S. G.; Elliott, A. B. S.; Gordon, K. C.; Lein, M.; Waterland, M. R., *Dalton Trans.* 2014, **43**, 17746-17753.
258. Hestand, N. J.; Spano, F. C., *Acc. Chem. Res.* 2017, **50**, 341-350.
259. Lecarme, L.; Chiang, L.; Philouze, C.; Jarjayes, O.; Storr, T.; Thomas, F., *Eur. J. Inorg. Chem.* 2014, **2014**, 3479-3487.
260. Kurahashi, T.; Fujii, H., *Inorg. Chem.* 2013, **52**, 3908-3919.
261. Kochem, A.; Gellon, G.; Leconte, N.; Baptiste, B.; Philouze, C.; Jarjayes, O.; Orio, M.; Thomas, F., *Chem. Eur. J.* 2013, **19**, 16707-16721.
262. Mews, N. M.; Berkefeld, A.; Hörner, G.; Schubert, H., *J. Am. Chem. Soc.* 2017, **139**, 2808-2815.
263. Dinolfo, P. H.; Coropceanu, V.; Brédas, J.-L.; Hupp, J. T., *J. Am. Chem. Soc.* 2006, **128**, 12592-12593.

264. Dinolfo, P. H.; Williams, M. E.; Stern, C. L.; Hupp, J. T., *J. Am. Chem. Soc.* 2004, **126**, 12989-13001.
265. Hananouchi, S.; Krull, B. T.; Ziller, J. W.; Furche, F.; Heyduk, A. F., *Dalton Trans.* 2014, **43**, 17991-18000.
266. Ray, K.; Petrenko, T.; Wieghardt, K.; Neese, F., *Dalton Trans.* 2007, 1552-1566.
267. Ray, K.; Weyhermüller, T.; Neese, F.; Wieghardt, K., *Inorg. Chem.* 2005, **44**, 5345-5360.
268. Song, I. H.; Rhee, C. H.; Park, S. H.; Lee, S. L.; Grudinin, D.; Song, K. H.; Choe, J., *Org. Process Res. Dev.* 2008, **12**, 1012-1015.
269. Garreau-de Bonneval, B.; Moineau-Chane Ching, K. I.; Alary, F.; Bui, T.-T.; Valade, L., *Coord. Chem. Rev.* 2010, **254**, 1457-1467.
270. Kambe, T.; Sakamoto, R.; Hoshiko, K.; Takada, K.; Miyachi, M.; Ryu, J.-H.; Sasaki, S.; Kim, J.; Nakazato, K.; Takata, M.; Nishihara, H., *J. Am. Chem. Soc.* 2013, **135**, 2462-2465.
271. Kambe, T.; Sakamoto, R.; Kusamoto, T.; Pal, T.; Fukui, N.; Hoshiko, K.; Shimojima, T.; Wang, Z.; Hirahara, T.; Ishizaka, K.; Hasegawa, S.; Liu, F.; Nishihara, H., *J. Am. Chem. Soc.* 2014, **136**, 14357-14360.
272. Cui, J.; Xu, Z., *Chem. Commun.* 2014, **50**, 3986-3988.
273. Aragoni, M. C.; Arca, M.; Caironi, M.; Denotti, C.; Devillanova, F. A.; Grigiotti, E.; Isaia, F.; Laschi, F.; Lippolis, V.; Natali, D.; Pala, L.; Sampietro, M.; Zanello, P., *Chem. Commun.* 2004, 1882-1883.
274. Shojaei, F.; Hahn, J. R.; Kang, H. S., *Chem. Mater.* 2014, **26**, 2967-2974.
275. Clarke, R. M.; Herasymchuk, K.; Storr, T., *Coord. Chem. Rev.* 2017, **352**, 67-82.
276. Thomas, F., *Dalton Trans.* 2016, **45**, 10866-10877.
277. Doistau, B.; Tron, A.; Denisov, S. A.; Jonusauskas, G.; McClenaghan, N. D.; Gontard, G.; Marvaud, V.; Hasenknopf, B.; Vives, G., *Chem. Eur. J.* 2014, **20**, 15799-15807.
278. Yam, V. W.-W.; Au, V. K.-M.; Leung, S. Y.-L., *Chem. Rev.* 2015, **115**, 7589-7728.
279. Wang, W.-J.; Hao, L.; Chen, C.-Y.; Qiu, Q.-M.; Wang, K.; Song, J.-B.; Li, H., *RSC Advances* 2017, **7**, 20488-20493.
280. Zhao, C.; Sun, S.; Tong, W.-L.; Chan, M. C. W., *Macromolecules* 2017, **50**, 6896-6902.
281. Hui, J. K. H.; Yu, Z.; MacLachlan, M. J., *Angew. Chem. Int. Ed.* 2007, **46**, 7980-7983.
282. Anselmo, D.; Salassa, G.; Escudero-Adan, E. C.; Martin, E.; Kleij, A. W., *Dalton Trans.* 2013, **42**, 7962-7970.

283. Escarcega-Bobadilla, M. V.; Anselmo, D.; Wezenberg, S. J.; Escudero-Adan, E. C.; Martinez Belmonte, M.; Martin, E.; Kleij, A. W., *Dalton Trans.* 2012, **41**, 9766-9772.
284. Lefler, K. M.; Brown, K. E.; Salamant, W. A.; Dyar, S. M.; Knowles, K. E.; Wasielewski, M. R., *J. Phys. Chem. A* 2013, **117**, 10333-10345.
285. Lindquist, R. J.; Lefler, K. M.; Brown, K. E.; Dyar, S. M.; Margulies, E. A.; Young, R. M.; Wasielewski, M. R., *J. Am. Chem. Soc.* 2014, **136**, 14912-14923.
286. Ammar, F.; Savéant, J. M., *J. Electroanal. Chem.* 1973, **47**, 215-221.
287. Bixon, M.; Jortner, J.; Michel-Beyerle, M. E.; Ogrodnik, A., *Biochim. Biophys. Acta* 1989, **977**, 273-286.
288. González-Rodríguez, D.; Torres, T.; Herranz, M. Á.; Echegoyen, L.; Carbonell, E.; Guldi, D. M., *Chem. Eur. J.* 2008, **14**, 7670-7679.
289. Dunn, T. J.; Webb, M. I.; Hazin, K.; Verma, P.; Wasinger, E. C.; Shimazaki, Y.; Storr, T., *Dalton Trans.* 2013, **42**, 3950-3956.
290. Koizumi, N.; Ishida, T., *Tetrahedron Lett.* 2017, **58**, 2804-2808.
291. Arumugam, K.; Shaw, M. C.; Mague, J. T.; Bill, E.; Sproules, S.; Donahue, J. P., *Inorg. Chem.* 2011, **50**, 2995-3002.
292. Riplinger, C.; Kao, J. P. Y.; Rosen, G. M.; Kathirvelu, V.; Eaton, G. R.; Eaton, S. S.; Kutateladze, A.; Neese, F., *J. Am. Chem. Soc.* 2009, **131**, 10092-10106.
293. Bertrand, P.; More, C.; Guigliarelli, B.; Fournel, A.; Bennett, B.; Howes, B., *J. Am. Chem. Soc.* 1994, **116**, 3078-3086.
294. Deumal, M.; Novoa, J. J.; Bearpark, M. J.; Celani, P.; Olivucci, M.; Robb, M. A., *J. Phys. Chem. A* 1998, **102**, 8404-8412.
295. Fatila, E. M.; Clerac, R.; Jennings, M.; Preuss, K. E., *Chem. Commun.* 2013, **49**, 9431-9433.
296. McConnell, H. M., *J. Chem. Phys.* 1963, **39**, 1910-1910.
297. Abe, M., *Chem. Rev.* 2013, **113**, 7011-7088.
298. Ottiger, P.; Koppel, H.; Leutwyler, S., *Chem. Sci.* 2015, **6**, 6059-6068.
299. Lü, J.-M.; Rosokha, S. V.; Kochi, J. K., *J. Am. Chem. Soc.* 2003, **125**, 12161-12171.
300. Giaimo, J. M.; Lockard, J. V.; Sinks, L. E.; Scott, A. M.; Wilson, T. M.; Wasielewski, M. R., *J. Phys. Chem. A* 2008, **112**, 2322-2330.
301. Yoo, H.; Furumaki, S.; Yang, J.; Lee, J.-E.; Chung, H.; Oba, T.; Kobayashi, H.; Rybtchinski, B.; Wilson, T. M.; Wasielewski, M. R.; Vacha, M.; Kim, D., *J. Phys. Chem. B* 2012, **116**, 12878-12886.

302. Würthner, F.; Yao, S.; Debaerdemaeker, T.; Wortmann, R., *J. Am. Chem. Soc.* 2002, **124**, 9431-9447.
303. Aggarwal, N.; Patnaik, A., *J. Phys. Chem. A* 2015, **119**, 8388-8399.
304. Han, S.; Yao, E.; Qin, W.; Zhang, S.; Ma, Y., *Macromolecules* 2012, **45**, 4054-4059.
305. Ibrahim, F.; Nasrallah, H.; Hong, X.; Mellah, M.; Hachem, A.; Ibrahim, G.; Jaber, N.; Schulz, E., *Tetrahedron* 2012, **68**, 9954-9961.
306. Murata, Y.; Cheng, F.; Kitagawa, T.; Komatsu, K., *J. Am. Chem. Soc.* 2004, **126**, 8874-8875.
307. Noviandri, I.; Brown, K. N.; Fleming, D. S.; Gulyas, P. T.; Lay, P. A.; Masters, A. F.; Phillips, L., *J. Phys. Chem. B* 1999, **103**, 6713-6722.
308. Stoll, S.; Schweiger, A., *J. Magn. Reson.* 2006, **178**, 42-55.
309. Farrugia, L., *J. Appl. Crystallogr.* 2012, **45**, 849-854.
310. *Persistence of Vision Raytracer (POV-Ray)*, 3.6.2; Persistence of Vision Pty. Ltd.: Victoria, Australia, 2004.
311. Sheldrick, G. M. *SHELXT v2014*, Bruker AXS Inc: Madison, WI.
312. Hubschle, C. B.; Sheldrick, G. M.; Dittrich, B., *J. Appl. Crystallogr.* 2011, **44**, 1281-1284.
313. van der Sluis, P.; Spek, A. L., *Acta Crystallographica Section A* 1990, **46**, 194-201.
314. Frisch, M. J., *et al. Gaussian 09*, Gaussian, Inc.: Wallingford, CT, USA, 2009.
315. Becke, A. D., *J. Chem. Phys.* 1993, **98**, 5648-5652.
316. Stephens, P. J.; Devlin, F. J.; Chabalowski, C. F.; Frisch, M. J., *J. Phys. Chem.* 1994, **98**, 11623-11627.
317. Schäfer, A.; Horn, H.; Ahlrichs, R., *J. Chem. Phys.* 1992, **97**, 2571-2577.
318. Schäfer, A.; Huber, C.; Ahlrichs, R., *J. Chem. Phys.* 1994, **100**, 5829-5835.
319. Casida, M. E., In *Recent Advances in Density Functional Methods*, Chong, D. P., Ed. World Scientific: Singapore, 1995; p 155.
320. Stratmann, R. E.; Scuseria, G. E.; Frisch, M. J., *J. Chem. Phys.* 1998, **109**, 8218-8224.
321. Barone, V.; Cossi, M.; Tomasi, J., *J. Comput. Chem.* 1998, **19**, 404-417.
322. Barone, V.; Cossi, M.; Tomasi, J., *J. Chem. Phys.* 1997, **107**, 3210-3221.
323. Miertuš, S.; Scrocco, E.; Tomasi, J., *Chem. Phys.* 1981, **55**, 117-129.

324. Tomasi, J.; Mennucci, B.; Cancès, E., *J. Mol. Struct. THEOCHEM* 1999, **464**, 211-226.
325. Balch, A. L.; Holm, R. H., *J. Am. Chem. Soc.* 1966, **88**, 5201-5209.
326. Peng, S.-M.; Chen, C.-T.; Liaw, D.-S.; Chen, C.-I.; Wang, Y., *Inorg. Chim. Acta* 1985, **101**, L31-L33.
327. Bill, E.; Bothe, E.; Chaudhuri, P.; Chlopek, K.; Herebian, D.; Kokatam, S.; Ray, K.; Weyhermüller, T.; Neese, F.; Wieghardt, K., *Chem. Eur. J.* 2005, **11**, 204-224.
328. Benisvy, L.; Bill, E.; Blake, A. J.; Collison, D.; Davies, E. S.; Garner, C. D.; Guindy, C. I.; McInnes, E. J. L.; McArdle, G.; McMaster, J.; Wilson, C.; Wolowska, J., *Dalton Trans.* 2004, 3647-3653.
329. Poddel'sky, A. I.; Cherkasov, V. K.; Fukin, G. K.; Bubnov, M. P.; Abakumova, L. G.; Abakumov, G. A., *Inorg. Chim. Acta* 2004, **357**, 3632-3640.
330. Herebian, D.; Ghosh, P.; Chun, H.; Bothe, E.; Weyhermüller, T.; Wieghardt, K., *Eur. J. Inorg. Chem.* 2002, **2002**, 1957-1967.
331. van der Meer, M.; Rechkemmer, Y.; Peremykin, I.; Hohloch, S.; van Slageren, J.; Sarkar, B., *Chem. Commun.* 2014, **50**, 11104-11106.
332. Khusniyarov, M. M.; Harms, K.; Burghaus, O.; Sundermeyer, J.; Sarkar, B.; Kaim, W.; van Slageren, J.; Duboc, C.; Fiedler, J., *Dalton Trans.* 2008, 1355-1365.
333. Ray, K.; Begum, A.; Weyhermüller, T.; Piligkos, S.; van Slageren, J.; Neese, F.; Wieghardt, K., *J. Am. Chem. Soc.* 2005, **127**, 4403-4415.
334. Sproules, S.; Kapre, R. R.; Roy, N.; Weyhermüller, T.; Wieghardt, K., *Inorg. Chim. Acta* 2010, **363**, 2702-2714.
335. Smith, A. L.; Clapp, L. A.; Hardcastle, K. I.; Soper, J. D., *Polyhedron* 2010, **29**, 164-169.
336. Smith, A. L.; Hardcastle, K. I.; Soper, J. D., *J. Am. Chem. Soc.* 2010, **132**, 14358-14360.
337. Nielsen, L. P. C.; Stevenson, C. P.; Blackmond, D. G.; Jacobsen, E. N., *J. Am. Chem. Soc.* 2004, **126**, 1360-1362.
338. Schaus, S. E.; Brandes, B. D.; Larrow, J. F.; Tokunaga, M.; Hansen, K. B.; Gould, A. E.; Furrow, M. E.; Jacobsen, E. N., *J. Am. Chem. Soc.* 2002, **124**, 1307-1315.
339. Jacobsen, E. N., *Acc. Chem. Res.* 2000, **33**, 421-431.
340. Furrow, M. E.; Schaus, S. E.; Jacobsen, E. N., *The Journal of Organic Chemistry* 1998, **63**, 6776-6777.
341. Bailey, C. L.; Drago, R. S., *Coord. Chem. Rev.* 1987, **79**, 321-332.

342. Kervinen, K.; Lahtinen, P.; Repo, T.; Svahn, M.; Leskelä, M., *Catal. Today* 2002, **75**, 183-188.
343. Collinson, S. R.; Thielemans, W., *Coord. Chem. Rev.* 2010, **254**, 1854-1870.
344. Ahmed, S. M.; Poater, A.; Childers, M. I.; Widger, P. C. B.; LaPointe, A. M.; Lobkovsky, E. B.; Coates, G. W.; Cavallo, L., *J. Am. Chem. Soc.* 2013, **135**, 18901-18911.
345. Thomas, R. M.; Widger, P. C. B.; Ahmed, S. M.; Jeske, R. C.; Hirahata, W.; Lobkovsky, E. B.; Coates, G. W., *J. Am. Chem. Soc.* 2010, **132**, 16520-16525.
346. Widger, P. C. B.; Ahmed, S. M.; Hirahata, W.; Thomas, R. M.; Lobkovsky, E. B.; Coates, G. W., *Chem. Commun.* 2010, **46**, 2935-2937.
347. Liu, Y.; Ren, W.-M.; Liu, J.; Lu, X.-B., *Angew. Chem. Int. Ed.* 2013, **52**, 11594-11598.
348. Liu, Y.; Ren, W.-M.; Liu, C.; Fu, S.; Wang, M.; He, K.-K.; Li, R.-R.; Zhang, R.; Lu, X.-B., *Macromolecules* 2014, **47**, 7775-7788.
349. Haak, R. M.; Martinez Belmonte, M.; Escudero-Adan, E. C.; Benet-Buchholz, J.; Kleij, A. W., *Dalton Trans.* 2010, **39**, 593-602.
350. Lang, K.; Park, J.; Hong, S., *Angew. Chem. Int. Ed.* 2012, **51**, 1620-1624.
351. Park, J.; Lang, K.; Abboud, K. A.; Hong, S., *Chem. Eur. J.* 2011, **17**, 2236-2245.
352. Devoille, A. M. J.; Love, J. B., *Dalton Trans.* 2012, **41**, 65-72.
353. Hansch, C.; Leo, A.; Taft, R. W., *Chem. Rev.* 1991, **91**, 165-195.
354. Unpublished work.
355. Kochem, A.; Kanso, H.; Baptiste, B.; Arora, H.; Philouze, C.; Jarjayes, O.; Vezin, H.; Luneau, D.; Orio, M.; Thomas, F., *Inorg. Chem.* 2012, **51**, 10557-10571.
356. Kemper, S.; Hrobárik, P.; Kaupp, M.; Schlörer, N. E., *J. Am. Chem. Soc.* 2009, **131**, 4172-4173.
357. Huber, A.; Müller, L.; Elias, H.; Klement, R.; Valko, M., *Eur. J. Inorg. Chem.* 2005, **2005**, 1459-1467.
358. The low solubility of $[\text{Co}_2\text{L}^2\text{-2H}_2\text{O}]^{2+}$ at the concentrations required for observable ^1H NMR peak shifting disallowed for an Evan's method NMR experiment.
359. Chiang, L.; Allan, L. E. N.; Alcantara, J.; Wang, M. C. P.; Storr, T.; Shaver, M. P., *Dalton Trans.* 2014, **43**, 4295-4304.
360. Daul, C.; Schläpfer, C.; von Zelewsky, A., The electronic structure of cobalt(II) complexes with schiff bases and related ligands. In *Inorganic Chemistry and Spectroscopy*, Springer Berlin Heidelberg: 1979; Vol. 36, pp 129-171.

361. Vinck, E.; Doorslaer, S. V.; Murphy, D. M.; Fallis, I. A., *Chem. Phys. Lett.* 2008, **464**, 31-37.
362. Zarembowitch, J.; Kahn, O., *Inorg. Chem.* 1984, **23**, 589-593.
363. Kennedy, B. J.; Fallon, G. D.; Gatehouse, B. M. K. C.; Murray, K. S., *Inorg. Chem.* 1984, **23**, 580-588.
364. Rudin, M.; Schweiger, A.; Berchten, N.; Günthard, H. H., *Mol. Phys.* 1980, **41**, 1317-1328.
365. Drago, R. S., *Physical Methods for Chemists*. 2 ed.; Saunders College Publishing: 1992.
366. Strečka, J.; Čanová, L.; Minami, K., *Physical Review E* 2009, **79**, 051103.
367. Bleaney, B.; Bowers, K. D., *Proc. R. Soc. Lond. A.* 1952, **214**, 451-465.
368. Gorelsky, S. I. *AOMix, Program for Molecular Orbital Analysis*, 6.85; 2014.
369. Kimura, S.; Bill, E.; Bothe, E.; Weyhermüller, T.; Wieghardt, K., *J. Am. Chem. Soc.* 2001, **123**, 6025-6039.
370. Zats, G. M.; Arora, H.; Lavi, R.; Yufit, D.; Benisvy, L., *Dalton Trans.* 2011, **40**, 10889-10896.
371. Shimazaki, Y.; Kabe, R.; Huth, S.; Tani, F.; Naruta, Y.; Yamauchi, O., *Inorg. Chem.* 2007, **46**, 6083-6090.
372. Müller, J.; Kikuchi, A.; Bill, E.; Weyhermüller, T.; Hildebrandt, P.; Ould-Moussa, L.; Wieghardt, K., *Inorg. Chim. Acta* 2000, **297**, 265-277.
373. Vinck, E.; Murphy, D. M.; Fallis, I. A.; Strevens, R. R.; Van Doorslaer, S., *Inorg. Chem.* 2010, **49**, 2083-2092.
374. Thomas, F.; Arora, H.; Philouze, C.; Jarjayes, O., *Inorg. Chim. Acta* 2010, **363**, 3122-3130.
375. Solomon, E. I.; Gorelsky, S. I.; Dey, A., *J. Comput. Chem.* 2006, **27**, 1415-1428.
376. Clarke, R. M.; Jeen, T.; Rigo, S.; Thompson, J. R.; Kaake, L. G.; Thomas, F.; Storr, T., *Chem. Sci.* 2018.
377. Valdes-Aguilera, O.; Neckers, D. C., *Acc. Chem. Res.* 1989, **22**, 171-177.
378. Yoon, M.-C.; Lee, S.; Tokuji, S.; Yorimitsu, H.; Osuka, A.; Kim, D., *Chem. Sci.* 2013, **4**, 1756-1764.
379. Perrin, D. D.; Armarego, W. L. F., *Purification of Laboratory Chemicals*. 1 ed.; Pergamo Press: New York, 1988.

380. Betteridge, P. W.; Carruthers, J. R.; Cooper, R. I.; Prout, K.; Watkin, D. J., *J. Appl. Crystallogr.* 2003, **36**, 1487.
381. Noodleman, L., *J. Chem. Phys.* 1981, **74**, 5737-5743.
382. Noodleman, L.; Case, D. A., Density-Functional Theory of Spin Polarization and Spin Coupling in Iron—Sulfur Clusters. In *Advances in Inorganic Chemistry*, Richard, C., Ed. Academic Press: 1992; Vol. Volume 38, pp 423-470.
383. Yandulov, D. V.; Schrock, R. R., *Science* 2003, **301**, 76-78.
384. Arashiba, K.; Kinoshita, E.; Kuriyama, S.; Eizawa, A.; Nakajima, K.; Tanaka, H.; Yoshizawa, K.; Nishibayashi, Y., *J. Am. Chem. Soc.* 2015, **137**, 5666-5669.
385. Curley, J. J.; Sceats, E. L.; Cummins, C. C., *J. Am. Chem. Soc.* 2006, **128**, 14036-14037.
386. Du Bois, J.; Tomooka, C. S.; Hong, J.; Carreira, E. M., *Acc. Chem. Res.* 1997, **30**, 364-372.
387. Gdula, R. L.; Johnson, M. J. A., *J. Am. Chem. Soc.* 2006, **128**, 9614-9615.
388. Chisholm, M. H.; Delbridge, E. E.; Kidwell, A. R.; Quinlan, K. B., *Chem. Commun.* 2003, 126-127.
389. Ertl, G., *Catalytic Ammonia Synthesis*. Plenum: New York, 1991.
390. Vogel, C.; Heinemann, F. W.; Sutter, J.; Anthon, C.; Meyer, K., *Angew. Chem.* 2008, **120**, 2721-2724.
391. Betley, T. A.; Peters, J. C., *J. Am. Chem. Soc.* 2004, **126**, 6252-6254.
392. Rohde, J.-U.; Betley, T. A.; Jackson, T. A.; Saouma, C. T.; Peters, J. C.; Que, L., *Inorg. Chem.* 2007, **46**, 5720-5726.
393. Scepaniak, J. J.; Young, J. A.; Bontchev, R. P.; Smith, J. M., *Angew. Chem. Int. Ed.* 2009, **48**, 3158-3160.
394. Scepaniak, J. J.; Bontchev, R. P.; Johnson, D. L.; Smith, J. M., *Angew. Chem. Int. Ed.* 2011, **50**, 6630-6633.
395. Scepaniak, J. J.; Fulton, M. D.; Bontchev, R. P.; Duesler, E. N.; Kirk, M. L.; Smith, J. M., *J. Am. Chem. Soc.* 2008, **130**, 10515-10517.
396. Muñoz, S. B.; Lee, W.-T.; Dickie, D. A.; Scepaniak, J. J.; Subedi, D.; Pink, M.; Johnson, M. D.; Smith, J. M., *Angew. Chem. Int. Ed.* 2015, **54**, 10600-10603.
397. Aliaga-Alcalde, N.; DeBeer George, S.; Mienert, B.; Bill, E.; Wieghardt, K.; Neese, F., *Angew. Chem. Int. Ed.* 2005, **44**, 2908-2912.
398. Meyer, K.; Bill, E.; Mienert, B.; Weyhermüller, T.; Wieghardt, K., *J. Am. Chem. Soc.* 1999, **121**, 4859-4876.

399. Scepaniak, J. J.; Vogel, C. S.; Khusniyarov, M. M.; Heinemann, F. W.; Meyer, K.; Smith, J. M., *Science* 2011, **331**, 1049-1052.
400. Berry, J. F.; Bill, E.; Bothe, E.; George, S. D.; Mienert, B.; Neese, F.; Wieghardt, K., *Science* 2006, **312**, 1937-1941.
401. Lee, W.-T.; Juarez, R. A.; Scepaniak, J. J.; Muñoz, S. B.; Dickie, D. A.; Wang, H.; Smith, J. M., *Inorg. Chem.* 2014, **53**, 8425-8430.
402. Smith, J. M., Reactive Transition Metal Nitride Complexes. In *Progress in Inorganic Chemistry Volume 58*, John Wiley & Sons, Inc.: 2014; pp 417-470.
403. Maestri, A. G.; Cherry, K. S.; Toboni, J. J.; Brown, S. N., *J. Am. Chem. Soc.* 2001, **123**, 7459-7460.
404. Brown, S. N., *J. Am. Chem. Soc.* 1999, **121**, 9752-9753.
405. Crevier, T. J.; Mayer, J. M., *J. Am. Chem. Soc.* 1998, **120**, 5595-5596.
406. Crevier, T. J.; Lovell, S.; Mayer, J. M.; Rheingold, A. L.; Guzei, I. A., *J. Am. Chem. Soc.* 1998, **120**, 6607-6608.
407. Meyer, T. J.; Huynh, M. H. V., *Inorg. Chem.* 2003, **42**, 8140-8160.
408. Xie, J.; Man, W.-L.; Wong, C.-Y.; Chang, X.; Che, C.-M.; Lau, T.-C., *J. Am. Chem. Soc.* 2016, **138**, 5817-5820.
409. Man, W.-L.; Lam, W. W. Y.; Kwong, H.-K.; Yiu, S.-M.; Lau, T.-C., *Angew. Chem. Int. Ed.* 2012, **51**, 9101-9104.
410. Man, W.-L.; Tang, T.-M.; Wong, T.-W.; Lau, T.-C.; Peng, S.-M.; Wong, W.-T., *J. Am. Chem. Soc.* 2004, **126**, 478-479.
411. Man, W.-L.; Lam, W. W. Y.; Yiu, S.-M.; Lau, T.-C.; Peng, S.-M., *J. Am. Chem. Soc.* 2004, **126**, 15336-15337.
412. Zolnhofer, E. M.; Käß, M.; Khusniyarov, M. M.; Heinemann, F. W.; Maron, L.; van Gastel, M.; Bill, E.; Meyer, K., *J. Am. Chem. Soc.* 2014, **136**, 15072-15078.
413. Scheibel, M. G.; Wu, Y.; Stückl, A. C.; Krause, L.; Carl, E.; Stalke, D.; de Bruin, B.; Schneider, S., *J. Am. Chem. Soc.* 2013, **135**, 17719-17722.
414. Schöffel, J.; Rogachev, A. Y.; DeBeer George, S.; Burger, P., *Angew. Chem. Int. Ed.* 2009, **48**, 4734-4738.
415. Scheibel, M. G.; Askevold, B.; Heinemann, F. W.; Reijerse, E. J.; de Bruin, B.; Schneider, S., *Nat Chem* 2012, **4**, 552-558.
416. Vreeken, V.; Siegler, M. A.; de Bruin, B.; Reek, J. N. H.; Lutz, M.; van der Vlugt, J. I., *Angew. Chem. Int. Ed.* 2015, **54**, 7055-7059.
417. Laplaza, C. E.; Cummins, C. C., *Science* 1995, **268**, 861-863.

418. Laplaza, C. E.; Johnson, M. J. A.; Peters, J. C.; Odom, A. L.; Kim, E.; Cummins, C. C.; George, G. N.; Pickering, I. J., *J. Am. Chem. Soc.* 1996, **118**, 8623-8638.
419. Curley, J. J.; Cook, T. R.; Reece, S. Y.; Müller, P.; Cummins, C. C., *J. Am. Chem. Soc.* 2008, **130**, 9394-9405.
420. Thompson, R.; Tran, B. L.; Ghosh, S.; Chen, C.-H.; Pink, M.; Gao, X.; Carroll, P. J.; Baik, M.-H.; Mindiola, D. J., *Inorg. Chem.* 2015, **54**, 3068-3077.
421. Eikey, R. A.; Abu-Omar, M. M., *Coord. Chem. Rev.* 2003, **243**, 83-124.
422. Groves, J. T.; Takahashi, T., *J. Am. Chem. Soc.* 1983, **105**, 2073-2074.
423. Ho, C.-M.; Lau, T.-C.; Kwong, H.-L.; Wong, W.-T., *J. Chem. Soc. Dalton Trans.* 1999, 2411-2414.
424. Minakata, S.; Ando, T.; Nishimura, M.; Ryu, I.; Komatsu, M., *Angew. Chem. Int. Ed.* 1998, **37**, 3392-3394.
425. Du Bois, J.; Tomooka, C. S.; Hong, J.; Carreira, E. M., *J. Am. Chem. Soc.* 1997, **119**, 3179-3180.
426. Du Bois, J.; Hong, J.; Carreira, E. M.; Day, M. W., *J. Am. Chem. Soc.* 1996, **118**, 915-916.
427. Bottomley, L. A.; Neely, F. L., *J. Am. Chem. Soc.* 1988, **110**, 6748-6752.
428. Golubkov, G.; Gross, Z., *J. Am. Chem. Soc.* 2005, **127**, 3258-3259.
429. Bendix, J., *J. Am. Chem. Soc.* 2003, **125**, 13348-13349.
430. Bendix, J.; Birk, T.; Weyhermuller, T., *Dalton Trans.* 2005, 2737-2741.
431. Bendix, J.; Wilson, S. R.; Prussak-Wieckowska, T., *Acta Crystallogr. Sect. C-Cryst. Struct. Commun.* 1998, **54**, 923-925.
432. Birk, T.; Bendix, J., *Inorg. Chem.* 2003, **42**, 7608-7615.
433. Hedegaard, E. D.; Schau-Magnussen, M.; Bendix, J., *Inorg. Chem. Commun.* 2011, **14**, 719-721.
434. Man, W.-L.; Lam, W. W. Y.; Lau, T.-C., *Acc. Chem. Res.* 2014, **47**, 427-439.
435. Man, W.-L.; Chen, G.; Yiu, S.-M.; Shek, L.; Wong, W.-Y.; Wong, W.-T.; Lau, T.-C., *Dalton Trans.* 2010, **39**, 11163-11170.
436. Man, W.-L.; Kwong, H.-K.; Lam, W. W. Y.; Xiang, J.; Wong, T.-W.; Lam, W.-H.; Wong, W.-T.; Peng, S.-M.; Lau, T.-C., *Inorg. Chem.* 2008, **47**, 5936-5944.
437. Yiu, S.-M.; Lam, W. W. Y.; Ho, C.-M.; Lau, T.-C., *J. Am. Chem. Soc.* 2007, **129**, 803-809.

438. Krahe, O.; Bill, E.; Neese, F., *Angew. Chem. Int. Ed.* 2014, **53**, 8727-8731.
439. Seymore, S. B.; Brown, S. N., *Inorg. Chem.* 2002, **41**, 462-469.
440. Arshankow, S. I.; Poznjak, A. L., *Z. Anorg. Allg. Chem.* 1981, **481**, 201-206.
441. Grapperhaus, C. A.; Bill, E.; Weyhermüller, T.; Neese, F.; Wieghardt, K., *Inorg. Chem.* 2001, **40**, 4191-4198.
442. Chang, C. J.; Connick, W. B.; Low, D. W.; Day, M. W.; Gray, H. B., *Inorg. Chem.* 1998, **37**, 3107-3110.
443. Kropp, H.; King, A. E.; Khusniyarov, M. M.; Heinemann, F. W.; Lancaster, K. M.; DeBeer, S.; Bill, E.; Meyer, K., *J. Am. Chem. Soc.* 2012, **134**, 15538-15544.
444. Svenstrup, N.; Bogevig, A.; G. Hazell, R.; Anker Jorgensen, K., *J. Chem. Soc., Perkin Trans.* 1999, 1559-1566.
445. Hewage, J. S.; Wanniarachchi, S.; Morin, T. J.; Liddle, B. J.; Banaszynski, M.; Lindeman, S. V.; Bennett, B.; Gardinier, J. R., *Inorg. Chem.* 2014, **53**, 10070-10084.
446. Solis, B. H.; Hammes-Schiffer, S., *J. Am. Chem. Soc.* 2011, **133**, 19036-19039.
447. Bosnich, B., *J. Am. Chem. Soc.* 1968, **90**, 627-632.
448. Bendix, J.; Meyer, K.; Weyhermüller, T.; Bill, E.; Metzler-Nolte, N.; Wieghardt, K., *Inorg. Chem.* 1998, **37**, 1767-1775.
449. Meyer, K.; Bendix, J.; Metzler-Nolte, N.; Weyhermüller, T.; Wieghardt, K., *J. Am. Chem. Soc.* 1998, **120**, 7260-7270.
450. The oxidized 50% ¹⁵N labelled **[Mn(Sal^{NMe2})N]⁺** shows no evidence of homocoupling up to 24 hours by GC-MS (Table 4.6 and 4.7, Fig. 4.15 and 4.16).
451. Bagh, B.; Broere, D. L. J.; Siegler, M. A.; van der Vlugt, J. I., *Angew. Chem. Int. Ed.* 2016, **55**, 8381-8385.
452. Keener, M.; Peterson, M.; Hernández Sánchez, R.; Oswald, V. F.; Wu, G.; Ménard, G., *Chem. Eur. J.* 2017, **23**, 11479-11484.
453. Ballhausen, C. J.; Gray, H. B., *Inorg. Chem.* 1962, **1**, 111-122.
454. Braun, M.; Fleischer, R.; Mai, B.; Schneider, M.-A.; Lachenicht, S., *Adv. Synth. Catal.* 2004, **346**, 474-482.
455. Michel, F.; Hamman, S.; Philouze, C.; Del Valle, C. P.; Saint-Aman, E.; Thomas, F., *Dalton Trans.* 2009, 832-842.
456. Barman, P.; Upadhyay, P.; Faponle, A. S.; Kumar, J.; Nag, S. S.; Kumar, D.; Sastri, C. V.; de Visser, S. P., *Angew. Chem.* 2016, **128**, 11257-11261.

457. de Visser, S. P.; Quesne, M. G.; Martin, B.; Comba, P.; Ryde, U., *Chem. Commun.* 2014, **50**, 262-282.
458. Kumar, S.; Faponle, A. S.; Barman, P.; Vardhaman, A. K.; Sastri, C. V.; Kumar, D.; de Visser, S. P., *J. Am. Chem. Soc.* 2014, **136**, 17102-17115.
459. Vardhaman, A. K.; Barman, P.; Kumar, S.; Sastri, C. V.; Kumar, D.; de Visser, S. P., *Angew. Chem. Int. Ed.* 2013, **52**, 12288-12292.
460. Liu, W.; Huang, X.; Placzek, M. S.; Krska, S. W.; McQuade, P.; Hooker, J. M.; Groves, J. T., *Chem. Sci.* 2018.
461. Huang, X.; Liu, W.; Ren, H.; Neelamegam, R.; Hooker, J. M.; Groves, J. T., *J. Am. Chem. Soc.* 2014, **136**, 6842-6845.
462. Liu, W.; Groves, J. T., *Angew. Chem. Int. Ed.* 2013, **52**, 6024-6027.
463. Liu, W.; Huang, X.; Cheng, M.-J.; Nielsen, R. J.; Goddard, W. A.; Groves, J. T., *Science* 2012, **337**, 1322-1325.
464. Borovik, A. S., *Chem. Soc. Rev.* 2011, **40**, 1870-1874.
465. Bryliakov, K. P.; Talsi, E. P., *Chem. Eur. J.* 2007, **13**, 8045-8050.
466. Legros, J.; Bolm, C., *Angew. Chem. Int. Ed.* 2003, **42**, 5487-5489.
467. Ware, D. C.; Taube, H., *Inorg. Chem.* 1991, **30**, 4605-4610.
468. Bendix, J.; Anthon, C.; Schau-Magnussen, M.; Brock-Nannestad, T.; Vibenholt, J.; Rehman, M.; Sauer, S. P. A., *Angew. Chem. Int. Ed.* 2011, **50**, 4480-4483.
469. Gupta, R.; Taguchi, T.; Borovik, A. S.; Hendrich, M. P., *Inorg. Chem.* 2013, **52**, 12568-12575.
470. Gupta, R.; Taguchi, T.; Lassalle-Kaiser, B.; Bominaar, E. L.; Yano, J.; Hendrich, M. P.; Borovik, A. S., *Proc. Natl. Acad. Sci. U. S. A.* 2015, **112**, 5319-5324.
471. Scepaniak, J. J.; Margarit, C. G.; Harvey, J. N.; Smith, J. M., *Inorg. Chem.* 2011, **50**, 9508-9517.
472. Eisenberg, D. C.; Lawrie, C. J. C.; Moody, A. E.; Norton, J. R., *J. Am. Chem. Soc.* 1991, **113**, 4888-4895.
473. Sholle, V. D.; Eduard, G. R., *Russ. Chem. Rev.* 1973, **42**, 1011.
474. Zaragoza, J. P. T.; Yosca, T. H.; Siegler, M. A.; Moënné-Loccoz, P.; Green, M. T.; Goldberg, D. P., *J. Am. Chem. Soc.* 2017, **139**, 13640-13643.
475. Gunay, A.; Theopold, K. H., *Chem. Rev.* 2010, **110**, 1060-1081.
476. Engelmann, X.; Monte-Pérez, I.; Ray, K., *Angew. Chem. Int. Ed.* 2016, **55**, 7632-7649.

477. Hohenberger, J.; Ray, K.; Meyer, K., *Nat Commun* 2012, **3**, 720.
478. Lu, H.; Zhang, X. P., *Chem. Soc. Rev.* 2011, **40**, 1899-1909.
479. Che, C.-M.; Lo, V. K.-Y.; Zhou, C.-Y.; Huang, J.-S., *Chem. Soc. Rev.* 2011, **40**, 1950-1975.
480. Henning, H.; Hofbauer, K.; Handke, K.; Stich, R., *Angew. Chem. Int. Ed.* 1997, **36**, 408-410.
481. Sieh, D.; Schoffel, J.; Burger, P., *Dalton Trans.* 2011, **40**, 9512-9524.
482. Musch Long, A. K.; Yu, R. P.; Timmer, G. H.; Berry, J. F., *J. Am. Chem. Soc.* 2010, **132**, 12228-12230.
483. Long, A. K. M.; Timmer, G. H.; Pap, J. S.; Snyder, J. L.; Yu, R. P.; Berry, J. F., *J. Am. Chem. Soc.* 2011, **133**, 13138-13150.
484. Thomson, R. K.; Cantat, T.; Scott, B. L.; Morris, D. E.; Batista, E. R.; Kiplinger, J. L., *Nature Chem.* 2010, **2**, 723.
485. Schlangen, M.; Neugebauer, J.; Reiher, M.; Schröder, D.; López, J. P.; Haryono, M.; Heinemann, F. W.; Grohmann, A.; Schwarz, H., *J. Am. Chem. Soc.* 2008, **130**, 4285-4294.
486. Hojilla Atienza, C. C.; Bowman, A. C.; Lobkovsky, E.; Chirik, P. J., *J. Am. Chem. Soc.* 2010, **132**, 16343-16345.
487. King, D. M.; Tuna, F.; McInnes, E. J. L.; McMaster, J.; Lewis, W.; Blake, A. J.; Liddle, S. T., *Nature Chem.* 2013, **5**, 482.
488. Stavropoulos, P., *Comments Inorg. Chem.* 2017, **37**, 1-57.
489. Lindley, B. M.; Appel, A. M.; Krogh-Jespersen, K.; Mayer, J. M.; Miller, A. J. M., *ACS Energy Letters* 2016, **1**, 698-704.
490. Grinberg Dana, A.; Elishav, O.; Bardow, A.; Shter, G. E.; Grader, G. S., *Angew. Chem. Int. Ed.* 2016, **55**, 8798-8805.
491. Lewis, N. S.; Nocera, D. G., *Proc. Natl. Acad. Sci. U. S. A.* 2006, **103**, 15729-15735.
492. Rees, N. V.; Compton, R. G., *Energy & Environmental Science* 2011, **4**, 1255-1260.
493. Arashiba, K.; Miyake, Y.; Nishibayashi, Y., *Nature Chem.* 2010, **3**, 120.
494. Tanaka, H.; Arashiba, K.; Kuriyama, S.; Sasada, A.; Nakajima, K.; Yoshizawa, K.; Nishibayashi, Y., *Nature Commun.* 2014, **5**, 3737.
495. Kuriyama, S.; Arashiba, K.; Nakajima, K.; Tanaka, H.; Kamaru, N.; Yoshizawa, K.; Nishibayashi, Y., *J. Am. Chem. Soc.* 2014, **136**, 9719-9731.
496. Anderson, J. S.; Rittle, J.; Peters, J. C., *Nature* 2013, **501**, 84.

497. Ung, G.; Peters, J. C., *Angew. Chem. Int. Ed.* 2015, **54**, 532-535.
498. Creutz, S. E.; Peters, J. C., *J. Am. Chem. Soc.* 2014, **136**, 1105-1115.
499. MacLeod, K. C.; Holland, P. L., *Nature Chem.* 2013, **5**, 559.
500. Burford, R. J.; Fryzuk, M. D., *Nat. Rev.Chem.* 2017, **1**, 0026.
501. Dalebrook, A. F.; Gan, W.; Grasemann, M.; Moret, S.; Laurenczy, G., *Chem. Commun.* 2013, **49**, 8735-8751.
502. Klerke, A.; Christensen, C. H.; Norskov, J. K.; Vegge, T., *J. Mater. Chem.* 2008, **18**, 2304-2310.
503. Casalnuovo, A. L.; Calabrese, J. C.; Milstein, D., *Inorg. Chem.* 1987, **26**, 971-973.
504. Zhao, J.; Goldman, A. S.; Hartwig, J. F., *Science* 2005, **307**, 1080-1082.
505. Morgan, E.; MacLean, D. F.; McDonald, R.; Turculet, L., *J. Am. Chem. Soc.* 2009, **131**, 14234-14236.
506. Hulley, E. B.; Bonanno, J. B.; Wolczanski, P. T.; Cundari, T. R.; Lobkovsky, E. B., *Inorg. Chem.* 2010, **49**, 8524-8544.
507. Hillhouse, G. L.; Bercaw, J. E., *J. Am. Chem. Soc.* 1984, **106**, 5472-5478.
508. Khaskin, E.; Iron, M. A.; Shimon, L. J. W.; Zhang, J.; Milstein, D., *J. Am. Chem. Soc.* 2010, **132**, 8542-8543.
509. Gutsulyak, D. V.; Piers, W. E.; Borau-Garcia, J.; Parvez, M., *J. Am. Chem. Soc.* 2013, **135**, 11776-11779.
510. Brown, R. M.; Borau Garcia, J.; Valjus, J.; Roberts, C. J.; Tuononen, H. M.; Parvez, M.; Roesler, R., *Angew. Chem. Int. Ed.* 2015, **54**, 6274-6277.
511. Fafard, C. M.; Adhikari, D.; Foxman, B. M.; Mindiola, D. J.; Ozerov, O. V., *J. Am. Chem. Soc.* 2007, **129**, 10318-10319.
512. Bezdek, M. J.; Guo, S.; Chirik, P. J., *Science* 2016, **354**, 730-733.
513. Margulieux, G. W.; Bezdek, M. J.; Turner, Z. R.; Chirik, P. J., *J. Am. Chem. Soc.* 2017, **139**, 6110-6113.
514. Liu, W.; Huang, X.; Groves, J. T., *Nature Protocols* 2013, **8**, 2348.
515. Abbenseth, J.; Bete, S. C.; Finger, M.; Volkmann, C.; Würtele, C.; Schneider, S., *Organometallics* 2017.

Appendix A. Supplementary Information for Chapter 2

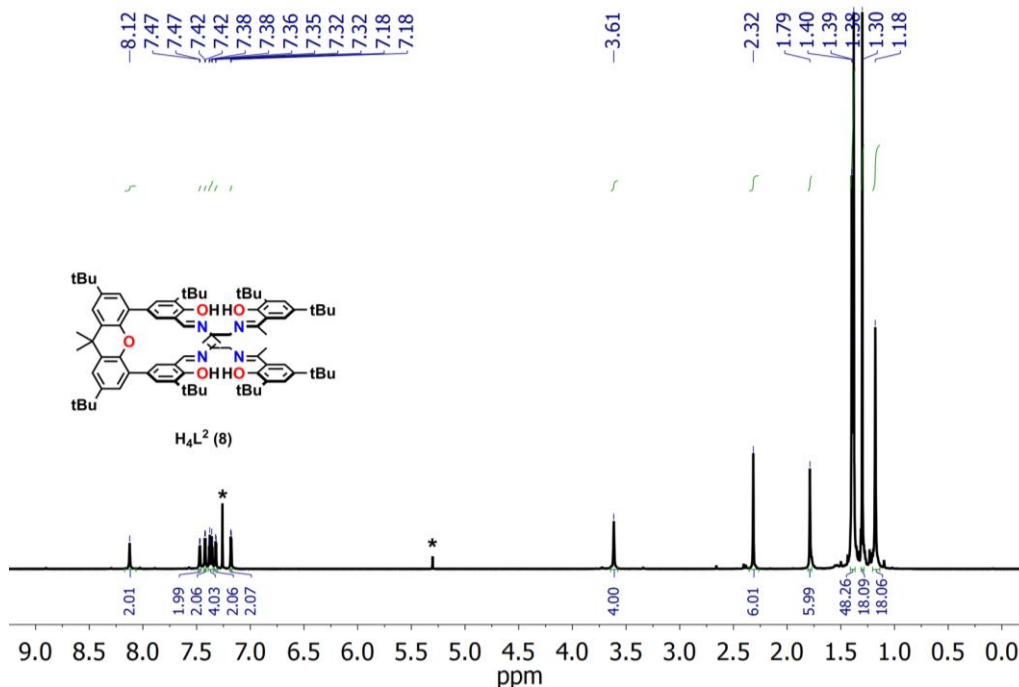


Figure A1. 1H NMR of **8** recorded in $CDCl_3$. Solvent peaks are denoted with an asterisk. Two tBu groups and the backbone methylene groups are very close to one another and integrate for 48 protons total.

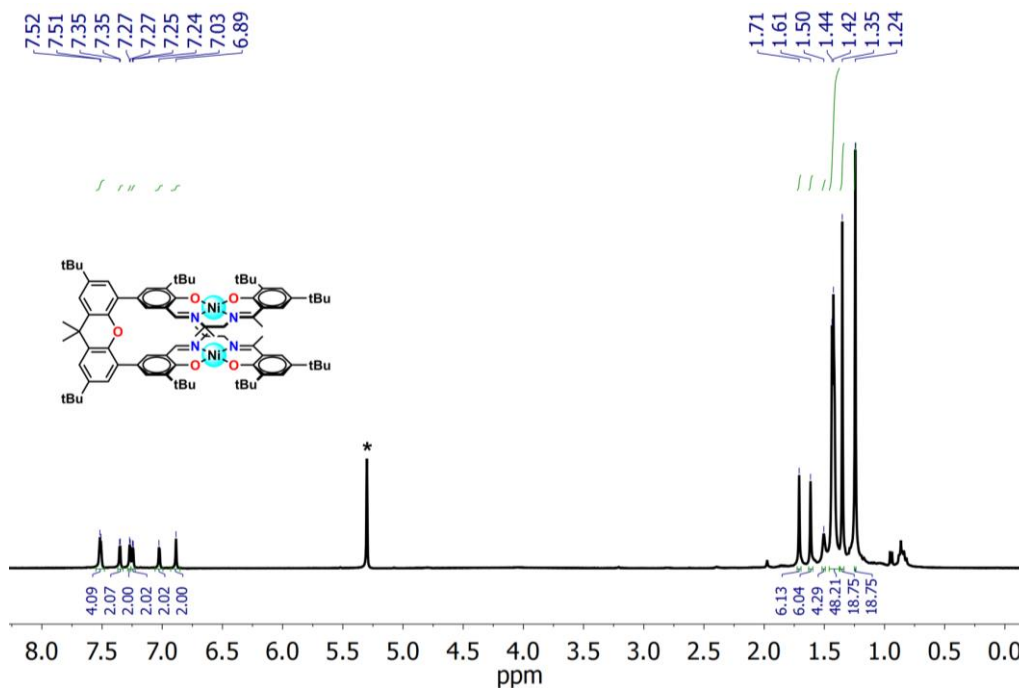


Figure A2. 1H NMR of **2** recorded in $CDCl_3$. The solvent peak is denoted with an asterisk. Two tBu groups and the backbone methylene groups are very close to one another and integrate for 48 protons total.

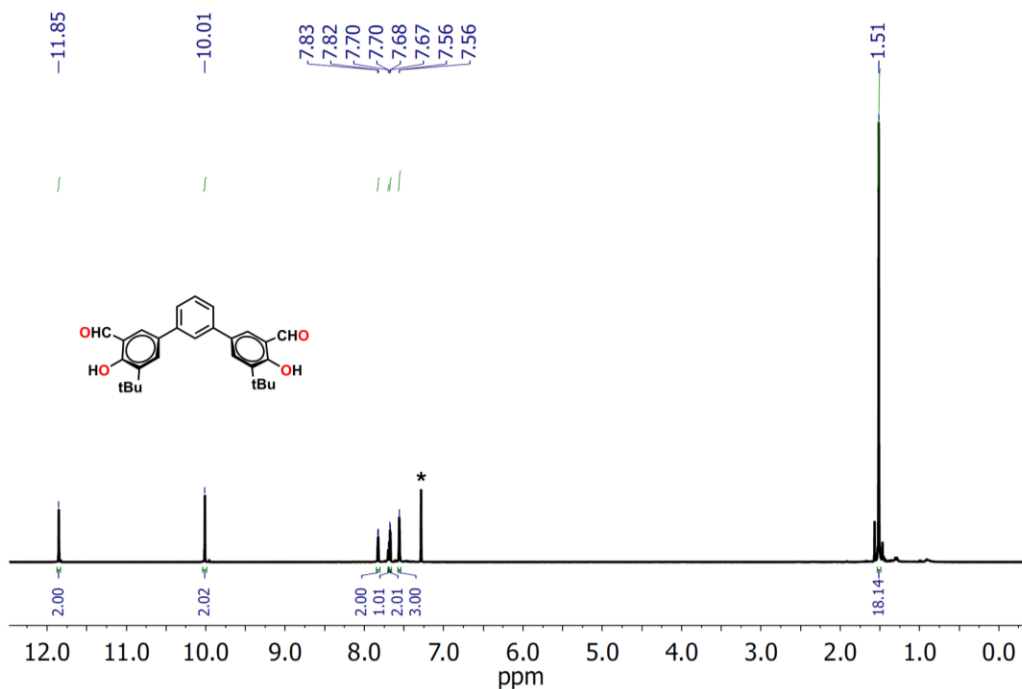


Figure A3. ¹H NMR of **10** recorded in CDCl₃. The solvent peak is denoted with an asterisk.

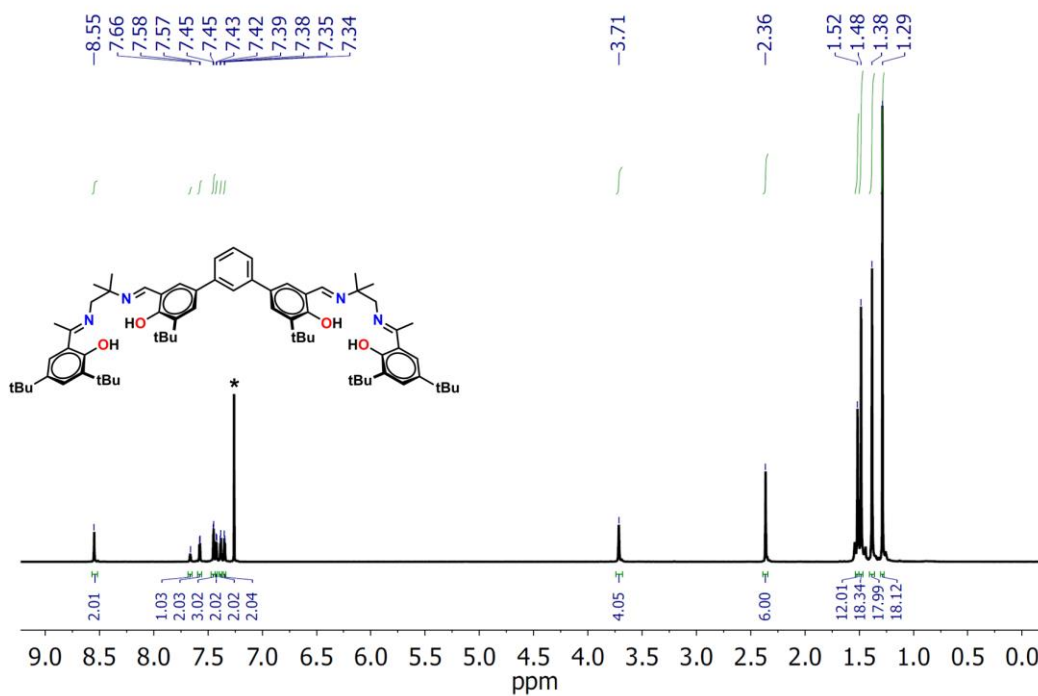


Figure A4. ¹H NMR of **11** recorded in CDCl₃. The solvent peak is denoted with an asterisk.

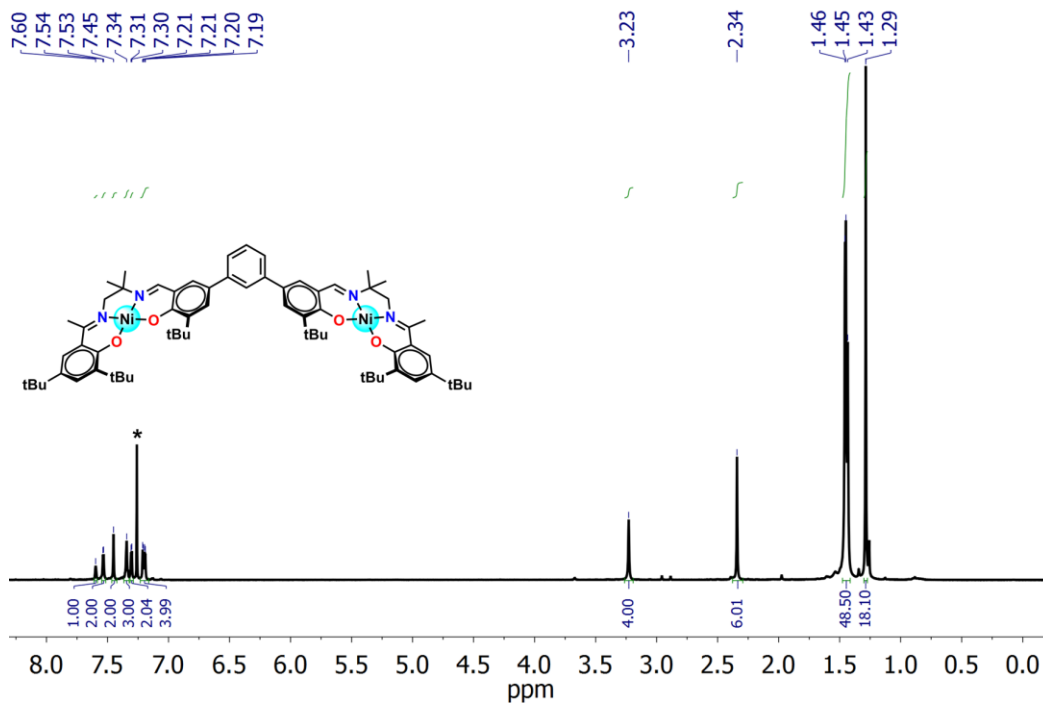


Figure A5. ^1H NMR of **4** recorded in CDCl_3 . The solvent peak is denoted with an asterisk. Two tBu groups, as well as the backbone methylene groups are very close to one another – this region integrates for 48 protons total.

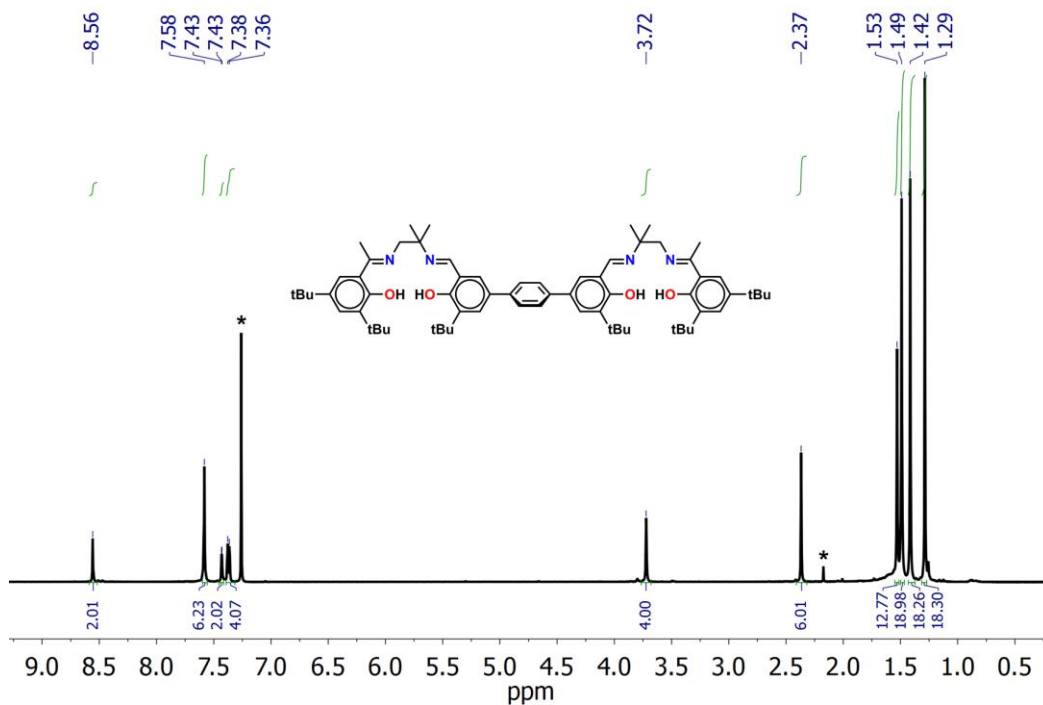


Figure A6. ^1H NMR of **13** recorded in CDCl_3 . The solvent peak is denoted with an asterisk.

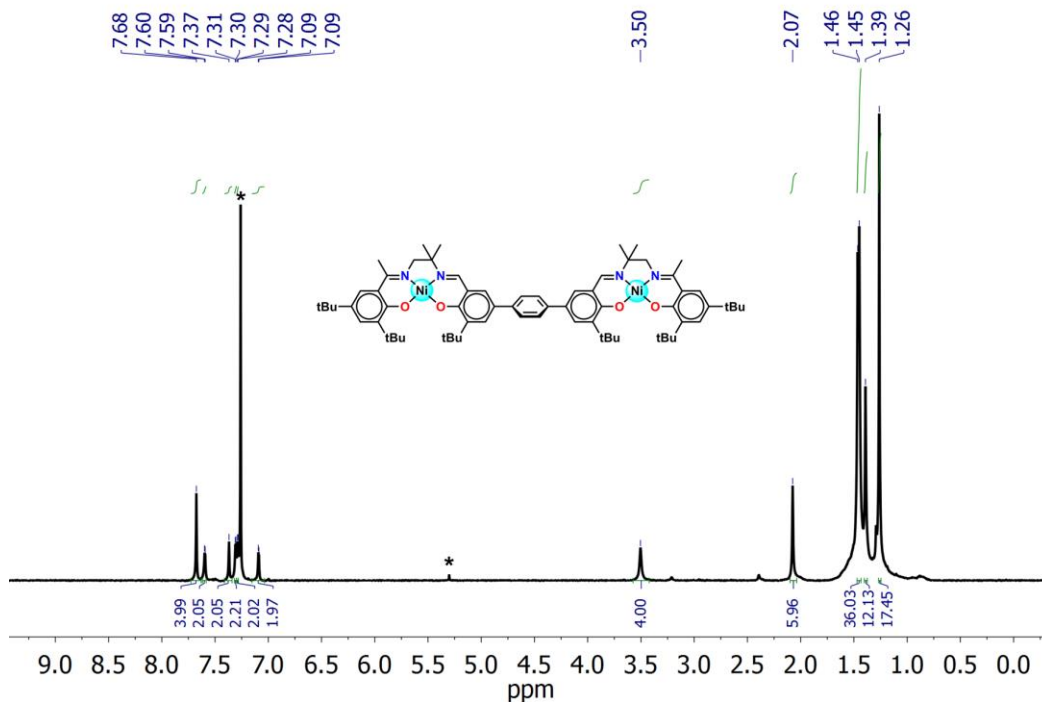


Figure A7. ^1H NMR of **5** recorded in CDCl_3 . Solvent peaks are denoted with asterisks. 2 tBu groups are very close to one another – this region integrates for 36 protons total.

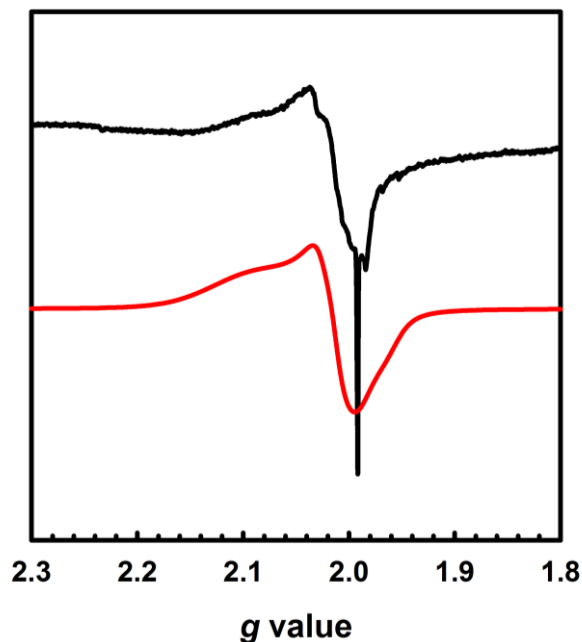


Figure A8. Q-band EPR spectrum of $[\mathbf{2}^*]^{2+}$ recorded in frozen CH_2Cl_2 at 0.8 mM. Conditions: frequency = 33.92 GHz; power = 1.4 mW; modulation frequency = 100 kHz; modulation amplitude = 0.5 mT; $T = 6$ K. The red line represents simulation to the data using the parameters given in the text. The sharp peak originates from the monoradical $[\mathbf{2}^*]^+$.

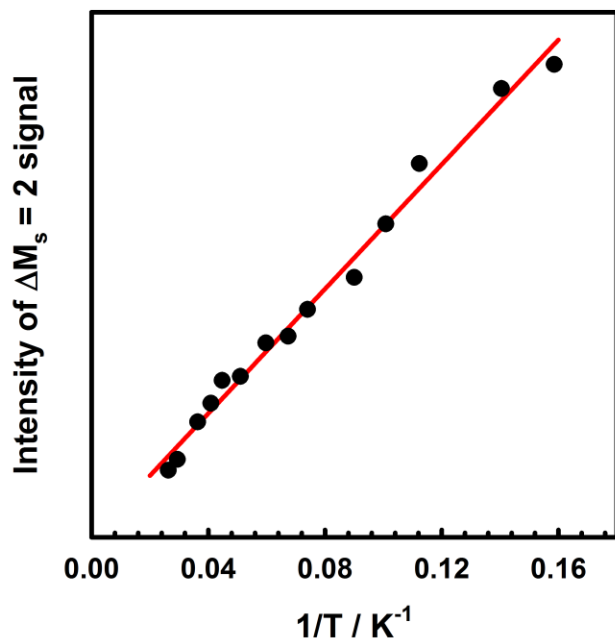


Figure A9. Curie-plot of the half-field signal for $[2^*]^{2+}$.

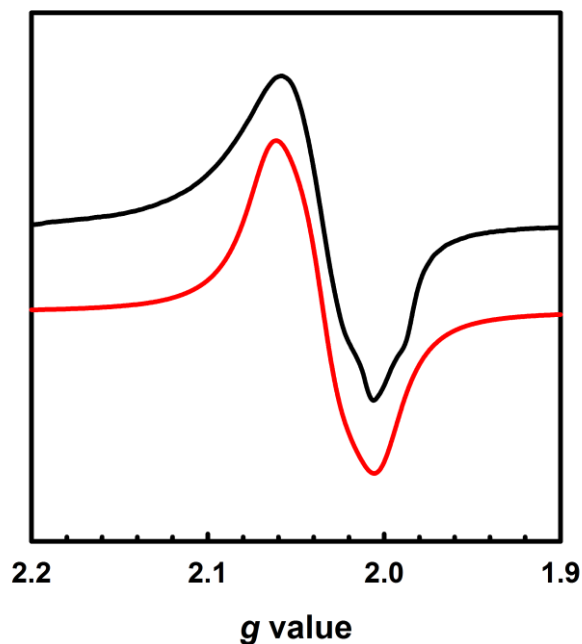


Figure A10. X-band EPR spectrum of $[4^*]^+$ recorded in frozen CH_2Cl_2 at 1.4 mM. Conditions: frequency = 9.64 GHz; power = 2 mW; modulation frequency = 100 kHz; modulation amplitude = 0.2 mT; $T = 16$ K. The red line represents simulation to the experimental data using the parameters: $g_1 = 2.062$, $g_2 = 2.034$, and $g_3 = 2.002$.

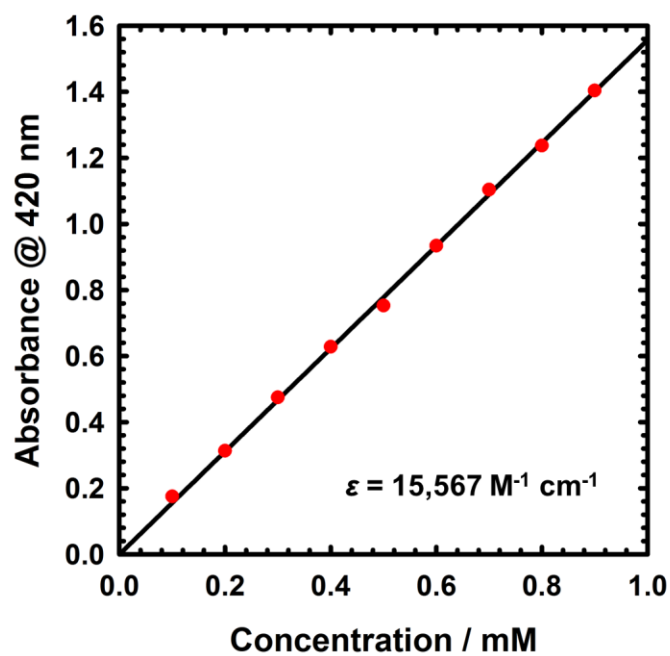


Figure A11. Beers law plot for 2 (0.1 – 0.9 mM) in CH_2Cl_2 at 298 K.

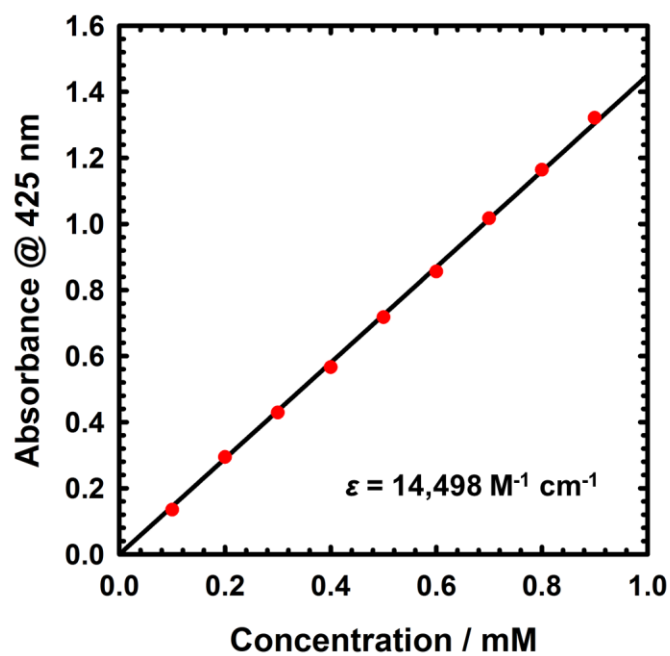


Figure A12. Beers law plot for 4 (0.1 – 0.9 mM) in CH_2Cl_2 at 298 K.

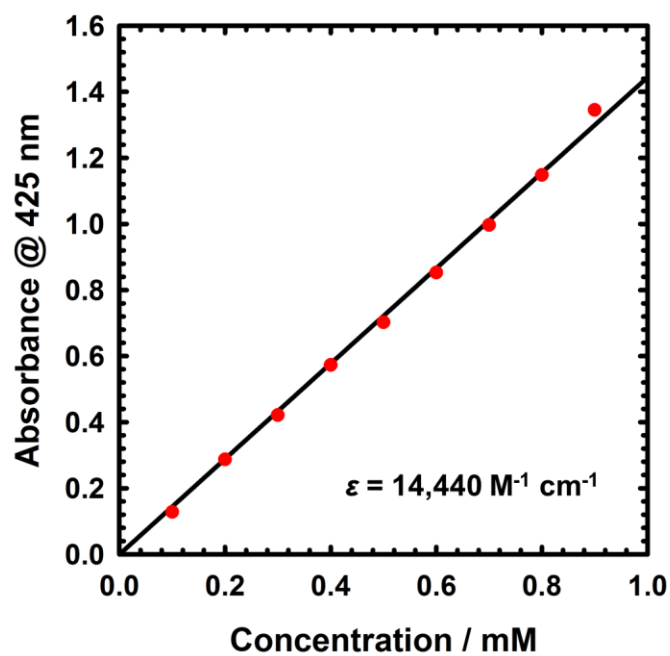


Figure A13. Beers law plot for **5** (0.1 – 0.9 mM) in CH₂Cl₂ at 298 K.

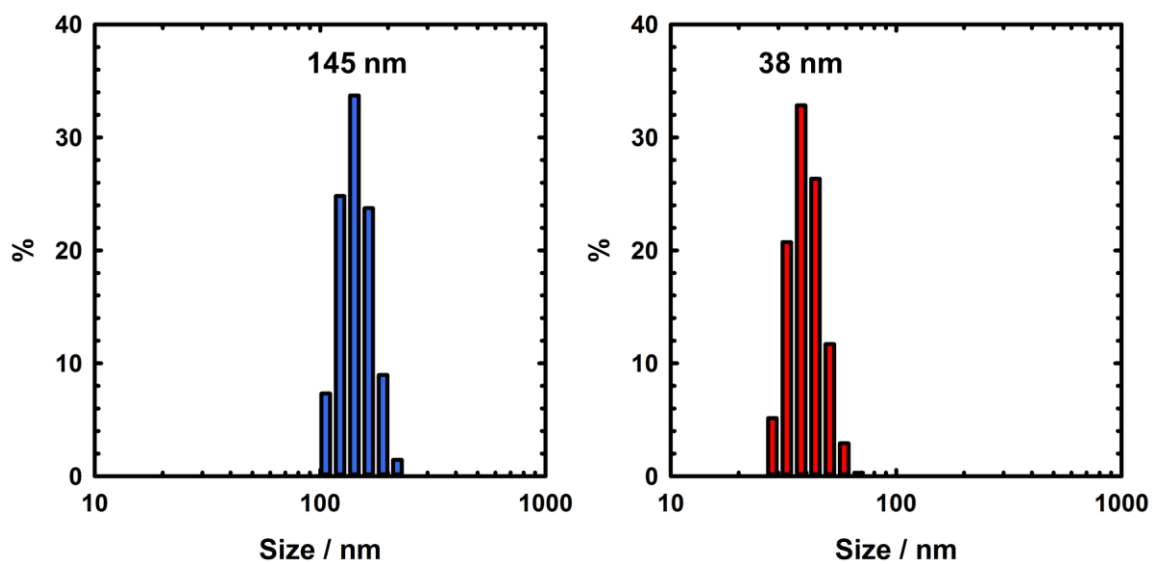


Figure A14. DLS measurements of aggregates formed via low temperature oxidation of **5** (left) and room temperature oxidation (right). Conditions: 0.33 mM, CH₂Cl₂.

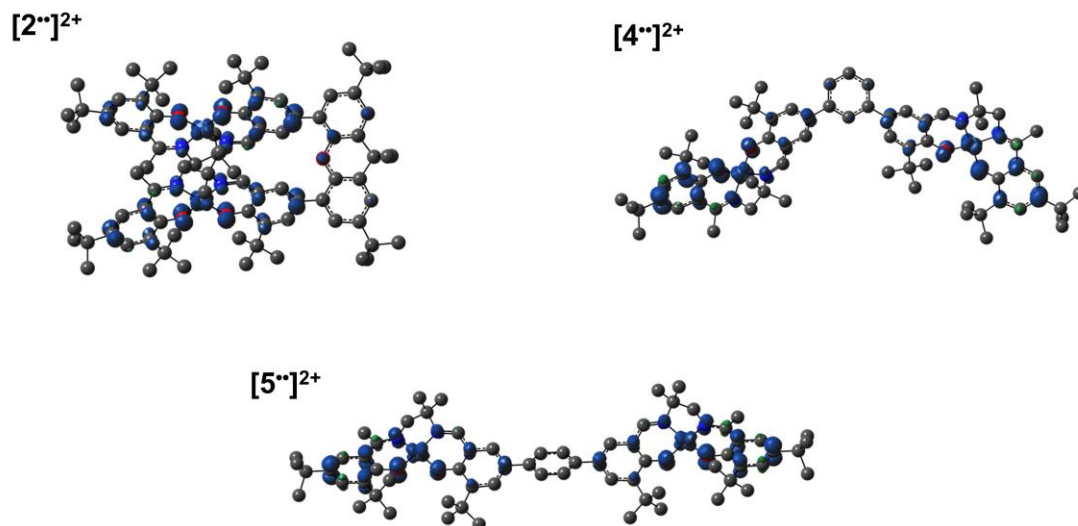


Figure A15. Spin density plots for the triplet ($S = 1$) solutions of $[2^{**}]^{2+}$, $[4^{**}]^{2+}$, and $[5^{**}]^{2+}$.

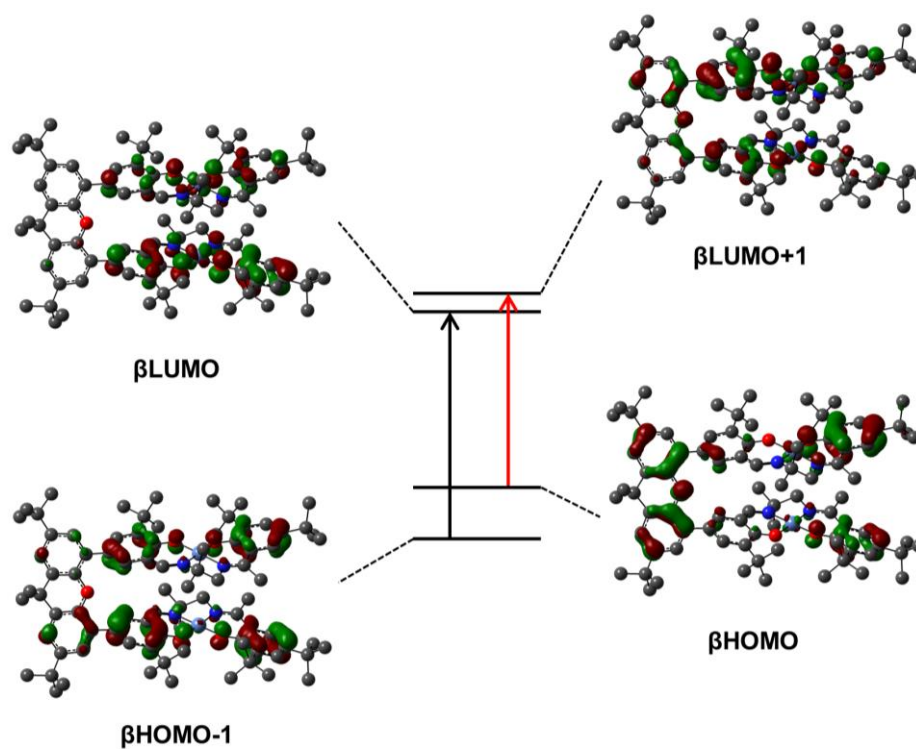


Figure A16. Kohn-Sham molecular orbitals of $[2^{**}]^{2+}$ ($S = 1$) associated with the calculated NIR transitions at $4,385 \text{ cm}^{-1}$ (β HOMO \rightarrow β LUMO+1; red arrow, oscillator strength, $f = 0.0704$) and $5,405 \text{ cm}^{-1}$ (β HOMO-1 \rightarrow β LUMO; black arrow; oscillator strength, $f = 0.3855$).

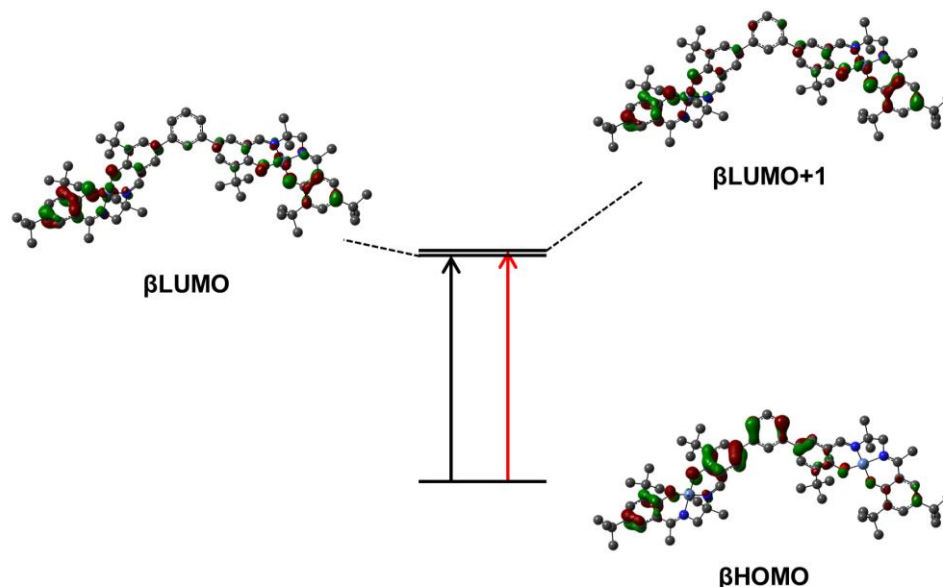


Figure A17. Kohn-Sham molecular orbitals of $[4^{**}]^{2+}$ ($S = 1$) associated with the calculated NIR transitions at $4,935\text{ cm}^{-1}$ ($\beta\text{HOMO} \rightarrow \beta\text{LUMO}$; black arrow; oscillator strength, $f = 0.3971$) and $5,530\text{ cm}^{-1}$ ($\beta\text{HOMO} \rightarrow \beta\text{LUMO}+1$; red arrow; oscillator strength, $f = 0.0931$).

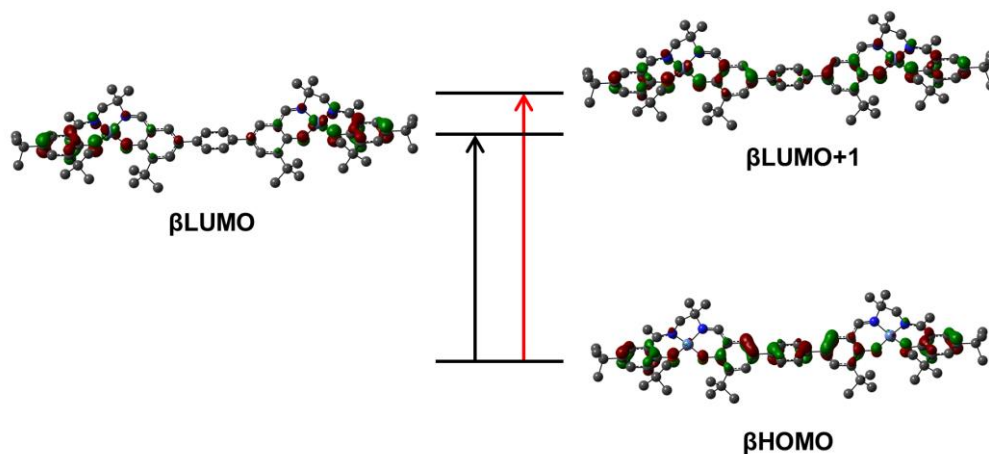


Figure A18. Kohn-Sham molecular orbitals of $[5^{**}]^{2+}$ associated with the calculated NIR transitions at $4,300\text{ cm}^{-1}$ ($\beta\text{HOMO} \rightarrow \beta\text{LUMO}$; black arrow; oscillator strength, $f = 0.7111$) and $5,605\text{ cm}^{-1}$ ($\beta\text{HOMO} \rightarrow \beta\text{LUMO}+1$; red arrow; oscillator strength, $f = 0.002$).

Appendix B. Supplementary Information for Chapter 3

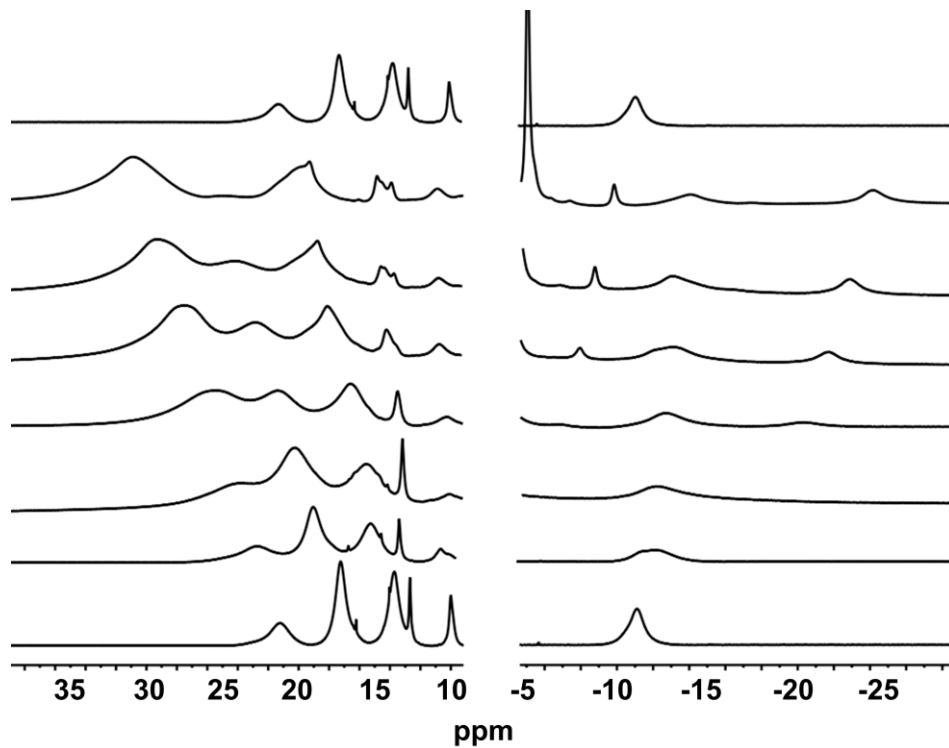


Figure B1. Paramagnetic VT ¹H NMR of Co_2L^2 in the regions 10 → 40 ppm and -5 → -30 ppm recorded in CD_2Cl_2 .

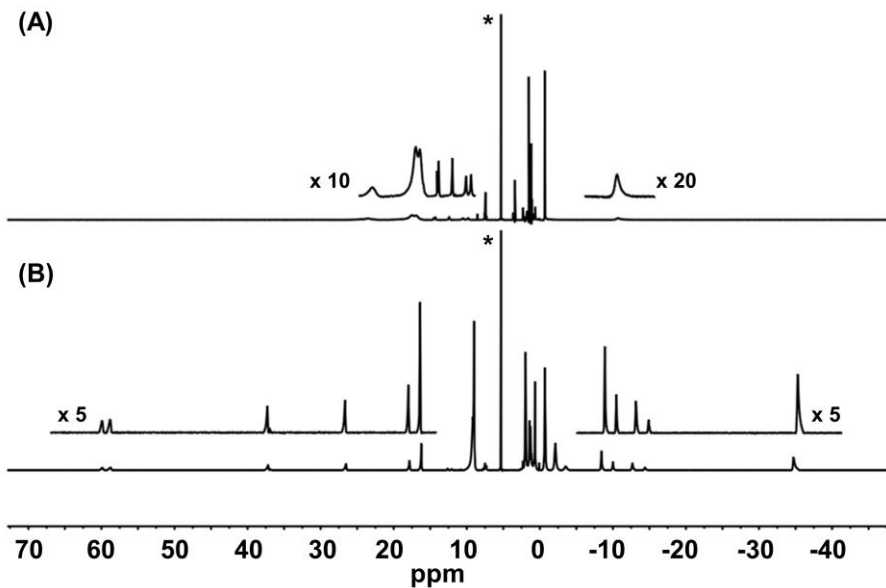


Figure B2. Paramagnetic ^1H NMR of (A) CoL^1 and (B) $[\text{CoL}^1\text{-H}_2\text{O}][\text{SbF}_6]$. Solvent peaks denoted by asterisks.

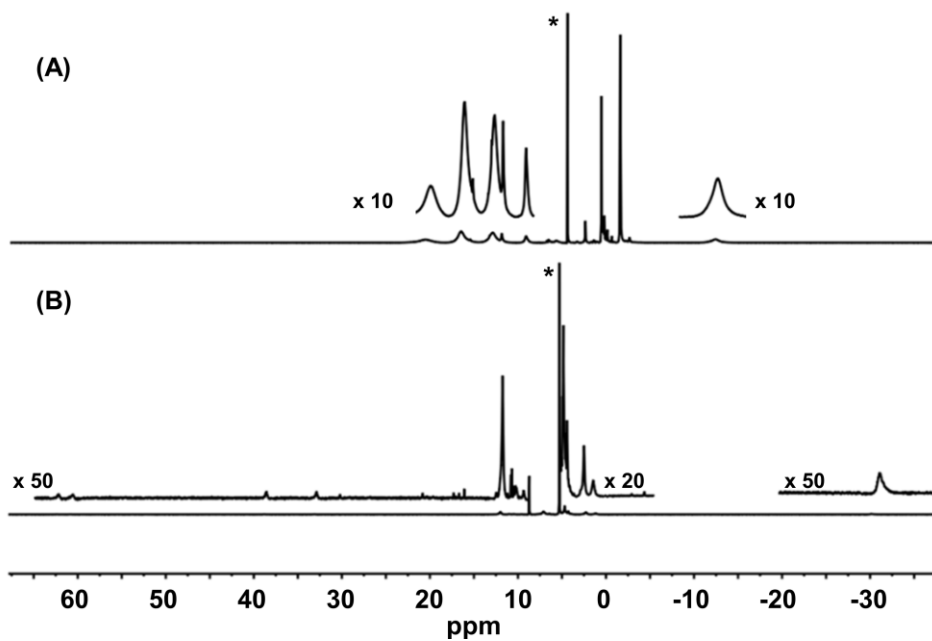


Figure B3. Paramagnetic ^1H NMR of (A) Co_2L^2 and (B) $[\text{Co}_2\text{L}^2\text{-2H}_2\text{O}][2\text{SbF}_6]$. Solvent peaks denoted by asterisks.

Appendix C Supplementary Information for Chapter 4

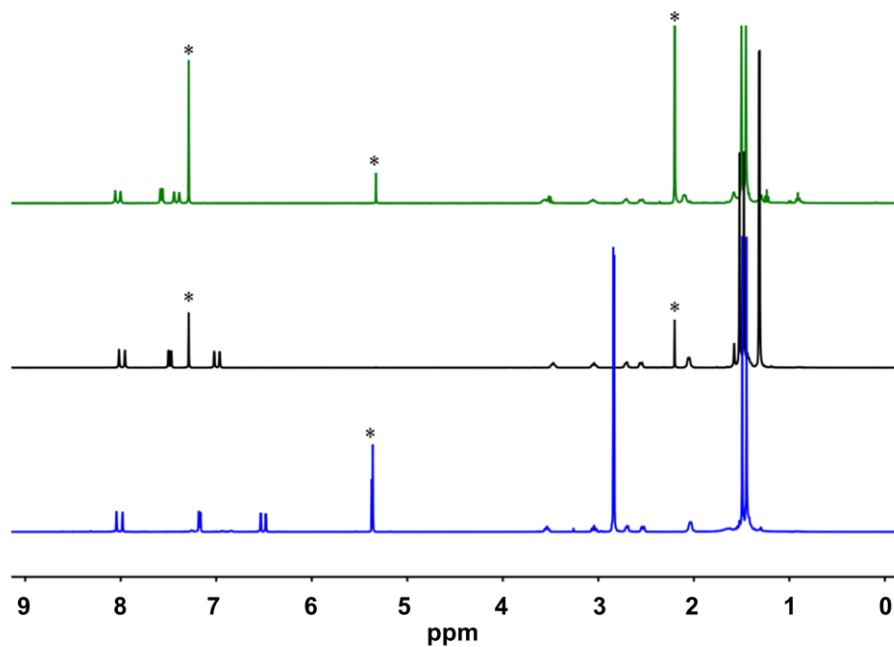


Figure C1. ^1H NMR spectra of $\text{Mn}(\text{Sal}^{\text{R}})\text{N}$ ($\text{R} = \text{CF}_3$, green; tBu , black; NMe_2 , blue). Solvent peaks are denoted with asterisks.

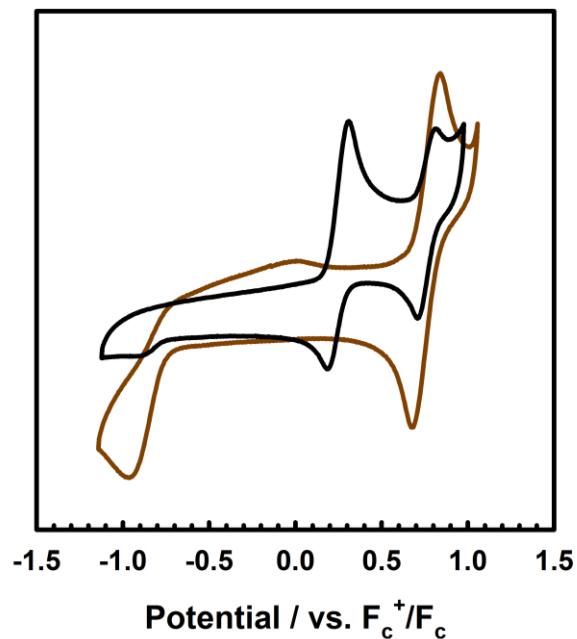


Figure C2. Cyclic voltammograms of $\text{Mn}(\text{Sal}^{\text{tBu}})\text{N}$ (black line) and $[\text{Mn}(\text{Sal}^{\text{tBu}})][\text{SbF}_6]$ (brown line) recorded in CH_2Cl_2 at 233 K.

Conditions: 1 mM complex, 0.1 M $n\text{Bu}_4\text{NClO}_4$, scan rate 100 mV s^{-1} , CH_2Cl_2 , 233 K.

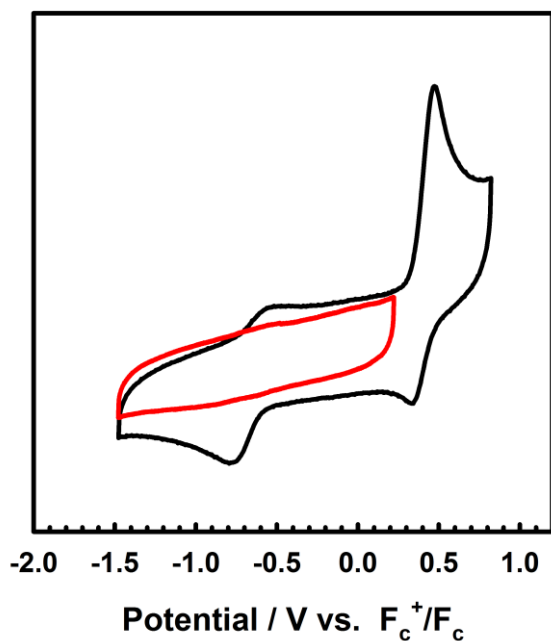


Figure C3. Cyclic voltammograms of $\text{Mn}(\text{Sal}^{\text{tBu}})\text{N}$ showing the association of the reduction process with the reduced $[\text{Mn}(\text{Sal}^{\text{tBu}})]^+$. Stopping the scan before scanning over the first oxidation event (inducing N-N homocoupling, red line) results in no observable reduction process.

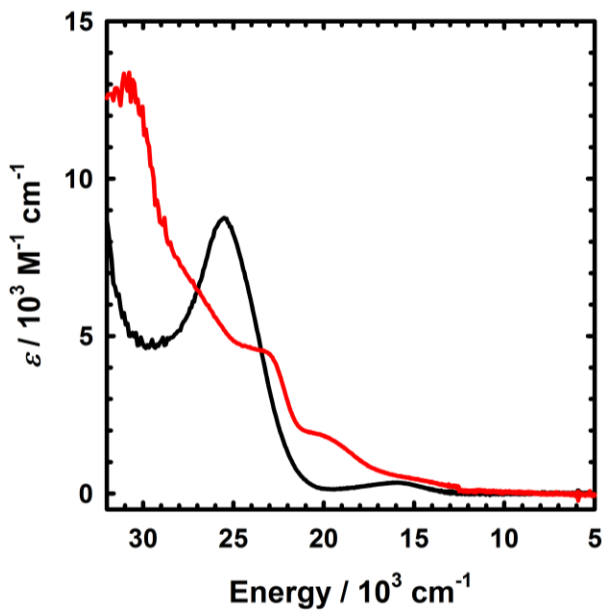


Figure C4. Vis-NIR spectrum of $\text{Mn}(\text{Sal}^{\text{tBu}})\text{N}$ (black line) and $[\text{Mn}(\text{Sal}^{\text{tBu}})][\text{SbF}_6]$ (red line) after addition of 1 equivalent AgSbF_6 . Conditions: 1 mM complex, 1 cm pathlength, CH_2Cl_2 , 298 K.

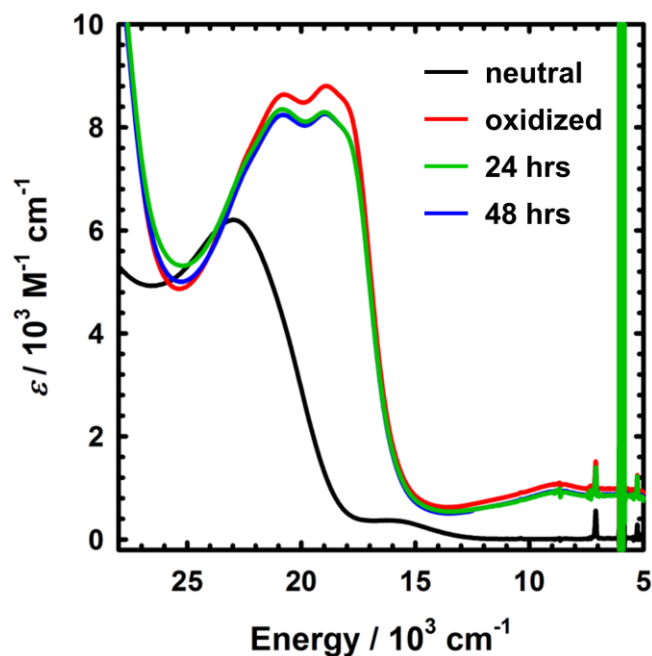


Figure C5. Slow decay of $[\text{Mn}^{\text{V}}(\text{Sal}^{\text{NMe}_2})\text{N}]^{2+}$ after room temperature oxidation with AgSbF_6 over a 48 hour period at 0.2 mM. Intense absorptions at $\sim 6,000 \text{ cm}^{-1}$ are due to the solvent. Employing ESI-MS, we see no evidence of multinuclear species up to 48 hours. Pathlength is 1 cm.

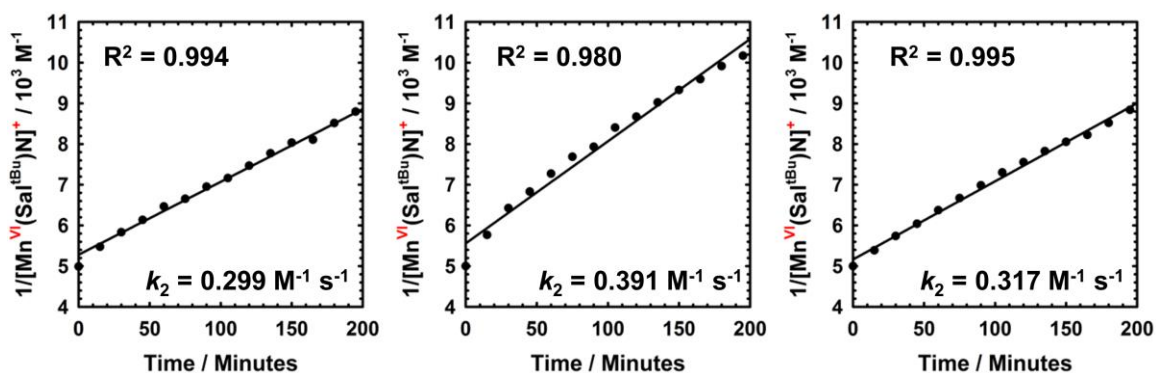


Figure C6. Kinetics data for the decay of $[\text{Mn}^{\text{VI}}(\text{Sal}^{\text{tBu}})\text{N}]^+$ run in triplicate. See the experimental section for full details on oxidation experiments with $[\text{N}(\text{C}_6\text{H}_3\text{Br}_2)_3][\text{SbF}_6]$. $k_{2\text{ave}} = 0.34 \pm 0.04 \text{ M}^{-1} \text{ s}^{-1}$.

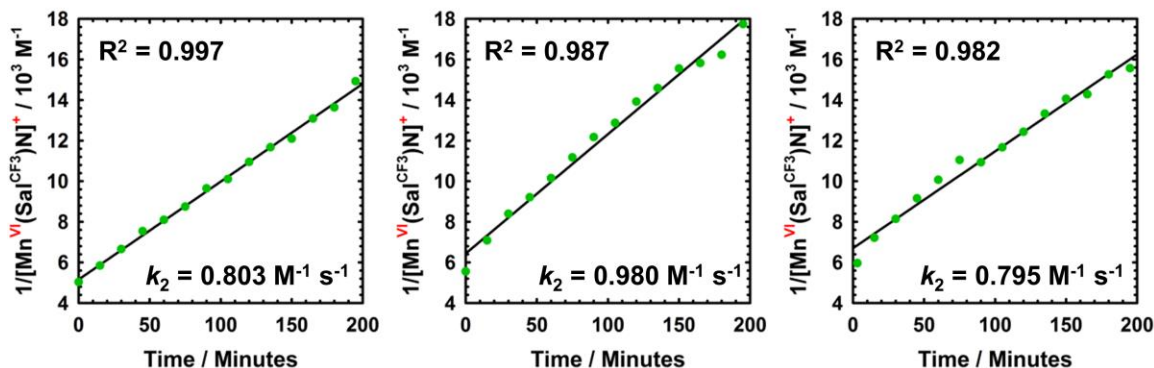


Figure C7. Kinetics data for the decay of $[\text{Mn}^{\text{VI}}(\text{Sal}^{\text{CF}_3})\text{N}]^+$ run in triplicate. See the experimental section for full details on the oxidation experiments with $[\text{N}(\text{C}_6\text{H}_3\text{Br}_2)_3][\text{SbF}_6]$. $k_{2\text{ave}} = 0.86 \pm 0.09 \text{ M}^{-1} \text{ s}^{-1}$.

Table C1. NBO analysis of $[\text{Mn}(\text{Sal}^{\text{R}})\text{N}]^+$ - alpha spin orbitals.

R	σ bond		π bond		π bond	
tBu	51.85% Mn	48.15% N	61.38% Mn	38.62% N	61.17% Mn	38.83% N
	s (12.90%)	s (13.64%)	s (0.07%)	s (0.01%)	s (2.54%)	s (0.12%)
	p (6.58%)	p (86.22%)	p (3.20%)	p (99.84%)	p (5.80%)	p (99.71%)
	d (80.51%)	d (0.15%)	d (96.73%)	d (0.16%)	d (91.66%)	d (0.16%)
CF ₃	53.49% Mn	46.51% N	60.49% Mn	39.51% N	63.14% Mn	36.86% N
	s (9.15%)	s (13.12%)	s (2.63%)	s (0.00%)	s (0.00%)	s (0.13%)
	p (5.11%)	p (86.72%)	p (8.05%)	p (99.83%)	p (2.89%)	p (99.70%)
	d (85.74%)	d (0.15%)	d (89.31%)	d (0.16%)	d (97.10%)	d (0.17%)
NMe ₂	49.10% Mn	50.90% N	50.96% Mn	49.04% N	53.00% Mn	47.00% N
	s (13.81%)	s (15.02%)	s (0.62%)	s (0.00%)	s (1.02%)	s (0.01%)
	p (2.46%)	p (84.86%)	p (17.22%)	p (99.85%)	p (12.72%)	p (99.84%)
	d (83.73%)	d (0.12%)	d (82.16%)	d (0.15%)	d (86.26%)	d (0.15%)

See the experimental section for calculation details.

Table C2. NBO analysis of $[\text{Mn}(\text{Sal}^{\text{R}})\text{N}]^+$ - beta spin orbitals.

R	σ bond		π bond		π bond	
tBu	49.22% Mn	50.78% N	50.16% Mn	49.84% N	52.93% Mn	47.07% N
	s (8.26%)	s (16.38%)	s (0.96%)	s (0.01%)	s (0.00%)	s (0.14%)
	p (3.33%)	p (83.48%)	p (13.50%)	p (99.85%)	p (6.40%)	p (99.71%)
	d (88.40%)	d (0.14%)	d (85.54%)	d (0.14%)	d (93.60%)	d (0.14%)
CF ₃	49.44% Mn	50.56% N	49.90% Mn	50.10% N	53.03% Mn	46.97% N
	s (7.98%)	s (16.06%)	s (1.38%)	s (0.00%)	s (0.01%)	s (0.14%)
	p (2.79%)	p (83.80%)	p (13.48%)	p (99.86%)	p (6.08%)	p (99.72%)
	d (89.24%)	d (0.14%)	d (85.14%)	d (0.14%)	d (93.91%)	d (0.15%)
NMe ₂	47.24% Mn	52.76% N	49.76% Mn	50.24% N	52.54% Mn	47.46% N
	s (16.05%)	s (15.74%)	s (0.09%)	s (0.02%)	s (1.34%)	s (0.01%)
	p (4.08%)	p (84.14%)	p (18.19%)	p (99.84%)	p (9.40%)	p (99.84%)
	d (79.87%)	d (0.12%)	d (81.71%)	d (0.14%)	d (89.26%)	d (0.15%)

See the experimental section for calculation details.

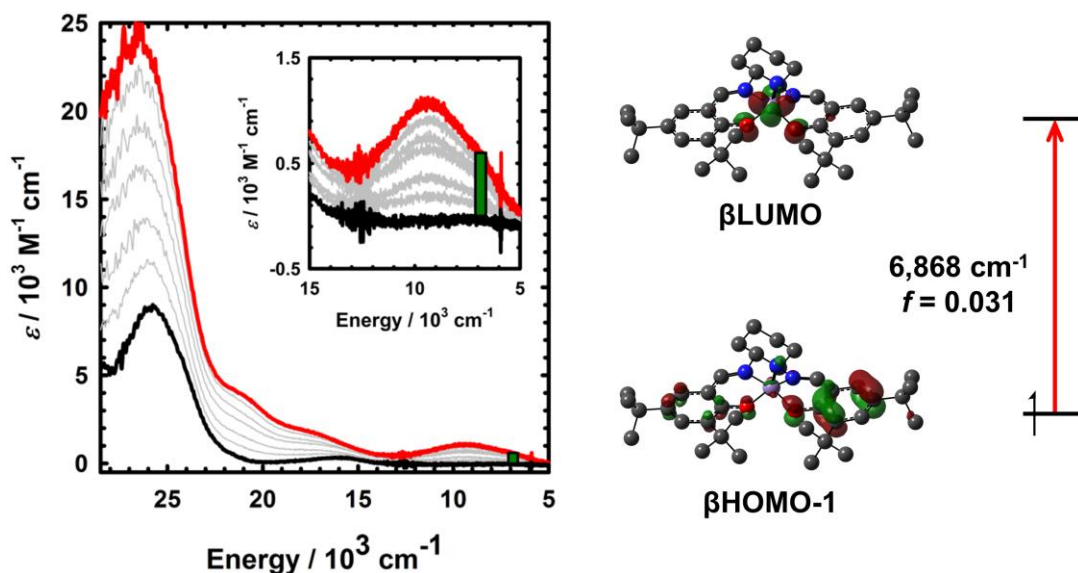


Figure C8. Oxidation titration data for **Mn(Sal^{tBu})N** (black) to the one-electron oxidized species (red). Intermediate grey lines are measured during the oxidation titration. The green bar represents the TD-DFT predicted low energy transition at 6,868 cm^{-1} ($f = 0.031$). TD-DFT predicts this transition to be composed largely of ligand-to-metal charge transfer character, as shown by the orbitals to the right.

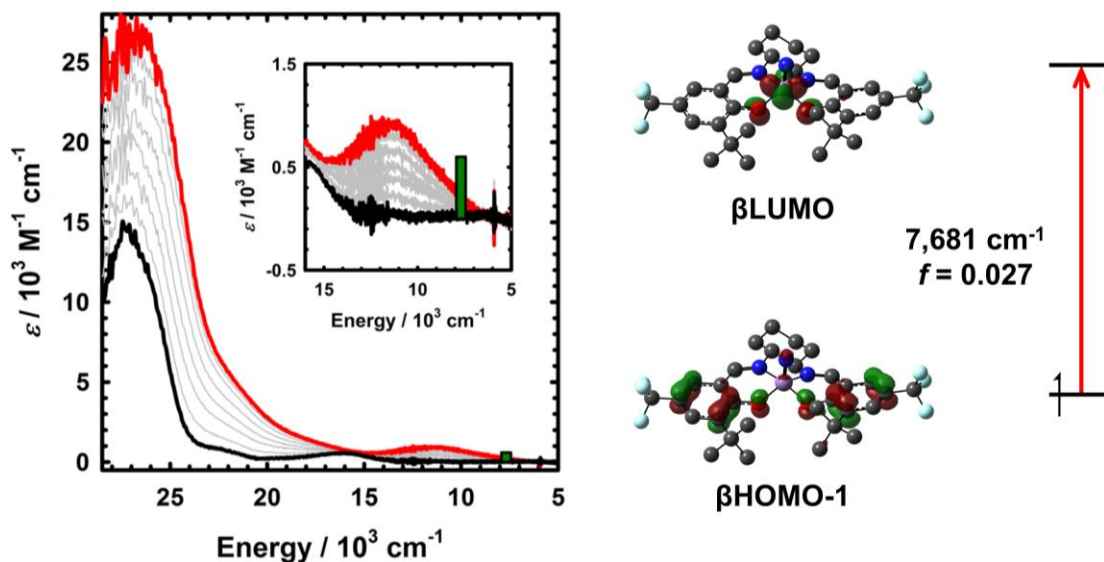


Figure C9. Oxidation titration data for **Mn(Sal^{CF₃})N** (black) to the one-electron oxidized species (red). Intermediate grey lines are measured during the oxidation titration. The green bar represents the TD-DFT predicted low energy transition at 7,681 cm^{-1} ($f = 0.027$). TD-DFT predicts this transition to be composed largely of ligand-to-metal charge transfer character, as shown by the orbitals to the right.

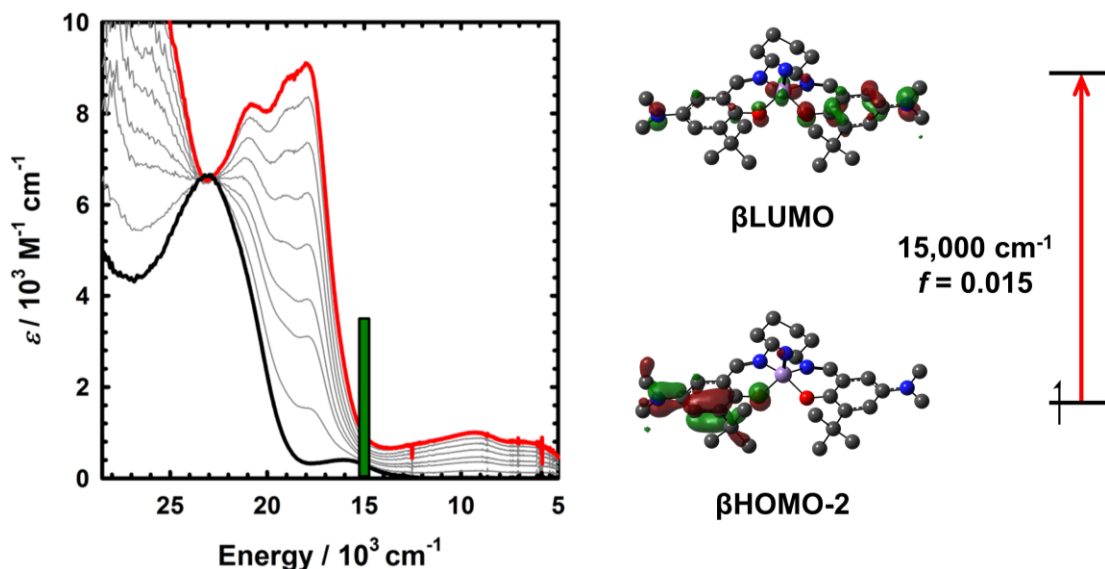


Figure C10. Oxidation titration data for $\text{Mn}(\text{Sal}^{\text{NMe}_2})\text{N}$ (black) to the one-electron oxidized species (red). Intermediate grey lines are measured during the oxidation titration. The green bar represents the TD-DFT predicted low energy transition at $15,000 \text{ cm}^{-1}$ ($f = 0.015$). The predicted transition is composed largely of ligand-to-ligand charge transfer character, as shown by the orbitals to the right. TD-DFT also predicts an intense low energy transition at $4,677 \text{ cm}^{-1}$ ($f = 0.133$), however this band is not observed experimentally.

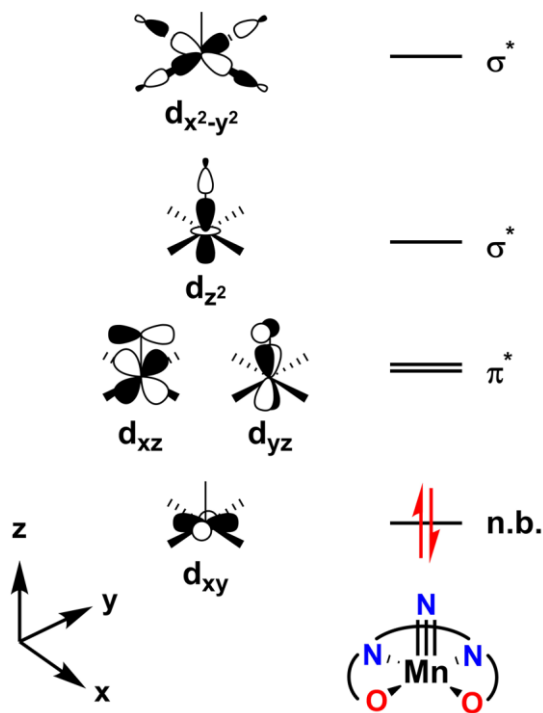


Figure C11. Qualitative partial d-orbital splitting diagram for a square-pyramidal $\text{Mn}(\text{V})$ nitride.⁵¹⁵